**Département d'Astrophysique,
Géophysique et Océanographie**

**Groupe d'AstroPhysique des
Hautes Énergies (GAPHE)**

**Université de Liège
Faculté des Sciences**

STAR Institute

Abundance determination in massive stars: challenges for mixing processes

THESIS FOR THE DEGREE OF
PHILOSOPHIÆ DOCTOR

CONSTANTIN CAZORLA

September 2017

Jury:

Dr. Yaël Nazé (supervisor)
University of Liège

Dr. Thierry Morel (co-supervisor)
University of Liège

Pr. Marc-Antoine Dupret
University of Liège

Dr. Sylvia Ekström
Observatory of Geneva

Dr. Yves Frémat
Royal Observatory of Belgium

Pr. Éric Gosset
University of Liège

Dr. Fabrice Martins
University of Montpellier

Pr. Gregor Rauw
University of Liège

Abstract:

Massive stars, the most luminous stars, are the true “cosmic engines” of our Universe. They eject large quantity of material throughout their life, which strongly influences their evolutionary path as well as their environment. An important feature of massive stars is their high rotational velocities that are either acquired at birth or due to the influence of a companion. Rotation is believed to transport nitrogen-rich and carbon/oxygen-poor material generated in the stellar core through the CNO cycle, to the surface. A way to test the efficiency of rotational mixing is to study the chemical composition at the surface of stars, in particular the fastest rotators.

The incentive for this study was the discovery, in the context of the VLT-FLAMES Survey of Massive Stars, of fast rotators exhibiting an unenriched nitrogen composition at their surface, contrary to predictions from single-star evolutionary models including rotation. However, their multiplicity may affect this conclusion, since both rotation and abundances can change as a result of binary interactions. In this work, we combined, for the first time, a detailed surface abundance analysis with a radial-velocity study to quantify the importance of binary effects. This work was conducted for a sample of 40 bright, OB fast rotators in our Galaxy. Statistical tests and period-search techniques revealed that $\sim 40\%$ of our targets whose multiplicity status can be probed, are binary or binary candidates. We derived the projected rotational velocity of our targets and model atmosphere codes were then used to derive stellar parameters and surface abundances of all sample stars. This abundance study revealed a correlation between the helium and nitrogen abundances of our targets, which is predicted by the rotational mixing theory. Finally, we compared our results to predictions of single-star evolutionary models. We found that $10-20\%$ of our 40 targets exhibit no enhancement of the [N/O] abundance ratio, in line with results of the VLT-FLAMES Survey of Massive Stars. The properties of only half of our sample are explained by such models, and surprisingly we also uncovered a quite common large abundance of helium at the surface of our targets. Modifying the diffusion coefficient in single-star models and models of non-rotating mergers did not reproduce simultaneously both the observed helium abundances and the [N/O] abundance ratios. Binary models considering a mass-transfer episode can, however, reproduce the [N/O] values of the majority of our targets and even the helium abundances of some of the most helium-enriched targets, but they cannot explain stars displaying little helium enrichment but high

[N/O] values. In conclusion, we found that not every feature of massive stars can be explained by models, suggesting that they lack a physical ingredient and thus require further improvements.

The second part of this thesis aimed at improving our knowledge of the X-ray emission of early B-type stars. We studied 11 such stars at high resolution thanks to two X-ray facilities, XMM-*Newton* and Chandra, doubling the number of B-stars analysed at high resolution. In many aspects, our study confirmed previous ones: early B-stars display rather narrow and unshifted lines arising from a warm (of typically 0.2 – 0.6 keV) plasma located at a few stellar radii over the stellar surface. We also found that abundances derived in the X-ray domain are in fair agreement with photospheric ones derived in the optical domain. Furthermore, most early B-stars are moderately bright X-ray emitters – though we also unexpectedly found that this X-ray emission varies, on short and/or long timescales, for half of our sample. A few stars display peculiar features: the presence of a very hot (1.6 – 4.4 keV) component and strong variations. These features suggest that the recorded X-ray emission may not be entirely linked to the B-stars, but could be contaminated by emission from a companion or an interaction with it. Indeed, in one case, HD 79351, a flare was detected, of a luminosity compatible with those from PMS stars, and which could be associated to its companion. Finally, the data used also led to the discovery of the second case of X-ray pulsations associated to β Cephei activity.

Résumé :

Les étoiles massives, qui sont les étoiles les plus lumineuses, sont les véritables "moteurs cosmiques" de notre Univers. Elles éjectent de grandes quantités de matière au cours de leur vie, ce qui influence fortement leur évolution ainsi que leur environnement. Une caractéristique importante de ces étoiles massives est leur vitesse de rotation élevée qu'elles acquièrent à leur naissance ou suite à l'influence d'un compagnon. Cette rotation est censée induire un transport de la matière riche en azote et pauvre en carbone/oxygène, créée au coeur des étoiles massives au travers du cycle CNO, à leur surface. Une façon de tester l'efficacité d'un tel mélange rotationnel est d'étudier la composition chimique à la surface d'étoiles, en particulier celles présentant la rotation la plus rapide.

La motivation de cette étude était la découverte, dans le contexte du projet VLT-FLAMES Survey of Massive Stars, de rotateurs rapides montrant une composition chimique non-enrichie en azote à leur surface, contrairement à ce qui est prédit par les modèles d'évolution d'étoiles isolées considérant la rotation de ces étoiles. Cependant, leur multiplicité peut affecter cette conclusion, du fait que la rotation et les abundances peuvent être modifiées à la suite d'interactions au sein de systèmes binaires. Dans ce travail, nous avons combiné, pour la première fois, une analyse détaillée des abondances de surface avec une étude des vitesses radiales pour quantifier l'importance des effets de binarité. Ce travail a été réalisé pour un échantillon de 40 rotateurs rapides brillants, de type spectraux OB et faisant partie de notre Galaxie. Des tests statistiques ainsi que des techniques de recherche de périodes ont révélé que $\sim$ 40% de nos cibles dont la multiplicité a pu être déterminée sont des binaires ou des candidats binaires. Nous avons déterminé la vitesse de rotation projetée de nos cibles. Des codes de modèles d'atmosphère ont ensuite été utilisés pour déterminer les paramètres stellaires ainsi que les abondances de surface des étoiles de notre échantillon. L'étude des abondances a révélé une correlation entre les abondances d'hélium et d'azote de nos cibles, comme prédit par la théorie du mélange rotationnel. Enfin, nous avons comparé nos résultats avec les prédictions de modèles d'évolution d'étoiles isolées. Nous avons trouvé que $10 - 20\%$ de nos 40 cibles ne montre pas d'élévation du rapport d'abondance [N/O], en accord avec les résultats du VLT-FLAMES Survey of Massive Stars. Seule la moitié des étoiles de notre échantillon ont leur propriétés expliquées par ces modèles,

et, étonnamment, une importante abondance d'hélium a fréquemment été trouvée à la surface de nos cibles. La modification du coefficient de diffusion dans les modèles d'étoiles isolées ainsi que les modèles résultant de la fusion de deux étoiles n'ont pas permis de reproduire simultanément les abondances d'hélium et les rapports d'abondance [N/O] observés. Les modèles d'étoiles binaires considérant un épisode de transfert de masse peuvent, cependant, reproduire les valeurs du rapport [N/O] de la majorité de nos cibles et même les abondances d'hélium de certaines étoiles qui présentent le plus important enrichissement en hélium, mais ils ne peuvent pas expliquer le fait que des étoiles présentent un faible enrichissement en hélium mais des rapports [N/O] élevés. En conclusion, nous avons trouvé que l'ensemble des propriétés des étoiles massives ne peut pas être expliqué par les modèles d'évolution actuels, ce qui suggère qu'un ingrédient physique nécessite d'y être intégré, nécessitant donc un développement supplémentaire.

La seconde partie de cette thèse avait pour but d'améliorer notre connaissance sur l'émission X d'étoiles de type spectral B précoces. Nous avons étudié 11 de ces étoiles grâce à deux télescopes (XMM-*Newton* et Chandra) permettant l'acquisition de données de haute résolution, ce qui a permis de doubler le nombre d'étoiles B étudiées à haute résolution. À bien des égards, notre étude a confirmé plusieurs études antérieures: les étoiles B précoces présentent des raies non décalées et plutôt étroites, qui sont créées par un plasma chaud (à typiquement 0.2 – 0.6 keV) localisé à plusieurs rayons stellaires à partir de la surface. Nous avons aussi trouvé que les abondances déterminées dans le domaine des rayons X sont en bon accord avec celles déterminées pour la photosphère dans le domaine visible. De plus, la plupart des étoiles B précoces sont des émetteurs de rayons X modérément brillantes – bien que nous ayons trouvé de manière inattendue une variation de cette émission X sur de courtes et/ou longues périodes de temps pour la moitié de notre échantillon. Certains objets montrent des propriétés particulières: la présence d'une composante très chaude (de 1.6 – 4.4 keV) et de fortes variations de l'émission X. Ces propriétés suggèrent que l'émission X observée peut ne pas être entièrement liée à l'étoile B, mais peut être contaminée par de l'émission par un compagnon ou une interaction avec celui-ci. En effet, dans le cas de HD 79351, une éruption stellaire a été détectée, avec une luminosité en accord avec celles des éruptions d'étoiles pré-séquence principale : le changement de luminosité est donc peut-être lié à son compagnon. Finalement, les données que nous avons utilisées ont aussi mené à la découverte d'un second cas de pulsations X associées à une activité β Cephei.

LIST OF PAPERS

Referred publications related to the thesis:

I **Cazorla, C.**, Morel, T., Nazé, Y., Rauw, G., Semaan, T., Daflon, S., Oey, M. S., 2017a,
Chemical abundances of fast-rotating massive stars. I. Description of the methods and individual results
A&A, **603**, A56

II **Cazorla, C.**, Nazé, Y., Morel, T., Georgy, G., Godart, M., Langer, N., 2017b,
Chemical abundances of fast-rotating massive stars. II. Interpretation and comparison with evolutionary models
A&A, accepted

III **Cazorla, C.** & Nazé, Y., 2017c,
B-stars seen at high resolution by XMM-Newton
A&A, submitted

Unreferred publications not related to the thesis:

I Proceedings following the IAU Symposium 307 (Geneva, 23rd – 27th June 2014): *New windows on massive stars: asteroseismology, interferometry, and spectropolarimetry*,
Cazorla, C., Morel, T., Nazé, Y., Rauw, G., 2015,
Chemical abundances of fast-rotating OB stars,
G. Meynet, C. Georgy, J.H. Groh & Ph. Stee, eds., **307**, 94

II Poster exhibiting results obtained in the X-ray domain with *XMM*-Newton, during the X-ray Universe 2017 Symposium (Rome, 6th – 9th June 2017)
Nazé, Y., **Cazorla, C.**, Rauw, G., Morel, T., 2017,
A legacy survey of early B-stars using the RGS

Referred publications not related to the thesis:

I **Cazorla, C.**, Nazé, Y., Rauw, G., 2014,
Wind collisions in three massive stars of Cygnus OB2
A&A, **561**, A92

II Nazé, Y., Rauw, G., **Cazorla, C.**, 2017,
π *Aqr is another* γ *Cas object*
A&A, **602**, L5

CONTENTS

Abstract **v**

List of Papers **xi**

List of Abbreviations **xv**

List of Tables **xix**

List of Figures **xxi**

1 Background and motivation **1**

1.1 General context . . . 2

1.1.1 Massive stars . . . 2

1.1.2 Stellar rotation . . . 4

1.1.2.1 Stellar shape and critical velocities . . . 6

1.1.2.2 Gravity darkening effect . . . 9

1.1.2.3 Transport of angular momentum and chemical elements . . . 16

1.1.3 Multiplicity . . . 23

1.1.4 X-rays from massive stars . . . 24

1.2 Thesis outline . . . 27

1.2.1 Rationale of the study . . . 27

2 Optical study **31**

2.1 Derivation of abundances . . . 32

2.1.1 Methods and tools . . . 32

2.1.1.1 Projected rotational velocity . . . 32

2.1.1.2 Turbulence broadening . . . 33

2.1.1.3 Atmospheric parameters and He, CNO abundances . . . 34

2.1.2 Published paper . . . 40

2.1.2.1 Complementary information . . . 98

2.2 Comparison with evolutionary models . . . 106

2.2.1 Stellar models . . . 106

2.2.2 Published paper . . . 113

2.2.2.1 Complementary information . . . 137

3 X-ray study **141**

3.1 Used X-ray facilities . . . 142

3.2 Some X-ray properties of stars 144
3.3 Published paper 147

4 Conclusions and Perspectives 163

5 Acknowledgements 169

Bibliography 171

A Proceedings and Poster 179

List of Abbreviations

ACIS	**A**dvanced **C**CD **I**maging **S**pectrometer
ALI	**A**ccelerated **L**ambda **I**teration
ATHENA/X-IFU	**A**dvanced **T**elescope for **H**igh-**EN**ergy **A**strophysics**/X**-ray **I**ntegral **F**ield **U**nit
BONNSAI	**BONN** **S**tellar **A**strophysics **I**nterface
CCD	**C**harge-**C**oupled **D**evice
CLÉS	**C**ode **L**iégeois d'**É**volution **S**tellaire
CMFGEN	**C**o**M**oving **F**rame **GEN**eral
CPU	**C**entral **P**rocessing **U**nit
ELT	**E**xtremely **L**arge **T**elescope
EPIC	**E**uropean **P**hoton **I**maging **C**amera
ESA	**E**uropean **S**pace **A**gency
eV	**E**lectron-**V**olt
EW	**E**quivalent **W**idth
FASTWIND	**F**ast **A**nalysis of **ST**ellar atmospheres with **WIND**s
FIP	**F**irst **I**onisation **P**otential
FLAMES	**F**ibre **L**arge **A**rray **M**ulti-**E**lement **S**pectrograph
FWHM	**F**ull-**W**idth at **H**alf **M**aximum
GSF	**G**oldreich-**S**chubert-**F**ricke
HEG	**H**igh **E**nergy **G**rating
HETGS	**H**igh **E**nergy **T**ransmission **G**rating **S**pectrometer
HMXB	**H**igh **M**ass **X**-ray **B**inary

HRC	**H**igh **R**esolution **C**amera
HRI	**H**igh **R**esolution **I**mager
HR	**H**ertzsprung-**R**ussell
LBV	**L**uminous **B**lue **V**ariable
LETGS	**L**ow **E**nergy **T**ransmission **G**rating **S**pectrometer
LMC	**L**arge **M**agellanic **C**loud
LOSP	**L**iège **O**rbital **S**olution **P**ackage
MCWS	**M**agnetically-**C**onfined **W**ind **S**hock
MC	**M**agellanic **C**loud
MEG	**M**edium **E**nergy **G**rating
MESA	**M**odules for **E**xperiments in **S**tellar **A**strophysics
MiMeS	**M**agnetism **i**n **M**assive **S**tars
MOS	**M**etal **O**xide **S**emi-conductor
MS	**M**ain **S**equence
NASA	**N**ational **A**eronautics and **S**pace **A**dministration
NLTE	**N**on-**L**ocal **T**hermodynamic **E**quilibrium
NS	**N**eutron **S**tar
OM	**O**ptical **M**onitor
PMS	**P**re-**M**ain **S**equence
PoWR	**Po**tsdam **W**olf-**R**ayet
PSPC	**P**osition **S**ensitive **P**roportional **C**ounters
RASS	**R**OSAT **A**ll **S**ky **S**urvey
RDI	**R**adiation-**D**riven **I**nstabilities

RGA	**R**eflection **G**rating **A**rray
RGS	**R**eflection **G**rating **S**pectrometer
RLOF	**R**oche-**L**obe **O**verflow
RV	**R**adial **V**elocity
SB1	Single-lined **S**pectroscopic **B**inary
SB2	Double-lined **S**pectroscopic **B**inary
sdO	**S**ub**d**warf **O** star
UV	**U**ltra**V**iolet
VLT	**V**ery **L**arge **T**elescope
WFC	**W**ide **F**ield **C**amera
WR	**W**olf-**R**ayet
XMM-*Newton*	**X**-ray **M**ulti-**M**irror **M**ission-*Newton*
XRT	**X**-**R**ay-**T**elescope
ZAMS	**Z**ero **A**ge **M**ain **S**equence

List of Tables

1.1 Predicted Eddington factor for MS stars (for a core hydrogen mass fraction of 0.30) at the middle of the MS phase and the first critical velocity as a function of the initial stellar mass 9
1.2 Galactic fast-rotating stars whose surface CNO abundances had been studied prior to our work 29

2.1 Differences in atmospheric parameters and He, CNO abundances found for HD 163892 when the broadening of DETAIL/SURFACE spectra is not only due to the stellar rotation (and microturbulence), but also to macroturbulence 35
2.2 Changes in the atmospheric parameters and surface abundances when HD 163892 is analysed with Kurucz models using a helium abundance twice solar 100
2.3 Impact of the uncertainty in effective temperature on CNO abundances 102
2.4 Tentative orbital solutions, presented for completeness, obtained with the LOSP program for two stars of our sample . 104
2.5 Information on the X-ray emission for our targets 105
2.6 Rotating single stellar models, starting from 2000 108
2.7 Comparison between the observed helium abundance and [N/O] abundance ratios with predicted values by BONNSAI, as a function of input parameters 138

3.1 List of our studied X-ray emitters 147

LIST OF FIGURES

1.1 HR diagram 3
1.2 Illustration of the energy transport processes at work in solar-type and more massive stars 3
1.3 CNO cycle 4
1.4 Illustration of the projected rotational velocity 6
1.5 Probability density of equatorial and projected rotational velocities for 496 stars with spectral types O9.5 – B8 6
1.6 Illustration of the stellar distorsion of a rotating star as a function of the ω ratio 10
1.7 Illustration of $v_{\rm crit,1}$ as a function of the stellar masses, for different Z 11
1.8 Predicted $v \sin i$ as a function of $\log g$ 11
1.9 Derived $v \sin i$ as a function of the $\log g_{\rm polar}$ for field and cluster stars 12
1.10 Illustration of the variation in $T_{\rm eff}$ over the surface of a rotating star as a function of θ 13
1.11 Near-infrared intensity image of Altair 13
1.12 Illustration of the rotational broadening of a line profile. Impact of the rotational velocity on line profiles. Line widths of the He I 4471 line profile predicted for a B2-type spherical or flattened star as a function of $v \sin i/v_{\rm crit,1}$ 14
1.13 Variation of the luminosity as a function of the ω ratio for several stellar masses 15
1.14 Illustration of the meridional circulation within a 20 $M_\odot$ rotating star with an initial rotational velocity of 300 km s^{-1} 17
1.15 Illustration of the differential rotation 19
1.16 Comparison of the diffusion coefficients in a 20 $M_\odot$ rotating star with an initial rotational velocity of 300 km s^{-1} at the beginning of the MS phase 20
1.17 Surface nitrogen abundance at the middle and at the end of the MS phase as a function of the initial stellar mass 22
1.18 Schematic evolution of a massive close binary system 25
1.19 Nitrogen abundance as a function of the projected rotational velocity for stars with $\log g \geq 3.20$ dex in extended regions around N11 and NGC 2004 in the LMC 28

2.1 Illustration of the way the projected rotational velocity was estimated, for HD 93521, with the He I 6678 line profile . . 33
2.2 Illustration of the variation of the EW of some Si III line profiles as a function of ξ 35
2.3 Illustration of the broadening of the wings of Hγ with $\log g$. 39
2.4 Illustration of the curve of growth: evolution of the EW as a function of the number of absorbing atoms 40
2.5 Predicted distribution of $v \sin i$ for MS massive stars assuming the binary properties of Sana et al. (2012) 99
2.6 Illustration of the determination of $v \sin i$ and $v_{\rm mac}$ of HD 93521 thanks to spectral synthesis, using the He I 4921 line 100
2.7 Grid of synthetic spectra used to derive the atmospheric parameters and helium abundance for the cooler stars 101
2.9 Fourier periodogram derived from the RVs of HD 28446A. Phase diagram of the RV values of HD 28446A folded with a 3.37730 d period 103
2.10 Fourier periodiogram derived from the RVs of HD 41161. Phase diagram of the RV values of HD 41161 folded on a 3.26594 days period 104
2.11 Difference between our parameter estimates and those found by Martins et al. (2015a,b) as a function of the difference in temperature 106
2.12 Difference between our parameter estimates and those found by Martins et al. (2015a,b) as a function of the difference in surface gravity 107
2.13 Difference between our [N/O] abundance ratio estimates and those found by Martins et al. (2015a,b) as a function of the difference in [N/C] 109
2.14 Histograms of the differences between our results and those derived by Martins et al. (2015a,b), normalised by the errors 110
2.15 Predicted $v \sin i$ as a function of $\log g_{\rm C}$ by the Geneva and Bonn models 111
2.16 Difference between the predicted [N/O] abundance ratios by BONNSAI when first and second sets and first and third sets of input parameters are used as a function of difference between the predicted y by BONNSAI 137

1

Background and motivation

The first chapter introduces massive stars, some of their properties, as well as the rationale for this thesis.

1.1 General context

1.1.1 Massive stars

Massive stars are stars whose mass is greater than 8 solar masses and with spectral types O and early-B when on the main sequence. They are therefore situated in the upper left part of the Hertzsprung-Russell (HR) diagram, as shown in Fig. 1.1. These massive stars are the true "cosmic engines" of our Universe. These stars are the most luminous ones and are able to ionise the interstellar medium. They eject large quantities of material in the interstellar medium throughout their life (through a clumped stellar wind) following the action of their strong ultraviolet (UV) radiation. Such winds modify their evolutionary path, shape the interstellar medium, trigger or halt neighbouring stellar formation, and largely contribute to the chemical enrichment of their surroundings. Their mass-loss rates amount to $\simeq 10^{-6}$ $M_\odot$ yr^{-1} for O-type star on the main-sequence (MS, Martins et al. 2004) with wind velocities of several thousands km s^{-1}, and up to 10^{-4} $M_\odot$ yr^{-1} for short-lived luminous blue variable (LBV) stages (Vink & de Koter 2002; Smith et al. 2004; de Koter 2006; Groh et al. 2009). Massive stars finally explode in supernovae, this phenomenon having a large impact on their surroundings. For all these reasons, it is essential to get an in-depth comprehension of massive stars. This work is aimed at modestly contributing to a better understanding of these fascinating objects.

Massive stars have a different internal structure than that of solar-type stars, as illustrated in Fig. 1.2. Stars similar to the Sun have, from the core to the surface, first a radiative zone and then a convective envelope. The situation is opposite for massive stars as they have a convective zone near their core and a radiative envelope. A thin convective zone due to opacity peaks linked with iron and helium ionisations is also present in the outer layers of some very luminous massive MS stars, but it contains a negligible amount of mass (Iglesias et al. 1992; Stothers & Chin 1993; Iglesias & Rogers 1996; Cantiello et al. 2009). Matter in the outer layers is therefore not mixed except if some additional process takes place.

Massive stars burn their central hydrogen content through the CNO cycle (Fig. 1.3). Stars whose mass does not exceed ~ 40 $M_\odot$ experience the CNO-I cycle, which starts by converting atoms of ${}^{12}_{6}$C into atoms of ${}^{14}_{7}$N.

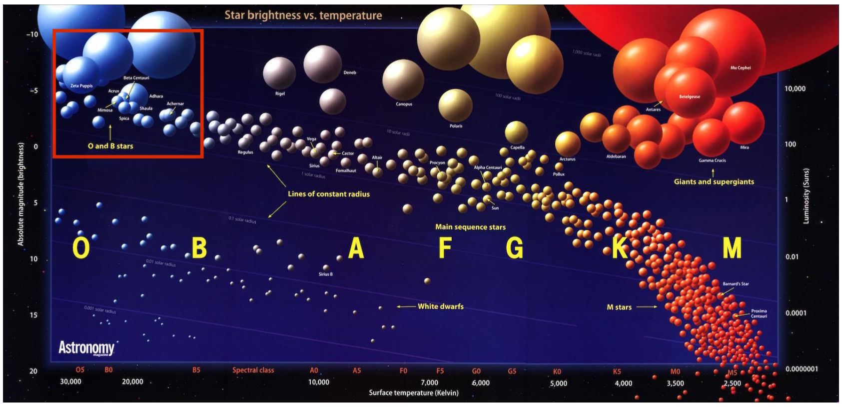

Figure 1.1: HR diagram. OB stars are highlighted with the red rectangle. *Source: Astronomy magazine* ©.

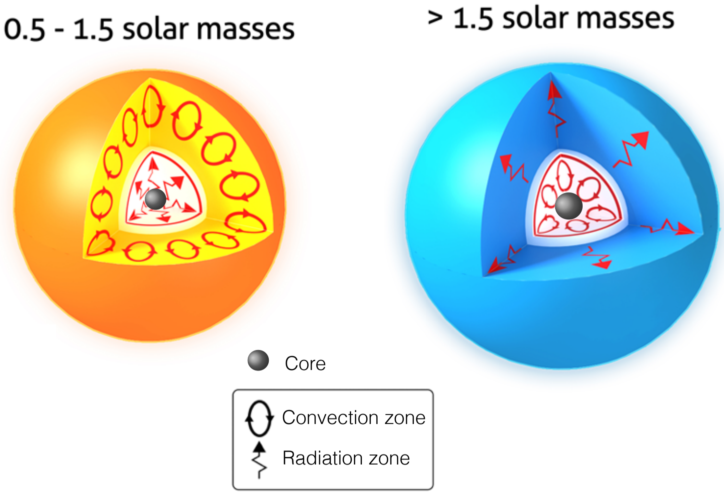

Figure 1.2: Illustration of the energy transport processes at work in solar-type (*left*) and massive stars (*right*). *Source:* adapted from `http://www.sun.org/images/heat-transfer-in-stars`

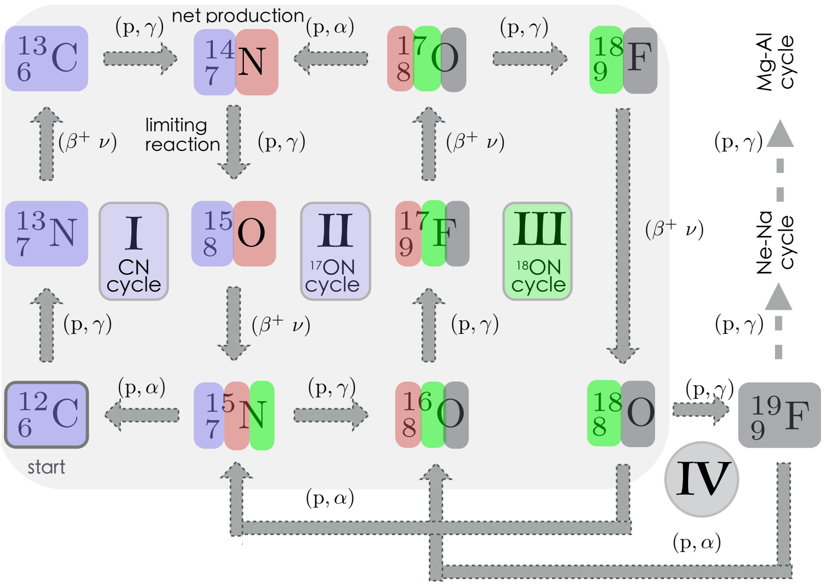

Figure 1.3: CNO cycle. The part of the diagram highlighted in gray shows the CN- and ON-cycles. Carbon and nitrogen, oxygen-17 and nitrogen, and oxygen-18 and nitrogen are the catalysts for the CN, ^{17}ON, and ^{18}ON cycles, respectively. The different branches of the CNO cycle are indicated by the roman numbers.

The limiting reaction that follows is the source of an excess of nitrogen and a depletion of carbon in the stellar core. This cycle is also called the CN cycle because it does not involve a stable isotope of oxygen. Heavier stars go even further by entering into the ON cycles (also called CNO-II & III cycles), in which the atoms of $^{16}_{8}$O are slowly destroyed to produce $^{14}_{7}$N atoms. The number of atoms of $^{12}_{6}$C can be considered as constant in these cycles, but it also leads to a nitrogen excess in the core.

1.1.2 Stellar rotation

Understandably, the first star that has been studied by astronomers is the Sun. Thomas Harriot was probably the first European to notice the presence of spots at the surface of the Sun, as demonstrated by drawings from 8th December 1610 found in his notebook. Johannes Fabricius was the first to observe the motion of sunspots on the solar surface and to publish these observations, in *De Maculis in Sole Observatis, et Apparente earum cum Sole Conversione Narratio*, 1611. His findings were in disagreement with the views of Christopher Scheiner, who proposed that the spots might be small planets revolving around the Sun. Galileo Galilei confirmed in 1612 the discovery of Fabricius, by noticing a change in the size and shape of sunspots as they move towards the solar equator, which is incompatible with the view of Scheiner, and that proves that the Sun is rather a rotating object. The Sun is not the only star to rotate, of course. In this context, it is important to note the high rotational velocities of massive stars. They are characterised by projected rotational velocities, $v \sin\, i$ (where v is the stellar rotational velocity at the equator and i the angle between the line of sight and the rotation axis; see Fig. 1.4), typically a hundred times the Sun's value (Fig. 1.5). Such fast rotation can be acquired at birth, as a result of their formation in molecular clouds under the action of gravity. The size r of these clouds is drastically reduced during the collapse (from typically a few parsecs to a few solar radii), which implies a severe increase of their angular velocity Ω according to the angular momentum conservation law $\Omega\, r^2 =$ constant – it has nevertheless to be noted that a significant amount of angular momentum is lost during the stellar formation process though interactions with the accretion disk. Fast rotation can also develop during the stellar evolution when a star interacts with its companion (see Sect. 1.1.3). The importance of rotation on the evolution of massive stars is now considered to be comparable to that of stellar winds, influencing all aspects of stellar evolution models (Meynet & Maeder, 2000). The next subsections briefly present these consequences.

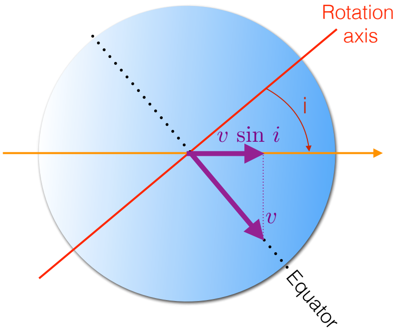

Figure 1.4: Illustration of the projected rotational velocity. *Source:* adapted from `https://en.wikipedia.org/wiki/Stellar_rotation`

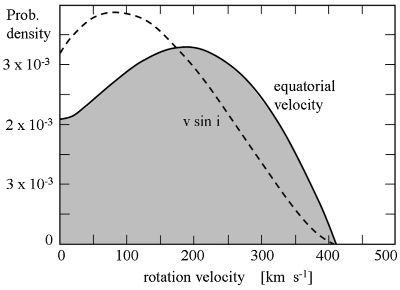

Figure 1.5: Probability density of rotational velocities for 496 stars with spectral types O9.5–B8 (Maeder & Meynet 2012, with data from Huang & Gies 2006). For comparison, the Sun's rotational velocity is $\sim$ 2 km s^{-1}.

1.1.2.1 Stellar shape and critical velocities

In the Roche approximation, in which the mass inside an isobar can be considered as point-like, the total potential ψ is the sum of the gravitational ϕ and the centrifugal χ potentials:

$$\psi(r,\theta) = \underbrace{-\frac{\mathrm{G}M_r}{r}}_{\phi} - \underbrace{\frac{1}{2}\Omega^2 r^2 \sin^2(\theta)}_{\chi},$$

where r is the distance to the stellar centre, θ the colatitude, M_r the mass inside the radius r, and Ω is the angular velocity. The stellar surface is an equipotential $\psi(r,\theta) =$ constant.

At the pole, $r = R_\mathrm{p}$, θ=0, and one can write

$$\psi(R_\mathrm{p}, 0) = -\frac{\mathrm{G}M}{R_\mathrm{p}}$$

where R_p is the polar radius and M the total stellar mass. This corresponds to the constant of the equipotential at the stellar surface. Thus, one has

$$\frac{\mathrm{G}M}{R_{\mathrm{p}}} = \frac{\mathrm{G}M_r}{r} + \frac{1}{2}\Omega^2 r^2 \sin^2(\theta) \tag{1.1}$$

Because of rotation, the effective gravity is thus modified:

$$\vec{g}_{\mathrm{eff}} = \vec{g}_{\mathrm{grav}} + \vec{g}_{\mathrm{cent}}.$$

In spherical coordinates, the centrifugal and gravitational acceleration can be expressed as

$$\begin{aligned} \vec{g}_{\mathrm{cent}} &= \Omega^2 r \sin(\theta)[\sin(\theta)\vec{e_r} + \cos(\theta)\vec{e_\theta}]; \\ \vec{g}_{\mathrm{grav}} &= -\frac{\mathrm{G}M}{r^2}\vec{e_r}, \end{aligned}$$

so that the effective gravity becomes

$$\vec{g}_{\mathrm{eff}} = \left(-\frac{\mathrm{G}M}{r^2} + \Omega^2 r \sin^2(\theta)\right)\vec{e_r} + \Omega^2 r \sin(\theta)\cos(\theta)\vec{e_\theta},$$

the modulus of $\vec{g}_{\mathrm{eff}}$ being

$$g_{\mathrm{eff}}(\Omega,\theta) = \sqrt{\left(-\frac{\mathrm{G}M}{r^2} + \Omega^2 r \sin^2(\theta)\right)^2 + \left(\Omega^2 r \sin(\theta)\cos(\theta)\right)^2} \tag{1.2}$$

One can define the *critical*, or *break-up*, *angular velocity* Ω_{crit}, which is reached when the modulus of the centrifugal acceleration $\vec{g}_{\mathrm{cent}}$ becomes equal to the modulus of the gravitational acceleration $\vec{g}_{\mathrm{grav}}$ at the equator. In this case, $g_{\mathrm{eff}} = 0$ at the equator (for which $\theta = \pi/2$), so from Eq. 1.2 one obtains

$$\Omega^2_{\mathrm{crit}} = \frac{\mathrm{G}M}{R^3_{\mathrm{E,crit}}} \tag{1.3}$$

where $R_{\mathrm{E,crit}}$ is the equatorial radius at critical velocity. Evaluating the Eq. 1.1 at the equator and introducing the expression of the critical angular velocity leads to

$$\frac{R_{\mathrm{E,crit}}}{R_{\mathrm{P,crit}}} = \frac{3}{2}. \tag{1.4}$$

This means that, at critical velocity, the equatorial radius is 1.5 times larger than the polar one. The stellar shape for different angular velocities is illustrated in Fig. 1.6. The stellar distorsion was investigated in some interferometric studies, through the estimation of the $R_{\mathrm{E}}/R_{\mathrm{P}}$ ratio. For example, for the fast-rotating star Achernar (α Eri; B6Vpe, Levenhagen & Leister 2006; $v \sin i \simeq 207$ km s^{-1}, Yudin 2001), the measurements yield $R_{\mathrm{E}}/R_{\mathrm{P}} \sim 1.4 - 1.5$ (Carciofi et al., 2008), in agreement with the Roche model with $\omega = \Omega/\Omega_{\mathrm{crit}} = 0.992$.

One can now define with Eqs. 1.3 and 1.4 the *first critical velocity*:

$$v^2_{\mathrm{crit},1} = \Omega^2_{\mathrm{crit}} R^2_{\mathrm{E,crit}} = \frac{\mathrm{G}M}{R_{\mathrm{E,crit}}} = \frac{2}{3}\frac{\mathrm{G}M}{R_{\mathrm{P,crit}}}. \tag{1.5}$$

This relation is valid under the Roche approximation (thus for solid body rotation). Figure 1.7 illustrates the variation of $v_{\mathrm{crit},1}$ as a function of the initial stellar mass, for different metallicities.

Rotation is, however, not the only important physical ingredient. The radiation pressure also plays a significant role inside massive stars by counterbalancing the gravity. In this context, it can be shown that the validity domain of Eq. 1.5 is limited to $\Gamma_{\mathrm{Edd}} < 0.639$, where Γ_{Edd} is the local Eddington factor at the surface of a rotating star. It typically describes the anisotropy of a radiation field, and is defined by

$$\Gamma_{\mathrm{Edd}}(\Omega, \theta) = \frac{\kappa(\Omega, \theta) L(P)}{4\pi \mathrm{c} \mathrm{G} M \left(1 - \frac{\Omega^2}{2\pi \mathrm{G} \bar{\rho}_M}\right)}, \tag{1.6}$$

where $\kappa(\Omega, \theta)$ is the electron scattering opacity, c the celerity, and $\bar{\rho}_{\mathrm{M}}$ the average stellar density. The first critical velocity does not depend on the Eddington factor. This is due to the fact that as rotation increases, the effective gravity at the equator decreases, thus, thanks to the von Zeipel theorem, its effective temperature at the equator decreases accordingly, keeping the radiation pressure negligible. However, the above expression of the first critical velocity is no longer valid for stars with high radiation pressure. For $\Gamma_{\mathrm{Edd}} > 0.639$, one defines the *second critical velocity* as:

$$v^2_{\mathrm{crit},2} = \frac{3}{2}\frac{\mathrm{G}M}{R^3_{\mathrm{P,crit}}} R^2_{\mathrm{E}}(\omega) \frac{1 - \Gamma}{V'(\omega)}.$$

with $V'(\omega) = V(\omega)/\left[4/(3\pi R^3_{\mathrm{P,crit}})\right]$, where $V(\omega)$ is the total stellar volume. The critical velocity decreases as Γ increases, so that a star with intense radiation can rotate at its break-up velocity even if its rotational velocity is low. Table 1.1 provides the Eddington factor for stars at the middle of the

Table 1.1: Predicted Eddington factor for MS stars (for a core hydrogen mass fraction X_{c} of 0.30) at the middle of the MS phase (Γ_{mid}) and the first critical velocity $v_{\mathrm{crit,1}}$ as a function of the initial stellar mass. *Source:* Maeder (2009b).

Initial M [$\mathrm{M}_\odot$]	Γ_{mid}	$v_{\mathrm{crit,1}}$ [km s^{-1}]
120	0.544	711
85	0.436	646
60	0.343	623
40	0.239	586
25	0.136	536
20	0.098	513
15	0.060	487
12	0.039	466
9	0.021	439

MS phase, as well as the first critical velocity $v_{\mathrm{crit,1}}$, as a function of the initial stellar mass.

Evolution of the rotational velocity. Single-star models predict a decrease of the rotational velocity of a rotating star during its MS evolution, as shown in Fig. 1.8 (see an example of observations in Fig. 1.9). This is due to the loss of angular momentum by stellar winds and the increase of the radius during the stellar evolution. Note, however, that the predicted rotational velocity in the models of Brott et al. (2011) for stellar masses $M \lesssim 20$ $\mathrm{M}_\odot$ does not drastically change during the MS phase. This is due to a competition of two effects: the increase of the rotational velocity thanks to the transport of angular momentum to the surface, and the decrease of the rotational velocity due to envelope expansion. This different behaviour in the evolution of the stellar rotational velocity, compared to the Geneva models, comes from the very different treatment of rotation, as the Geneva models consider a less strong coupling between the stellar core and the envelope, so that the spin-down by stellar winds is more effective (see Sect. 2.2.1 for further comparisons between these two types of models).

1.1.2.2 Gravity darkening effect

The stellar deformation due to rotation induces a higher effective gravity and a larger temperature at the stellar poles, hence a higher radiative flux

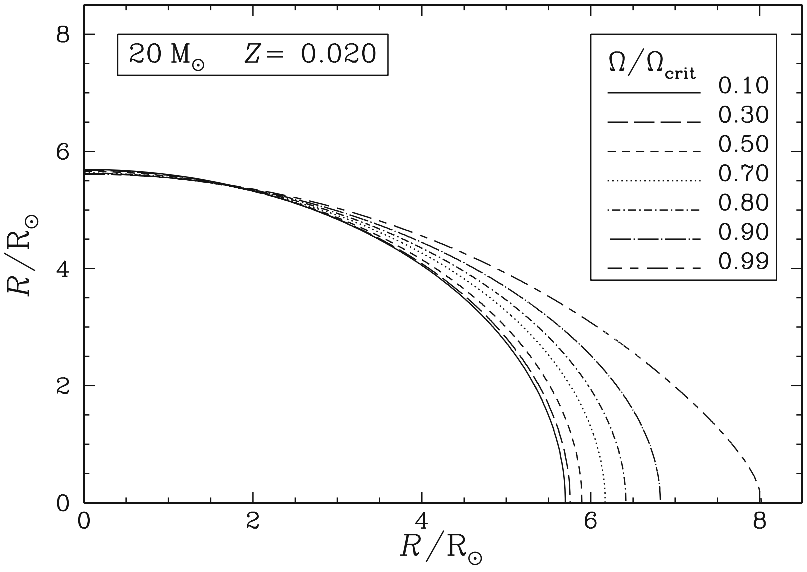

Figure 1.6: The centrifugal forces triggered by rotation affect the stellar shape, since their effect is to increase the equatorial radius, while slightly decreasing the polar one (e.g., Collins 1963; Domiciano de Souza et al. 2003). Illustration of the distorsion of a rotating star of 20 M$_\odot$ on the zero age main sequence (ZAMS), with Z = 0.020, as a function of the $\Omega/\Omega_{\rm crit}$ ratio. *Source:* Maeder (2009b).

(*gravity darkening effect*; Fig. 1.10). A confirmation of this effect is given by the observation of Altair, whose projected rotational velocity is $\sim$ 240 km s^{-1} and for which the ratio between its polar and equatorial effective temperatures is 1.23 – 1.27 (Fig. 1.11, Monnier et al. 2007). Equation 1.2 shows that the effective gravity varies over the stellar surface. Since the von Zeipel theorem provides a relation between the radiative flux (hence the effective temperature) and the effective gravity, the effective temperature will follow

$$T_{\rm eff}(\Omega,\theta) = \left(\frac{L}{4\pi\sigma {\rm G} M^{*}}\right)^{\frac{1}{4}} (g_{\rm eff})^{\frac{1}{4}}, \tag{1.7}$$

with

$$M^{*} = M\left(1 - \frac{\Omega^2}{2\pi {\rm G}\bar{\rho}_{\rm M}}\right),$$

where σ is the Stefan-Boltzmann constant. Note that another formulation has been proposed by Espinosa Lara & Rieutord (2011), which implies a less

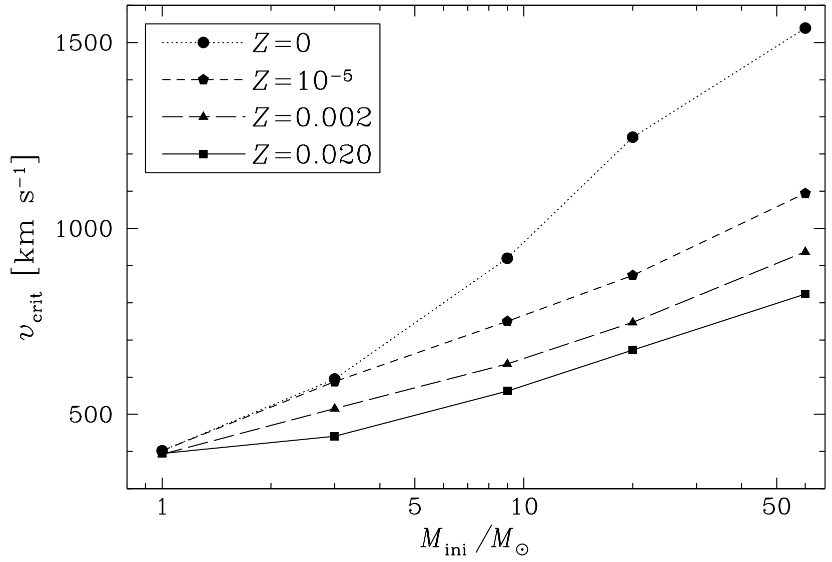

Figure 1.7: Illustration of the first critical velocity as a function of the initial stellar mass, for different metallicities. *Source:* Ekström et al. (2008b).

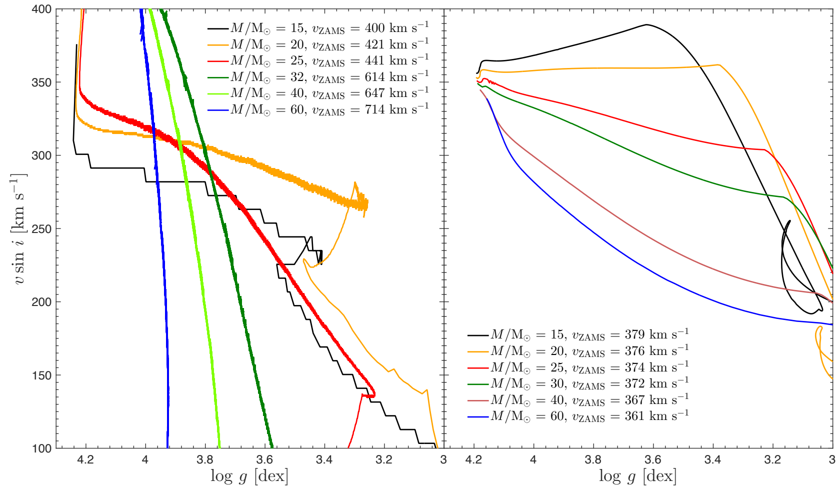

Figure 1.8: Predicted projected rotational velocity as a function of the surface gravity by Georgy et al. (2013a) and private comm. with Dr Georgy (*left*) and Brott et al. (2011, *right)*. We assume $i = 70°$ as fast rotators are preferentially seen close to equator on.

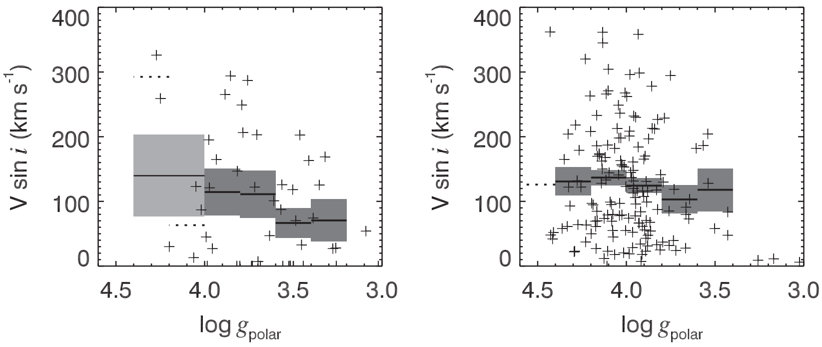

Figure 1.9: Projected rotational velocity as a function of the polar surface gravity for field (*left*) and cluster (*right*) stars with masses in the range 8≤M$\lesssim$20 $M_\odot$ (plus signs). Solid horizontal lines represent the mean $v \sin i$ of each bin having six or more stars, while dotted lines show the mean value for the bins containing fewer stars. Shaded rectangles illustrate the standard deviation of the mean $v \sin i$ for each bin. *Source:* Huang et al. (2010).

steep variation in T_{eff}.

One can also interpret the difference in flux (thus in effective temperature) along the stellar surface as a consequence of the variation in the distance between equipotentials. Several consequences of the gravity darkening effect induced by rotation are worth mentioning.

Impact on the line widths. Rotation significantly modifies the emergent spectrum of a rotating star as the Doppler effect broadens the spectral lines (Figs. 1.12a and 1.12b). The gravity darkening effect induces a decrease in the continuum emission of the equatorial regions, leading to smaller line widths than in an uniform model. The line width even becomes insensitive to rotation for very fast rotators, suggesting that the observational estimate of their $v \sin i$ may systematically be underestimated (Fig. 1.12c).

Impact on the luminosity. The flattening of a rotating star is also the cause of a decrease in its surface averaged temperature, hence its luminosity. An illustration of this effect is shown in Fig. 1.13. The position in a HR diagram of a rotating star is thus affected since the derived effective temperature and luminosity depend on the angle of view under which the star is seen.

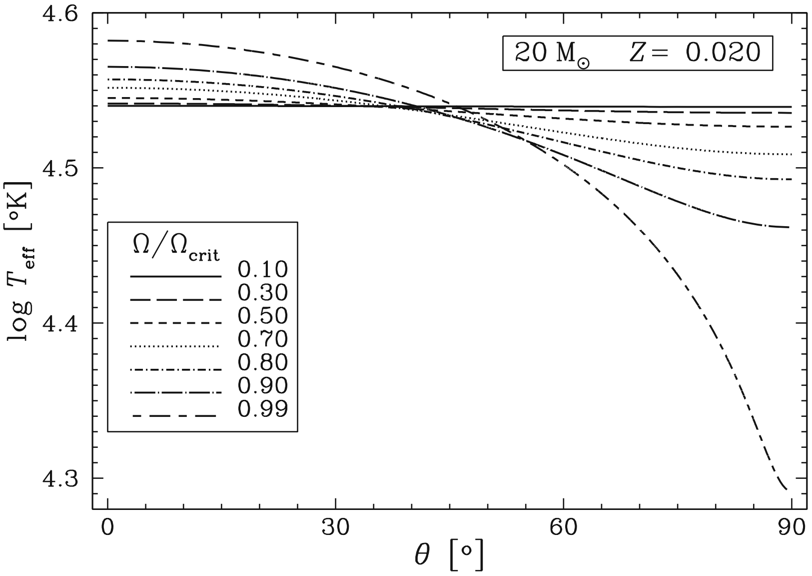

Figure 1.10: Illustration of the variation in effective temperature over the surface of a rotating star of 20 $M_\odot$ on the ZAMS, with $Z = 0.020$, as a function of the colatitude. Different ω ratios are considered. *Source:* Maeder (2009b).

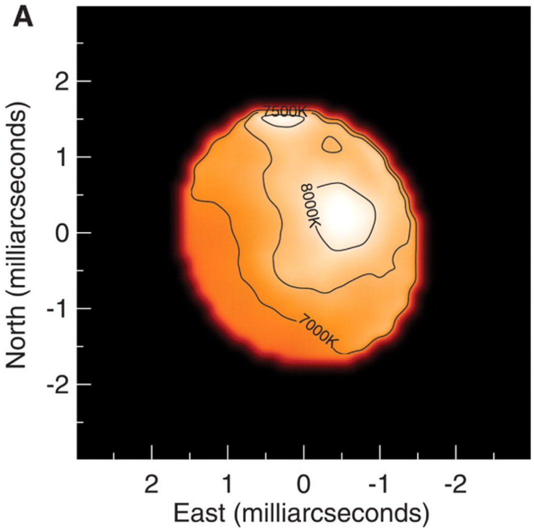

Figure 1.11: Near-infrared intensity image of Altair. *Source:* Monnier et al. (2007).

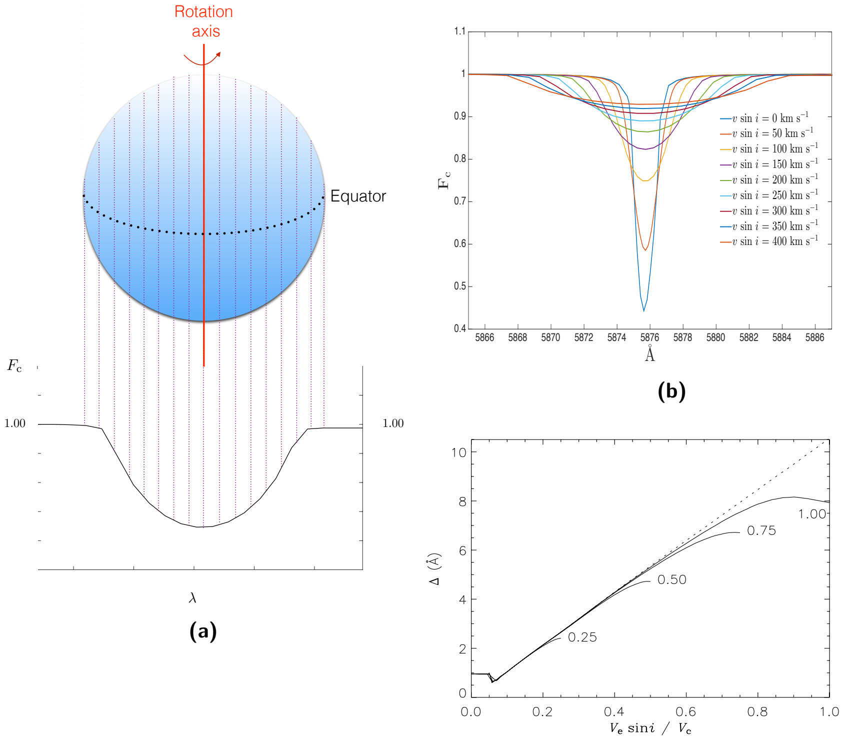

(a)

(b)

(c)

Figure 1.12: (a): Illustration of the rotational broadening of a line profile. Parts of the stellar surface contributing to the line profile are indicated with dotted lines. **(b)**: Impact of the rotational velocity on the He I 5876 line profile. **(c)**: Line widths of the He I 4471 line profile predicted for a B2-type spherical (dotted line) or flattened (solid lines) star as a function of the projected rotational velocity normalised to the first critical velocity. Labels refer to the assumed $\sin\, i$ values. *Source:* Townsend et al. (2004).

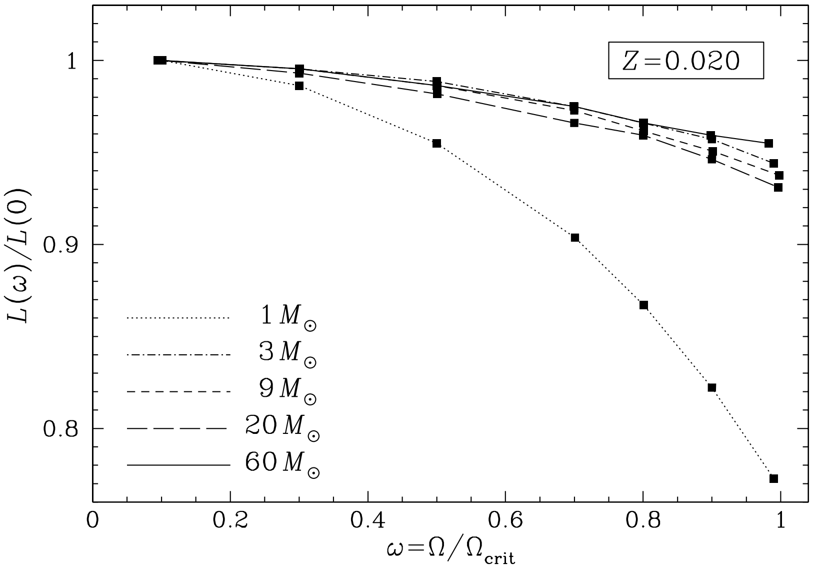

Figure 1.13: Variation of the luminosity, normalised to the luminosity in the non-rotating case, as a function of the ω ratio for several stellar initial masses, and with $Z = 0.020$. *Source:* Ekström et al. (2008b).

Impact on the mass-loss rate. Based on the von Zeipel theorem, one can show that the ratio of the mass-loss rate of a rotating star to that of a non-rotating star $\dot{M}(\Omega)/\dot{M}(0)$ can be expressed as (Maeder & Meynet, 2000b):

$$\frac{\dot{M}(\Omega)}{\dot{M}(0)} \simeq \frac{(1-\Gamma)^{\frac{1}{\alpha}-1}}{\left(1-\frac{4}{9}\left(\frac{v}{v_{\rm crit,1}}\right)^2-\Gamma\right)^{\frac{1}{\alpha}-1}},$$

where α is a *force multiplier parameter* which empirical values determined by Lamers et al. (1995) are, e.g., $\alpha \sim$ 0.51 for 30 000 K $\leq T_{\rm eff} \leq$ 40 000 K or $\alpha \sim$ 0.13 for $T_{\rm eff} \leq$ 10 000 K. When the Eddington factor is high, rotation may significantly increase the mass-loss rate, especially for low effective temperatures (hence low α values). Besides, as polar regions are hotter than equatorial ones, anisotropies appear in the stellar winds, more precisely winds from polar regions are stronger, removing a great quantity of mass without significant angular momentum loss. The difference in temperature between the polar and equatorial regions of a rotating star also generates a thermal imbalance in its interior. This thermal imbalance is the cause of some fluid motions in the stellar interior that are described in the next section.

1.1.2.3 Transport of angular momentum and chemical elements

Large scale currents develop inside a rotating star to overcome the thermal imbalance induced by centrifugal forces and to guarantee the conservation of energy (Eddington 1925; Sweet 1950; Maeder & Zahn 1998). These currents form the *meridional*, or *Eddington-Sweet circulation*. Two quantities are transported within the rotating star by the meridional circulation: some angular momentum and, to a lesser extent, chemical elements (see below). Under the assumption of a *shellular rotation* (in which the angular rotational velocity is constant on an isobar and depends, to first order, to the distance to the stellar centre), the transport of angular momentum can be described, in the lagrangian formulation that concentrates on a fluid mass element, by:

$$\rho \frac{\mathrm{d}}{\mathrm{d}t}\left(r^2\bar{\Omega}\right)_{M_r} = \underbrace{\frac{1}{5}\frac{1}{r^2}\frac{\partial}{\partial r}\left(\rho r^4 \bar{\Omega} U_2(r)\right)}_{\text{advective term}} + \underbrace{\frac{1}{r^2}\frac{\partial}{\partial r}\left(\rho D_{\mathrm{v}} r^4 \frac{\partial \bar{\Omega}}{\partial r}\right)}_{\text{diffusive term}}, \qquad (1.8)$$

where

- $\frac{\mathrm{d}}{\mathrm{d}t} = \frac{\partial}{\partial t} + \dot{r}\frac{\partial}{\partial r}$, $\dot{r}$ being the stellar expansion velocity;
- $\bar{\Omega}$ is defined as the angular velocity of a shell assumed to rotate as a solid body with the same angular momentum as the shell. One can write:
$$\bar{\Omega}(r) = \frac{\int_0^\pi \Omega(r,\theta)\sin^3(\theta)\mathrm{d}\theta}{\int_0^\pi \sin^3(\theta)\mathrm{d}\theta};$$
- U_2 can be considered as a measure of the vertical[1] component of the velocity of the motion $\vec{U}$ that can be expressed with Legendre polynomials as $\vec{U} = U_r(r)\vec{e_r} + U_\theta \vec{e_\theta}$, with $U_r(r) = U_2(r)P_2(\cos(\theta))$, where P_2 is the second Legendre polynomial, and $U_\theta = V_2(r)\frac{\mathrm{d}P_2(\cos(\theta))}{\mathrm{d}\theta}$;
- D_{v} is the diffusion coefficient in the vertical direction, due to convection and shear. Shear instabilities, to which a coefficient diffusion D_{shear} can be associated, arise from the differential rotation. Two prescriptions can be associated to D_{shear} (Maeder 1997; Talon & Zahn 1997).

---

[1] In the following, "vertical" will be used to refer to the radial direction. Consequently, the horizontal direction is perpendicular to the radial one.

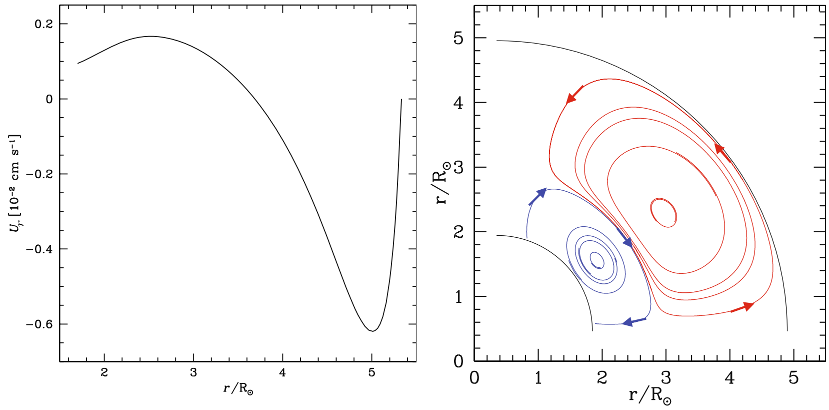

Figure 1.14: Illustration of the meridional circulation within a 20 $M_\odot$ rotating star with an initial rotational velocity of 300 km s^{-1}. *Left:* vertical component of the meridional circulation U_r as a function of the position inside the star. *Source:* adapted from Meynet & Maeder (2000). *Right:* circulation cells within the star in the middle of the MS phase. *Source:* adapted from Maeder (2009b).

The right-hand side of Eq. 1.8 shows that the transport of angular momentum is due to the combination of advective and diffusive transports. The behaviour of the vertical component of the meridional circulation U_r is shown in the left panel of Fig. 1.14: U_r is positive in the inner regions and negative in the outer regions. This is linked to the presence of two circulation cells (see right panel of Fig. 1.14). The inner cell transports the angular momentum inwards by turning upwards along the polar axis and then by going down in the equatorial plane. The outer cell, called the Gratton-Öpik cell, rotates in the opposite direction and transports the angular momentum outwards, which increases the surface rotation rate. One can show that the Gratton-Öpik cell deepens in radius during the MS phase, due to the lower density of the envelope.

The circulation timescale, known as the *Eddington-Sweet timescale*, $\tau_{\rm ES}$, can be expressed as:

$$\tau_{\rm ES} \approx \frac{\tau_{\rm KH}}{\Omega^2 R^3} {\rm G}M,$$

where $\tau_{\rm KH}$ is the Kelvin-Helmholtz timescale, that can in turn be expressed as $\tau_{\rm KH} \sim \frac{{\rm G}M^2}{R\bar{L}}$, with $\bar{L}$ the average stellar luminosity. It corresponds to the time for a star to thermally adjust its structure (or, in other words, to release its gravitational energy). For example, $\tau_{\rm ES} \approx 5 \times 10^5$ yr for a 20 $M_\odot$ star with an initial rotational velocity of 300 km s^{-1} and $U_2 = 2 \times 10^{-2}$

cm s^{-1}. Compared to its typical MS lifetime (9.3×10^6 yr), this timescale is shorter, hence the transport of angular momentum by the Eddington-Sweet circulation will play a significant role during the MS phase (Maeder, 2009b).

In the absence of loss of angular momentum, the meridional circulation is weak and can even vanish for slow rotators. This classical picture of the meridional circulation does not take the stellar wind (and tidal effects; see Sect. 1.1.3) into account though, as mentioned in Sect. 1.1.2.2, rotation influences the mass loss which in turn leads to a decrease in angular momentum, leading to the stellar spin-down. After a transient phase of $\sim \tau_{\rm ES}$, some angular momentum will be transported to the surface by an induced (and in this case strong) meridional circulation (e.g., Rieutord 1992; Zahn 1992; Rieutord & Zahn 1997).

The redistribution of angular momentum inside a rotating star leads to *differential rotation*, i.e., neighbouring horizontal layers moving at different rotation rates. In the case of massive stars, the angular velocity decreases as the distance to the stellar centre increases (Fig. 1.15). In addition, the strength of differential rotation increases during the MS evolution. Note, however, that the ratio between the angular velocity at the centre to the one at the surface remains relatively small during the MS ($<\sim$ 4 for the example illustrated in Fig. 1.15, which is in fair agreement with asteroseismic studies; Aerts 2015). There is also a flattening of the angular velocity profile at radii greater than $\sim$ 4 $R_\odot$ for the particular case illustrated in Fig. 1.15. It is due to the different mechanisms of transport of angular momentum: the inner cell of meridional circulation drives the angular momentum in the deep interior, while the outer cell and shear transport it to the surface. One also notes the general decrease of the angular velocity during the MS phase, which is due to the loss of angular momentum by the stellar winds.

This differential rotation leads to turbulences that are stronger in the horizontal direction than in the vertical one. This is due to the strong (vertical) thermal gradient that hampers fluid motions in the vertical direction. The *horizontal turbulence*, that homogenises the layers, is characterised by a diffusion coefficient $D_{\rm h}$ for which three expressions have been proposed (Maeder 2003; Mathis et al. 2004; Zahn 1992). It must be noted that it is the main contributor to diffusion processes (Fig. 1.16).

The transport of chemicals is governed by the same processes as those at work for the angular momentum (Eq. 1.8). However, it can be shown that the combined effect of the transport of chemicals by meridional circulation,

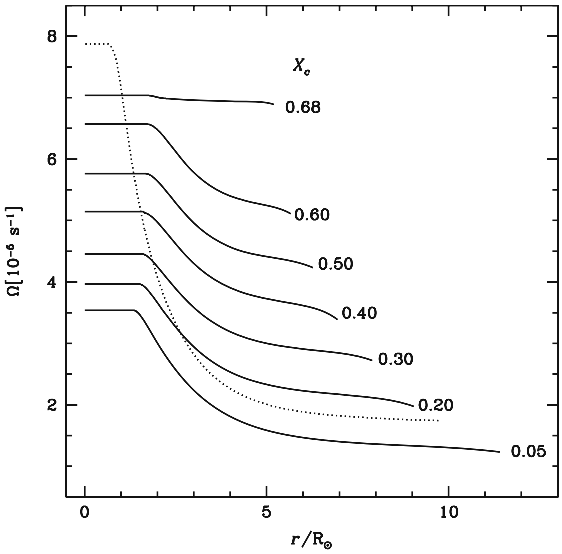

Figure 1.15: Evolution of the angular velocity Ω at a given position (r) inside the star as a function of time (the temporal evolution is here represented by lower values of the core hydrogen mass fraction $X_{\rm c}$). This figure considers a 20 $M_\odot$ rotating star with an initial rotational velocity of 300 km s^{-1} and a metallicity of $Z = 0.020$. At the end of the MS phase, the core contracts, hence it speeds up leading to the structural profile shown by the dotted line. *Source:* Meynet & Maeder (2000).

which is an advective motion, and horizontal turbulence leads to a transport that can be seen as a diffusion process (Chaboyer & Zahn, 1992). The equation of transport of an element i can in fact be written:

$$\rho \frac{\mathrm{d}\bar{X}_i}{\mathrm{d}t} = \underbrace{\frac{1}{r^2}\frac{\partial}{\partial r}\left(\rho r^2 (D_{\rm v} + D_{\rm eff})\frac{\partial \bar{X}_i}{\partial r}\right)}_{\text{diffusive term}}, \tag{1.9}$$

where $\bar{X}$ represents the mean mass fraction over an isobar and $D_{\rm eff}$ the effective diffusion coefficient resulting from the combination of the transport by meridional circulation and horizontal turbulence:

$$D_{\rm eff} = \frac{(rU_2)^2}{30 D_{\rm h}}.$$

One sees in this expression that the horizontal turbulence $(D_{\rm h})$ hampers the transport of chemicals triggered by the meridional circulation.

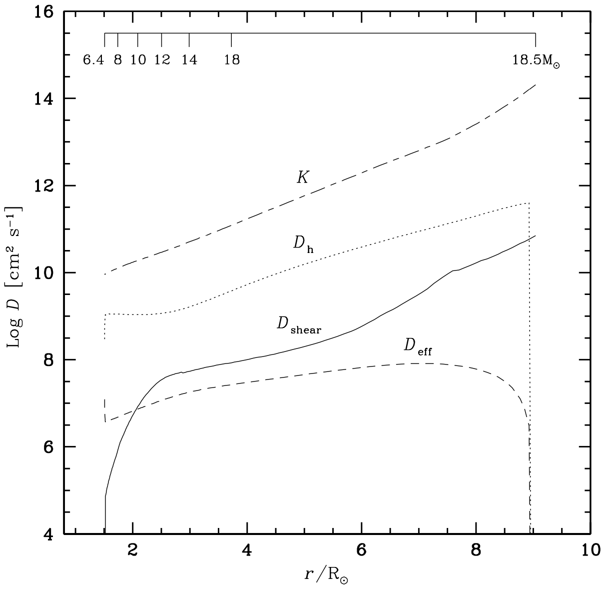

Figure 1.16: Comparison of the diffusion coefficients in a 20 $M_\odot$ rotating star with an initial rotational velocity of 300 km s^{-1} at the beginning of the MS phase. K is the thermal diffusivity. The lagrangian mass coordinate is given at the top. *Source:* adapted from Meynet & Maeder (2000).

As mentioned in Sect. 1.1.1, the nuclear reactions inside the core change the CNO relative abundances, with an excess of nitrogen in all cases, and a depletion in carbon or oxygen, depending on the stellar mass. The abundance modifications can be seen at the surface thanks to transport processes, and since they depend on rotation, surface abundances should vary with the spin rate. Since the nitrogen variation is the greatest, it is usually considered as the best probe of rotational mixing. In principle, boron could also be used as tracer since it is easily destroyed by warm protons, and even quite shallow mixing between the atmosphere and the stellar interior can transport the boron-depleted material to the stellar surface (Fliegner et al., 1996). However, its spectral lines being in the UV range where few instruments are available, it is less convenient to use.

The helium abundance may, in principle, also be used as an indicator of rotational mixing, but, since its production proceeds with the nuclear timescale ($\sim 10^7$ yr for a star of 25 $M_\odot$), its surface abundance enrichment is predicted to be modest. However, when rotationally induced mixing occurs on timescales shorter than the time by which a chemical stratification is established inside the rotating star, a mean molecular weight barrier may never develop. The star then follows a *quasi-chemically homogeneous evolution*. Yoon et al. (2006) and Brott et al. (2011) showed that this evolution is more likely in metal-poor environments since stars with low metallicities have on average higher rotational velocities.

The transport of chemical elements is not only a function of rotation, however. It also depends on other parameters, among which the main ones are the stellar age, mass, metallicity, multiplicity status (see next section), and, possibly, magnetic field. Care must therefore be exercised when studying rotational mixing from chemical abundances, as a variety of parameters control the abundances observed at the stellar surface.

- **Age.** As stars evolve, the nitrogen atoms produced by the CNO cycle are gradually transported to the surface leading to the increase of the nitrogen abundance at the surface. In this context, it has to be noted that the amount of mixing in the stellar interior of massive stars influences, among other quantities, their MS lifetime by bringing fresh combustible to the core;

- **Mass.** The mixing is expected to be stronger for more massive stars as they have a larger convective core, with a mixing timescale scaling as $1/M^{1.8}$. Figure 1.17 illustrates this effect, demonstrating how the surface nitrogen abundance increases with mass and age.

- **Metallicity.** The loss of mass and angular momentum by stellar winds is weak at low metallicities: $\dot{M} \propto Z^{\alpha}$, with $\alpha = 0.69$ applying for stars with $T_{\rm eff} \gtrsim$ 25 000 K (Vink et al., 2001). Besides, stars with low CNO abundances must adopt a more compact structure to overcome the low content of these catalysts. The density thus remains relatively high in stellar envelopes, so the term representing the Gratton-Öpik cell, that is inversely proportional to the density, is very small. The outward transport of angular momentum carried by the Gratton-Öpik cell is therefore weak, leading to a steep Ω gradient, which in turn leads to a strong shear mixing. The compact structure further leads to shorter distances for the diffusion of chemicals and, on average, faster rotational velocities. Higher abundances of nitrogen are therefore expected at the surface of low Z stars. This is illustrated by the nitrogen abundances reported for a sample of B-stars with $v \sin i \geq 150$ km s^{-1} and $3.6 \leq \log g \leq 3.9$ dex by Hunter et al. (2009) in the Galaxy, Large Magellanic Cloud (LMC), and Small Magellanic Cloud (SMC).

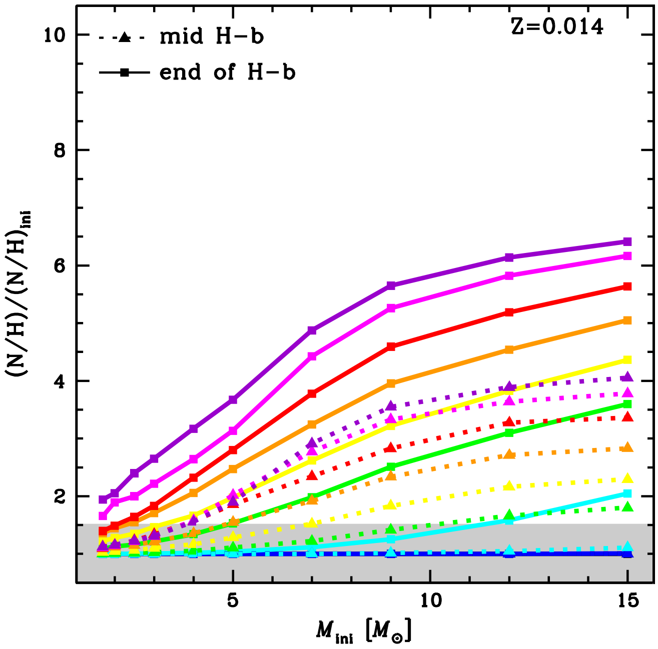

Figure 1.17: Surface nitrogen abundance at the middle (dotted lines) and at the end (solid lines) of the MS phase as a function of the initial stellar mass. Different initial ω values are considered: $\omega_{\rm ini}=0$ (black), 0.1 (blue), 0.3 (cyan), 0.5 (green), 0.6 (yellow), 0.7 (orange), 0.8 (red), 0.9 (magenta), and 0.95 (purple). Models are for a metallicity Z=0.014. *Source:* Georgy et al. (2013a).

Excluding upper limits, the departures with respect to the baseline values are ~ -0.1 dex, $\sim +0.8$ and $\sim +1.2$ dex, respectively.

- **Magnetic field.** Internal and external magnetic fields are also expected to have an impact on the surface chemical abundances. Internal magnetic fields (Spruit 2002; Maeder & Meynet 2005) produce a strong coupling inside the stars, which favours solid body rotation, hence a strong meridional circulation, leading to a strong mixing. It is nowadays unclear whether these internal magnetic fields can be detected at the stellar surface or not. External magnetic fields generate a mechanical coupling between the stellar surface and the winds, taking away some angular momentum from the star (ud-Doula & Owocki 2002; ud-Doula et al. 2008), and producing a magnetic braking (ud-Doula et al. 2009; Meynet et al. 2011). This magnetic braking should then lead to strong shears in the stellar interior, generating additional mixing. Magnetic stars could therefore be slow rotators exhibiting nitrogen excess at their surface. However, up to now, no evidence has been provided to confirm the influence of magnetic fields on CNO surface abundances (Morel 2012; Martins et al. 2015a; Wade et al. 2015).

1.1.3 Multiplicity

Multiplicity also plays a crucial role in massive stars' lives. Indeed, according to Sana et al. (2012), the evolution of more than 70% of them is influenced by the presence of a companion. In the context of the transport of chemicals and angular momentum, three processes linked to the influence of companions may play a significant role.

First, tidal interactions induced by a companion star may cause the spin-up, or the spin-down of a star. These two specific cases may in turn generate a strong internal mixing; in the latter case, tidal interactions generate a braking, especially in the outer layers, which may increase the differential rotation that in turn contributes to the internal mixing (Song et al., 2013).

Second, in binary systems, a Roche Lobe Overflow (RLOF) may occur. The evolution of a massive close binary system is illustrated in Fig. 1.18: the system is initially composed of two MS stars (a). When the initially most massive star enters the supergiant phase, it fills its Roche lobe and a mass transfer is initiated towards the initially less massive star (b). After this phase, the system, which is composed of a Wolf-Rayet (WR) star (formed by the great loss of its external hydrogen content) and an O-type star, has a greater orbital period (c). The WR star then explodes in a supernova event, producing a compact star (either a neutron star or a black hole). The components may then be dissociated or remain gravitationally bound (d). In the latter case, the initially less massive star evolves until the supergiant phase during which it has a strong wind. The accretion of this material by the compact star produces a strong X-ray emission (e). The initially less massive star then fills its Roche lobe, generating a second mass-transfer episode, in which a great amount of mass is lost from the system, further forming a nebula around it (f). After this exchange of mass, the initially less massive star is a star that burns helium. This star then becomes a WR star (g). This object then explodes in a supernova event, producing either the disruption of the system, or a system composed of two compact objects (h). It has to be noted that the case presented here is illustrative, and different scenarii may happen, according, e.g., to the type of mass transfer: three cases (A, B, and C) can be defined, in which the mass transfer is initiated from a core hydrogen burning donor star, a core hydrogen shell-burning star, and a helium burning star, respectively. In any case, mass transfer leads to a transfer of angular momentum which affects the rotational velocity of both components (Struve 1963; Huang 1966; Shu & Lubow 1981). Packet (1981) demonstrated that a MS star gainer in a rigid rotation will reach critical rotation at its surface after a small gain of mass ($\sim$ 5–10%) through an accretion disk. Mass gainers that underwent a mass-transfer event are therefore expected to be fast rotators. When a gainer star reaches its critical rotation, the accretion may stop (Langer, 2012). The mass exchange also involved in such and event can affect the surface abundances as the gainer star can receive CNO-cycle processed material from the donor star.

Finally, stars in close systems may get in contact and eventually merge. This event affects both the angular momentum and surface abundances (e.g., Langer 2012).

1.1.4 X-rays from massive stars

X-rays are a form of electromagnetic radiation with a wavelength range between 0.01 and 10 nanometers, corresponding to energies from 123 eV[2] to 123 keV. Two subcategories of X-rays can be defined: the so-called *soft* X-rays that have wavelengths in the range 0.1 – 10 nm (corresponding to energies from 0.123 to 12.3 keV) and the *hard* X-rays with wavelengths ranging from 0.01 to 0.1 nm (corresponding to energies from 12.3 to 123 keV).

In astrophysics, two kinds of processes, qualified as *thermal* and *non-thermal*, are responsible for the X-ray emission. An emission is thermal when the energetic distribution of electrons is Maxwellian, and is thus associated to a specific temperature. Examples of thermal processes are the one responsible for the blackbody emission, or the thermal Bremsstrahlung process[3]. Since the loss of energy during the deceleration of electrons is not quantified, the

---

[2] An electron-volt (eV) is the energy acquired by an electron which is accelerated from its state of rest by a difference of potential of one volt. The temperature (in K) is related to the energy (in keV) by 1 K = 8.621738×10^{-8} keV.

[3] The Bremsstrahlung radiation, also sometimes called the free-free radiation, is the emission associated to the deceleration of (relativistic, in the case of the non-thermal Bremsstrahlung) electrons in the presence of an electric field.

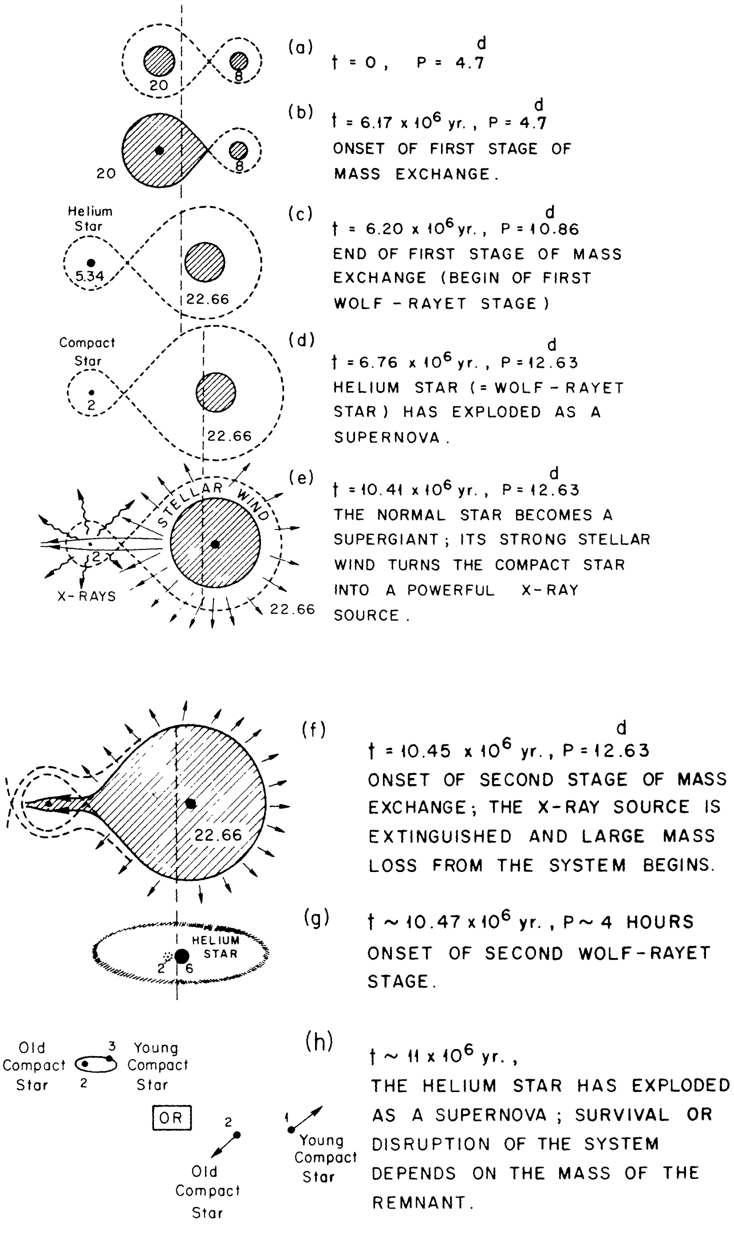

Figure 1.18: Schematic evolution of a massive close binary system. Numbers indicate the masses of each component at each stage. *Source:* van den Heuvel (1976).

spectrum associated to this radiation is continuous. In contrast, there are three examples of non-thermal emissions:

- the inverse Compton scattering, which happens when a highly energetic electron concedes some of its energy to a microwave, infrared, visible, or ultraviolet photon, the latter then becoming an X-ray photon;

- the synchrotron process, when a relativistic electron is accelerated by a strong magnetic field in a direction perpendicular to its velocity, which produces the emission of radiation;

- the non-thermal Bremsstrahlung, which occurs for relativistic electrons.

The continuous spectrum of X-ray sources can also be combined to discrete spectral lines in absorption or in emission. Usually, the observation of X-ray lines in emission is a reliable evidence of the thermal nature of the source.

X-rays are emitted by powerful events. Hot plasmas with temperatures that can reach several millions of degrees can be the source of an X-ray emission and can be found in stellar coronae, accretion disks, or in regions where the winds of stars in multiple systems collide, for example. Let us focus on the X-rays emitted by massive stars. As already stated in Sect. 1.1.1, the wind of massive stars are accelerated thanks to their strong UV emission. These stellar winds are unstable (one talks about radiation-driven instabilities, RDI; Owocki & Rybicki 1984), thus producing hydrodynamic shocks[4]. The post-shock plasma temperature is high, generating an X-ray emission that is made of a continuous thermal Bremsstrahlung emission with spectral lines associated to metal ions that are abundant in stellar atmospheres. The X-ray spectra of most of OB stars are usually well reproduced by a thermal emission model with temperatures between 0.5 and 0.7 keV, X-ray luminosities of $L_{\rm X} \sim 10^{31} - 10^{33}$ erg s^{-1} (and tightly linked to the stellar luminosity following $L_{\rm X}/L_{\rm BOL} \sim 10^{-7}$, e.g., Nazé et al. 2011). Absorption is also present, since there are the interstellar medium and the stellar wind along the line of sight. In massive binaries, the stellar winds collide, generating in some cases additional X-ray emission (e.g., Güdel & Nazé 2009).

---

[4] Such shocks happen when a fluid is moving with a velocity higher than the sound velocity of the local medium and encounters an obstacle or another fluid. While the sound does not propagate within the interstellar medium, a sound velocity can be determined thanks to the thermal agitation of the particles in the medium. In the ionised interstellar medium the speed of sound is $\sim$ 10 km s^{-1}, while this velocity is $\sim$ 1 km s^{-1} in a neutral medium.

The X-ray emission of massive stars thus constitutes a unique probe of the stellar outflows. The most sensitive diagnostics in this context are the X-ray variability and the X-ray line profiles.

1.2 Thesis outline

1.2.1 Rationale of the study

Although the rotational mixing theory predicts considerable surface nitrogen enrichment for fast rotators, observations of relatively large samples of MS B-stars in the Galaxy and in the Magellanic Clouds (MCs) in the framework of the Very Large Telescope (VLT)-Fibre Large Array Multi-Element Spectrograph (FLAMES) Survey of Massive Stars (Evans et al. 2005; Evans et al. 2011) have revealed a population of fast rotators with a lack of nitrogen excess at their surface. They form the Group 1 of stars in the *Hunter diagram* (Fig. 1.19). Maeder et al. (2009) nevertheless pointed out the different evolutionary stages (on and away from the MS) and the large range of masses (from 10 to 30 $M_{\odot}$) of the stars studied in the VLT-FLAMES Survey, which could affect conclusions. They found a better agreement with the model predictions after the sample is split into groups of stars with similar properties. In particular, they found that only binaries might remain in Group 1 when restricting the sample to stars with similar mass and age. Such putative binaries might have undergone a non-conservative mass-transfer episode (Langer et al. 2008), but this hypothesis could not be tested as a complete binary identification for stars in Group 1 could not be performed. Moreover, the lack of high precision abundance determinations (e.g., lots of upper limits) hampers a clear interpretation of the observations.

Recently, Ahmed & Sigut (2017) studied the nitrogen abundance of a sample of 16 normal B stars and 26 Be stars from the Galaxy in the context of the Magnetism in Massive Stars (MiMeS) spectropolarimetric survey. They found a nitrogen enrichment for half of the studied normal B stars and for about one third of the Be stars. The average nitrogen abundance of their sample is in fair agreement with the solar abundance, although the subsample of Be stars exhibits a larger dispersion in the nitrogen abundances. This sample also displays a large fraction of sub-solar nitrogen abundances,

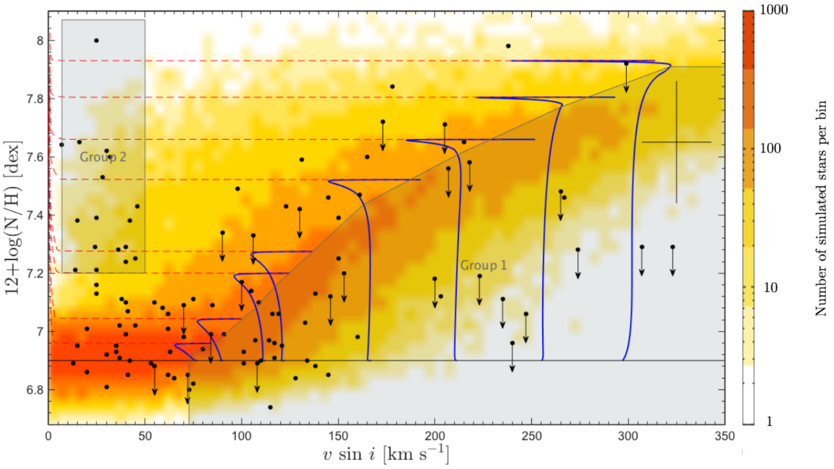

Figure 1.19: Nitrogen abundance as a function of the projected rotational velocity for stars with $\log g \geq 3.20$ dex in extended regions around N11 and NGC 2004 in the LMC. The cross to the upper right represents the mean error bars. Upper limits in the nitrogen abundance are illustrated with downward arrows. Blue solid lines represent the predictions for the MS phase of 13 $M_\odot$ stars from models of Brott et al. (2011), while red dashed lines show the predictions for post-MS phases. The rotational velocities of the models have been multiplied by $\pi/4$ to take the average projection effect into account. The black solid line illustrates the LMC baseline nitrogen abundance used in models of Brott et al. (2011). *Source:* adapted from Hunter et al. (2009). Overplotted in the background is a population synthesis from Brott et al. (2011), the colour coding corresponding to the number of stars per pixel.

contrary to the B star sample.

Prior to our study, only few Galactic OB stars with high rotational velocities (typically with $\geq$ 200 km s^{-1}) had their metal content well-determined, and the associated studies have been led by different authors with different methods (see Table 1.2). These studies did not clearly reveal any stars with properties similar to those of the Group 1 of Hunter et al. (2009). This is why we decided to undertake an in-depth study of the multiplicity status and abundances of bright Galactic OB stars with high rotational velocities.

Our X-ray study aims at assessing the potential interest in deriving abundances from X-ray data. X-ray thus may constitute a tool to determine abundances of fast rotators without the problems encountered in the optical domain. However, this method must be first validated and our X-ray study of early B-stars is a step towards this goal. This study also allows us to investigate the wind properties of a sample of massive stars.

Table 1.2: Galactic fast-rotating stars whose surface CNO abundances had been studied previously to our work. References: [1]: Sota et al. (2011), [2]: Sota et al. (2014), [3]: Martins et al. (2015a), [4]: Martins et al. (2015b), [5]: Martins et al. (2012a), [6]: Bouret et al. (2012), [7]: Villamariz & Herrero (2005), [8]: Villamariz et al. (2002), [9]: Mahy et al. (2015).

Star	Spectral type	Reference	$v \sin i$ [km s^{-1}]	Reference	Abundance study	[N/O]
HD 13268	ON8.5IIIn	1	301	This work	4	0.21
HD 36879	O7V(n)((f))z	2	200	3	3	0.08
HD 46056	O8Vn	1	350	This work	3, 5	–0.67
HD 46485	O7V((f))nz	2	315	This work	3, 5	–0.69
HD 66811 (ζ Pup)	O4I(n)fp	2	225	This work	3, 6	0.97
HD 69106	O9.7IIn	2	306	This work	3	$\leq$–0.40
HD 91651	ON8.5IIIn	2	310	3	4	0.37
HD 102415	ON9IV:nn	2	357	This work	4	$\geq$0.40
HD 117490	ON9.5IIInn	2	361	This work	4	0.48
HD 149757 (ζ Oph)	O9.2 IVnn	1	378	This work	7	–0.35
HD 150574	ON9III(n)	2	233	This work	4	$\geq$0.22
HD 191423	ON9 II-IIIn	1	420	This work	4, 8, 9	0.13
HD 192281 (V2011 Cyg)	O4.5V(n)((f))	2	276	This work	3	0.77
HD 203064 (68 Cyg)	O7.5IIIn((f))	1	298	This work	3	...
HD 210839 (λ Cep)	O6.5I(n)fp	1	214	This work	3	0.38, 0.22

2

OPTICAL STUDY

"Astronomy compels the soul to look upwards and leads us from this world to another."

— Plato

This chapter introduces and provides the results of our abundance study of fast rotators in the optical.

The main part of our project focuses on the study of the abundances of CNO-cycle material (He, C, N, and O) at the surface of an extensive sample of bright fast rotators in our Galaxy. This was performed through the analysis of their optical spectrum. The abundance derivation was complemented by a radial velocity (RV) study to assess the presence of a companion near our targets. The latter information is essential for the interpretation of their abundances as seen in the previous chapter. Our results, published in Cazorla et al. (2017a, hereafter Paper I), were interpreted and compared to predictions for single and binary stars in Cazorla et al. (2017b, hereafter Paper II). Additional information on the physical principles behind the methods used are provided in the following sections.

2.1 Derivation of abundances

2.1.1 Methods and tools

2.1.1.1 Projected rotational velocity

An elegant way to estimate the projected rotational velocity of a star is to use the Fourier transform (Simón-Díaz & Herrero, 2007). In a(n) (idealised) case, where there is no noise affecting the data, the observed line profile, D, is the result of the convolution of the intrinsic, H, rotational, G, and instrumental profiles, L:

$$D(\Delta\lambda) = 1 - \frac{\mathscr{F}_\nu}{\mathscr{F}_c} = H(\Delta\lambda) * G(\Delta\lambda) * L(\Delta\lambda), \tag{2.1}$$

where $\mathscr{F}_\nu$ and $\mathscr{F}_c$ represent the emergent flux of a spectral line and the continuum flux, respectively. In this equation, $\Delta\lambda = \lambda_0\,\frac{v_z}{c}$, λ_0 being the rest wavelength, and v_z the component of the rotational velocity towards the observer. $H(\Delta\lambda) = I_\nu(\Delta\lambda)/I_c$, i.e., it is the ratio between the local, intrinsic specific intensities in the line I_ν and in the continuum I_c at a Doppler shift $\Delta\lambda$. The function $G(\Delta\lambda)$ is defined as

$$\begin{aligned} G(\Delta\lambda) = G(v_z) = {} & \frac{2\,(1-\varepsilon)}{\pi\,(1-\frac{\varepsilon}{3})\,v_{\rm eq}\,\sin i}\left[1-\left(\frac{v_z}{v_{\rm eq}\,\sin i}\right)^2\right]^{\frac{1}{2}} \\ & + \frac{\varepsilon}{2\,(1-\frac{\varepsilon}{3})\,v_{\rm eq}\,\sin i}\left[1-\left(\frac{v_z}{v_{\rm eq}\,\sin i}\right)^2\right], \end{aligned}$$

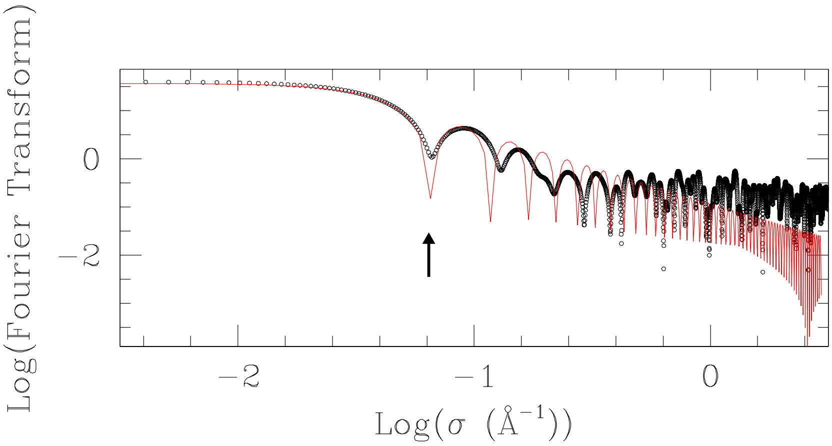

Figure 2.1: Illustration of the way the projected rotational velocity was estimated, for HD 93521, with the He I 6678 line profile, by finding the first zero of the Fourier transform $g(\sigma)$ (see arrow).

where ε is the coefficient in the assumed linear limb-darkening law $I_c = I_c^0\,(1 - \varepsilon + \varepsilon\,\cos\,\theta)$, with $I_c^0 = I_c(\theta = 0)$, and $v_{\rm eq}$ the equatorial stellar rotational velocity.

Since the convolution operation in the real space translates into a multiplication operation in the Fourier space, and that the equivalent in Fourier space of the wavelengths is given in cycles per Å, written σ, the equation 2.1 becomes:

$$d(\sigma) = h(\sigma)\,g(\sigma)\,l(\sigma). \tag{2.2}$$

The intrinsic line profile $H(\Delta\lambda)$ is close to a Dirac impulse function, hence $h(\sigma)$ is a constant. Assuming the instrumental profile $L(\Delta\lambda)$ to be represented by a Gaussian function, $l(\sigma)$ is also a Gaussian. Therefore, $d(\sigma)$ is mostly dominated by $g(\sigma)$. Interestingly, the first zero of $g(\sigma)$ directly provides an estimate of the projected rotational velocity of a star (Fig. 2.1). Moreover, noise affecting the data is unavoidable and deteriorates the $v\,\sin\,i$ determination.

2.1.1.2 Turbulence broadening

Microturbulence is due to small-scale motions (shorter than the mean free path of the photons) inside the stellar atmosphere. It generates a line-profile broadening similar to the thermal broadening, i.e., it can be represented by a Gaussian velocity distribution of width ξ. In addition, it will also change the strength of the line profile (Fig. 2.2), especially for strong lines whose equivalent width is more sensitive to microturbulence than weak lines. A dependency between the luminosity class and microturbulence exists, as the latter increases with decreasing surface gravity (Gray, 2005). In our work, the microturbulence velocity cannot be constrained by the data and was therefore fixed. We assumed ξ=10 km s^{-1} for the coolest stars and a value that depends on the luminosity class for the hottest ones. In addition, it varies from the photosphere to the top of the atmosphere for these latter stars (see Paper I).

In addition, there is the macroturbulence, linked to large-scale variations. Its origin remains uncertain as it can stem from large individual granulation cells in cool stars (with a spatial scale larger than the mean free path of the photons), or be due to pulsations in massive stars (Simón-Díaz et al. 2017). In the former case, the cells associated to macroturbulence generate a complete spectrum which is shifted due to the motion of the cells, leading to slightly asymmetric line profiles, while in the latter case there is a variability in the line profiles. In this thesis, we considered the rotational velocity as the main source of spectral line broadening. Our tests indeed revealed that the inclusion of the macroturbulence as one of the broadening mechanisms when computing the synthetic spectra had no significant effects on the atmospheric parameter and abundance values. These tests were performed using the `macturb` programme of the `SPECTRUM` suite of routines[1], that allows the convolution of synthetic spectra with radial-tangential macroturbulent profiles (see Gray 2005 for a definition of the radial-tangential prescription). Results show that changes are smaller than (or compatible with) the error bars (Table 2.1). In addition, we did not consider the macroturbulence effect in the synthetic spectra broadening as it cannot be constrained reliably for fast rotators (Fig. 2.6, Simón-Díaz & Herrero 2014).

2.1.1.3 Atmospheric parameters and He, CNO abundances

We describe in this section the different methods used in the determinations of the atmospheric parameters as well as the surface He and CNO abundances.

---

[1] `http://www.appstate.edu/~grayro/spectrum/spectrum276/node38.html`

Table 2.1: Differences in atmospheric parameters and He, CNO abundances found for HD 163892 when the broadening of DETAIL/SURFACE spectra is not only due to the stellar rotation (and microturbulence), but also to macroturbulence. (1) and (2) refer to the spectral regions 4060 – 4082 Å and 4691 – 4709 Å, respectively (see Paper I).

Parameters		Changes in parameters when $v_{\rm mac}$ is taken into account	Typical errors
$\Delta\,T_{\rm eff}$ [K]		–15	1000
$\Delta\,\log g$ [dex]		0	0.10
$\Delta\,y$		+0.030	0.025
$\Delta\,\log\varepsilon({\rm C})$ [dex]		+0.04	0.12
$\Delta\,\log\varepsilon({\rm N})$ [dex]		+0.04	0.13
$\Delta\,\log\varepsilon$(O) [dex]	(1)	+0.02	0.21
	(2)	+0.02	

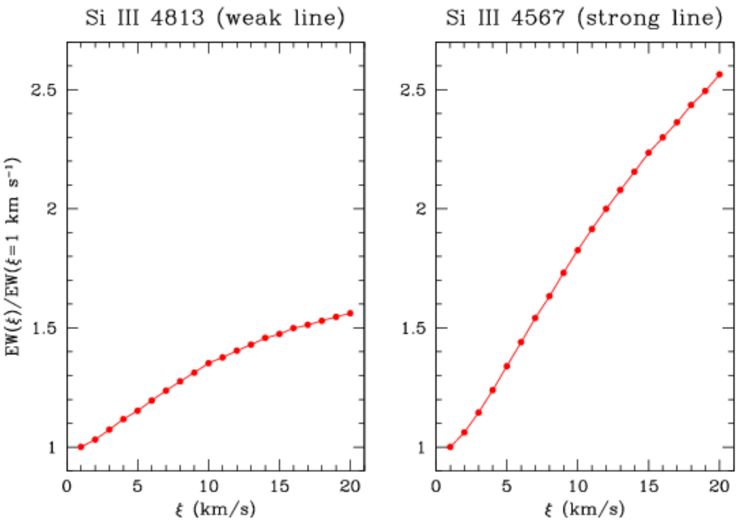

Figure 2.2: Illustration of the variation of the equivalent widths (EW) of some Si III line profiles as a function of ξ. *Source:* Courtesy of Dr. Thierry Morel.

Model atmosphere/line-formation codes. Modern stellar model atmosphere codes include line-blanketing, i.e., they consider the presence of metals in the stellar atmosphere, the overlapping of their spectral lines (and the preferential absorption of radiation at short wavelengths). Typically, a model atmosphere provides some physical parameters (e.g., the temperature) as a function of the position within the atmosphere, an information being then used to estimate the flux at the stellar surface. To do so, a model atmosphere code makes the use of approximations and simplifications (e.g., no granulation or spots at the stellar surface, no magnetic field). There is also one main assumption: the description of the thermodynamic state of the atmosphere, which can be at local thermodynamic equilibrium (LTE) or not (NLTE). In an atmosphere in LTE, the population of electron energy levels is only a function of the temperature and density. This assumption is no longer valid for early-type stars since their strong radiation field also contributes to the population of electron energy levels; a great departure from LTE is thus observed. Line-formation codes can either consider a plane-parallel or a spherical geometry but must include a NLTE treatment of the line formation.

Five major model atmosphere/line-formation codes are currently available for massive stars, in all cases except for DETAIL/SUFACE, NLTE model atmospheres are considered:

- **TLUSTY**: metal line-blanketed, plane-parallel geometry, hydrostatic model atmospheres (Hubeny & Lanz 1995);
- **DETAIL/SURFACE**: metal line-blanketed, plane-parallel geometry, hydrostatic model atmospheres (Butler & Giddings 1985; Giddings 1981);
- **Fast Analysis of STellar atmospheres with WINDs (FASTWIND)**: metal line-blanketed, spherical geometry model atmospheres including winds (Santolaya-Rey et al. 1997; Repolust et al. 2004; Puls et al. 2005);
- **CoMoving Frame GENeral (CMFGEN)**: metal line-blanketed, spherical geometry model atmospheres including winds (Hillier & Miller 1998; Hillier & Lanz 2001);
- **Potsdam Wolf-Rayet (PoWR)**: spherical geometry model atmospheres for WR stars, including winds and iron line blanketing (Hamann & Gräfener 2004).

The two codes that were used in this thesis are:

DETAIL/SURFACE. While the atmosphere of massive stars is affected by NLTE effects, the hybrid technique of combining the ATLAS9 LTE atmosphere models (Kurucz, 1993) with the NLTE line-formation code DETAIL/SURFACE is appropriate to study cooler massive stars on – or close to – the main sequence (Nieva & Przybilla 2007; Przybilla et al. 2011). The solving of the radiative transfer and statistical-equilibrium equations are performed by the DETAIL program, while the computation of the emergent flux is performed by SURFACE. The use of detailed model atoms is made possible by the inclusion of an Accelerated Lambda Iteration (ALI) scheme (Rybicki & Hummer, 1991). DETAIL/SURFACE does not take the ouflows of the hotter massive stars into account.

CMFGEN. The CMFGEN code, developed by Pr. John Hillier, solves the statistical and radiative transfer equations in 1D, taking the spherical geometry and the stellar radial outflow of material into account. Spectral lines are treated in the co-moving frame. CMFGEN is not a truly hydrodynamic code since the density structure must be given as an input. Then, a pseudo-photospheric structure, provided by TLUSTY models, is linked to a stellar wind structure described by a β-velocity law (e.g., Lamers & Cassinelli 1999). CMFGEN can take the clumping of the stellar wind into account, through the use of a volume filling factor f. It is assumed to vary monotonously through the atmosphere: a value of 1 is assumed at the photosphere, and a value f_∞ at the atmosphere boundary. The evolution of the volume filling factor is ruled by $f = f_\infty + (1 - f_\infty)\, e^{-\frac{v}{v_{\rm cl}}}$, where v is the velocity of the wind and $v_{\rm cl}$ the velocity at which clumping starts. An X-ray emission can also be taken into account as X-rays influence the ionisation balance in the wind. A simplified view of the X-ray emission (which in reality is distributed throughout the stellar winds) is considered, with two parameters (the plasma temperature and the volume filling factor).

The computational time is generally large ($\sim$ 15 hours on 1 Central Processing Unit; CPU), although some efforts have been made to reduce it, such as the use of the “super levels” approximation. It lowers the number of levels whose atomic populations have to be solved by computing statistical and radiative transfer equations for similar energies. The population of each level in a super level is treated in LTE. A microturbulence velocity can be included in the computation of populations of levels and of the temperature structure. After the atmospheric structure has been obtained, a formal solution of the radiative transfer equation in the observer’s frame is computed in order to produce a synthetic spectrum that can be confronted to observations. This is performed by the auxiliary code CMF_FLUX. A Stark broadening can be added to individual lines. Furthermore, a microturbulence velocity can be added in this auxiliary code, starting from the photosphere where values are generally chosen to be in the range 10 – 20 km s^{-1}, then increasing linearly to reach a maximum value of typically 10% of the terminal velocity in the outer part of the wind.

Effective temperature. The determination of the effective temperature of our stars is based on the ionisation balance of an element, which is derived by equating the ionisation and recombination rates. The larger the temperature, the more ionised an element is. Therefore, the effective temperature can be estimated from ionisation equilibrium of various ions; in our case, we used He I and He II lines for that purpose as these lines are in general present (and strong enough) in the optical spectrum of our targets.

Surface gravity. The wings of Balmer lines were used to derive the surface gravity of our targets, as they are the best diagnostics at hand in the optical domain. In fact, the Balmer line strength increases with pressure, so with the surface gravity (Fig. 2.3). This is due to the fact that these lines are quite sensitive to pressure broadening, in this case through the Stark effect which corresponds to the splitting of spectral lines in the presence of an external electric field. As a matter of fact, the line absorption coefficient in the wings is proportional to the electron pressure, which is in turn proportional to the continuum opacity in the case of OB stars (mainly due to bound-free absorption by neutral hydrogen).

Determination of surface abundances. Two methods are usually used to derive the surface abundances of stars, namely the curve of growth technique, and the spectral analysis.

The curve of growth method is based on the fact that the spectral line strength of an isotope of an element increases with the abundance of the element. This translates into a dependence between the EW and the abundance, which is illustrated in Fig. 2.4. Three parts are present in a typical curve of growth. In the first part, called the linear regime, the thermal (Doppler) broadening is very important and the equivalent width, which is mainly due to the high opacity of the line center (the Doppler core), increases proportionally to the number of absorbers. Weak lines are thus the best abundance indicators for this method, but the EW measurements are less accurate for such lines. As

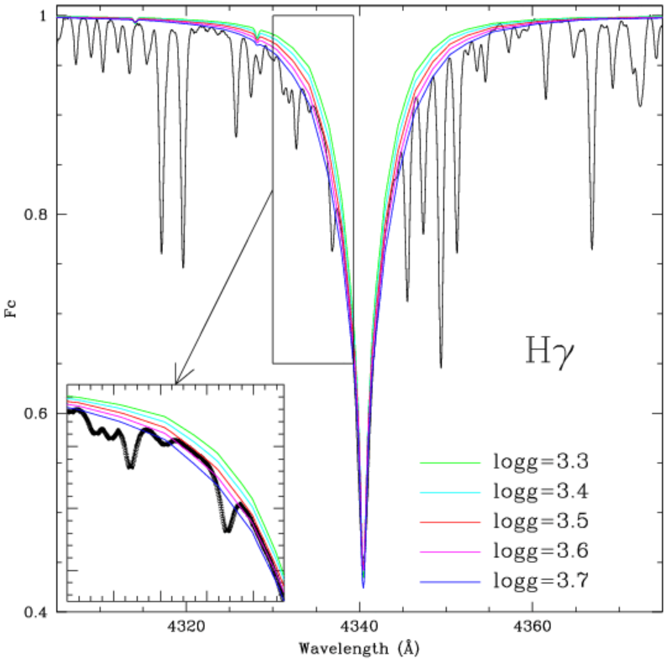

Figure 2.3: Illustration of the broadening of the wings of Hγ with $\log g$. *Source:* Courtesy of Dr. Thierry Morel.

the abundance, thus the opacity in the core, increases, the core becomes opaque and the EW increases moderately; this is the saturation regime where EW increases roughly with the common logarithm of the number of absorbing atoms. At some point the opacity of the line wings becomes significant and it gives rise to a new growing trend, this time depending on the square root of the number of absorbers. This last part of the curve of growth is sometimes referred as the damping regime. Since the individual EWs cannot be derived for our sample stars because metal lines are blended in the presence of fast rotation, the curve of growth technique was not used to derive the surface abundances. Therefore, the only way to derive these abundances is the spectral synthesis technique, that consists in finding the best models describing the observed data.

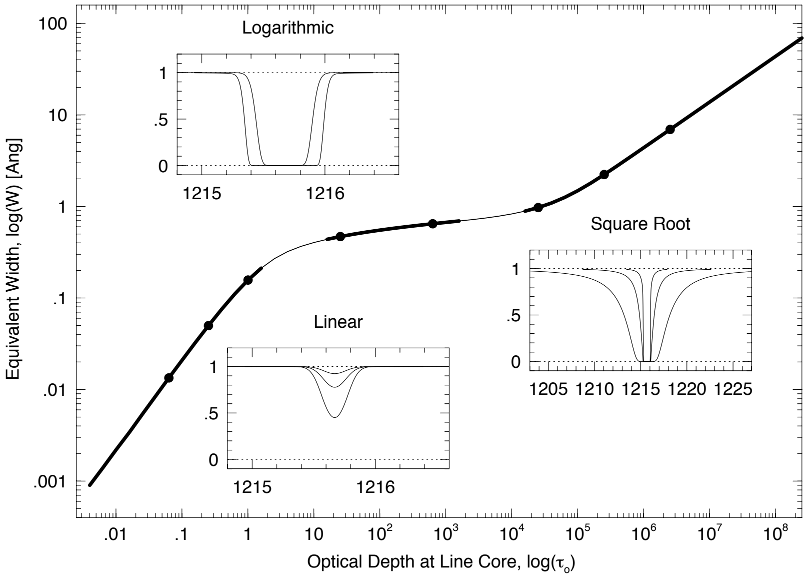

Figure 2.4: Illustration of the curve of growth: evolution of the equivalent width (here noted as W) as a function of the number of absorbing atoms. *Source:* lecture by Pr. Max Pettini, `http://www.ast.cam.ac.uk/~pettini/STARS/Lecture06.pdf`.

2.1.2 Published paper

The first paper of our study first introduces our sample stars, then presents the methods used to derive their projected rotational and macroturbulence velocities, their RVs, atmospheric parameters, and surface abundances. Validations of these methods are then presented. Finally, results for each object are given.

A&A 603, A56 (2017)
DOI: 10.1051/0004-6361/201629841

Astronomy & Astrophysics

Chemical abundances of fast-rotating massive stars

I. Description of the methods and individual results[⋆,⋆⋆]

Constantin Cazorla[1], Thierry Morel[1], Yaël Nazé[1⋆⋆⋆], Gregor Rauw[1], Thierry Semaan[2,1],
Simone Daflon[3], and M. S. Oey[4]

[1] Space sciences, Technologies and Astrophysics Research (STAR) Institute, Université de Liège, Quartier Agora,
Allée du 6 Août 19c, Bât. B5C, 4000 Liège, Belgium
e-mail: `cazorla@astro.ulg.ac.be`
[2] Observatoire de Genève, Université de Genève, Chemin des Maillettes 51, 1290 Versoix, Switzerland
[3] Observatório Nacional, Rua General José Cristino 77, 20921-400 Rio de Janeiro, Brazil
[4] University of Michigan, Department of Astronomy, 311 West Hall, 1085 S. University Ave, Ann Arbor, MI 48109–1107, USA

Received 4 October 2016 / Accepted 15 February 2017

ABSTRACT

Aims. Recent observations have challenged our understanding of rotational mixing in massive stars by revealing a population of fast-rotating objects with apparently normal surface nitrogen abundances. However, several questions have arisen because of a number of issues, which have rendered a reinvestigation necessary; these issues include the presence of numerous upper limits for the nitrogen abundance, unknown multiplicity status, and a mix of stars with different physical properties, such as their mass and evolutionary state, which are known to control the amount of rotational mixing.

Methods. We have carefully selected a large sample of bright, fast-rotating early-type stars of our Galaxy (40 objects with spectral types between B0.5 and O4). Their high-quality, high-resolution optical spectra were then analysed with the stellar atmosphere modelling codes DETAIL/SURFACE or CMFGEN, depending on the temperature of the target. Several internal and external checks were performed to validate our methods; notably, we compared our results with literature data for some well-known objects, studied the effect of gravity darkening, or confronted the results provided by the two codes for stars amenable to both analyses. Furthermore, we studied the radial velocities of the stars to assess their binarity.

Results. This first part of our study presents our methods and provides the derived stellar parameters, He, CNO abundances, and the multiplicity status of every star of the sample. It is the first time that He and CNO abundances of such a large number of Galactic massive fast rotators are determined in a homogeneous way.

Key words. stars: abundances – stars: early-type – stars: fundamental parameters – stars: massive – stars: rotation

1. Introduction

Massive stars are defined as objects born with O or early B spectral types (subsequently evolving to later types during their life) and by their death as a supernova (thus having initial masses larger than ~8 $M_{\odot}$). These OB stars are the true cosmic engines of our Universe. They emit an intense ionising radiation and eject large quantities of material throughout their life, shaping the interstellar medium, affecting star formation, and largely contributing to the chemical enrichment of their surroundings. It is therefore of utmost importance to develop a good understanding of the physical processes at play in these objects and to properly model their evolution.

One important feature of massive stars is their high rotational velocities, which can be up to at least 400 km s^{-1} (Howarth et al. 1997; Dufton et al. 2011). Such a fast rotation can be produced by several mechanisms: it can be acquired at birth as a result of their formation or develop subsequently during their evolution as they interact with a companion (through tidal forces, mass accretion, or even merging; Zahn 1975; Hut 1981; Packet 1981; Pols et al. 1991; Podsiadlowski et al. 1992; Langer et al. 2003; Petrovic et al. 2005a,b; de Mink et al. 2009, 2013; Dervişoğlu et al. 2010; Tylenda et al. 2011; Song et al. 2013).

[⋆] Based on observations obtained with the Heidelberg Extended Range Optical Spectrograph (HEROS) at the Telescopio Internacional de Guanajuato (TIGRE) with the SOPHIE échelle spectrograph at the Haute-Provence Observatory (OHP; Institut Pytheas; CNRS, France), and with the *Magellan* Inamori Kyocera Echelle (MIKE) spectrograph at the *Magellan* II Clay telescope. Based also on archival data from the Galactic O-Star Spectroscopic Survey (GOSSS), the Anglo-Australian Telescope (AAT) equipped with the University College London Echelle Spectrograph (UCLES), the ESO/La Silla Observatory with the Fiber-fed Extended Range Optical Spectrograph (FEROS; programmes 70.D-0110, 075.D-0061, 076.C-0431, 081.D-2008, 083.D-0589, 086.D-0997, 087.D-0946, 089.D-0189, 089.D-0975, 179.C-0197, and the High Accuracy Radial velocity Planet Searcher (HARPS; programme 60.A-9036), the Pic du Midi Observatory equipped with the NARVAL spectropolarimeter, the San Pedro Mártir (SPM) observatory with the Echelle SPectrograph for Rocky Exoplanet and Stable Spectroscopic Observations (ESPRESSO), the OHP with the AURELIE and ELODIE échelle spectrographs, the Nordic Optical Telescope (NOT) with the FIbre-fed Echelle Spectrograph (FIES), the Canada-France-Hawaii Telescope (CFHT), with the Echelle SpectroPolarimetric Device for the Observation of Stars (ESPaDOnS) spectrograph, the *Leonhard Euler* Telescope with the CORALIE spectrograph.

[⋆⋆] Table F.2 is also available at the CDS via anonymous ftp to `cdsarc.u-strasbg.fr` (`130.79.128.5`) or via `http://cdsarc.u-strasbg.fr/viz-bin/qcat?J/A+A/603/A56`

[⋆⋆⋆] Research associate FNRS.

Despite the rotational velocity of OB stars, which can amount to a significant fraction of the critical (break up) velocity[1], rotation had been considered for a long time as a minor ingredient of stellar evolution until some important discrepancies between model predictions and observations were brought to light (e.g. Maeder 1995). The importance of rotation on the evolution of massive stars is now considered to be comparable to that of stellar winds (Meynet & Maeder 2000), influencing all aspects of stellar evolution models (Maeder & Meynet 2015). For example, rotation increases the main-sequence (MS) lifetime by bringing fresh combustibles to the core. It also modifies the stellar temperature, thus the radiative flux.

Rotation also triggers the transport of angular momentum and chemicals in the interior (Maeder & Meynet 1996). This can notably lead to a modification of the wind properties and to changes in the chemical abundances seen at the stellar surface. In this context, it might be useful to recall that massive stars burn their central hydrogen content through the CNO cycle, which can be partial or complete depending on the temperature. For stars whose mass does not exceed 40 $M_\odot$, the ^{16}O abundance can be considered constant and that of ^{12}C depleted in the core. For more massive stars, the constancy applies to the ^{12}C abundance, while the core is depleted in ^{16}O. In all cases, the slow reaction rate of $^{14}_{7}\text{N} \longrightarrow {}^{15}_{8}\text{O}$ leads to an excess of nitrogen nuclei in the core. These elements may then be dredged up to the stellar surface, but the actual amount transported depends on the mixing efficiency, which is primarily a function of the rotation rate. Because it is the most affected, the nitrogen abundance at the stellar surface is considered the best indicator of rotational mixing (along with boron, but UV spectra are needed to study the abundance of this latter element; Proffitt & Quigley 2001). In contrast, slow rotation is expected in principle not to lead to any detectable nitrogen enrichment during the main-sequence phase, at least for stars in the mass range 5–60 $M_\odot$ (Maeder et al. 2014).

However, recent observations of B stars in the Galaxy and the Magellanic Clouds (MCs) in the framework of the VLT-FLAMES Survey of Massive Stars (Evans et al. 2008) have revealed two stellar populations that exhibit surface nitrogen abundances not predicted by single-star evolutionary models incorporating rotational mixing (Hunter et al. 2007, 2009). For instance, in the LMC, the first population (15% of the sample) is composed of slow rotators that unexpectedly exhibit an excess of nitrogen, while stars of the second group (also 15% of the sample) are fast rotators with $v \sin i$ up to ~330 km s^{-1} showing no strong nitrogen enrichment at their surface, if any (Brott et al. 2011). Additional examples of the former category have been found amongst O stars in the LMC (Rivero González et al. 2012a,b; Grin et al. 2017). The origin of this population is a matter of speculation, but has been proposed to result from the action of magnetic fields (Meynet et al. 2011; Potter et al. 2012). On the other hand, it is conceivable that stars in the second group are binaries that have undergone an episode of highly non-conservative mass transfer, with transport of angular momentum, but little transfer of CNO-processed material (see Langer et al. 2008).

A clear interpretation of these observations is, however, hampered by the limited quality of the abundance determinations. The reported nitrogen abundance of the fast rotators frequently are upper limits and information is unavailable or uncertain for other key elements, such as helium or carbon (e.g. Hunter et al. 2009 in the case of carbon). Furthermore, Maeder et al. (2009) pointed out the different evolutionary stages (on and away from the main sequence) and the large range of masses (from 10 to 30 $M_\odot$) of the stars studied in the VLT-FLAMES Survey. These authors found a better agreement with model predictions after the sample was split into groups of stars with similar properties (but see Brott et al. 2011, who addressed this issue through population synthesis). Maeder et al. (2014) also questioned some results obtained by Hunter et al. (2007, 2009) based on a reanalysis of their data. Finally, Bouret et al. (2013) and Martins et al. (2015a) argued that the CNO abundances of most O stars in their studies are compatible with the expectations from single-star evolutionary models, although their samples only contain few fast rotators. The observed efficiency of rotational mixing thus appears unclear, and more data is required to make progress.

2. Rationale of our study

Up to now, only a few comprehensive investigations of the metal content of fast-rotating, Galactic OB stars have been undertaken. HD 191423 (ON9 II-IIIn, Sota et al. 2011; $v \sin i$ ~ 420 km s^{-1}) has been studied by Villamariz et al. (2002), Mahy et al. (2015), and Martins et al. (2015a). HD 149757 (ζ Oph; O9.2 IVnn, Sota et al. 2011; $v \sin i$ ~ 378 km s^{-1}) has been studied by Villamariz & Herrero (2005). In addition, the CNO abundances of two O-type supergiants, two O dwarfs, five additional O giants, and four other O-stars with $v \sin i \geq 200$ km s^{-1} have been derived by Bouret et al. (2012), and Martins et al. (2012b, 2015b,a), respectively. The small number of high-resolution studies combined with the heterogeneity of the analyses has motivated us to undertake an in-depth study of bright OB stars with high rotational velocities.

The stars in our sample span a limited range in rotational velocities and evolutionary status (as they are all core-hydrogen burning stars). This restricts the number of parameters potentially affecting the abundances and allows us to more easily interpret our results. Enhancement of the surface nitrogen abundance (and accompanying carbon depletion) arising from rotational mixing is expected to be more subtle at Galactic metallicities than in the MCs. However, the detailed study of fast rotators in the MCs (with typically m_V ~ 13 mag) would be a major observational undertaking (see Grin et al. 2017). In contrast, focussing on nearby stars permits a detailed abundance study with only a modest investment of telescope time. As we show below, a large body of spectroscopic data is even already available in public archives.

For all stars, we have self-consistently determined the stellar properties from high-resolution spectra: effective temperature, $T_{\rm eff}$, surface gravity, $\log g$, projected rotational velocity, $v \sin i$, macroturbulence, $v_{\rm mac}$, as well as He and CNO abundances. An interaction with a companion may dramatically affect the evolution of the rotational and chemical properties of stars in binary systems. However, little is known about the binary status of the fast rotators previously studied in the literature. Therefore, another important aspect of our analysis is the determination of the multiplicity as a result of a radial-velocity (RV) study of our targets. To reinforce the point made above, such an investigation for the faint MC targets is also too demanding in terms of observing resources.

The results of our spectroscopic study of fast rotators are presented in two parts. This first paper describes the methods that have been used and the numerous checks performed to ensure the quality of the results. It also presents the results obtained for each star, while a follow-up paper (Cazorla et al. 2017, hereafter Paper II) will focus on the global interpretation of these results.

---

[1] The critical velocity of a star is reached when the centrifugal acceleration is equal to the gravitational one at the equator.

This paper is organised as follows. The sample, observations, and data reduction are outlined in Sect. 3; the spectroscopic analysis is described in Sect. 4; uncertainties in the derived physical parameters and abundances are discussed in Sect. 5; several checks of our methods are presented in Sect. 6; and conclusions are given in Sect. 7. Finally, Appendices A and B provide some individual information in tabular format, while notes on the binary and runaway status of individual stars are given in Appendix C, Appendix D compares our results to those in the literature and Appendix E provides a comparison between the observations of the hotter stars and their best-fit CMFGEN models.

3. Sample, observations, and data reduction

Our sample is composed of Galactic OB stars that have a projected rotational velocity exceeding 200 km s^{-1}; the vast majority have $m_V \lesssim 10$ to ensure good quality spectra. This is further separated into two subsamples.

The first subsample comprises dwarfs and (sub)giants with spectral types between B0.5 and O9. The constraints on the spectral type and luminosity class arise from the applicability domain of our first analysis tool, DETAIL/SURFACE, which is only suitable for stars with weak winds. In addition, He II features must be present, which excludes cooler objects. The second subsample contains hotter stars with spectral types up to O4, which were studied with CMFGEN, as this code can treat stars with extended atmospheres. For the sake of homogeneity, it would have been relevant to analyse the whole sample with CMFGEN. However, it is intractable in practice because of the time-consuming nature of the CMFGEN analysis. To demonstrate the validity of our approach, in Sect. 6.3 we compare the results provided by the two codes for a few representative cases and show that they are consistent.

We excluded double-lined spectroscopic binaries because a correct extraction of each spectral component through disentangling techniques is very difficult when spectral lines are heavily broadened. Besides, it requires a large number of spectra with a good phase coverage, which are often not available. We also excluded classical Oe and Be stars because circumstellar discs cannot be modelled with the chosen tools. The weak Hα emission observed in a few stars rather originates from a stellar outflow (e.g. HD 184915; Rivinius et al. 2013). In addition, we also avoided confirmed β Cephei stars (Stankov & Handler 2005) for which revealing binarity can be challenging because of line-profile variations arising from pulsations. Furthermore, this peculiarity makes the atmospheric parameter and abundance determinations difficult.

We ended up with 40 targets (Table F.1) that fulfilled the aforementioned criteria. While this sample of massive Galactic fast rotators is certainly not complete, it does represent a very large portion of those known in the solar vicinity. For example, SIMBAD lists only 50 stars with spectral type earlier than B0.5, $m_V \leq 13$, and $\upsilon \sin i > 200$ km s^{-1}, while Howarth et al. (1997) list 32 O-type stars with $\upsilon \sin i > 200$ km s^{-1} but it has to be noted that these catalogues include SB2 systems, Oe/Be stars, and pulsating stars that were discarded from our sample.

Part of the high-resolution spectra were obtained through our dedicated programmes on the following échelle spectrographs:

- The CORALIE spectrograph mounted on the 1.2 m *Euler* Swiss telescope located at the ESO La Silla Observatory (Chile). CORALIE has the same optical design as ELODIE (Baranne et al. 1996). All the steps of the reduction were carried out with the dedicated pipeline called DRS. The spectra cover the wavelength range 3870–6890 Å with a resolving power, R, of 60 000.
- The HEROS spectrograph mounted on the 1.2 m TIGRE telescope at La Luz Observatory (Mexico; Schmitt et al. 2014). The spectral domain covered by HEROS spans from 3500 to 5600 Å and from 5800 to 8800 Å (blue and red channels, respectively) for $R \sim 20\,000$. The spectra were automatically reduced with an Interactive Data Language (IDL) pipeline based on the reduction package REDUCE written by Piskunov & Valenti (2002).
- The MIKE spectrograph mounted on the 6.5 m *Magellan* II Clay telescope located at the Las Campanas Observatory (LCO; Chile). MIKE is a double échelle spectrograph yielding blue (3350–5000 Å) and red (4900–9500 Å) spectra simultaneously. In the blue part, $R \sim 53\,000$. The spectral reduction was carried out using the Carnegie Observatories python pipeline[2] (Bragança et al. 2012; Garmany et al. 2015).
- The SOPHIE spectrograph at the 1.93 m telescope at Observatoire de Haute-Provence (OHP; France). The spectra cover the wavelength range 3872–6943 Å with $R \sim 40\,000$ (high-efficiency mode). The data were processed by the SOPHIE fully automatic data reduction pipeline. As a check, we reduced the raw data using standard IRAF[3] routines, but found negligible differences with respect to the pipeline products.

The rest of the data were collected from several archives (unless otherwise noted, the spectra were reduced with the instrument pipeline):

- The AURELIE spectrograph mounted on the 1.52 m telescope at OHP (Gillet et al. 1994). The spectra have $R \sim 9000$ and either cover the wavelength range 4100–4950 (see De Becker & Rauw 2004) or 4450–4900 Å (see Mahy et al. 2013). The data reduction procedure is described in Rauw et al. (2003) and Rauw & De Becker (2004). Other reduced AURELIE data were retrieved from the Information Bulletin on Variable Stars (IBVS; De Becker et al. 2008)[4].
- The ELODIE échelle spectrograph mounted on the 1.93 m telescope at OHP, which was operational from 1993 to 2006 (Baranne et al. 1996). This instrument[5] covers the spectral range from 3850 to 6800 Å and has $R \sim 42\,000$.
- The ESPaDOnS échelle spectrograph mounted on the Canada-France-Hawaii Telescope (CFHT) on Mauna Kea. Spectra were retrieved from the Canadian Astronomy Data Centre[6] and cover the wavelength range 3700–10 500 Å with $R \sim 81\,000$ in "object only" spectroscopic mode.
- The ESPRESSO échelle spectrograph mounted on the 2.12 m telescope at Observatory Astronómico Nacional of San Pedro Mártir (SPM; Mexico). The spectra cover the wavelength domain 3780–6950 Å with $R \sim 18\,000$ (Mahy et al. 2013). The data reduction was completed using the échelle package included in the ESO-MIDAS software[7], as carried out by Mahy et al. (2013).

---

[2] `http://obs.carnegiescience.edu/Code/mike`

[3] `http://iraf.noao.edu`

[4] `http://ibvs.konkoly.hu/cgi-bin/IBVSetable?5841-t1.tex`

[5] `http://atlas.obs-hp.fr/elodie/`

[6] `http://www.cadc-ccda.hia-iha.nrc-cnrc.gc.ca`

[7] `http://www.eso.org/sci/software/esomidas/`

- The FEROS échelle spectrograph mounted on the 2.2 m telescope at La Silla. The ESO archives provide already reduced data for most of the sample but, when this was not the case, we reduced the raw data with the standard dedicated ESO pipeline (except for the HD 52266 data taken in 2011 for which J. Pritchard's personal pipeline[8] was used). The FEROS spectrograph covers the spectral domain from 3500 to 9200 Å and provides spectra with $R \sim 48\,000$.
- The FIES échelle spectrograph at the 2.5 m Nordic Optical Telescope (NOT) located at the Observatorio del Roque de los Muchachos (La Palma, Spain). This spectrograph covers the spectral range 3700–7300 Å with $R \sim 46\,000$ (in medium-resolution mode) or 25 000 (in low-resolution mode). FIES data were reduced with the dedicated reduction software FIEStool[9].
- The Galactic O-Star Spectroscopic Survey (GOSSS). The normalised spectra were retrieved from the GOSSS database[10] (Maíz Apellániz et al. 2011). These spectra come from two facilities: the 1.5 m telescope at Observatorio de Sierra Nevada (OSN; Loma de Dilar, Spain) with the Albireo spectrograph (spectral range coverage: 3740–5090 Å) and the 2.5 m du Pont telescope at LCO with the Boller & Chivens spectrograph (spectral range coverage: 3900–5510 Å). Because the spectral resolution of both instruments ($R \sim 3000$) is much lower than that of the other spectrographs used in this work, GOSSS spectra were only used for the RV study (see Sect. 4.1).
- The HARPS échelle spectrograph mounted on the 3.6 m telescope at La Silla. The spectrograph covers the spectral range 3780–6910 Å with $R \sim 120\,000$.
- The NARVAL spectropolarimeter mounted on the 2 m Telescope *Bernard Lyot* (TBL). NARVAL covers the wavelength range ~3700–10 500 Å with $R \sim 75\,000$ in "object only" mode. Spectra were retrieved from the PolarBase database[11].
- The UCLES échelle spectrograph mounted on the 3.9 m Anglo-Australian Telescope (AAT; Siding Spring Observatory, Australia). UCLES covers the wavelength range ~4340–6810 Å with a resolving power of at least 40 000, depending on the slit width. The raw data[12] were reduced in a standard way with the IRAF échelle package.

Some spectra extracted from the archives were already normalised and, in that case, we simply checked that the normalisation was satisfactory. Otherwise, the spectra were normalised within IRAF using low-order polynomials in selected continuum windows. These "clean" windows were identified after a SOPHIE spectrum of the slow rotator 10 Lac (O9 V) was broadened[13] with the $v \sin i$ value corresponding to each target.

All spectra were considered for the RV study. However, only a limited number were used to derive the parameters and abundances. The choice was based on several criteria (spectral resolution, wavelength coverage, S/N). Further details on this point can be found in Sect. 4.1.

4. Spectroscopic analysis

4.1. Radial velocities and binary analysis

For each stellar spectrum, the first step of our analysis was to determine the radial velocity with a cross-correlation technique available in the IRAF package RVSAO[14] (Kurtz & Mink 1998). The closest TLUSTY synthetic spectrum (BSTAR06 and OSTAR02 grids; Lanz & Hubeny 2003, 2007) for each star was determined by a χ^2 analysis and used as template. The correlation was performed only in the wavelength range from about 4350 to 4730 Å. This region was chosen because of the relatively large number of spectral features (mostly helium lines), the absence of Balmer lines (which may be affected by emissions linked to stellar winds and colliding wind effects in binaries), and the fact that it was covered by all the spectrographs used in this work. Undesirable features (e.g. diffuse interstellar bands) were masked out. Table A.1 provides the RVs measured for each spectrum alongside the observation date.

To get the best quality data for the determination of physical parameters, we then corrected the individual spectra for their radial velocity and, when necessary, averaged on an instrument-by-instrument basis with a weight depending on the signal-to-noise ratio (S/N). These spectra, which were subsequently used for the stellar parameters determination, are identified in boldface in Table A.1.

To establish whether the measured RVs are variable or not, we adopt a criterion inspired by that of Sana et al. (2013): the maximum RV difference larger than 4σ and above a given threshold (20 km s^{-1} as appropriate for O stars). The multiplicity status of our targets depends on the outcome of this test. If the differences are not significant, then the star is presumably considered to be single; otherwise the star is considered a RV variable (and thus a probable binary). Among the latter category, we further classify as SB1 those for which a full orbital solution can be calculated (see below). For some targets, additional information is available in the literature and the multiplicity status may then be revisited (see Appendix C for details).

Finally, when there were at least 15 RV measurements, including all available literature values (even if their error is unknown), we also analysed the RV datasets using the following period search algorithms: (1) the Fourier algorithm adapted to sparse/uneven datasets (Heck et al. 1985; Gosset et al. 2001; Zechmeister & Kürster 2009); (2) two different string length methods (Lafler & Kinman 1965; Renson 1978); (3) three binned analyses of variances (Whittaker & Robinson 1944; Jurkevich 1971, which is identical, with no bin overlap, to the "pdm" method of Stellingwerf 1978; and Cuypers 1987, which is identical to the "AOV" method of Schwarzenberg-Czerny 1989); and (4) conditional entropy (Cincotta et al. 1999; Cincotta 1999, see also Graham et al. 2013). Although the most trustworthy technique is the Fourier method, a reliable detection is guaranteed by the repeated recovery of the same signal with different methods. When a potential period was identified, an orbital solution was then calculated using the Liège Orbital Solution Package (LOSP; see Sana 2013). The results of these variability tests and period searches are presented in Appendix C for each star.

4.2. Rotational velocities

The second step of our analysis was to derive the projected rotational velocity through Fourier techniques (Gray 2005; Simón-Díaz & Herrero 2007). In the Fourier space, the

---

[8] http://www.eso.org/~jpritcha/jFEROS-DRS/index.html

[9] http://www.not.iac.es/instruments/fies/fiestool

[10] http://ssg.iaa.es/en/content/galactic-o-star-catalog/

[11] http://polarbase.irap.omp.eu

[12] http://site.aao.gov.au/arc-bin/wdb/aat_database/user/query

[13] This broadening was performed by the `ROTIN3` programme that is part of the SYNSPEC routines; http://nova.astro.umd.edu/Synspec43/synspec.html

[14] http://tdc-www.harvard.edu/iraf/rvsao

rotational broadening indeed expresses itself through a simple multiplication with the Fourier transform of the line profiles, hence providing a direct estimate of $v \sin i$. We considered as many lines as possible (notably He I 4026, 4471, 4713, 4922, 5016, 5048, 5876, 6678; He II 4542, 5412; C IV 5801, 5812; and O III 5592) in order to enhance the precision of our determinations. We also made use of the `iacob-broad` tool (Simón-Díaz & Herrero 2014) to determine the macroturbulent velocities. As this tool also provides an independent estimate of $v \sin i$ – albeit it is also based on Fourier techniques – it allows us to check the robustness of our $v \sin i$ values. These values were consistently recovered within the error bars. We caution that the derived macroturbulent velocities are upper limits only since they cannot be determined reliably for fast rotators (Simón-Díaz & Herrero 2014). No significant change in stellar parameters and abundances was found whether or not the macroturbulence was considered in the computation of the synthetic spectra; the macroturbulence broadening of our synthetic spectra was performed with the `macturb` programme of the SPECTRUM suite of routines[15] that makes use of the formulation of Gray 2005. Furthermore, our spectral fits are already satisfactory when rotational velocity is the only source of broadening considered. After some preliminary tests, we therefore chose not to consider macroturbulence in our determination of the stellar parameters.

To further validate our method, we compared the $v \sin i$ for eight stars with those obtained by Bragança et al. (2012) and Garmany et al. (2015) with a different method based on the full width at half-minimum [FWHM] of He I lines. The results are presented in Table 1: they show a good agreement within errors, although there is some indication of slightly larger values in our case. This might be attributed to differences in the normalisation.

4.3. Atmospheric parameters and abundances

Two methods were used to determine the atmospheric parameters ($T_{\rm eff}$, $\log g$) and chemical abundances depending on the sample considered. They are both based on spectral synthesis whereby a search is made for the best match between each observed spectrum and a grid of synthetic profiles broadened with the appropriate instrumental and rotational velocity profiles. They are now presented in turn. Our full results can be found in Table F.2, and a comparison with literature values, when available, is given in Table D.1.

We provide $\log g_{\rm C}$, which is the surface gravity corrected for the effects of centrifugal forces: $g_{\rm C} = g + (v \sin i)^2/R_*$, where R_* is the star radius (Repolust et al. 2004). The radius was always estimated, for consistency, from the gravity value ($g = GM/R_*^2$) taking the appropriate mass M for each star (see Paper II for details) into account. Radii can also be computed from the temperatures (our best-fit $T_{\rm eff}$) and the luminosities, which are derived from the magnitude and distance of the target under consideration. While distances are not available for all our targets, two stars are believed to be part of clusters and, therefore, have their distance d estimated: HD 46056 and HD 46485 in NGC 2244 (d = 1.4 kpc). Furthermore, the HIPPARCOS distances of HD 66811 and HD 149757 are known: 335^{+12}_{-11} and 112 ± 3 pc, respectively (van Leeuwen et al. 1997; Maíz Apellániz et al. 2008). In addition, we used V magnitudes taken from SIMBAD, reddenings taken from WEBDA[16] for the cluster members or from Bastiaansen (1992) and Morton (1975) for HD 66811 and HD 149757, respectively, as well as typical bolometric corrections for the appropriate spectral type (Martins et al. 2005). The radii derived from both methods agree well; however, a full comparison must await the availability of accurate distances from *Gaia* (Gaia Collaboration et al. 2016).

Table 1. Comparison between our projected rotational velocities and those in the literature based on the FWHM of He I lines.

Star	$v \sin i$ [km s^{-1}] this work	$v \sin i$ [km s^{-1}] literature	Reference
ALS 491	228 ± 15	223 ± 56	1
ALS 535	200 ± 15	179 ± 14	1
ALS 851	167 ± 15	165 ± 31	1
ALS 897	180 ± 15	175 ± 10	1
ALS 864	249 ± 15	232 ± 22	1
ALS 18675	236 ± 15	212 ± 11	1
HD 42259	256 ± 15	249 ± 25	2
HD 52533	305 ± 15	291 ± 29	2

References. [1] Garmany et al. (2015); [2] Bragança et al. (2012).

4.3.1. Method for the cooler stars

The synthetic spectra for the stars whose spectral types are comprised between B0.5 and O9 were computed using Kurucz LTE atmosphere models assuming a solar helium abundance and the non-LTE line-formation code DETAIL/SURFACE (Giddings 1981; Butler & Giddings 1985). The choice of a solar helium abundance was motivated by the fact that no appreciable differences in stellar parameters and CNO abundances were found when considering model atmospheres with a helium abundance that is twice solar, as is the case for some of our targets (Table F.2). The model atoms implemented in DETAIL/SURFACE are the same as those employed in Morel et al. (2006). This combination of LTE atmospheric models and non-LTE line-formation computations has been shown to be adequate for late O- and early B-type stars for which wind effects can be neglected (Nieva & Przybilla 2007; Przybilla et al. 2011).

We assumed a typical microturbulence to compute the synthetic spectra (ξ = 10 km s^{-1}; e.g. Hunter et al. 2009). However, we explore the impact of this choice on our results in Sect. 5.3.1.

We performed the analysis in three steps (see Rauw et al. 2012 for further details). The stellar parameters and helium abundance (by number, noted $y = \mathcal{N}({\rm He})/[\mathcal{N}({\rm H}) + \mathcal{N}({\rm He})]$) were first determined for each star. We only summarise the procedure briefly here. The grid of synthetic spectra used was constructed by varying $\log g$ in the range 3.5–4.5 dex with a step of 0.1 dex, $T_{\rm eff}$ in the domain 27–35 kK with a step of 1 kK, and y in the range 0.005–0.250 with a step of 0.005. A few models with both large $T_{\rm eff}$ and low $\log g$ are lacking because of convergence issues. We selected four Balmer lines (Hϵ, Hδ, Hγ, and Hβ) to derive the surface gravity, and we chose nine prominent helium lines (He I 4026, 4388, 4471, 4713, 4922, 5016, and He II 4542, 4686, 5412) because they are sensitive to both the stellar temperature, through the ionisation balance of He I and He II lines, and the abundance of helium. Metallic lines falling across the Balmer and He lines, but that are not modelled by DETAIL/SURFACE, were masked out during the fitting procedure. For the other metallic features, abundances typical of

---

[15] `http://www.appstate.edu/~grayro/spectrum/spectrum276/node38.html`
[16] `https://www.univie.ac.at/webda/`

early-B stars determined with the same code were assumed (see Table 6 of Morel et al. 2008).

For the initial step, we chose a value of $\log g$ (either 3.5 or 4.0) as a first guess. Both values were tried and, if results differed after convergence, those associated with the input $\log g$ yielding the smallest residuals were kept. A comparison between the observed and synthetic spectra for the aforementioned He I lines provides values of $T_{\rm eff}$ and y for each line. The helium abundances were then averaged by weighting the results according to the residuals. The y value of the grid closest to this mean helium abundance was then fixed for the next step, the fit of the He II lines, which was performed in a similar way. We calculated the mean temperatures for each ion separately and results from individual lines were weighted according to their residuals. We then averaged the two mean values, considering equal weights for the two ions, to derive a new $T_{\rm eff}$ value. The values of $T_{\rm eff}$ and y in the grid, which are closest to the values just derived, were then fixed to determine $\log g$ by fitting the wings of the Balmer lines. If the value of $\log g$ was not equal to the input value, we performed additional iterations until convergence (see sketch in Fig. 1). Caution must be exercised when fitting spectral regions where orders of the échelle spectra are connected, especially when this occurs over the broad Balmer lines. It should, however, be noted that no deterioration of the fit in these regions was apparent. An illustration of the fits of He line profiles is given in Fig. 2, demonstrating that the observed features are satisfactorily reproduced. Achieving a good fit for the Balmer lines using DETAIL/SURFACE is more challenging (Fig. 3), as found in previous studies (e.g. Firnstein & Przybilla 2012 for Galactic BA supergiants), but remains possible when carefully selecting the regions that are deemed reliable.

The next step is to determine the CNO abundances[17]. To this end, we built a grid of CNO synthetic spectra for the ($T_{\rm eff}$, $\log g$) pair determined previously. We created these grids by varying $\log \epsilon$(C) in the range 7.24–8.94 dex, $\log \epsilon$(N) in the range 7.24–8.64 dex, and $\log \epsilon$(O) in the range 7.74–9.24 dex, with a step of 0.02 dex in each case. We used synthetic spectra linearly interpolated to the exact $T_{\rm eff}$ values because the CNO abundances may be very sensitive to the temperature in certain $T_{\rm eff}$ regimes.

The choice of suitable CNO lines is complicated by the high rotation rates of our targets. We chose to consider some spectral domains that have been shown not to be significantly contaminated by lines of other species and to provide results that are consistent for a set of well-studied stars with those of more detailed and much more time consuming analyses (see Rauw et al. 2012 for a discussion). These regions are illustrated in Fig. 4: the features in the first region (4060–4082 Å) are mostly C III and O II lines, whereas O II lines contribute predominantly to the second region (4691–4709 Å) and N II to the third (4995–5011 Å). The associated CNO abundances were then found by minimising the residuals between the observed and synthetic spectra.

The final abundance of oxygen is the unweighted mean of the values found for the first and second regions. Since the C III lines allowing us to probe the carbon abundance are weak for the coolest stars in our sample and become a minor contributor to the blend with the nearby O II lines, carbon abundances cannot be reliably determined for the B0.5 stars.

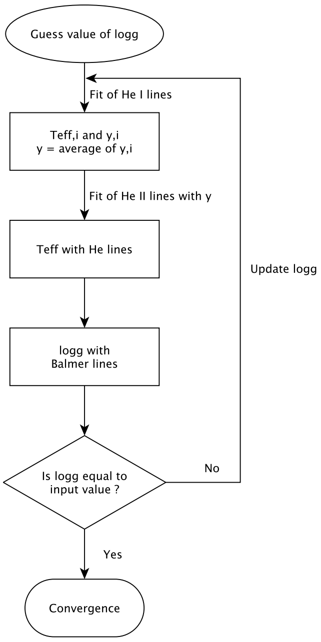

Fig. 1. Flowchart of the method used for the cooler stars to derive the atmospheric parameters and helium abundance.

4.3.2. Method for the hotter stars

For the hotter stars that possess strong winds, we used the non-LTE spherical atmosphere code CMFGEN to derive stellar parameters. Full details about this code (e.g. atomic data) can be found in Hillier & Miller (1998)[18].

As a starting point, CMFGEN makes use of a hydrodynamical structure, characterising the velocity and density profiles, which is created from TLUSTY models (Lanz & Hubeny 2003). The wind is described by a mass-loss rate, $\dot{M}$, a β-like velocity law, $v = v_\infty\ (1 - R_*/r)^\beta$, where R_* is the stellar radius, and r the distance from the stellar centre, β a parameter with typical values for massive stars close to 0.8–1, and v_∞ the terminal velocity. We adopted a volume filling factor at terminal velocity of 0.1 and a clumping velocity factor of 100 km s^{-1}; for the clumping formalism implemented in CMFGEN, see e.g. Raucq et al. (2016). The following elements are included in the calculations of our models: H, He, C, N, O, Ne, Mg, Al, Si, P, S, Ca, Fe, and Ni. Computing time was reduced thanks to the use of the super-level approach, but remains much longer than for DETAIL/SURFACE.

A synthetic spectrum was created after finding the formal solution of the radiative transfer equation. A microturbulent velocity varying linearly from the photosphere to $0.1\,v_\infty$ at the top of the atmosphere was considered. The value at the photosphere depends on the luminosity class: 10 km s^{-1} for dwarfs, 12 km s^{-1} for (sub)giants, and 15 km s^{-1} for supergiants

---

[17] CNO abundances are given in the form $\log \epsilon(X) = 12 + \log[\mathcal{N}(X)/\mathcal{N}(H)]$, where X ≡ C, N, O.

[18] See also `http://kookaburra.phyast.pitt.edu/hillier/web/CMFGEN.htm` for upgrades since the original publication.

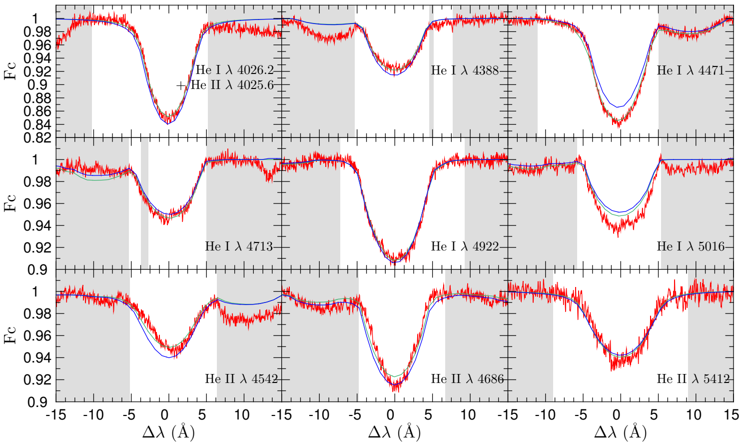

Fig. 2. Comparison between the observed FEROS spectrum of HD 90087 (red) and the best-fitting synthetic He line profiles (green). The line profiles computed for the final, mean parameters are shown in blue. The white areas delineate the regions where the fit quality was evaluated.

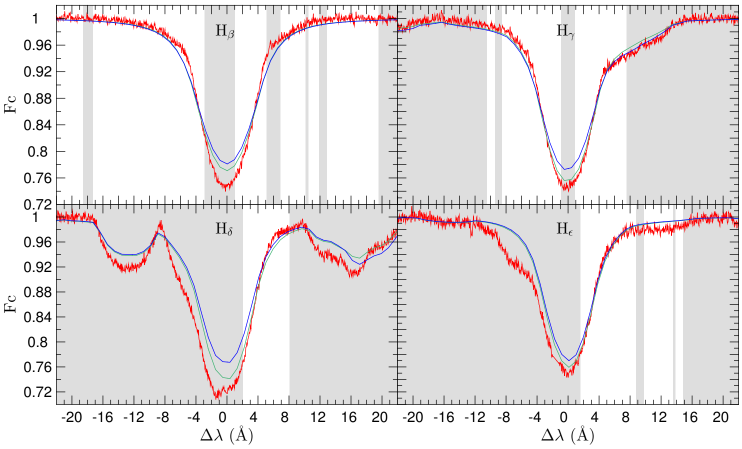

Fig. 3. Same as Fig. 2, but for the Balmer line profiles. As in previous studies (e.g. Firnstein & Przybilla 2012), achieving a good fit may be difficult, but selecting specific regions helps in this regard.

(Bouret et al. 2012). A typical X-ray flux corresponding to $L_X/L_{BOL} \sim 10^{-7}$ is considered in our models, as X-rays have an impact on the ionisation balance. After transforming vacuum wavelengths into air wavelengths, the spectrum was then broadened in order to take the appropriate instrumental resolution and object's projected rotational velocity into account.

Given the large number of free input parameters entering the CMFGEN code and the fact that the computing time necessary to create a new model is in general very lengthy, computation of a complete grid of models is virtually impossible. We therefore adopted a procedure slightly different from that described in the previous subsection. A first guess of stellar parameters, wind parameters, and surface abundances for each star was adopted (either from the literature, if available, or from typical values for the considered spectral type given by Muijres et al. 2012). Wind parameters are not investigated in this study, hence they were not fitted since our main concern was to unveil surface abundances (an approach previously used by Martins et al. 2015b). In particular, v_∞ is fixed, when possible, to values provided by Prinja et al. (1990). We nevertheless checked that the fits of wind-sensitive lines were reasonable, and the wind parameters were slightly modified for stars with strong outflows (e.g. HD 66811) when these fits were not deemed satisfactory. We calculated a small grid of CMFGEN spectra with five temperature ($\Delta T_{\rm eff}$ = 500 K) and five gravity values ($\Delta \log g$ = 0.125 dex) around the initial guesses. We then computed the residuals for

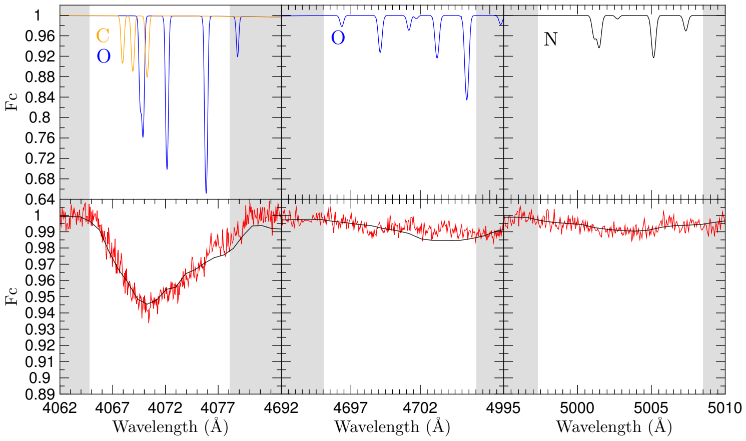

Fig. 4. Comparison for HD 90087 between the observed profiles (red; FEROS spectrum) and best-fitting synthetic metal line profiles (black). The white areas delineate the regions where the fit quality was evaluated. The *top panels* show the non-rotationally broadened synthetic profiles computed for the final parameters and abundances.

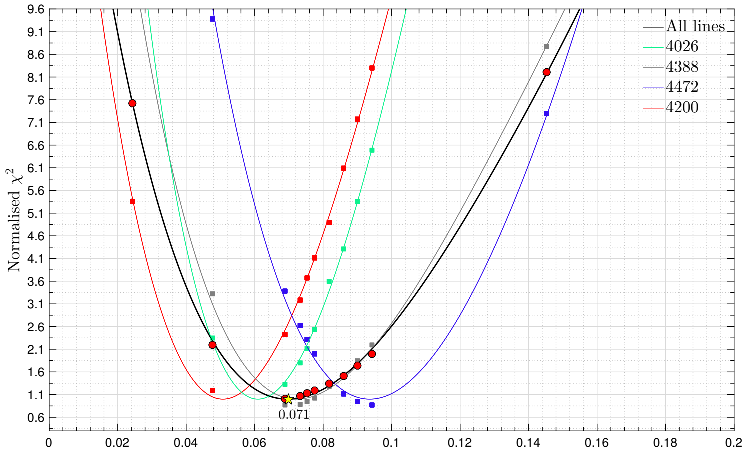

Fig. 5. Illustration of the helium abundance determination for HD 163892 with CMFGEN (see Sect. 6.3). Only a few lines are shown for clarity. Results of the χ^2 analysis are shown as solid red circles. The black curve is the global, polynomial fit for all lines. The solid yellow star indicates the abundance providing the best fit (Table 4).

each point of the grid between the observed spectrum and the synthetic spectra. This was performed over the same regions, encompassing the Balmer and He lines, as those used for the cooler objects (Sect. 4.3.1). A surface corresponding to a piecewise cubic interpolation was fitted to the χ^2 results of this analysis. The best-fit values of $T_{\rm eff}$ and log g are at the minimum of this surface fit. The good agreement for the hotter stars between CMFGEN spectra and observations is illustrated in Appendix E.

Next, we determined the helium abundance by performing a χ^2 analysis similar to that of Martins et al. (2015b), considering the same helium lines as in Sect. 4.3.1, with the addition of He II 4200. This time points in the grid were separated by $\Delta y \sim 0.025$. A polynomial fit (of degree smaller than or equal to 4) of individual features first allowed us to identify discrepant lines (the fit quality was an additional criterion). Then, a global fit of the remaining lines enabled us to find the best value of y (see illustration in Fig. 5).

The carbon, nitrogen, and oxygen abundances were derived following the same approach, with the grids usually having $\Delta[\mathcal{N}(\mathrm{X})/\mathcal{N}(\mathrm{H})] = 2\times10^{-4}$, where X ≡ C, N, O. The initial line list used to derive the CNO abundances is taken from Martins et al. (2012a, 2015a,b), and shown in plots of

Appendix E, while the lines actually used for each star are listed in Table B.1.

5. Uncertainties of the results

5.1. RVs

High-resolution spectrometers usually yield low errors on RVs. For example, RV dispersions below 1 km s^{-1} are commonly found for narrow interstellar features (Bates et al. 1992). In our case, however, the lines are very broad, generally leading to larger errors. Indeed, RVSAO calculates errors on RVs, which are of the order of 1–20 km s^{-1} (and typically 7 km s^{-1}) for our sample stars, depending on noise level, spectral type, $v \sin i$, and spectral resolving power. The uncertainty arising from the wavelength calibration ($\sim$ 1 km s^{-1}, as determined from narrow interstellar lines) is generally negligible in comparison.

To check the RVSAO error values, we performed Monte Carlo simulations. Synthetic TLUSTY spectra of a typical B0.5 V and O5 V star were convolved with two rotational profiles ($v \sin i$ = 200 and 400 km s^{-1}, corresponding to the extreme values of our sample), blurred by noise ($S/N \sim 125$, typical of our data), and shifted with different radial velocities (from –250 to 250 km s^{-1} with a step of 10 km s^{-1}). Their RV was estimated as for real spectra and the dispersion of the difference between applied shifts and derived velocities examined. We found that the distributions of the velocity differences can be reasonably represented by Gaussians whose standard deviations agree well with the errors provided by RVSAO (e.g. $\sim$1 km s^{-1} found in both cases for a B0.5 V star with $v \sin i$ = 400 km s^{-1} and observed with R = 50 000, see Fig. 6).

5.2. v sin i

The errors on the projected rotational velocities can be empirically estimated by comparing results obtained for a star observed with various instruments and analysed using different diagnostic lines. Taking HD 149757 (ζ Oph) as a prototypical example, we found dispersions of $v \sin i$ values of $\sim$8 km s^{-1} when considering different lines (He I 4026, 4471, 4922), but the same instrument. Alternatively, this translates to $\sim$12 km s^{-1} for the same lines, but different instruments (ELODIE, FEROS, and HARPS). The overall dispersion considering all values amounts to 13 km s^{-1}. We therefore consider a representative error of $\sim$15 km s^{-1} for our sample stars.

5.3. Atmospheric parameters and abundances

5.3.1. Cooler stars

To estimate the precision of our parameters ($T_{\rm eff}$, $\log g$) and abundances, we first examined the dispersion of the results obtained for different spectra (ELODIE, FEROS, and HARPS) of the same star (HD 149757). The differences are expected to mainly reflect the uncertainties related to the nature of the data and their treatment, especially errors in the normalisation to the continuum. In the case of HD 149757, our procedure also accounts for line-profile variations arising from non-radial pulsations (e.g. Kambe et al. 1997). As a second step, we explored the impact of the choice of the microturbulence by repeating the analysis of HD 149757 after adopting ξ = 5 rather than 10 km s^{-1}.

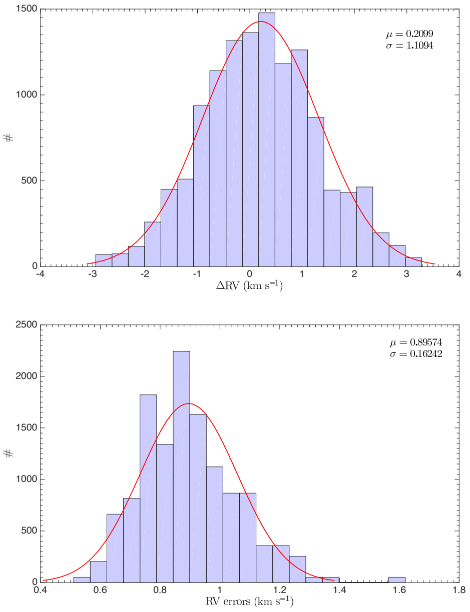

Fig. 6. Example of Monte Carlo simulations for a B0.5 V star with $v \sin i$ = 400 km s^{-1} observed with R = 50 000. A total of 12 750 trials were made. *Upper panel*: deviations of the derived velocities with respect to the input values. *Lower panel*: breakdown of the derived errors provided by RVSAO. The Gaussian that best represents each distribution is overplotted in red.

To accommodate both sources of errors, we quadratically summed the derived dispersions to get the final uncertainties that are quoted in Table 2. These uncertainties typically amount to 1000 K for $T_{\rm eff}$, 0.10 dex for $\log g$, 0.025 for y, and 0.12, 0.13, and 0.21 dex for the abundances of carbon, nitrogen, and oxygen, respectively. The errors on the nitrogen-to-carbon and nitrogen-to-oxygen abundance ratios ([N/C] and [N/O], defined as $\log[\mathcal{N}(\mathrm{N})/\mathcal{N}(\mathrm{C})]$ and $\log[\mathcal{N}(\mathrm{N})/\mathcal{N}(\mathrm{O})]$, respectively) were then estimated to be 0.21 and 0.12 dex, respectively.

5.3.2. Hotter stars

Typical errors on $T_{\rm eff}$ and $\log g$ were assumed to be 1500 K and 0.15 dex, respectively, as generally adopted in CMFGEN analyses in the literature (Martins et al. 2015b; Raucq et al. 2016). These values are higher than those considered for DETAIL/SURFACE since stronger winds have an impact on the resultant spectrum, making the analysis more challenging. The chosen errors are also comparable to the differences found when comparing our values of $T_{\rm eff}$ and $\log g$ with those in the literature (Appendix D), which supports our choice. HD 41161, which is representative of the sample of hotter stars, was chosen to determine the typical errors on He and CNO abundances. These errors were derived from the unnormalised χ^2 function, considering values corresponding to $\Delta\chi^2$ = 1 above its minimum. This approach is different from that of Martins et al. (2015a) who first normalised the χ^2 function such that the minimum is equal to one before considering $\Delta\chi^2$ = 1 (a procedure less valid than

Table 2. Errors on the atmospheric parameters and abundances of HD 149757 arising from the choice of the instrument and microturbulence value.

Parameter	$\sigma_{\rm instr}$	$\sigma_{\rm micro}$	σ
$T_{\rm eff}$ [K]	630	320	1000
$\log g$	0.06	0.07	0.10
y	0.010	0.022	0.025
$\log \epsilon$(C)	0.10	0.06	0.12
$\log \epsilon$(N)	0.12	0.04	0.13
$\log \epsilon$(O)	0.13	0.16	0.21
[N/C]	0.21	0.02	0.21
[N/O]	0.01	0.12	0.12

Notes. The last column gives the adopted (combined) uncertainty. σ corresponds to $\sqrt{\sigma^2_{\rm instr} + \sigma^2_{\rm micro}}$.

ours, statistically speaking). We caution that the errors on He and CNO abundances do not take the uncertainties on atmospheric parameters into account so that they are likely underestimated.

6. Method validation

6.1. Comparison of atmospheric parameters and abundances with literature

Half of our targets had been previously investigated in some detail (though usually CNO abundances are missing; Table D.1). We note a good agreement overall, considering error bars. In particular, we underline the study of Martins et al. (2015a,b), which has 11 objects in common with our analysis. On average, differences in stellar parameters (ours minus Martins et al.) amount to $\Delta T_{\rm eff}$ = +282 ± 627 K, $\Delta \log g$ = +0.02 ± 0.12 dex, Δy = −0.010 ± 0.044, $\Delta \log \epsilon$(C) = 0.00 ± 0.19 dex, $\Delta \log \epsilon$(N) = −0.10 ± 0.13 dex, and $\Delta \log \epsilon$(O) = −0.12 ± 0.18 dex, which are well within error bars. The largest differences are within, or close to, 2σ: HD 46485 ($\Delta \log g$ = 0.25 dex), HD 191423 (Δy = –0.066), and HD 13268 ($\Delta \log \epsilon$(O) = –0.39 dex).

Some differences are nevertheless worth mentioning. Our lower limit for the oxygen abundance in HD 150574 is larger than the value derived by Martins et al. (2015b). For HD 191423, we derive an upper limit for the carbon abundance that is lower than the value derived by Villamariz et al. (2002) and a nitrogen abundance that is lower than the lower limit reported by Martins et al. (2015b). However, the differences for HD 191423 are below 2σ, hence barely significant. In addition, this star has an extreme rotational velocity ($v \sin i$ = 420 km s^{-1}), which renders its analysis very difficult.

6.2. Comparison of DETAIL/SURFACE results with those previously obtained for well-studied slow rotators

In order to validate the procedures used for the analysis of the cooler stars of our sample, the following four narrow-lined, well-studied objects were analysed (see Rauw et al. 2012; Morel et al. 2008): ξ^1 CMa (B0.5 IV; $v \sin i \sim 10$ km s^{-1}), τ Sco (B0 V; $v \sin i \sim 8$ km s^{-1}), HD 57682 (O9.2 IV; $v \sin i \sim 25$ km s^{-1}), and 10 Lac (O9 V; $v \sin i \sim 25$ km s^{-1}). For ξ^1 CMa, which is a well-known β Cephei pulsator with slight variations of the physical parameters along the pulsation cycle (Morel et al. 2006), the HEROS exposure corresponding to the highest effective temperature was chosen.

A high rotation rate may bias our results because of, for example, blending issues or a more uncertain continuum placement. To assess the importance of these effects, we repeated the analysis after convolving the spectra with a rotational broadening function corresponding to 300 km s^{-1}, which is a value representative of our sample.

Table 3 presents our results and Fig. 7 compares them to literature values. Some study-to-study scatter exists, but there is an overall good agreement between our values and those in the literature. In particular, there is no evidence for systematic differences compared to previous results despite the different techniques employed; in fact, 10 Lac displays a large dispersion in the literature values of $T_{\rm eff}$, hence provides a less significant comparison point. Furthermore, our results appear largely insensitive to the amount of rotational broadening, thereby validating our method.

6.3. CMFGEN versus DETAIL/SURFACE

Previous studies have revealed a good agreement for main-sequence, early B-type stars between the parameters/abundances determined with DETAIL/SURFACE and the unified code FASTWIND (Lefever et al. 2010; Nieva & Simón-Díaz 2011). However, a full comparison of the results provided by DETAIL/SURFACE and CMFGEN was seldom performed. To our knowledge, only two stars have been analysed with both codes: τ Sco (studied with DETAIL/SURFACE by Hubrig et al. (2008) as well as by Nieva & Przybilla 2012, and with CMFGEN by Martins et al. 2012a) and HD 57682 (studied with DETAIL/SURFACE by Morel (2011) and with CMFGEN by Martins et al. 2015a). In these cases, the results appear to agree within the errors. The only exception is the nitrogen abundance in HD 57682, but the origin of this discrepancy is unclear.

Since we made use of these two different line-formation codes for the analysis, our results for the subsamples of cool and hot objects could be affected by systematic errors. To be able to fully assess the magnitude of such differences, if any, it is necessary to study at least a few objects with both codes. To this end, three objects have been chosen: HD 102415, HD 149757, and HD 163892. The three stars were selected because they exhibit different degrees of nitrogen enrichment, spanning the range observed in our sample.

Table 4 presents our results. The effective temperatures are in good agreement, within the error bars: the largest difference is $\Delta T_{\rm eff}$ = 500 K for HD 149757, which is still below the typical error bars of 1–1.5 kK. The differences in gravities are also generally small (< 0.1 dex), although the largest difference (for HD 102415) reaches 0.24 dex, which is slightly larger than the errors (estimated to be 0.10–0.15 dex). The helium abundances agree well with the largest difference, Δy = 0.034, found for HD 102415, being similar to the error bars. The CNO abundances yielded by the two codes also agree within the error bars. Therefore, we can conclude that there is no evidence for significant differences when analysing our targets with DETAIL/SURFACE or CMFGEN, ensuring that our overall results are to first order homogeneous.

6.4. Comparison with the CNO cycle predictions

The abundance ratios [N/C] and [N/O] are very good indicators of rotational mixing in massive stars. The transformation of carbon into nitrogen is more efficient than that of oxygen into nitrogen for our sample stars. Hence, their surface carbon

Table 3. Atmospheric parameters and metal abundances derived in this work for the slow rotators.

Star	$T_{\rm eff}$ [K]	$\log g$	y	$\log \epsilon$(C) 4060–4082 Å	$\log \epsilon$(N) 4995–5011 Å	$\log \epsilon$(O) 4060–4082 Å	$\log \epsilon$(O) 4691–4709 Å	$\log \epsilon$(O) Adopted	[N/C]	[N/O]
ξ^1 CMa	28 200	3.90	0.105	7.90	7.84	8.40	8.54	8.47	–0.06	–0.63
	28 500	*4.00*	*0.112*	*8.10*	*7.80*	*8.46*	*8.60*	*8.53*	*–0.30*	*–0.73*
τ Sco	31 200	4.30	0.083	8.18	7.90	8.27	8.50	8.39	–0.28	–0.49
	31 000	*4.40*	*0.083*	*8.40*	*7.90*	*8.24*	*8.62*	*8.43*	*–0.50*	*–0.53*
HD 57682	33 400	4.00	0.082	8.06	7.60	8.24	8.26	8.25	–0.46	–0.65
	33 300	*4.00*	*0.083*	*7.98*	*7.76*	*8.42*	*8.30*	*8.36*	*–0.22*	*–0.60*
10 Lac	34 300	4.20	0.077	8.22	7.42	8.34	8.28	8.31	–0.80	–0.89
	34 000	*4.20*	*0.072*	*8.20*	*7.80*	*8.48*	*8.24*	*8.36*	*–0.40*	*–0.56*
Typical errors	*1000*	*0.10*	*0.025*	*0.12*	*0.13*	...	...	*0.21*	*0.21*	*0.12*

Notes. For each star, the first row gives our nominal results, while the second row (in italics) provides the results obtained with spectra convolved with $v \sin i$ = 300 km s^{-1}. Note that solar [N/C] and [N/O] abundance ratios are –0.60 and –0.86, respectively (Asplund et al. 2009).

Table 4. Results obtained with DETAIL/SURFACE (columns D/S) and CMFGEN (columns CMF).

Star	$T_{\rm eff}$ [K] D/S	$T_{\rm eff}$ [K] CMF	$\log g$ D/S	$\log g$ CMF	y D/S	y CMF	$\log \epsilon$(C) D/S	$\log \epsilon$(C) CMF	$\log \epsilon$(N) D/S	$\log \epsilon$(N) CMF	$\log \epsilon$(O) D/S	$\log \epsilon$(O) CMF	[N/C] D/S	[N/C] CMF	[N/O] D/S	[N/O] CMF
HD 102415	32 900	33 000	4.10	3.86	0.158	0.124	<7.54	7.32	8.16	8.51	8.22	8.02	>0.62	1.19	–0.06	0.49
HD 149757 (FEROS)	31 800	32 300	3.90	3.87	0.124	0.096	8.06	8.19	7.92	7.54	8.45	8.27	–0.14	–0.65	–0.53	–0.73
HD 163892	32 000	32 400	3.80	3.80	0.082	0.071	8.24	8.15	7.34	7.44	8.38	8.40	–0.90	–0.71	–1.04	–0.96
Typical errors	*1000*	*1500*	*0.10*	*0.15*	*0.025*	*0.030*	*0.12*	*0.27*	*0.13*	*0.34*	*0.21*	*0.21*	*0.21*	*0.43*	*0.12*	*0.40*

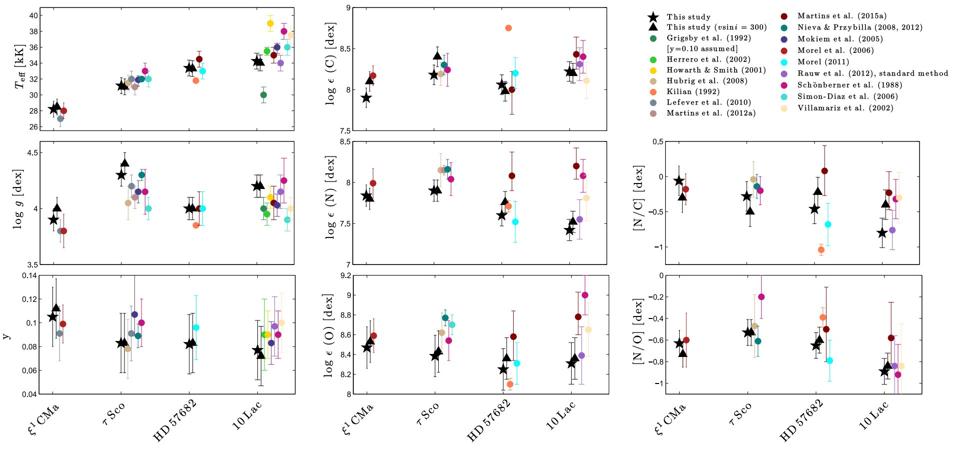

Fig. 7. Comparison between our results for the slow rotators and those in the literature. For the β Cephei ξ^1 CMa, the results of Lefever et al. (2010) are the values averaged along the pulsation cycle, while those of Morel et al. (2006) correspond to the highest temperature.

and nitrogen abundances should decrease and increase, respectively, whereas the surface abundance of oxygen should remain nearly constant as the star evolves. The loci in the [N/C] versus [N/O] diagram predicted by stellar evolution models reflect the efficiency of the mixing of the CNO material at equilibrium with the initial abundances (Przybilla et al. 2011; Maeder et al. 2014). Figure 8 shows very good consistency between our results and theoretical predictions for most of our targets. The consistent behaviour is preserved when comparing our results with predictions of models covering the full range of initial rotational velocities and masses spanned by our targets. Therefore, the abundances of fast rotators are in agreement with the predictions of CNO cycle nucleosynthesis.

6.5. Effect of stellar shape

Rotation affects the stellar shape, increasing the equatorial radius while decreasing the polar one. This distortion implies that the equipotentials are closer in polar regions than near the equator. The local effective gravity, which is a measure of the gradient between equipotentials, is thus stronger at the pole than at the equator. As the energy passing through an equipotential is

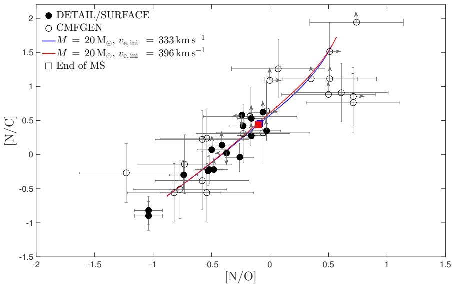

Fig. 8. [N/C] as a function of [N/O] for the sample stars, along with theoretical predictions from Geneva models (solid lines for $Z = 0.014$, Dr C. Georgy, private communication). Filled and open circles show values for the cool (studied with DETAIL/SURFACE) and hot (studied with CMFGEN) objects, respectively.

Table 5. Polar effective temperatures and radii of HD 149757 and HD 163892 as a function of the inclination of the rotation axis.

Star	i [°]	$T_{\mathrm{eff,p}}$ [K]	R_{p} [$R_\odot$]
HD 149757 (HARPS)	45	34 800	6.38
	60	33 800	6.91
	90	33 300	7.20
HD 163892 (FEROS)	45	33 300	7.89
	60	33 000	8.12
	90	32 800	8.24

Table 6. Derived abundances for the fast rotators HD 149757 and HD 163892 for different models (spherical case vs. flattened star seen under different inclinations).

Star	i [°]	Abundances C	N	O (1)	O (2)	O Av.
HD 149757 (HARPS)	Sph. case	7.98	7.92	8.50	8.36	8.43
	45	7.82	7.82	8.45	8.30	8.38
	60	8.06	7.91	8.50	8.35	8.43
	90	7.98	7.92	8.50	8.35	8.43
HD 163892 (FEROS)	Sph. case	8.24	7.34	8.44	8.32	8.38
	45	8.24	7.37	8.45	8.33	8.39
	60	8.24	7.37	8.45	8.33	8.39
	90	8.24	7.37	8.45	8.33	8.39

Notes. (1) and (2) refer to the spectral regions 4060–4082 and 4691–4709 Å, respectively. "Av." refers to the average of the oxygen abundances derived in the two regions.

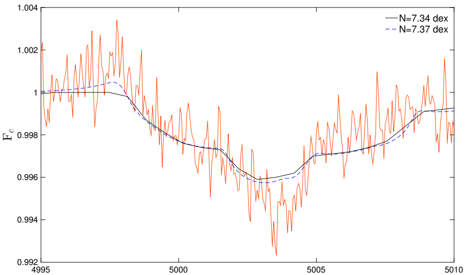

Fig. 9. Observed N II lines in HD 163892 (solid red line) and best-fitting spectra for the spherical case (solid black line) or a flattened star seen under an inclination of $i = 90°$ (dashed blue line).

conserved in the absence of local energy production or destruction, polar regions are hotter than equatorial regions and more flux is emitted from the pole compared to the equator. This gravity darkening effect implies that the lines of a fast rotator can be created from different regions around the star; thus, He II lines are preferentially formed near the poles, while He I lines originate from a larger area of the stellar surface.

We used the Code of Massive Binary Spectral Computation (CoMBISpeC; Palate & Rauw 2012; Palate et al. 2013) to examine the effect of gravity darkening and stellar rotational flattening on the determination of stellar parameters. To this aim, two stars representing the extreme $v \sin i$ values encountered in our sample (HD 149757, $v \sin i \sim 378$ km s^{-1} and HD 163892, $v \sin i = 205$ km s^{-1}) were considered.

We first determine the polar effective temperatures, $T_{\mathrm{eff,p}}$, and the polar radii, R_{p}, of the stars depending on the inclination of the rotation axis, i, in such a way that T_{eff} and $\log g$ averaged over the visible hemisphere are equal to the values found with the method described in Sect. 4.3.1. This was carried out by fixing some parameters: the stellar mass was chosen to be 20 $M_\odot$ since HD 149757 and HD 163892 are close to the corresponding evolutionary tracks in the $\log g_{\mathrm{C}}$–$\log T_{\mathrm{eff}}$ diagram (Paper II), the gravity darkening exponent was chosen to be 0.1875, as suggested by interferometric observations of rapidly rotating B stars (Kraus et al. 2012), and finally the projected rotational velocities were fixed to the values that we derived (Table F.2). In these calculations, the $v \sin i$ is held fixed. As a result, the true rotation rate varies as a function of i (star intrinsically more rapidly rotating as i decreases). Table 5 presents the resulting parameters. Once these parameters are known, we then explore how spectra of those flattened stars change with the CNO abundances. As both He I and He II line-formation zones are always seen, the helium abundance is correctly determined and we thus do not need to explore changes in y. Table 6 illustrates how the resulting abundances vary for the various cases considered. For HD 163892, we observe that different combinations of inclinations and rotation rates yield very similar best-fitting abundances (Fig. 9). Furthermore, the results are similar to those found with spherically symmetric models, yielding strong support to our methodology. The other star, HD 149757, is an apparently faster rotator. As expected, this translates into larger differences in the emerging spectrum. Figure 10 shows an example of the variations affecting the C and O line profiles for a fixed abundance set. In fact, as inclination increases, cooler surface regions come into view and the true rotational velocity decreases (as $v \sin i$ is kept constant), modifying the strength of C III, N II, and O II lines, which are our abundance diagnostics (see Sect. 4.3.1). For low inclinations, it appears that all CNO abundances of HD 149757 are lower than those derived in the spherical case, while these abundances increase with inclination, reaching values similar to the spherical case when $i = 90°$; it should be noted that the carbon abundance is, however, difficult to pinpoint precisely. Whatever the inclination, however, the differences remain well within the error bars and we therefore conclude that the spherically symmetric models used in this work are suitable to study our sample stars.

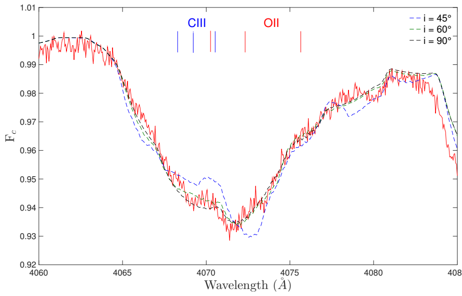

Fig. 10. Example of the influence of the inclination and the related change of the rotational velocity on the strength of C III and O II lines for very fast rotators. The observed HARPS spectrum of HD 149757 is shown as a solid red line, while model spectra for different inclinations are shown as dashed blue (i = 45°), green (i = 60°), and black (i = 90°) lines. The abundances of carbon and oxygen are set to 7.98 and 8.35 dex, respectively.

6.6. Impact of binarity

A few of our targets are firmly identified as SB1 systems. To examine the impact of the contamination of the spectrum by the secondary, we considered the system with by far the largest mass function hence the largest potential contamination (HD 52533; see Table C.1). Assuming an edge-on orbit and a primary mass of ~20 $M_\odot$ (Paper II), we infer that the companion is a B1-B2 star. We repeated the analysis described in Sect. 4.3.1 assuming for simplicity that the companion is on the zero age main sequence (ZAMS) and rotates at the same speed as the primary. We further adopted the following parameters: $T_{\rm eff}$ = 28 000 K, log g = 4.3, ξ = 10 km s^{-1} and abundances typical of nearby B-type dwarfs (Table 6 of Morel et al. 2008). Grids of composite, synthetic spectra similar to those discussed in Sect. 4.3.1 were computed assuming at each mesh point an appropriate flux ratio between the two components (typically ~0.1–0.2 for the default parameters of the primary).

As can be seen in Table 7, taking the cooler secondary in HD 52533 into account would result in modest differences, close to or below the uncertainties. In any event, this more sophisticated approach strengthens the case for a lack of a He and N excess in this star. Furthermore, as the companions are less massive and much fainter for the other SB1 systems (Table C.1), even more negligible differences are expected for the parameters of these binaries.

Table 7. Impact on parameters and abundances when taking the secondary in HD 52533 into account.

	Difference	Typical error
$\Delta T_{\rm eff}$ [K]	+313	1000
$\Delta\log g$	–0.10	0.10
Δy	+0.007	0.025
$\Delta\log\epsilon$(C)	+0.08	0.12
$\Delta\log\epsilon$(N)	–0.24	0.13
$\Delta\log\epsilon$(O)	–0.13	0.21
Δ[N/C]	–0.32	0.21
Δ[N/O]	–0.11	0.12

Notes. The differences are values considering the companion minus values not considering it (from Table F.2).

7. Summary

The importance of rotational mixing was recently questioned after the discovery of a population of fast rotators with no or little evidence for a nitrogen enrichment.

We decided to revisit this issue by performing an in-depth study of the physical properties of a large sample of massive, fast rotators. Their properties were derived in several steps. First, the RVs were estimated with a cross-correlation technique, while a Fourier transform method yielded the projected rotational velocity. Then, a comparison with synthetic spectra, calculated either with DETAIL/SURFACE for the 17 late-type (B0.5-O9 V-III) stars or with CMFGEN for the 23 objects with earlier types, was performed in a homogeneous way within the two subgroups. This provided the effective temperatures, surface gravities, and the He and CNO abundances for each object.

We performed several checks to validate our method and, hence, its results. First, we studied a sample of well-known slow rotators and showed that our results are in good agreement with previous studies. Furthermore, after convolving the spectra of these stars to mimic a broadening typical of our sample stars, we again obtained similar results, demonstrating the limited impact of broadening on our derivation of physical parameters. Second, the synthetic spectra used in this work correspond to spherically symmetric stars, while fast rotators are flattened objects. We therefore compared our results with those obtained with CoMBISpeC, which takes the stellar deformation into account. Again, results were similar, within errors, further validating our method. Finally, a few targets could be analysed by both CMFGEN and DETAIL/SURFACE models, again showing a good agreement. Further confidence in our results comes from the fact that the [N/C] and [N/O] abundance ratios correlate along the theoretical locus expected for the CNO cycle.

This paper presents the stellar parameters and CNO abundances of 40 fast rotators, along with their multiplicity status, including two new and three revised orbital solutions (see Appendix C). The second paper of this series will compare these results to predictions of evolutionary models of single stars or of interacting binaries with the aim to assess the impact of rotational mixing in hot stars.

Acknowledgements. We are very grateful to the referee for providing useful comments. We thank John Pritchard from the User Support Department of the European Southern Observatory and the FIES team for their precious help in the reduction of data. We also thank Dr. Keith Butler, Dr. John Hillier, Dr. Hugues Sana, and Dr. Matthieu Palate for making their codes available to us. We acknowledge the support from the Universities of Hamburg, Guanajuato, and Liège for the TIGRE telescope. We thank the team that proposed, observed, and reduced the MIKE data: Marcelo Borges, Gustavo Bragança, Thomas Bensby, Katia Cunha, Katy Garmany, and John Glaspey. To get SOPHIE observations, the authors received funding from the European Community's Seventh Framework Programme (FP7/2013–2016) under grant agreement number 312430 (OPTICON). We thank Dr. Sergi Blanco-Cuaresma and Dr. Maroussia Roelens for obtaining CORALIE observations. CC also acknowledges funding from "Patrimoine de l'ULg" for his stay at Rio de Janeiro and people at the Observatório Nacional for their kind hospitality during his stay in Rio. This research has made use of the WEBDA database, operated at the Department of Theoretical Physics and Astrophysics of the Masaryk University. Computational resources have been provided by the Consortium des Équipements de Calcul Intensif (CÉCI), funded by the Fonds de la Recherche Scientifique (F.R.S.-FNRS) under Grant No. 2.5020.11. The Liège team also acknowledges support from the Fonds National de la Recherche Scientifique (Belgium), the Communauté Française de Belgique, the PRODEX XMM and GAIA-DPAC contracts (Belspo), and an ARC grant for concerted research actions financed by the French community of Belgium (Wallonia-Brussels Federation). ADS and CDS were used for preparing this document.

References

Abt, H. A., Levy, S. G., & Gandet, T. L. 1972, AJ, 77, 138
Aldoretta, E. J., Caballero-Nieves, S. M., Gies, D. R., et al. 2015, AJ, 149, 26
Alduseva, V. I., Aslanov, A. A., Kolotilov, E. A., & Cherepashchuk, A. M. 1982, Soviet Astron. Lett., 8, 717
Asplund, M., Grevesse, N., Sauval, A. J., & Scott, P. 2009, ARA&A, 47, 481
Bates, B., Wood, K. D., Catney, M. G., & Gilheany, S. 1992, MNRAS, 254, 221
Baranne, A., Queloz, D., Mayor, M., et al. 1996, A&AS, 119, 373
Barannikov, A. A. 1993, Astron. Lett., 19, 420
Barbá, R. H., Gamen, R., Arias, J. I., et al. 2010, Rev. Mex. Astron. Astrofis. Conf. Ser., 38, 30
Bastiaansen, P. A. 1992, A&AS, 93, 449
Bekenstein, J. D., & Bowers, R. L. 1974, ApJ, 190, 653
Blaauw, A. 1961, Bull. Astron. Inst. Netherlands, 15, 265
Bohannan, B., & Garmany, C. D. 1978, ApJ, 223, 908
Bouret, J.-C., Hillier, D. J., Lanz, T., & Fullerton, A. W. 2012, A&A, 544, A67
Bouret, J.-C., Lanz, T., Martins, F., et al. 2013, A&A, 555, A1
Boyajian, T. S., Beaulieu, T. D., Gies, D. R., et al. 2005, ApJ, 621, 978
Bragança, G. A., Daflon, S., Cunha, K., et al. 2012, AJ, 144, 130
Brott, I., Evans, C. J., Hunter, I., et al. 2011, A&A, 530, A116
Butler, K., & Giddings, J. R. 1985, Newsletter of Analysis of Astronomical Spectra, No. 9 (Univ. London)
Carrasco, L., & Creze, M. 1978, A&A, 65, 279
Cazorla, C., Nazé, Y., Morel, T., et al. 2017, A&A, submitted (Paper II)
Cherepashchuk, A. M., & Aslanov, A. A. 1984, Ap&SS, 102, 97
Cincotta, P. M. 1999, MNRAS, 307, 941
Cincotta, P. M., Helmi, A., Mendez, M., Nunez, J. A., & Vucetich, H. 1999, MNRAS, 302, 582
Conti, P. S., Leep, E. M., & Lorre, J. J. 1977, ApJ, 214, 759
Cuypers, J. 1987, A&AS, 69, 445
De Becker, M., & Rauw, G. 2004, A&A, 427, 995
De Becker, M., Linder, N., & Rauw, G. 2008, Information Bulletin on Variable Stars, 5841, 1
de Mink, S. E., Cantiello, M., Langer, N., et al. 2009, A&A, 497, 243
de Mink, S. E., Langer, N., Izzard, R. G., Sana, H., & de Koter, A. 2013, ApJ, 764, 166
Dervişoğlu, A., Tout, C. A., & Ibanoğlu, C. 2010, MNRAS, 406, 1071
de Wit, W. J., Testi, L., Palla, F., & Zinnecker, H. 2005, A&A, 437, 247
Dufton, P. L., Dunstall, P. R., Evans, C. J., et al. 2011, ApJ, 743, L22
Eggleton, P. P., & Tokovinin, A. A. 2008, MNRAS, 389, 869
Evans, C., Hunter, I., Smartt, S., et al. 2008, The Messenger, 131, 25
Feast, M. W., & Thackeray, A. D. 1963, MmRAS, 68, 173
Feast, M. W., Thackeray, A. D., & Wesselink, A. J. 1957, MmRAS, 68, 1
Firnstein, M., & Przybilla, N. 2012, A&A, 543, A80
Fitzgerald, M. P., & Moffat, A. F. J. 1975, A&AS, 20, 289
Frémat, Y., Zorec, J., Hubert, A.-M., & Floquet, M. 2005, A&A, 440, 305
Frost, E. B., Barrett, S. B., & Struve, O. 1926, ApJ, 64, 1
Gaia Collaboration (Prusti, T., et al.) 2016, A&A, 595, A1
Garmany, C. D., Conti, P. S., & Massey, P. 1980, ApJ, 242, 1063
Garmany, C. D., Glaspey, J. W., Bragança, G. A., et al. 2015, AJ, 150, 41
Garrison, R. F., Hiltner, W. A., & Schild, R. E. 1977, ApJS, 35, 111
Garrison, R. F., Schild, R. E., & Hiltner, W. A. 1983, ApJS, 52, 1
Gies, D. R., & Bolton, C. T. 1986, ApJS, 61, 419
Giddings, J. R. 1981, Ph.D. Thesis, University of London, UK
Gillet, D., Burnage, R., Kohler, D., et al. 1994, A&AS, 108, 181
Gosset, E., Royer, P., Rauw, G., Manfroid, J., & Vreux, J.-M. 2001, MNRAS, 327, 435
Graham, M. J., Drake, A. J., Djorgovski, S. G., Mahabal, A. A., & Donalek, C. 2013, MNRAS, 434, 2629
Grigsby, J. A., Morrison, N. D., & Anderson, L. S. 1992, ApJS, 78, 205
Grin, N. J., Ramirez-Agudelo, O. H., de Koter, A., et al. 2017, A&A, 600, A82
Gray, D. F. 2005, The Observation and Analysis of Stellar Photospheres, 3rd edn. (Cambridge University Press)
Heck, A., Manfroid, J., & Mersch, G. 1985, A&AS, 59, 63
Herrero, A., Kudritzki, R. P., Vilchez, J. M., et al. 1992, A&A, 261, 209
Herrero, A., Puls, J., & Villamariz, M. R. 2000, A&A, 354, 193
Herrero, A., Puls, J., & Najarro, F. 2002, A&A, 396, 949
Hillier, D. J., & Miller, D. L. 1998, ApJ, 496, 407
Hillwig, T. C., Gies, D. R., Bagnuolo, W. G., Jr., et al. 2006, ApJ, 639, 1069
Hiltner, W. A., Garrison, R. F., & Schild, R. E. 1969, ApJ, 157, 313
Hoogerwerf, R., de Bruijne, J. H. J., & de Zeeuw, P. T. 2001, A&A, 365, 49
Howarth, I. D., & Smith, K. C. 2001, MNRAS, 327, 353
Howarth, I. D., Siebert, K. W., Hussain, G. A. J., & Prinja, R. K. 1997, MNRAS, 284, 265
Huang, W., & Gies, D. R. 2008, ApJ, 683, 1045
Hubrig, S., Briquet, M., Morel, T., et al. 2008, A&A, 488, 287
Humphreys, R. M. 1973, A&AS, 9, 85
Humphreys, R. M. 1978, ApJS, 38, 309
Hunter, I., Dufton, P. L., Smartt, S. J., et al. 2007, A&A, 466, 277
Hunter, I., Brott, I., Langer, N., et al. 2009, A&A, 496, 841
Hut, P. 1981, A&A, 99, 126
Jerzykiewicz, M. 1993, A&AS, 97, 421
Jurkevich, I. 1971, Ap&SS, 13, 154
Kaper, L., Henrichs, H. F., Nichols, J. S., et al. 1996, A&AS, 116, 257
Kambe, E., Hirata, R., Ando, H., et al. 1997, ApJ, 481, 406
Kendall, T. R., Dufton, P. L., & Lennon, D. J. 1996, A&A, 310, 564
Kilian, J. 1992, A&A, 262, 171
Kilkenny, D., & Hill, P. W. 1975, MNRAS, 172, 649
Kirsten, F., Vlemmings, W., Campbell, R. M., Kramer, M., & Chatterjee, S. 2015, A&A, 577, A111
Koen, C., & Eyer, L. 2002, MNRAS, 331, 45
Kraus, S., Monnier, J. D., Che, X., et al. 2012, ApJ, 744, 19
Kurtz, M. J., & Mink, D. J. 1998, PASP, 110, 934
Lafler, J., & Kinman, T. D. 1965, ApJS, 11, 216
Langer, N., Cantiello, M., Yoon, S.-C., et al. 2008, Massive Stars as Cosmic Engines, 250, 167
Lanz, T., & Hubeny, I. 2003, ApJS, 146, 417
Langer, N., Wellstein, S., & Petrovic, J. 2003, A Massive Star Odyssey: From Main Sequence to Supernova, 212, 275
Lanz, T., & Hubeny, I. 2007, ApJS, 169, 83
Lefever, K., Puls, J., Morel, T., et al. 2010, A&A, 515, A74
Lennon, D. J., Dufton, P. L., Keenan, F. P., & Holmgren, D. E. 1991, A&A, 246, 175
Lesh, J. R. 1968, ApJS, 17, 371
Lozinskaya, T. A., & Lyuty, V. M. 1981, Astronomicheskij Tsirkulyar, 1196, 1
Lynds, C. R. 1959, ApJ, 130, 577
Lyubimkov, L. S., Rostopchin, S. I., & Lambert, D. L. 2004, MNRAS, 351, 745
Maeder, A. 1995, IAU Colloq. 155: Astrophysical Applications of Stellar Pulsation, 83, 1
Maeder, A., & Meynet, G. 1996, A&A, 313, 140
Maeder, A., & Meynet, G. 2015, IAU Symp., 307, 9
Maeder, A., Meynet, G., Ekström, S., & Georgy, C. 2009, Commun. Asteroseismol., 158, 72
Maeder, A., Przybilla, N., Nieva, M.-F., et al. 2014, A&A, 565, A39
Mahy, L., Nazé, Y., Rauw, G., et al. 2009, A&A, 502, 937
Mahy, L., Rauw, G., De Becker, M., Eenens, P., & Flores, C. A. 2013, A&A, 550, A27
Mahy, L., Rauw, G., De Becker, M., Eenens, P., & Flores, C. A. 2015, A&A, 577, A23
Maíz Apellániz, J., Alfaro, E. J., & Sota, A. 2008, ArXiv e-prints [`arXiv:0804.2553`]
Maíz Apellániz, J., Sota, A., Walborn, N. R., et al. 2011, Highlights of Spanish Astrophysics VI, 467
Marcolino, W. L. F., Bouret, J.-C., Martins, F., et al. 2009, A&A, 498, 837
Martins, F., Schaerer, D., & Hillier, D. J. 2005, A&A, 436, 1049
Martins, F., Escolano, C., Wade, G. A., et al. 2012a, A&A, 538, A29
Martins, F., Mahy, L., Hillier, D. J., & Rauw, G. 2012b, A&A, 538, A39
Martins, F., Hervé, A., Bouret, J.-C., et al. 2015a, A&A, 575, A34
Martins, F., Simón-Díaz, S., Palacios, A., et al. 2015b, A&A, 578, A109
Mason, B. D., Gies, D. R., Hartkopf, W. I., et al. 1998, AJ, 115, 821
Mason, B. D., Hartkopf, W. I., Wycoff, G. L., et al. 2004, AJ, 128, 3012
Mason, B. D., Hartkopf, W. I., Gies, D. R., Henry, T. J., & Helsel, J. W. 2009, AJ, 137, 3358
Mason, B. D., Hartkopf, W. I., & Wycoff, G. L. 2011, AJ, 141, 157
Mayer, P., Chochol, D., Hanna, M. A.-M. ., & Wolf, M. 1994, Contributions of the Astronomical Observatory Skalnate Pleso, 24, 65
Mayer, P., Hanna, M. A., Wolf, M., & Chochol, D. 1998, Ap&SS, 262, 163
Mayer, P., Drechsel, H., & Irrgang, A. 2014, A&A, 565, A86
McSwain, M. V., Boyajian, T. S., Grundstrom, E. D., & Gies, D. R. 2007, ApJ, 655, 473
McSwain, M. V., De Becker, M., Roberts, M. S. E., et al. 2010, AJ, 139, 857
Meurs, E. J. A., Fennell, G., & Norci, L. 2005, ApJ, 624, 307
Meynet, G., & Maeder, A. 2000, A&A, 361, 101
Meynet, G., Eggenberger, P., & Maeder, A. 2011, A&A, 525, L11
Mokiem, M. R., de Koter, A., Puls, J., et al. 2005, A&A, 441, 711
Morel, T. 2011, Bulletin de la Societe Royale des Sciences de Liege, 80, 405
Morel, T., Butler, K., Aerts, C., Neiner, C., & Briquet, M. 2006, A&A, 457, 651
Morel, T., Hubrig, S., & Briquet, M. 2008, A&A, 481, 453
Morgan, W. W., Code, A. D., & Whitford, A. E. 1955, ApJS, 2, 41
Morton, D. C. 1975, ApJ, 197, 85
Motch, C., Guillout, P., Haberl, F., et al. 1998, A&AS, 132, 341
Muijres, L. E., Vink, J. S., de Koter, A., Müller, P. E., & Langer, N. 2012, A&A, 537, A37
Murphy, R. E. 1969, AJ, 74, 1082

Nieva, M. F., & Przybilla, N. 2007, A&A, 467, 295
Nieva, M. F., & Przybilla, N. 2008, A&A, 481, 199
Nieva, M.-F., & Przybilla, N. 2012, A&A, 539, A143
Nieva, M.-F., & Simón-Díaz, S. 2011, A&A, 532, A2
Packet, W. 1981, A&A, 102, 17
Palate, M., & Rauw, G. 2012, A&A, 537, A119
Palate, M., Rauw, G., Koenigsberger, G., & Moreno, E. 2013, A&A, 552, A39
Penny, L. R. 1996, ApJ, 463, 737
Peri, C. S., Benaglia, P., Brookes, D. P., Stevens, I. R., & Isequilla, N. L. 2012, A&A, 538, A108
Petrovic, J., Langer, N., Yoon, S.-C., & Heger, A. 2005a, A&A, 435, 247
Petrovic, J., Langer, N., & van der Hucht, K. A. 2005b, A&A, 435, 1013
Philp, C. J., Evans, C. R., Leonard, P. J. T., & Frail, D. A. 1996, AJ, 111, 1220
Piskunov, N. E., & Valenti, J. A. 2002, A&A, 385, 1095
Plaskett, J. S., & Pearce, J. A. 1931, Publications of the Dominion Astrophysical Observatory Victoria, 5, 1
Podsiadlowski, P., Joss, P. C., & Hsu, J. J. L. 1992, ApJ, 391, 246
Pols, O. R., Cote, J., Waters, L. B. F. M., & Heise, J. 1991, A&A, 241, 419
Potter, A. T., Chitre, S. M., & Tout, C. A. 2012, MNRAS, 424, 2358
Prinja, R. K., Barlow, M. J., & Howarth, I. D. 1990, ApJ, 361, 607
Proffitt, C. R., & Quigley, M. F. 2001, ApJ, 548, 429
Przybilla, N., Nieva, M.-F., & Butler, K. 2011, J. Phys. Conf. Ser., 328, 012015
Puls, J., Kudritzki, R.-P., Herrero, A., et al. 1996, A&A, 305, 171
Raucq, F., Rauw, G., Gosset, E., et al. 2016, A&A, 588, A10
Rauw, G., & De Becker, M. 2004, A&A, 421, 693
Rauw, G., De Becker, M., & Vreux, J.-M. 2003, A&A, 399, 287
Rauw, G., Morel, T., & Palate, M. 2012, A&A, 546, A77
Renson, P. 1978, A&A, 63, 125
Repolust, T., Puls, J., & Herrero, A. 2004, A&A, 415, 349
Repolust, T., Puls, J., Hanson, M. M., Kudritzki, R.-P., & Mokiem, M. R. 2005, A&A, 440, 261
Rivero González, J. G., Puls, J., Najarro, F., & Brott, I. 2012a, A&A, 537, A79
Rivero González, J. G., Puls, J., Massey, P., & Najarro, F. 2012b, A&A, 543, A95
Rivinius, T., Carciofi, A. C., & Martayan, C. 2013, A&ARv, 21, 69
Sana, H. 2013, Astrophysics Source Code Library [record ascl: 1309.003]
Sana, H., de Koter, A., de Mink, S. E., et al. 2013, A&A, 550, A107
Sana, H., Le Bouquin, J.-B., Lacour, S., et al. 2014, ApJS, 215, 15
Schmitt, J. H. M. M., Schröder, K.-P., Rauw, G., et al. 2014, Astron. Nachr., 335, 787
Schönberner, D., Herrero, A., Becker, S., et al. 1988, A&A, 197, 209
Schwarzenberg-Czerny, A. 1989, MNRAS, 241, 153
Simón-Díaz, S., & Herrero, A. 2007, A&A, 468, 1063
Simón-Díaz, S., & Herrero, A. 2014, A&A, 562, A135
Simón-Díaz, S., Herrero, A., Esteban, C., & Najarro, F. 2006, A&A, 448, 351
Song, H. F., Maeder, A., Meynet, G., et al. 2013, A&A, 556, A100
Sota, A., Maíz Apellániz, J., Walborn, N. R., et al. 2011, ApJS, 193, 24
Sota, A., Maíz Apellániz, J., Morrell, N. I., et al. 2014, ApJS, 211, 10
Stankov, A., & Handler, G. 2005, ApJS, 158, 193
Stellingwerf, R. F. 1978, ApJ, 224, 953
Stickland, D. J., & Lloyd, C. 2001, The Observatory, 121, 1
Straižys, V., & Laugalys, V. 2007, Baltic Astronomy, 16, 167
Tetzlaff, N., Neuhäuser, R., Hohle, M. M., & Maciejewski, G. 2010, MNRAS, 402, 2369
Tetzlaff, N., Neuhäuser, R., & Hohle, M. M. 2011, MNRAS, 410, 190
Tokovinin, A., Mason, B. D., & Hartkopf, W. I. 2010, AJ, 139, 743
Turner, N. H., ten Brummelaar, T. A., Roberts, L. C., et al. 2008, AJ, 136, 554
Tylenda, R., Hajduk, M., Kamiński, T., et al. 2011, A&A, 528, A114
Underhill, A. B., & Gilroy, K. K. 1990, ApJ, 364, 626
van Buren, D., & McCray, R. 1988, ApJ, 329, L93
van Leeuwen, F., Evans, D. W., Grenon, M., et al. 1997, A&A, 323, L61
van Rensbergen, W., Vanbeveren, D., & De Loore, C. 1996, A&A, 305, 825
Villamariz, M. R., & Herrero, A. 2005, A&A, 442, 263
Villamariz, M. R., Herrero, A., Becker, S. R., & Butler, K. 2002, A&A, 388, 940
Walborn, N. R. 1973, AJ, 78, 1067
Walborn, N. R., Maíz Apellániz, J., Sota, A., et al. 2011, AJ, 142, 150
Whittaker, E. T., & Robinson, G. 1944, The calculus of observations; a treatise on numerical mathematics, eds. E. T. Whittaker, & G. Robinson (London: Blackie)
Williams, S. J., Gies, D. R., Hillwig, T. C., McSwain, M. V., & Huang, W. 2011, AJ, 142, 146
Zahn, J.-P. 1975, A&A, 41, 329
Zechmeister, M., & Kürster, M. 2009, A&A, 496, 577

Appendix A: Journal of observations and radial velocities of our targets

Table A.1 provides the journal of observations and RVs of our sample stars. The RVs taken from the literature are not included.

Table A.1. Journal of observations and individual RV measurements.

Name	Instrument	Mid-exp. (HJD –2 450 000)	RV [km s^{-1}]
Slow rotators			
HD 214680 (10 Lac)	**HEROS**	6561.713	–7.3 ± 0.5
HD 46328 (ξ^1 CMa)	**HEROS**	7017.855	21.9 ± 0.5
HD 57682	**HEROS**	6565.951	28.3 ± 0.3
		6644.722	24.9 ± 0.3
		6644.736	24.9 ± 0.4
		6667.769	27.7 ± 0.4
		6667.783	28.0 ± 0.4
HD 149438 (τ Sco)	**HEROS**	6685.022	3.0 ± 0.7
		6685.022	3.3 ± 0.7
Fast rotators			
ALS 864	**MIKE**	4468.750	94.3 ± 6.9
ALS 18675	**MIKE**	4466.681	64.6 ± 5.1
BD +60°594	ELODIE	3682.540	–50.9 ± 4.7
	SOPHIE	7267.549	–14.6 ± 8.9
BD +34°1058	**SOPHIE**	7267.617	41.2 ± 11.7
HD 13268	ELODIE	2238.280	–87.9 ± 7.6
		3328.321	–86.0 ± 7.3
	AURELIE	3286.512	–110.3 ± 7.1
		3289.595	–112.0 ± 6.9
		3290.490	–108.7 ± 6.5
		3294.634	–110.0 ± 6.6
		3295.482	–108.2 ± 7.0
		3295.672	–107.4 ± 7.0
		3296.597	–104.6 ± 6.7
		3648.620	–114.7 ± 6.7
		3652.586	–112.7 ± 7.0
		3654.456	–107.8 ± 7.0
		3982.621	–117.4 ± 6.6
		3984.575	–121.3 ± 7.4
		4034.408	–104.6 ± 6.3
		4034.466	–103.5 ± 7.0
		4034.524	–105.3 ± 6.6
		4034.585	–110.1 ± 6.4
		4035.386	–113.2 ± 6.4
		4396.369	–99.5 ± 6.7
		4396.392	–99.0 ± 6.7
		4396.414	–98.5 ± 6.8
		4396.462	–104.3 ± 6.4
		4396.484	–102.8 ± 6.8
		4396.505	–104.3 ± 6.7
		4396.551	–103.7 ± 6.5
		4396.574	–105.2 ± 6.6
		4396.595	–106.6 ± 6.2
		4407.364	–102.7 ± 6.7
		4407.381	–100.8 ± 6.8
		4407.399	–100.0 ± 6.5
		4407.418	–100.1 ± 6.9
		4407.436	–98.9 ± 6.7
		4407.454	–97.3 ± 7.2
		4407.473	–100.7 ± 6.6
		4407.490	–98.8 ± 6.5
		4407.553	–97.8 ± 6.5
		4407.570	–98.7 ± 6.8
		4407.691	–98.6 ± 6.4
		4421.613	–96.2 ± 6.9
		4421.350	–94.0 ± 6.7
		4421.370	–95.1 ± 6.5
		4421.393	–94.3 ± 6.9
		4421.433	–96.2 ± 6.9
		4421.454	–94.6 ± 6.8
		4421.475	–91.9 ± 6.7

Notes. Heliocentric corrections were applied to both Julian dates and RVs. Spectra indicated in boldface were used to determine the stellar properties (multiple exposures were averaged).

Table A.1. continued.

Name	Instrument	Mid-exp. (HJD –2 450 000)	RV [km s^{-1}]
HD 13268	AURELIE	4421.499	–90.1 ± 6.6
		4421.549	–94.3 ± 6.4
		4421.573	–95.1 ± 6.3
		4421.598	–91.0 ± 6.8
		4422.356	–94.1 ± 6.9
		4422.373	–100.0 ± 7.1
		4422.388	–96.7 ± 6.8
		4422.402	–95.5 ± 6.5
		4422.439	–99.2 ± 6.7
		4422.454	–96.5 ± 6.5
		4422.469	–97.0 ± 6.8
		4422.484	–97.4 ± 6.8
		4422.516	–93.5 ± 6.4
		4422.533	–92.3 ± 6.9
		4422.557	–95.6 ± 6.8
		4422.570	–94.9 ± 6.5
		4422.594	–92.6 ± 6.5
		4422.608	–92.2 ± 6.2
	FIES	5574.347	–94.2 ± 8.2
		6321.398	–94.1 ± 8.3
		6322.390	–90.9 ± 8.0
HD 14434	AURELIE	2916.489	0.3 ± 13.7
		2918.511	–6.2 ± 12.7
		2919.538	–21.4 ± 13.3
		2925.512	–12.2 ± 13.5
		2925.570	–21.1 ± 15.0
		2922.539	–29.6 ± 12.3
	ESPaDOnS	**6702.713**	–22.4 ± 13.8
		6702.733	–17.8 ± 12.7
		6702.754	–18.1 ± 12.7
		6702.775	–21.3 ± 12.2
		6708.720	–27.6 ± 13.1
		6708.730	–23.3 ± 12.9
		6708.761	–23.3 ± 13.6
		6708.782	–24.4 ± 12.9
	SOPHIE	7267.535	–8.6 ± 12.5
HD 14442	AURELIE	**1375.584**	–52.1 ± 12.6
		1376.578	–55.7 ± 12.2
		1377.574	–52.2 ± 12.0
		1378.576	–48.2 ± 18.9
		1379.597	–38.6 ± 12.8
		1396.628	–40.1 ± 11.3
		1397.627	–61.6 ± 12.4
		1399.567	–47.2 ± 13.6
		1402.568	–61.4 ± 13.6
		1405.625	–59.3 ± 12.9
		1408.619	–40.3 ± 11.8
		1409.623	–48.5 ± 13.6
		1810.614	–53.0 ± 12.0
		1811.593	–42.9 ± 12.4
		1812.613	–59.8 ± 11.8
		1813.624	–47.1 ± 15.3
		1814.615	–57.3 ± 11.3
		1815.620	–64.1 ± 12.3
		1819.634	–47.9 ± 13.0
		1820.618	–59.0 ± 10.5
		1821.581	–49.7 ± 12.6
HD 14442	AURELIE	2163.526	–73.4 ± 14.0
		2163.550	–72.2 ± 15.6
		2164.550	–41.9 ± 15.1
		2164.572	–41.4 ± 15.1
		2165.532	–72.3 ± 13.4
		2165.555	–71.3 ± 13.4
		2167.501	–40.2 ± 13.9
		2167.526	–44.4 ± 13.2
		2169.502	–57.3 ± 17.2
		2169.535	–50.3 ± 18.3
		2170.533	–60.9 ± 12.3
		2170.555	–60.4 ± 12.4
		2916.525	–59.8 ± 15.6
		2918.470	–53.3 ± 13.8
		2919.503	–36.6 ± 14.1
		2923.474	–75.6 ± 14.0
		2922.506	–59.8 ± 15.9
HD 15137	ELODIE	3325.451	–27.7 ± 4.5
	FIES	5148.663	–40.6 ± 4.7
		5814.603	–18.6 ± 3.7
		6287.430	–34.9 ± 4.1
HD 15642	**FIES**	5812.628	–12.9 ± 10.3
		5815.652	–13.4 ± 9.5
		6287.580	–11.4 ± 8.4
HD 28446A (1 Cam A)	**HEROS**	6560.966	10.1 ± 8.2
		6568.944	10.3 ± 7.5
		6644.622	7.3 ± 9.7
		6662.687	8.3 ± 5.6
		6672.588	4.4 ± 5.3
		6673.652	8.7 ± 5.9
		6674.683	11.1 ± 10.6
		6676.656	5.6 ± 10.5
		6677.802	11.5 ± 7.9
		6684.618	7.6 ± 10.4
		6693.633	5.7 ± 7.8
		6700.676	11.1 ± 4.7
		6707.570	12.7 ± 4.8
		6717.614	9.8 ± 3.5

Table A.1. continued.

Name	Instrument	Mid-exp. (HJD –2 450 000)	RV [km s^{-1}]
HD 41161	ELODIE	3330.687	–18.4 ± 6.1
	FIES	4779.634	–23.3 ± 5.3
		5577.688	–20.3 ± 5.6
		5815.715	–16.4 ± 5.5
	HEROS	6563.745	–22.0 ± 4.8
		6574.779	–23.0 ± 5.9
		6579.781	–27.1 ± 7.1
		6580.758	–22.6 ± 6.5
		6581.784	–29.0 ± 7.0
		6592.701	–22.3 ± 6.7
		6606.653	–26.5 ± 6.6
		6640.593	–32.0 ± 8.0
		6642.548	–33.3 ± 11.1
		6643.574	–31.8 ± 11.5
		6644.533	–24.5 ± 4.9
		6646.577	–30.0 ± 9.4
		6662.521	–26.6 ± 6.6
		6663.401	–25.6 ± 8.2
		6663.496	–28.8 ± 7.3
		6675.535	–26.3 ± 6.3
		6676.409	–26.7 ± 6.6
		6688.408	–29.4 ± 10.5
		6688.413	–20.6 ± 6.4
		6690.452	–20.9 ± 5.3
		6691.453	–26.3 ± 9.1
		6692.462	–30.4 ± 6.9
HD 41997	**ELODIE**	3683.515	–19.2 ± 6.9
HD 46056	ESPRESSO	4545.673	31.1 ± 5.4
	ESPaDOnS	**4809.072**	28.7 ± 5.3
		4809.083	28.7 ± 5.5
		4809.094	27.4 ± 5.6
		4809.103	28.8 ± 5.4
		4809.116	29.3 ± 5.6
		4809.126	30.0 ± 5.4
		4809.136	29.6 ± 5.7
		4809.148	29.6 ± 5.7
HD 46485	ELODIE	3683.640	10.7 ± 7.3
	FEROS	3740.629	28.4 ± 6.1
HD 52266	Boller & Chivens	4942.495	10.8 ± 4.8
	FEROS	**2656.728**	13.6 ± 5.1
		3739.610	20.2 ± 4.9
		4541.608	21.6 ± 5.0
		4956.528	25.8 ± 4.9
		5606.536	18.2 ± 4.6
		5641.579	25.0 ± 4.4
	FIES	5576.578	31.1 ± 5.0
		6339.488	36.3 ± 5.0
HD 52533	Boller & Chivens	4942.502	24.4 ± 11.1
	CORALIE	7443.627	126.3 ± 10.8
	FEROS	2657.743	88.2 ± 13.1
		4953.481	23.6 ± 9.3
	FIES	5576.625	149.5 ± 15.8
		6339.500	33.2 ± 9.23
	MIKE	4109.658	116.8 ± 10.8
HD 53755 (V 569 Mon)	**UCLES**	3776.992	34.6 ± 6.6

Table A.1. continued.

Name	Instrument	Mid-expo. (HJD –2 450 000)	RV [km s^{-1}]
HD 66811 (ζ Pup)	**ESPaDOnS**	5971.798	–10.6 ± 3.9
		6701.928	–4.4 ± 4.0
HD 69106	Boller & Chivens	5646.564	8.2 ± 4.9
	CORALIE	7443.743	14.1 ± 5.3
		7447.562	26.9 ± 5.4
		7501.568	4.9 ± 5.5
	ESPaDOnS	**5937.013**	1.0 ± 12.0
		5937.033	19.9 ± 5.9
		5937.053	21.5 ± 5.8
		5937.073	20.2 ± 6.0
HD 74920	Boller & Chivens	5647.584	14.7 ± 4.7
	CORALIE	7441.634	14.5 ± 4.7
		7443.774	12.7 ± 4.6
		7447.575	10.4 ± 4.7
HD 84567	**CORALIE**	7441.542	36.4 ± 4.6
		7536.585	0.4 ± 4.7
HD 90087	**FEROS**	4955.528	–7.5 ± 2.5
		6098.524	–1.4 ± 2.3
HD 92554	**CORALIE**	7536.608	–56.5 ± 6.9
		7536.640	–61.2 ± 6.9
HD 93521	ELODIE	3123.414	5.0 ± 13.2
		3126.377	8.5 ± 12.9
		3126.400	18.6 ± 12.9
		3126.423	16.9 ± 12.5
		3126.446	6.5 ± 13.5
		3126.471	5.6 ± 14.9
		3126.556	5.5 ± 20.4
		3127.322	5.3 ± 13.5
		3127.345	10.9 ± 15.3
		3127.367	15.2 ± 14.7
		3127.390	11.8 ± 13.7
		3127.413	–1.7 ± 13.7
		3127.435	2.5 ± 13.5
		3127.458	–3.4 ± 13.3
		3127.480	4.0 ± 12.6
		3127.516	22.9 ± 19.3
		3127.539	16.7 ± 15.8
		3128.411	6.3 ± 13.3
		3128.446	1.6 ± 13.9
		3128.468	7.9 ± 15.6
	HEROS	6671.803	–0.4 ± 12.6
		6671.825	4.7 ± 11.4
	SOPHIE	5517.710	13.3 ± 11.0
HD 102415	CORALIE	7536.723	–45.6 ± 11.7
	FEROS	4599.689	–11.7 ± 12.3
		4627.648	–10.7 ± 12.1
		5698.689	–35.2 ± 12.7
		5699.730	–30.7 ± 12.7
HD 117490	FEROS	4627.675	6.4 ± 19.8
		4600.665	7.5 ± 18.9
		5696.780	12.2 ± 19.2
		5697.686	9.7 ± 18.8
		6068.667	11.8 ± 18.9
		7115.784	8.1 ± 19.8
		7116.650	7.9 ± 19.9
		7118.995	11.9 ± 19.0
HD 124979	**FEROS**	6067.740	–71.4 ± 2.4
		6098.632	–76.3 ± 1.6
HD 149757 (ζ Oph)	**ELODIE**	976.454	15.2 ± 8.6
	FEROS	4955.716	–10.9 ± 6.9
	HARPS	5979.400	–6.0 ± 6.8
HD 150574	**FEROS**	4599.773	–36.8 ± 10.0
		4627.692	–38.2 ± 9.9

Table A.1. continued.

Name	Instrument	Mid-expo. (HJD –2 450 000)	RV [km s^{-1}]
HD 163892	CORALIE	7441.865	55.1 ± 2.6
		7530.880	–34.8 ± 2.3
		7536.832	15.4 ± 2.2
	FEROS	**3546.882**	30.6 ± 3.5
		4600.887	–49.0 ± 3.5
		4626.849	–1.5 ± 3.0
		4953.925	–50.0 ± 3.0
		4954.871	–30.8 ± 3.1
		4955.725	–6.3 ± 3.0
		4956.801	24.0 ± 3.3
		4976.843	–48.1 ± 3.0
		5697.813	–53.6 ± 3.3
		6059.816	–25.5 ± 3.0
		6067.906	–18.5 ± 3.0
		6097.845	–50.0 ± 2.7
	FIES	5812.354	26.7 ± 2.3
		5816.380	–39.5 ± 2.8
HD 172367	**SOPHIE**	7267.332	–4.5 ± 6.0
HD 175876	**FEROS**	3546.941	0.2 ± 7.9
		3856.895	4.2 ± 8.2
		3912.913	3.7 ± 7.4
		3913.923	9.7 ± 8.3
		3914.907	2.3 ± 8.0
		4625.932	–2.2 ± 8.7
		4625.938	–2.8 ± 8.7
		4626.935	8.6 ± 8.2
		4626.956	6.6 ± 8.4
		5698.950	6.7 ± 8.4
		6067.955	1.8 ± 8.0
	CORALIE	7529.925	16.6 ± 9.9
HD 184915 (κ Aql)	FIES	5448.350	–7.9 ± 5.1
		6468.611	–12.4 ± 4.2
		6468.608	–13.3 ± 4.6
		6468.614	–14.7 ± 5.9
	HEROS	6569.659	–12.2 ± 2.6
		6787.970	–9.4 ± 3.7
		6792.953	–13.9 ± 3.9
	SOPHIE	7267.384	–7.9 ± 7.5
HD 188439 (V 819 Cyg)	FIES	5812.552	–76.3 ± 6.6
		6468.500	–77.5 ± 8.2
		6468.504	–76.9 ± 7.9
		6468.506	–78.1 ± 8.2
	HEROS	6568.744	–69.4 ± 6.1
		6795.941	–78.5 ± 12.2
		6798.944	–67.7 ± 7.2
		6810.915	–75.1 ± 7.6
		6820.907	–75.8 ± 7.8
	SOPHIE	7267.389	–78.9 ± 6.7
HD 191423	Albireo	5014.482	38.5 ± 21.4
	AURELIE	4711.496	–34.8 ± 20.3
		4712.551	–23.6 ± 20.2
		4717.444	–27.2 ± 20.6
		4718.588	–18.3 ± 21.8
		4743.328	–30.2 ± 20.4
		5418.419	–28.0 ± 20.6
		5421.593	–25.0 ± 20.1
	ELODIE	3247.311	–31.4 ± 19.0
		3247.322	–27.7 ± 19.6
	ESPRESSO	4986.858	–12.9 ± 25.1
		4991.939	–42.3 ± 27.2
	FIES	5802.562	–14.3 ± 22.8
		5815.547	–14.7 ± 20.9

Table A.1. continued.

Name	Instrument	Mid-exp. (HJD –2 450 000)	RV [km s^{-1}]
HD 192281 (V 2011 Cyg)	AURELIE	1065.387	–42.3 ± 8.8
		1065.387	–45.7 ± 8.7
		1067.390	–44.8 ± 9.0
		1069.386	–42.4 ± 9.4
		1071.396	–31.9 ± 8.5
		1073.364	–37.6 ± 8.4
		1373.422	–47.8 ± 7.2
		1374.448	–41.7 ± 7.5
		1375.366	–36.7 ± 7.5
		1376.357	–45.8 ± 8.6
		1377.369	–41.8 ± 8.0
		1378.367	–29.6 ± 9.3
		1379.406	–33.2 ± 7.9
		1399.532	–39.2 ± 8.1
		1404.461	–41.9 ± 7.8
		1406.557	–53.0 ± 8.3
		1407.457	–39.0 ± 8.0
		1410.513	–42.7 ± 14.2
		2163.430	–29.8 ± 7.5
		2164.416	–39.1 ± 7.1
		2164.430	–39.8 ± 7.0
		2165.395	–40.1 ± 7.7
		2165.410	–40.6 ± 8.0
		2167.418	–43.0 ± 7.5
		2167.432	–41.7 ± 7.7
		2168.415	–43.2 ± 9.2
		2168.436	–48.2 ± 8.6
		2168.464	–48.3 ± 8.3
		2169.421	–39.2 ± 7.7
		2169.444	–37.8 ± 7.4
		2170.387	–42.8 ± 7.3
		2170.409	–45.6 ± 7.9
		2918.427	–42.3 ± 8.4
		2919.450	–46.4 ± 8.0
		2923.383	–44.5 ± 7.5
		2925.460	–34.4 ± 7.5
		2922.446	–44.2 ± 7.4
	ELODIE	1733.604	–40.3 ± 7.4
		1800.345	–45.1 ± 13.4
		3246.417	–34.4 ± 7.6
		3600.453	–40.6 ± 7.8
	SOPHIE	7267.400	–30.9 ± 7.9
HD 198781	**HEROS**	6568.690	–17.0 ± 7.3
		6580.597	–10.1 ± 7.4
		6592.576	–22.0 ± 7.9
		6860.864	–26.7 ± 7.1
		6860.885	–25.5 ± 6.9
HD 203064 (68 Cyg)	**ESPaDOnS**	6200.773	32.6 ± 8.0
	FIES	4779.428	6.7 ± 9.4
		5812.582	25.5 ± 8.4
		6285.318	31.3 ± 8.7
	NARVAL	4086.329	23.9 ± 9.1
		4354.542	9.3 ± 8.3
		4358.413	9.5 ± 9.0
		4417.275	44.5 ± 8.9
HD 210839 (λ Cep)	ESPaDOnS	3605.079	–55.6 ± 8.1
	NARVAL	**4083.316**	–54.2 ± 7.6
		5371.550	–60.5 ± 7.6
		5385.588	–55.8 ± 7.5
		5784.532	–57.8 ± 7.1
		5801.577	–56.3 ± 7.8
		5802.543	–61.6 ± 7.9
	SOPHIE	7256.476	–43.5 ± 7.4
HD 228841	**SOPHIE**	7267.431	–62.3 ± 9.8

Appendix B: Diagnostic lines used for the CNO abundance determinations with CMFGEN

Table B.1 gives the spectral lines used to derive the carbon, nitrogen, and oxygen abundances with CMFGEN.

Table B.1. Lines used within CMFGEN to derive the CNO abundances.

Line	BD	HD											
	+34°1058	13268	14434	14442	15137	15642	41161	41997	46056	46485	66811	69106	74920
C II 4267	√	√		√	√	√		√	√			√	√
C III 4068–70	√	√	√		√	√	√		√	√			√
C III 4153	√	√	√	√	√				√	√		√	√
C III 4156	√	√	√	√	√				√	√		√	√
C III 4163	√	√	√	√	√				√			√	√
C III 4187				√	√		√		√	√		√	
C III 4325		√	√	√				√					
C III 4666													√
C III 5246					√				√			√	√
C III 5272		√			√						√	√	√
C III 5353						√							
C III 5826		√			√			√	√				√
C III 6205			√										

Line	HD												
	92554	102415	117490	124979	149757	150574	163892	175876	191423	192281	203064	210839	228841
C II 4267	√	√	√			√	√				√		
C III 4068–70	√		√	√	√	√	√	√	√	√	√	√	√
C III 4153	√		√	√	√	√	√	√	√		√	√	√
C III 4156	√		√	√	√	√	√	√	√		√	√	√
C III 4163	√	√	√	√		√	√	√	√		√	√	√
C III 4187	√	√	√	√		√	√	√			√	√	√
C III 4325	√			√				√		√		√	√
C III 4666													
C III 5246		√				√	√				√		
C III 5272		√				√							
C III 5353													
C III 5826						√	√			√			
C III 6205													

Table B.1. continued.

Line	BD	HD											
	+34°1058	13268	14434	14442	15137	15642	41161	41997	46056	46485	66811	69106	74920
N II 3995			√										√
N III 4004		√	√		√		√	√					√
N IV 4058		√	√				√			√			√
N III 4095	√		√	√	√			√			√	√	√
N III 4196		√	√	√	√	√						√	√
N III 4216													
N II 4447													
N III 4511	√	√	√		√	√	√	√	√		√	√	
N III 4515	√	√	√		√	√	√	√			√	√	
N III 4518	√	√	√		√	√	√	√			√	√	
N III 4524	√	√	√		√	√	√	√		√		√	
N III 4535	√	√	√				√	√		√		√	
N II 4602				√									
N II 4607				√									
N II 4613				√									
N III 4634–4643	√		√		√	√			√			√	
N II 4788											√		
N III 4907			√	√							√		
N II 4995													
N II 5001													
N II 5005													
N II 5011			√										
N IV 5200			√								√		√
N IV 5204			√								√		√

Line	HD												
	92554	102415	117490	124979	149757	150574	163892	175876	191423	192281	203064	210839	228841
N II 3995		√		√								√	
N III 4004		√	√	√		√		√		√		√	√
N IV 4058	√					√				√			√
N III 4095	√		√	√	√		√	√	√				√
N III 4196	√	√		√		√		√	√			√	√
N III 4216				√									
N II 4447										√			
N III 4511	√	√	√	√	√	√	√	√	√		√	√	
N III 4515	√	√	√	√	√	√		√	√	√	√	√	√
N III 4518	√			√	√	√		√	√	√	√	√	√
N III 4524	√		√		√	√		√	√	√	√	√	√
N III 4535	√			√	√	√		√		√	√	√	√
N II 4602													
N II 4607													
N II 4613													
N III 4634–4643		√	√			√				√			√
N II 4788													
N III 4907	√	√	√			√						√	
N II 4995									√				
N II 5001									√				
N II 5005									√				
N II 5011									√				
N IV 5200												√	
N IV 5204												√	

Table B.1. continued.

Line	BD	HD											
	+34°1058	13268	14434	14442	15137	15642	41161	41997	46056	46485	66811	69106	74920
O II 3792		√	√							√	√	√	
O II 3913						√						√	
O II 3955					√	√						√	
O II 3963		√	√		√	√	√		√	√		√	
O II 4277–78										√			
O II 4284										√			
O II 4305				√					√				√
O II 4318	√	√	√	√	√	√	√	√	√			√	√
O II 4321	√	√		√	√	√	√	√	√	√		√	√
O II 4368	√	√	√	√		√				√	√	√	√
O II 4416		√			√	√						√	√
O II 4418		√			√	√						√	
O II 4592	√	√		√	√	√	√		√			√	√
O II 4597	√	√		√	√	√	√		√			√	√
O II 4603				√	√				√				
O II 4611				√									
O II 4663					√	√		√					
O II 4678					√	√		√				√	
O II 4700		√		√	√	√	√		√			√	
O II 4707					√	√			√			√	

Line	HD												
	92554	102415	117490	124979	149757	150574	163892	175876	191423	192281	203064	210839	228841
O II 3792			√		√			√	√			√	
O II 3913		√	√		√	√	√						
O II 3955	√	√	√		√		√						√
O II 3963	√	√	√	√	√	√	√	√	√		√	√	√
O II 4277–78													
O II 4284													
O II 4305			√		√							√	
O II 4318	√			√	√	√	√	√	√	√		√	√
O II 4321	√				√	√	√	√	√	√			√
O II 4368	√	√	√	√	√	√	√	√	√		√	√	√
O II 4416	√	√	√			√	√		√				√
O II 4418	√	√	√			√	√		√				
O II 4592	√		√	√	√	√	√		√			√	√
O II 4597	√		√	√	√	√	√		√			√	√
O II 4603			√			√							
O II 4611			√										
O II 4663			√		√								
O II 4678	√		√		√	√	√		√				
O II 4700	√	√	√		√	√	√		√				
O II 4707	√	√	√		√	√	√		√				

Appendix C: Binary and runaway status

We determined the multiplicity status of our targets using our own RV measurements (Table A.1) complemented with literature information. Whenever possible, new or improved orbital elements are presented (Table C.1).

Table C.2 summarises the detection status of visual companion(s) in the close vicinity of our targets, when available. The widely different field of view and sensitivity in terms of magnitude differences and angular separations may explain why some close companions are detected in some surveys, but not in others. It should be noted that the presence of such companions is not reflected in RV variations, considering our error bars, as they are too distant.

C.1. ALS 864

There is only a little information about this object in the literature and only one spectrum is available in our dataset. Therefore, we could not assess its multiplicity.

C.2. ALS 18675

The literature provides no additional information and we have only one spectrum of this object, hence its multiplicity status cannot be established.

C.3. BD +60°594

Hillwig et al. (2006) claimed that this star is probably a single-lined spectroscopic binary with an orbital period of the order of 20 days. Indeed, Conti et al. (1977) gave a RV value of –50 km s^{-1}, while Hillwig et al. (2006) quoted decreasing RVs (from –60 to –110 km s^{-1}) on a timescale of 4 d. Our measurements further yield −51 and −15 km s^{-1}. Accordingly, we classify this star as RV variable.

C.4. BD +34°1058

As we have only a single spectrum of this star and no additional RV measurements are available in the literature, therefore, we cannot assess its multiplicity status.

C.5. HD 13268

Low-amplitude, short-term (a few hours) periodic line-profile variations have been detected by De Becker et al. (2008). They attributed these variations to non-radial pulsations or structures associated with material in the circumstellar environment. Bekenstein & Bowers (1974) further suggested that this star is a runaway with a peculiar velocity greater than 89 km s^{-1} and Kendall et al. (1996) proposed that it was ejected from within Per OB1.

The variability test indicates no significant variation of the RVs in our dataset, but variations are clearly detected when literature values are added. Indeed, all recent RVs (HJD > 2 450 000) fall inside the interval −90 to −120 km s^{-1}, while much older data (HJD ∼ 2 440 500; Abt et al. 1972) provide RVs typically ranging from −110 to −130 km s^{-1}. As there are 78 RV measurements in total, we attempted a period determination. A search performed on all or only the recent data yields no clear periodicity, simply favouring variations occurring on long timescales, hence we thus simply – and tentatively – classify the star as RV variable.

C.6. HD 14434

Significant line-profile variability of the He II 4686 double-peaked emission and the Hβ absorption line has been reported by De Becker & Rauw (2004), but we found no significant RV variation for this star, even when considering literature values (Conti et al. 1977). Hence we classify it as presumably single.

C.7. HD 14442

Significant line-profile variability of the He II 4686 double-peaked emission and of the Hβ absorption line has been interpreted as co-rotating features formed in the wind (De Becker & Rauw 2004). In our data, we found no significant RV variation so we classify HD 14442 as presumably single.

C.8. HD 15137

HD 15137 is a known runaway with a peculiar space velocity $V_{\rm pec}$ = 62.7 ± 11.8 km s^{-1} (McSwain et al. 2007). This star was proposed to be an SB1 system that was probably expelled from the open cluster NGC 654 (Boyajian et al. 2005). The high eccentricity of the system ($e \sim 0.5$) can be explained by the widening of the orbit during the supernova event that also imparted the velocity kick. The mass of the companion star must be low ($1.4\ M_\odot \leq M_{\rm comp} \leq 3.0\ M_\odot$; McSwain et al. 2010), as indicated by the mass function of the system. It may also be noted that this system is a faint X-ray emitter, although it could still be a high mass X-Ray binary (HMXB) with a very low accretion rate (Boyajian et al. 2005).

We re-investigated the system with our dataset, complemented by literature data (Conti et al. 1977; Boyajian et al. 2005; McSwain et al. 2007, 2010) and found evidence for significant RV variations. An error of 8.5 km s^{-1} is considered for RV values from McSwain et al. (2007) and Boyajian et al. (2005), as in McSwain et al. (2010). Analysing the RVs with period search algorithms yields, however, no clear periodicity, simply favouring variations occurring on long timescales; we do not find significant peaks at the periods proposed by these authors. Furthermore, when we fold all data with the 28.61 d period of Boyajian et al. (2005), the RVs appear scattered. Folding them with the 55.40 d period of McSwain et al. (2010) results in slightly more coherent variations, although no convincing peak is seen in the periodograms at this orbital period. Therefore, we simply classify the star as RV variable. Eliminating the oldest data point (HJD = 2 440 074.970; Conti et al. 1977) does not modify our conclusions.

C.9. HD 15642

Our RVs do not show any significant variations and no other information is available in the literature. Therefore, we classify this star as presumably single.

C.10. HD 28446A

HD 28446 was first suggested to be a spectroscopic binary by Frost et al. (1926). In this context, Plaskett & Pearce (1931) claimed that HD 28446 is an SB2 with a large velocity amplitude

(K ∼ 140 km s^{-1}). However, the spectra of Mayer et al. (1994) show no trace of a secondary and these authors only found a RV variability with a period of 1.3 d. More recently, Straižys & Laugalys (2007) suggested that HD 28446 is a triple system with three visual components surrounded by a H II region of 1.5–2° diameter, while Eggleton & Tokovinin (2008) found only two components separated by 10″. For our HEROS observations, we made sure that the brightest component of this system was observed (HD 28446A).

Jerzykiewicz (1993) reported small variations in the photometric data of HD 28446A, which is consistent with a period of 0.22132 day and suggesting a β Cephei nature for this star. Stankov & Handler (2005) rather proposed it to be a slowly pulsating B star (SPB). Our RVs do not significantly vary, but when combined with literature values (Mayer et al. 1998), evidence for variability is found. Period searches on the full RV set yield peaks near 1.5 or 3 d, with numerous close aliases. Phasing the RVs with such periods yields a noisy RV curve with variation amplitude of ∼10 km s^{-1}. It must, however, be noted that Mayer's values appear mostly below ours with an offset of ∼20 km s^{-1} between both datasets. Furthermore, the existence of line-profile variations arising from the non-radial pulsations and the possible presence of a gravitationally bound tertiary might lead to such noisy RV curves. Therefore, more data are needed to clarify the source of the RV variations. We thus refrain from calculating an orbital solution, simply classifying the star as RV variable.

C.11. HD 41161

HD 41161 is a runaway star located about 355 pc above the Galactic plane (de Wit et al. 2005). It is also a bow shock candidate (Peri et al. 2012).

Significant RV changes are found when all data (our work + literature; Conti et al. 1977; Garmany et al. 1980) are combined, with a maximum RV difference of 35 km s^{-1} (corresponding to a 5σ variation). All periodograms have some peaks around a period of ∼3 d – the best Fourier value is $P = 3.26592 \pm 0.00006$ d (Fig. C.1). The period error is certainly underestimated. In fact, there are numerous close aliases of that period because the data consist of widely separated observing blocks. The amplitude of the variations, however, is very small, i.e. only 6 km s^{-1}. This is not formally significant since peaks with this amplitude are typically found in periodograms calculated based on Monte Carlo simulations (using only the observing dates and noise). Besides, such a small amplitude could arise from line-profile variations, and we thus do not attempt to calculate an orbital solution, waiting for more data taken with a more appropriate sampling, to solve the issue. In the meantime, we classify this object as RV variable.

C.12. HD 41997

HD 41997 is a runaway star with a peculiar RV of –40 km s^{-1} (Carrasco & Creze 1978). Only one spectrum is available for this star and no further RV measurements are available in the literature, so its multiplicity cannot be assessed.

C.13. HD 46056

HD 46056 was suggested to be an SB1 (Walborn 1973; Underhill & Gilroy 1990). Mahy et al. (2009) rather found it to be single. These authors noticed variations of the line profiles, which could have led to a spurious detection of RV changes. In line with this result, we do not find any significant RV variation in the ESPaDOnS and ESPRESSO spectra, and we thus classify this star as presumably single. Feast et al. (1957) observed a large RV variation (from –21 to +65 km s^{-1}), but this needs to be confirmed because of the low precision of measurements on photographic plates.

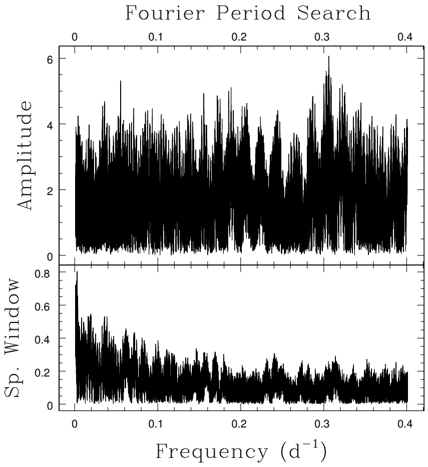

Fig. C.1. Fourier periodogram derived from the RVs (our work + literature) of HD 41161. We note the peak at 0.306 d^{-1}.

C.14. HD 46485

We find a RV difference of ∼20 km s^{-1} between our two spectra of this star, which are separated by about two months. A similar difference was reported by Feast et al. (1957) over two years. However, it corresponds only to a 1.9σ variation, which is not significant. Therefore, we classify this star as presumably single. Adding a value from Conti et al. (1977) does not change this multiplicity status (maximum RV difference of 27 km s^{-1} corresponding to a 3.5σ variation).

C.15. HD 52266

The peculiar velocity of HD 52266 is not very large (19.4 ± 9.0 km s^{-1}) and it is thus presumably not a runaway star (McSwain et al. 2007). McSwain et al. (2007) further suggested that HD 52266 is likely an SB1 system, but they could not determine an orbital period. They only constrained it to be longer than the time span of their data (i.e. RV variation from 12 to 39 km s^{-1} over 40 days). We obtained many additional observations and our RV measurements span the range 14–36 km s^{-1}, confirming previous results. The RV changes are found to be significant when all data (our work + literature; Conti et al. 1977; McSwain et al. 2007) are combined. We decided to search for a period and a clear signal was found: $P = 75.84 \pm 0.04$ d for the modified Fourier algorithm (Fig. C.2). The associated semi-amplitude is moderate (13 km s^{-1}) and the period error is certainly underestimated; there are numerous close aliases of that period because the data consist of widely separated observing

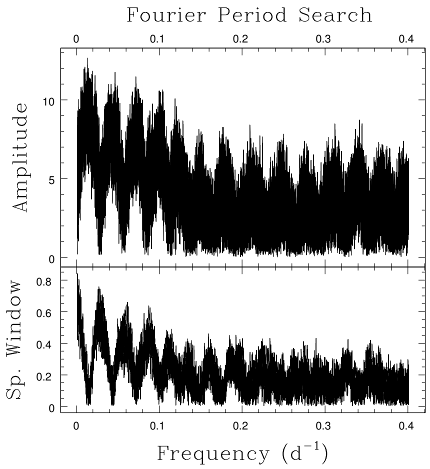

Fig. C.2. Fourier periodogram derived from the RVs (our work + literature) of HD 52266. We note the peak near 0.01 d^{-1}.

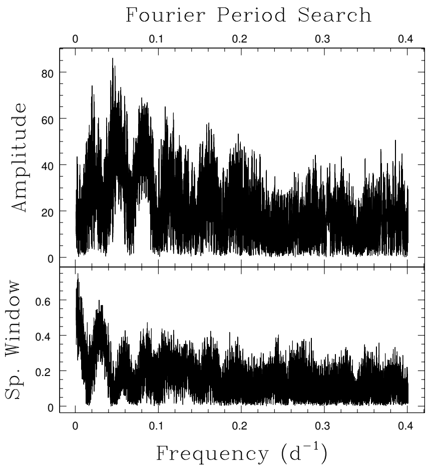

Fig. C.4. Fourier periodogram derived from the RVs (our work + literature) of HD 52533. We note the peak near 0.045 d^{-1}.

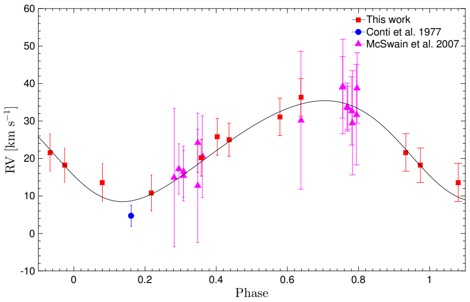

Fig. C.3. Phase diagram of the RV values of HD 52266 folded with a 75.84 d period. The best-fit orbital solution (Table C.1) is represented as a black curve.

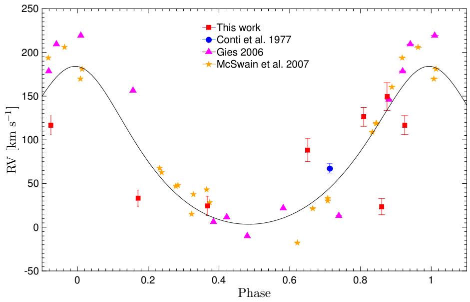

Fig. C.5. Phase diagram of the RV values of HD 52533 folded with a 22.244 d period. The best-fit orbital solution (Table C.1) derived is shown as a black curve.

blocks. Adopting the period mentioned above, we nevertheless derived an orbital solution with LOSP (see Table C.1 and Fig. C.3). We caution, however, that the sampling is far from perfect, implying that this solution is still preliminary and requires confirmation.

C.16. HD 52533

Gies & Bolton (1986) found an SB1 solution for HD 52533 with a 3.29 d period, while McSwain et al. (2007) suggested that it might be an SB3. The He II lines would originate from the primary O star, while a distant B companion would contribute to He I and Balmer line profiles. McSwain et al. (2007) found a period of 22.1861 ± 0.0002 d from the lines associated with the O star, while the B-star lines appeared stationary. In addition, the peculiar velocity of HD 52533 is 47.0 ± 27.9 km s^{-1}, suggesting that it might be a runaway star (McSwain et al. 2007). In this context, the invisible companion of the O star could be a compact object, but its X-ray emission is typical of that of single O stars (Motch et al. 1998). A modest accretion rate could render the presence of a compact companion undetectable, however (Meurs et al. 2005). A search for radio emission originating from a pulsar was unsuccessful (Philp et al. 1996).

Our RV values, which are significantly variable, indicate a phase shift relative to McSwain et al. (2007) ephemeris. This leads us to recalculate an orbital solution, adding values from literature (Conti et al. 1977; D.R. Gies, priv. comm.; although these values were also used in McSwain et al. 2007). To this aim, we first use period search algorithms and found P(Fourier) = 22.243 ± 0.003 d (Fig. C.4; again, because of the imperfect sampling with long intervals without observations, the period error is certainly underestimated). The large amplitude of this peak makes it highly significant (significance level SL ≪ 1%). Using this period as first guess, we then derived an orbital solution thanks to the LOSP programme (Table C.1). This solution, illustrated in Fig. C.5, agrees well with that of McSwain et al. (2007), but it would certainly be improved by collecting data with a better phase coverage.

C.17. HD 53755

HD 53755 is a candidate β Cephei according to Stankov & Handler (2005). Our sole UCLES spectrum of HD 53755, along with the lack of other RV measurements in the literature, does not allow us to investigate the multiplicity of this star.

C.18. HD 66811

This star is a runaway with a peculiar RV of -40 km s^{-1} (Carrasco & Creze 1978). The RVs derived in our two spectra separated by about two years appear compatible within the error bars, but those reported by Garmany et al. (1980) range from –11 to –28 km s^{-1}, which leads to a maximum RV difference of 24 km s^{-1} corresponding to 3.5σ; the RV changes are thus only on the verge of being significant. Therefore, in view of current data, we are forced to keep a presumably single status for this star.

C.19. HD 69106

Feast et al. (1957) noticed that two Balmer lines (Hδ and Hγ) were double on one photographic plate, but no further study of this object was performed since then. In our data, we see no doubling of the lines and detect a maximum RV difference of 26 km s^{-1}, corresponding only to a 2.9σ variation. Feast et al. (1957) provided additional RV measurements that are all in agreement with our data except one discrepant point at –31 km s^{-1}. Without further information, we discard this value as outlier and we tentatively classify the star as presumably single.

C.20. HD 74920

We found no significant RV variation for this star in our data. Hence we classify it as presumably single.

C.21. HD 84567

HD 84567 is a runaway star candidate ($V_{\rm pec} = 33.4^{+10.9}_{-13.1}$ km s^{-1}; Tetzlaff et al. 2011). A difference of 36 km s^{-1} is found between our two RV measurements separated by ~3 months, corresponding to a 5.5σ variation. We hence classify this star as RV variable.

C.22. HD 90087

The two sole RV measurements taken about three years apart (Table A.1) are compatible within the error bars. We therefore consider this star as presumably single.

C.23. HD 92554

As we only have two exposures of this star that are separated by less than one hour, and since no additional RV measurements are available in the literature, we cannot assess its multiplicity status.

C.24. HD 93521

No significant RV variation is found for this star in our data and, while Rauw et al. (2012) reported line-to-line RV variations and RV changes between different observing years, they attributed these changes to non-radial pulsations. Therefore, we concur with their classification of a presumably single object. This also agrees with the fact that no significant variation is found when examining values from Garmany et al. (1980) and ours; the maximum RV difference of 71 km s^{-1} corresponds only to a 3.6σ variation in view of the large error bars. The runaway status of this star is still uncertain, but no evidence for an accreting compact companion has been found in X-rays (Rauw et al. 2012).

C.25. HD 102415

Hints of RV variability were reported for this star by Walborn et al. (2011), Sota et al. (2014), and Martins et al. (2015b). In our data, we found no significant RV variation so we classify HD 102415 as presumably single.

C.26. HD 117490

Some RV variability has previously been reported for this star (Martins et al. 2015b), but all our RV values are similar within the error bars, hence our choice of a presumably single status.

C.27. HD 124979

HD 124979 is a runaway star characterised by a peculiar velocity of $74.4^{+7.7}_{-8.3}$ km s^{-1} (Mason et al. 1998; Tetzlaff et al. 2011). It was suggested to be an SB2 (Penny 1996; Barbá et al. 2010; Sota et al. 2014). However, we do not observe the usual line doubling in our spectra. All recent data (our work and literature; Williams et al. 2011) are very similar with RVs between -70 and -90 km s^{-1}; old RV measurements (Feast & Thackeray 1963; Kilkenny & Hill 1975) differ from these, reaching higher and lower values. However, even after discarding them, the RV changes are found to be significant hence we classify this star as RV variable. Period searches yield no clear periodicity; we therefore need more data to assess the timescale of this variability.

C.28. HD 149757

HD 149757, best known as ζ Oph, is a runaway star (Blaauw 1961; Tetzlaff et al. 2011, $V_{\rm pec} = 25^{+2.9}_{-1.1}$ km s^{-1}) as testified by the bow shock in its vicinity (e.g. van Buren & McCray 1988). It was claimed that this star was part of a binary and was ejected when its companion (now the pulsar PSR B1929+10) exploded as a supernova about 1 Myr ago (van Rensbergen et al. 1996; Hoogerwerf et al. 2001; Tetzlaff et al. 2010), but Kirsten et al. (2015) recently refuted this hypothesis. In any case, it appears to be currently single; we found no significant RV variation in the data.

C.29. HD 150574

Garrison et al. (1977, 1983) suggested HD 150574 to be an SB2 based on the observation of double lines in the spectrum, although we do not detect any signature of a secondary in our high-resolution spectra. Furthermore, these new spectra do not reveal any significant RV variations, hence we classify this object as presumably single.

C.30. HD 163892

This star is a member of the Sgr OB1 association (Humphreys 1978). It has long been recognised as an SB1 system (Feast et al. 1957; Conti et al. 1977), as recently confirmed by Stickland & Lloyd (2001) and the OWN Survey (Barbá et al. 2010; Sota et al. 2014). An orbital solution for the SB1 was presented by Mayer et al. (2014) who found a 7.8 d period. In the context of this work, we redetermined the RVs of the FEROS spectra used by Mayer et al. and complemented the set of RV values thanks to another FEROS spectrum, three CORALIE, and two FIES spectra (Table A.1). Our RVs appear systematically lower by ∼10 km s^{-1} than those reported by Mayer et al. (2014). This difference is not surprising as they used Gaussian fits of individual lines to derive their values, which can differ from correlation results by about 10 km s^{-1}, depending on the chosen rest wavelength of the fitted lines. It may further be noted that lowering by 10 km s^{-1} the primary systemic velocity $V_{\gamma,\mathrm{pri}}$ given by Mayer et al. (2014) yields a value more consistent with the average RV of the Sgr OB1 members that they quote (∼−10 km s^{-1}). Such a change in the orbital solution, however, implies that two out of the three RV measurements of Feast & Thackeray (1963) and the Stickland & Lloyd (2001) measurement do not fit well the RV curve anymore; but these RVs were measured on photographic plates, hence have a larger error than ours based on high-resolution échelle spectra. We performed a period search on all available RVs and one peak slightly stands out in the periodograms (e.g. Fig. C.6) with a period P(Fourier) = 7.8347 ± 0.0003 d, although the long gaps without observations lead to the presence of numerous close aliases that increase the actual error on that value. The large amplitude of this peak makes it highly significant (SL≪ 1%). Furthermore, when folded with this period, RVs yield a clear sinusoidal variation with phase. The best-fit orbital solution was derived with the LOSP programme (Table C.1 and Fig. C.7); this orbital solution was computed with an eccentricity fixed to zero after it was found to be compatible with this value within the error bars. This orbital solution is in good agreement with the solution of Mayer et al. (2014) within the error bars, except for the primary systemic velocity ($V_{\gamma,\mathrm{pri}}$ = +2.8 vs. −3.1 km s^{-1}).

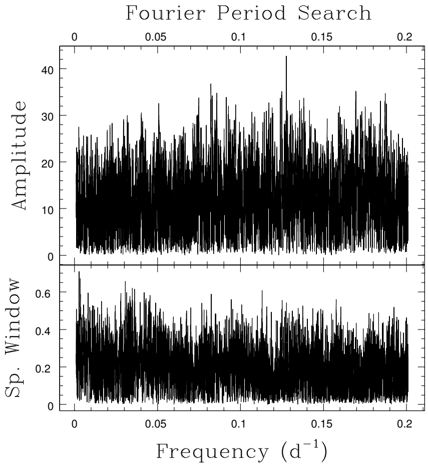

Fig. C.6. Fourier periodogram derived from the RVs (our work + literature) of HD 163892. We note the peak at 0.128 d^{-1}.

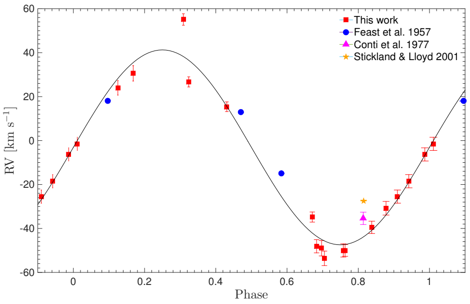

Fig. C.7. Phase diagram of the RV values of HD 163892 folded with a 7.8348 d period. The black curve shows the best-fit orbital solution derived with the LOSP programme (Table C.1).

C.31. HD 172367

We cannot investigate the multiplicity status because we only have one spectrum and no previous investigation of the RVs exists.

C.32. HD 175876

Tetzlaff et al. (2011) suggested that HD 175876 is a runaway star candidate; their value for the peculiar spatial velocity is $22.2^{+5.9}_{-8.1}$ km s^{-1}. The analysis of the RVs (ours complemented by literature values; Kilkenny & Hill 1975; Conti et al. 1977; Bohannan & Garmany 1978; Garmany et al. 1980) leads us to reject RV variability. We nevertheless investigated the extensive RV set with period search algorithms, but without conclusive results. We thus conclude that this star is presumably single.

C.33. HD 184915

Weak emission is noticed in both wings of Hα, but according to Rivinius et al. (2013) this emission is not produced in a circumstellar disc (as in Be stars), but arises from a stellar outflow. We found no significant RV variation for this star in our data. Hence we classify it as presumably single.

C.34. HD 188439

HD 188439, or V819 Cyg, is a runaway star candidate with a peculiar velocity of $61.9^{+3.7}_{-4.3}$ km s^{-1} (Tetzlaff et al. 2011). According to Stankov & Handler (2005), it is not a β Cephei star even though its photometric variations have been associated with pulsational activity with periods of ∼0.3775 d (Lynds 1959) or ∼0.7137 d (Koen & Eyer 2002). Lynds (1959) also suggested that HD 188439 might be a very short-period binary in which the stars are partially merged.

Our RV values do not present significant variations, but the full RV dataset (our work + literature; Gies & Bolton 1986) indicates the presence of significant changes. In addition, we performed a period search on our data combined to those of Gies & Bolton (1986), excluding an outlier value (−50.1 ±

4.6 km s^{-1} at HJD = 2 444 803.737), but no significant period could be derived. We therefore classify the star as RV variable, requiring more data to constrain the periodicity.

C.35. HD 191423

HD 191423, also known as "Howarth's star", is considered as one of the fastest rotators known amongst O stars since its rotation rate is believed to be close to critical ($\Omega/\Omega_{\rm crit}$ = 0.9; Howarth & Smith 2001). From spectroscopic time series, Mahy et al. (2013) argued that HD 191423 is probably single. Excluding one deviant RV measured on the GOSSS spectrum, the RV differences in our data are not significant (maximum ΔRV of 29 km s^{-1} corresponding to a 0.8σ difference because of the large error bars). Furthermore, while no clear periodicity can be identified in the whole RV dataset, a potential variability timescale of about 2.1 d is apparently detected in the Fourier periodogram when excluding the GOSSS measurement. However, the large RV uncertainties imply that this peak is totally insignificant after comparison with simulated data. The sampling is not at all adapted to identify such a timescale and the phased RVs do not result in a convincing diagram, hence we keep the presumably single status until further information becomes available.

C.36. HD 192281

Significant variability of the He II 4686 double-peaked emission and of the Hβ absorption line was found by De Becker & Rauw (2004): they interpreted them as an effect of co-rotating features present in the wind. Barannikov (1993) found RV variations with a period of 5.48 d compatible with the presence of a low-mass companion. This was challenged by De Becker & Rauw (2004). These authors, after showing that this star is not a runaway, derived instead a 9.57 d period for the RV variability, but with a so small amplitude that it was not considered significant. We do detect a significant variability in the RVs when combining our measurements with those in the literature. However, there is a clear outlier: one measurement by Barannikov (1993) is positive while all others are clearly negative. Eliminating it, though, does not modify our conclusions, i.e. there is evidence for variability. However, there is no convincing detection of periodicity. We therefore classify this star as RV variable.

C.37. HD 198781

Our RVs do not display significant variations and no other measurements are available in the literature; we thus classify this star as presumably single.

C.38. HD 203064

HD 203064, or 68 Cyg, is a known runaway ($V_{\rm pec}$ = $59.4^{+12.8}_{-23.2}$ km s^{-1}; Gies & Bolton 1986; Tetzlaff et al. 2011). Lozinskaya & Lyuty (1981) further detected a small photometric variability with a 3.34 d period. It is also a known SB1 presenting discrete absorption components (DACs; Kaper et al. 1996). From the study of Hδ, Alduseva et al. (1982, see also Cherepashchuk & Aslanov 1984) derived an orbital solution with a period of 5.1 d. The amplitude of our RVs is large (ΔRV ~ 38 km s^{-1}), but this corresponds to a 2.9σ variation only. However, a significant RV variability is detected when literature values (Conti et al. 1977; Bohannan & Garmany 1978; Garmany et al. 1980; Alduseva et al. 1982; Cherepashchuk & Aslanov 1984; Gies & Bolton 1986) are added; we find a maximum ΔRV of 117 km s^{-1} or a 14σ difference. In our period searches, one peak slightly stands out from the Fourier periodogram (Fig. C.8), with a period P = 5.02290 ± 0.00016 d. Its rather large amplitude, seldom reached in periodograms derived from Monte Carlo simulations, makes it highly significant (SL ≪ 1%). We tentatively calculated an orbital solution for this period using the LOSP programme. The derived orbital elements are presented in Table C.1 and the orbital solution is shown in Fig. C.9; this orbital solution was computed with an eccentricity fixed to zero since it was found to be compatible with this value within the error bars. There is an indication for systematically lower RVs derived from Hδ, which leads to the noisy appearance of the RV curve. Our derived orbital period is slightly shorter and our velocity amplitude is smaller than previous solutions (Alduseva et al. 1982; Cherepashchuk & Aslanov 1984). However, since the sampling is far from being perfectly adequate for a 5 d period, new data are required to confirm this tentative solution.

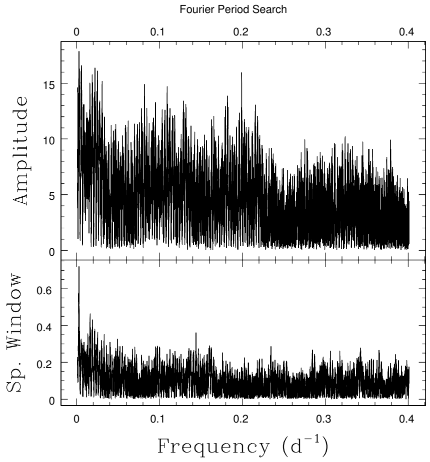

Fig. C.8. Fourier periodogram derived from the RVs (our work + literature) of HD 203064. We note the peak near 0.199 d^{-1}.

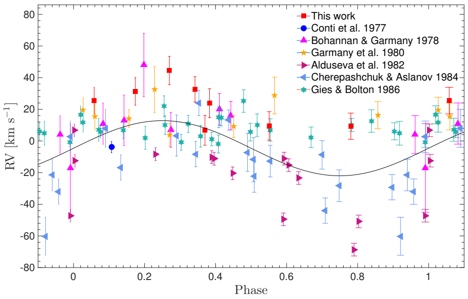

Fig. C.9. Phase diagram of the RV values of HD 203064 folded with a 5.02292 d period. The best-fit orbital solution (Table C.1) is shown as a black curve.

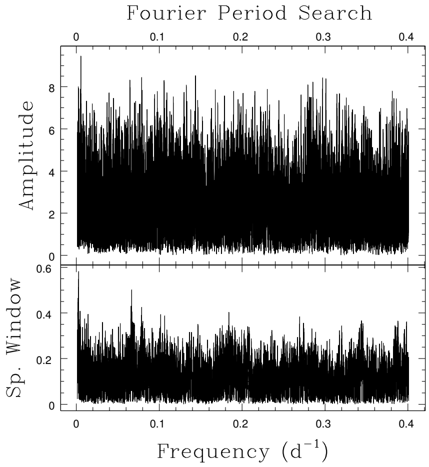

Fig. C.10. Fourier periodogram derived from the RVs (our work + literature) of HD 210839. We note the peak near 0.005 d^{-1}

C.39. HD 210839

HD 210839 is a runaway star with a peculiar space velocity of $66.4^{+3.7}_{-2.3}$ km s^{-1} (Tetzlaff et al. 2011). No significant RV variation is detected in our dataset, but adding the literature values (Garmany et al. 1980; Gies & Bolton 1986) results in a clear detection of RV variability; in this case, we find a maximum ΔRV of 52 km s^{-1} or a 4.7σ difference. Our period searches yield a small but significant peak in the periodograms at low frequencies, corresponding to P(Fourier) = 186.4 ± 0.2 d (Fig. C.10). Although this period is tentative, we used LOSP to calculate a preliminary orbital solution (see Table C.1 and Fig. C.11); this orbital solution was computed with an eccentricity fixed to zero since it was found to be compatible with this value within the error bars. It requires new data to be confirmed.

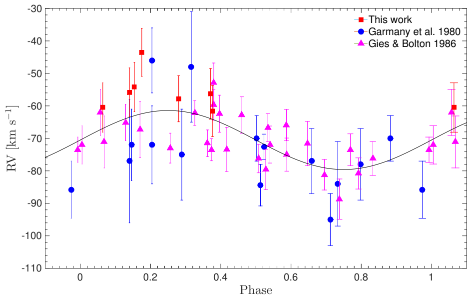

Fig. C.11. Phase diagram of the RV values of HD 210839 folded with a 186.4 d period. The best-fit orbital solution (Table C.1) is shown as a black curve.

C.40. HD 228841

Williams et al. (2011) suggested that it is a runaway star (with a peculiar space velocity of 87 km s^{-1}). Following a short-term RV monitoring, Mahy et al. (2013) found no significant variability and thus favoured a single status for HD 228841. Having a single spectrum of this star, we cannot assess this statement in detail, but our RV measurement agrees well with those of Mahy et al. (2013) for He I. Therefore, we simply adopt their presumably “single” status.

Table C.1. Orbital solutions obtained with the LOSP programme for some confirmed or suspected single-lined spectroscopic binaries in our sample.

Elements	HD 52266	HD 52533	HD 163892	HD 203064	HD 210839
P [d]	75.84 ± 0.04	22.244 ± 0.003	7.8348 ± 0.0003	5.02292 ± 0.00016	186.4 ± 0.2
T_0 [HJD–2 400 000]	53 560.8 ± 6.9	51 130.7 ± 1.7	50 842.6 ± 0.1	56 284.4 ± 0.1	41 191.1 ± 5.4
e	0.12 ± 0.07	0.23 ± 0.13	0 (Fixed)	0 (Fixed)	0 (Fixed)
ω [°]	119.0 ± 33.2	3.8 ± 28.9	...	...	...
$K_{\rm prim}$ [km s^{-1}]	13.5 ± 0.8	90.4 ± 11.8	44.4 ± 2.0	17.4 ± 3.8	9.1 ± 1.5
$V_{\gamma,\rm pri}$ [km s^{-1}]	22.8 ± 0.6	73.3 ± 7.3	–3.1 ± 1.6	–4.6 ± 2.2	–70.5 ± 1.2
f(m) [$M_\odot$]	0.0188 ± 0.0035	1.57 ± 0.63	0.0708 ± 0.0095	0.0027 ± 0.0018	0.0145 ± 0.0074
a sin i [$R_\odot$]	20.02 ± 1.26	38.67 ± 5.20	6.86 ± 0.31	1.73 ± 0.38	33.46 ± 5.70
rms [km s^{-1}]	2.7	36.6	6.7	19.7	8.1

Notes. As a first guess of the period, we used that corresponding to the Fourier periodogram peak, and then refinement was performed, if needed, within LOSP. These solutions are tentative since the temporal coverage of the period is not satisfactory. Thus, intensive monitoring over at least one full period is needed to ascertain these orbital solutions. T_0 stands for the time of passage at periastron when $e \neq 0$ and at conjunction (primary in front) otherwise.

Table C.2. Results from high-resolution angular observations of our targets, with Y or N indicating whether close companion(s) have been detected or not (ρ is the angular separation).

	Reference								
Star	[1]	[2]	[3]	[4]	[5]	[6]	[7]	[8]	Comments
HD 14434	...	...	N	...	...	...	...	...	
HD 14442	...	...	N	...	...	...	...	...	
HD 15137	N	...	N	...	N	...	...	N	
HD 15642	...	...	N	...	...	...	...	...	
HD 28446A	...	...	...	Y	...	...	...	...	$\rho = 10.32''$ [4]
HD 41161	Y	...	N	...	N	...	...	N	$\rho = 9.8''$, $P \sim 243\,000$ yr assuming $d = 1.5$ kpc [1]
HD 41997	...	...	N	...	...	...	...	N	
HD 46056	...	...	N	...	...	...	...	N	
HD 46485	...	...	N	...	...	...	N	N	
HD 52266	N	...	N	...	N	...	N	N	2MASS companion at 7.1″ [5]
HD 52533	Y	...	N	...	...	...	Y	Y	A-B with $\rho = 2.5''$ ($P \sim 40\,000$ yr assuming $d = 2.0$ kpc) + A-C with $\rho = 22.6''$ [1] Aa-Ab with $\rho = 0.64''$ ($\Delta H \sim 3.50$ mag) + A-B with $\rho = 2.64''$ ($\Delta H \sim 5.02$ mag) + A-G with $\rho = 2.86''$ ($\Delta H \sim 6.37$ mag) [7] Aa-Ab with $\rho = 0.6259''$ ($\Delta F5ND \sim 3.812$ mag) [8]
HD 53755	...	Y	...	...	...	...	...	...	A-B with $\rho = 6.42''$ + A-C with $\rho = 35.77''$ [2]
HD 66811	N	...	N	...	N	...	N	...	
HD 74920	...	...	...	...	...	...	N	...	
HD 90087	N	...	N	...	...	...	...	...	
HD 93521	N	...	N	...	N	...	...	N	
HD 102415	...	...	N	...	...	...	...	N	
HD 117490	...	...	N	...	...	...	...	...	
HD 124979	N	...	N	...	...	...	...	...	
HD 149757	N	...	N	...	N	N	N	...	
HD 150574	...	...	N	...	...	...	...	...	
HD 163892	N	...	N	...	N	...	Y	N	A-B with $\rho = 2.01''$ ($\Delta Ks \sim 5.31$ mag) + A-C with $\rho = 2.45''$ ($\Delta Ks \sim 5.87$ mag) + A-D with $\rho = 6.45''$ ($\Delta Ks \sim 6.31$ mag) + A-E with $\rho = 6.50''$ ($\Delta Ks \sim 5.05$ mag) [7] 2MASS companion at 6.4″ [5]
HD 175876	Y	...	N	...	N	...	N	...	$\rho = 17.0''$ [1]
HD 184915	...	...	N	...	...	N	...	...	
HD 191423	...	...	N	...	...	...	...	...	
HD 192281	N	...	N	...	N	...	...	N	
HD 203064	N	...	N	...	Y	...	...	N	$\rho = 3.84''$ ($\Delta I \sim 9.48$ mag) [5]
HD 210839	N	...	N	...	N	...	...	...	
HD 228841	...	...	N	...	...	...	...	...	

References. [1] Mason et al. (1998); [2] Mason et al. (2004); [3] Mason et al. (2009); [4] Mason et al. (2011); [5] Turner et al. (2008); [6] Tokovinin et al. (2010); [7] Sana et al. (2014); [8] Aldoretta et al. (2015).

Appendix D: Comparison with literature data

Table D.1 compares our stellar parameters with those in the literature.

Table D.1. Comparison between stellar parameters and abundances derived in this work and those in the literature.

Star	$v \sin i$ [km s^{-1}]	$T_{\rm eff}$ [K]	$\log g$	$\log g_{\rm C}$	y	$\log \epsilon$(C)	$\log \epsilon$(N)	$\log \epsilon$(O)	[N/C]	[N/O]	Source
Cooler stars (DETAIL/SURFACE)											
HD 93521	405 ± 15	30 000 ± 1000	3.60 ± 0.10	3.78 ± 0.10	0.166 ± 0.025	7.68 ± 0.12	8.10 ± 0.13	8.33 ± 0.21	0.42 ± 0.21	–0.23 ± 0.12	This work
	400 ± 25	33 500 ± 1500	...	3.80 ± 0.20	0.200 ± 0.050	...	...	...	...	...	Lennon et al. (1991)
	435 ± 20	33 500 ± 1500	...	...	0.180 ± 0.030	...	...	...	...	...	Howarth & Smith (2001)
	390 ± 10	30 900 ± 700	3.67 ± 0.12	...	0.178 ± 0.020	7.56	7.97	8.24	0.41	–0.27	Rauw et al. (2012)
HD 102415	357 ± 15	32 900 ± 1000	4.10 ± 0.10	4.19 ± 0.10	0.158 ± 0.025	<7.54	8.16 ± 0.13	8.22 ± 0.21	>0.62	–0.06 ± 0.12	This work
	376 ± 10	31 000 ± 1500	3.50 ± 0.15	3.70	0.174 ± 0.068	≤7.78	$8.88^{+0.24}_{-0.21}$	≤8.48	≥1.10	≥0.40	Martins et al. (2015b)
HD 149757 (ζ Oph)	378 ± 15	31 500 ± 1000	3.87 ± 0.10	3.99 ± 0.10	0.135 ± 0.025	8.07 ± 0.12	7.85 ± 0.13	8.37 ± 0.21	–0.22 ± 0.21	–0.52 ± 0.12	This work
	400	32 500	3.70	3.85	0.160	...	...	...	...	...	Puls et al. (1996)
	399 ± 20	34 300 ± 1500	...	...	0.200 ± 0.030	...	...	...	...	...	Howarth & Smith (2001)
	400	32 500 ± 1500	3.50 ± 0.10	3.77	0.160 ± 0.030	...	...	...	...	...	Herrero et al. (2002)
	400	32 000 ± 1000	3.65 ± 0.10	$3.85^{+0.10}_{-0.08}$	0.145 ± 0.022	...	...	...	...	...	Repolust et al. (2004)
	340 ± 25	26 400 ± 700	3.80 ± 0.09	4.05 ± 0.07	...	...	...	...	...	...	Frémat et al. (2005)
	400	32 100 ± 700	3.62	$3.83^{+0.16}_{-0.05}$	$0.099^{+0.032}_{-0.016}$	...	...	...	...	...	Mokiem et al. (2005)
	...	33 500 ± 1700	...	3.85 ± 0.10	0.145	...	...	...	...	...	Repolust et al. (2005)[b]
	400 ± 20	34 000 ± 1000	3.70 ± 0.10	...	0.110 ± 0.028	7.86 ± 0.30	8.34 ± 0.30	8.69 ± 0.30	0.48	–0.35	Villamariz & Herrero (2005)
	400	32 000 ± 2000	3.60 ± 0.20	3.80	...	...	...	...	...	...	Marcolino et al. (2009)
	400 ± 10	31 000 ± 1000	3.60 ± 0.15	...	...	...	...	...	...	...	Martins et al. (2015a)
HD 184915 (κ Aql)	252 ± 15	27 800 ± 1000	3.70 ± 0.10	3.77 ± 0.10	0.183 ± 0.025	<8.18	8.46 ± 0.13	8.62 ± 0.21	>0.28	–0.16	This work
	270	26 800	3.56	...	0.160 ± 0.011	...	...	...	...	...	Lyubimkov et al. (2004)[a]
	229 ± 13	27 100 ± 500	3.49 ± 0.05	3.53 ± 0.06	...	...	...	...	...	...	Frémat et al. (2005)
	249 ± 7	26 700 ± 750	3.59 ± 0.07	...	...	...	...	...	...	...	Huang & Gies (2008)
HD 198781	222 ± 15	29 100 ± 1000	3.90 ± 0.10	3.94 ± 0.10	0.230 ± 0.025	<8.09	8.62 ± 0.13	8.78 ± 0.21	>0.53	–0.16 ± 0.12	This work
	224	24 400	3.50	...	0.148 ± 0.011	...	...	...	...	...	Lyubimkov et al. (2004)[a]
Hotter stars (CMFGEN)											
HD 13268	301 ± 15	32 500 ± 1500	3.42 ± 0.15	3.55 ± 0.15	0.206 ± 0.030	≤7.50	8.61 ± 0.34	8.10 ± 0.21	≥1.11	0.51 ± 0.40	This work
	300	36 000 ± 2000	3.70 ± 0.30	...	...	...	...	...	...	...	Kendall et al. (1996)
	320	35 000	3.30	3.50	0.200	...	...	...	...	...	Puls et al. (1996)
	320	35 000 ± 1500	3.30 ± 0.10	3.42	≥0.200	...	...	...	...	...	Herrero et al. (1992)
	300	33 000 ± 1000	3.25 ± 0.10	$3.48^{+0.11}_{-0.08}$	0.200 ± 0.019	...	...	...	...	...	Repolust et al. (2004)
	...	33 000 ± 1650	...	3.48 ± 0.10	0.200	...	...	...	...	...	Repolust et al. (2005)[b]
	310 ± 10	32 000 ± 1500	3.50 ± 0.15	3.63	0.167 ± 0.069	≤7.70	$8.70^{+0.24}_{-0.17}$	$8.49^{+0.35}_{-0.20}$	≥1.00	0.21	Martins et al. (2015b)
HD 14434	408 ± 15	40 000 ± 1500	3.89 ± 0.15	4.03 ± 0.15	0.103 ± 0.030	7.96 ± 0.27	8.81 ± 0.34	≤8.10	0.85 ± 0.43	≥0.71	This work
	380	43 000 ± 2000	3.80 ± 0.20	...	...	...	...	...	...	...	Kendall et al. (1996)
HD 14442	285 ± 15	39 200 ± 1500	3.69 ± 0.15	3.78 ± 0.15	0.097 ± 0.030	7.10 ± 0.27	8.61 ± 0.34	≤8.10	1.51 ± 0.43	≥0.51	This work
	260	43 000 ± 2000	3.60 ± 0.20	...	...	...	...	...	...	...	Kendall et al. (1996)
HD 15137	267 ± 15	29 500 ± 1500	3.18 ± 0.15	3.31 ± 0.15	0.112 ± 0.030	7.63 ± 0.27	8.27 ± 0.34	≤8.30	0.64 ± 0.43	≥–0.03	This work
	234 ± 10	29 700 ± 700	3.50 ± 0.10	...	...	...	...	...	...	...	McSwain et al. (2007)
	258 ± 20	29 700 ± 1700	3.50 ± 0.25	...	...	...	...	...	...	...	McSwain et al. (2010)
HD 46056	350 ± 15	34 500 ± 1500	3.90 ± 0.15	4.00 ± 0.15	0.088 ± 0.030	8.34 ± 0.27	7.78 ± 0.34	8.32 ± 0.21	–0.56 ± 0.43	–0.54 ± 0.40	This work
	330 ± 10	34 500 ± 1000	3.75 ± 0.15	...	...	8.28 ± 0.07	7.78 ± 0.14	8.45 ± 0.28	–0.50	–0.67	Martins et al. (2015a)
HD 46485	315 ± 15	37 000 ± 1500	4.00 ± 0.15	4.08 ± 0.15	0.076 ± 0.030	8.46 ± 0.27	7.95 ± 0.34	8.72 ± 0.21	–0.51 ± 0.43	–0.77 ± 0.40	This work
	300 ± 10	36 000 ± 1000	3.75 ± 0.15	...	...	$8.43^{+0.11}_{-0.08}$	7.95 ± 0.10	$8.64^{+0.22}_{-0.20}$	–0.48	–0.69	Martins et al. (2015a)

Notes. [a] The value of y corresponding to ξ derived from He I lines is chosen. [b] Only values from the infrared analysis are indicated. [c] Values not corrected for Galactic chemical gradient.

Table D.1. continued.

Star	$v \sin i$ [km s^{-1}]	$T_{\rm eff}$ [K]	$\log g$	$\log g_{\rm C}$	y	$\log \epsilon$(C)	$\log \epsilon$(N)	$\log \epsilon$(O)	[N/C]	[N/O]	Source
HD 66811 (ζ Pup)	225 ± 15	41 000 ± 1500	3.55 ± 0.15	3.62 ± 0.15	0.148 ± 0.030	≤7.00	8.94 ± 0.34	8.20 ± 0.21	≥1.94	0.74	This work
	220	42 000	3.50	3.60	0.107	...	...	...	...	...	Puls et al. (1996)
	220	39 000 ± 1500	3.55 ± 0.10	3.59 ± 0.09	0.167 ± 0.021	...	...	...	...	...	Repolust et al. (2004)
	...	39 000 ± 1950	...	3.59 ± 0.10	0.145	...	...	...	...	...	Repolust et al. (2005)[b]
	210	40 000 ± 1000	...	3.64 ± 0.10	0.140	6.60 ± 0.25	9.10 ± 0.17	8.13 ± 0.30	2.50	0.97	Bouret et al. (2012)
	210 ± 10	40 000 ± 1000	3.64 ± 0.15	...	...	6.60 ± 0.22	9.10 ± 0.17	8.13 ± 0.29	2.50	0.97	Martins et al. (2015a)
HD 69106	306 ± 15	29 500 ± 1500	3.45 ± 0.15	3.58 ± 0.15	0.091 ± 0.030	7.88 ± 0.27	7.74 ± 0.34	8.47 ± 0.21	–0.14 ± 0.43	–0.73 ± 0.40	This work
	320 ± 10	29 000 ± 1000	3.40 ± 0.15	...	...	$7.60^{+0.22}_{-0.11}$	≤8.00	$8.40^{+0.21}_{-0.14}$	≤0.40	≤–0.40	Martins et al. (2015a)
HD 117490	361 ± 15	30 000 ± 1500	3.55 ± 0.15	3.70 ± 0.15	0.141 ± 0.030	≤7.39	8.50 ± 0.34	8.15 ± 0.21	≥1.11	0.35 ± 0.40	This work
	375 ± 10	30 500 ± 1500	3.50 ± 0.15	3.66	$0.138^{+0.067}_{-0.037}$	≤7.48	$8.88^{+0.17}_{-0.15}$	$8.40^{+0.45}_{-0.35}$	≥1.40	0.48	Martins et al. (2015b)
HD 150574	233 ± 15	31 500 ± 1500	3.32 ± 0.15	3.41 ± 0.15	0.172 ± 0.030	7.48 ± 0.27	≥9.08	≥8.93	≥1.60	...	This work
	240 ± 10	31 000 ± 1500	3.40 ± 0.15	3.49	0.187 ± 0.040	≤7.70	≥9.00	$8.78^{+0.21}_{-0.17}$	≥1.30	≥0.22	Martins et al. (2015b)
HD 191423	420 ± 15	30 600 ± 1500	3.33 ± 0.15	3.57 ± 0.15	0.134 ± 0.030	≤7.24	8.33 ± 0.34	≤8.33	≥1.09	≥0.00	This work
	450	34 000 ± 1500	3.40 ± 0.10	3.68	$0.200^{+0.050}_{-0.030}$	...	...	...	...	...	Herrero et al. (1992)
	450	34 000	3.40	3.70	0.200	...	...	...	...	...	Puls et al. (1996)
	435	$34\,300^{+700}_{-800}$	...	...	0.190 ± 0.030	...	...	...	...	...	Howarth & Smith (2001)
	450	35 000 ± 1000	3.40 ± 0.10	...	0.120 ± 0.030	7.57 ± 0.24	8.36 ± 0.17	8.23 ± 0.48	0.79	0.13	Villamariz et al. (2002)[c]
	400	32 500 ± 1000	3.35 ± 0.10	$3.60^{+0.11}_{-0.08}$	0.167 ± 0.021	...	...	...	...	...	Repolust et al. (2004)
	...	32 000 ± 1600	...	3.56 ± 0.10	0.167	...	...	...	...	...	Repolust et al. (2005)[b]
	410	30 600 ± 1000	3.50 ± 0.10	3.67	...	...	8.73 ± 0.20	...	...	...	Mahy et al. (2015)
	445 ± 10	31 500 ± 1500	3.50 ± 0.15	3.72	0.200 ± 0.051	...	≥8.70	...	...	...	Martins et al. (2015b)
HD 192281 (V819 Cyg)	276 ± 15	39 000 ± 1500	3.64 ± 0.15	3.73 ± 0.15	0.103 ± 0.030	8.00 ± 0.27	8.76 ± 0.34	8.05 ± 0.21	0.76 ± 0.43	0.71 ± 0.40	This work
	245 ± 10	39 000 ± 1000	3.65 ± 0.15	...	...	$8.11^{+0.37}_{-0.33}$	$8.92^{+0.41}_{-0.22}$	8.15 ± 0.09	0.81	0.77	Martins et al. (2015a)
HD 203064 (68 Cyg)	298 ± 15	35 000 ± 1500	3.73 ± 0.15	3.82 ± 0.15	0.076 ± 0.030	7.92 ± 0.27	8.23 ± 0.34	8.46 ± 0.21	0.31 ± 0.43	–0.23 ± 0.40	This work
	315	37 500	3.50	3.65	0.123	...	...	...	...	...	Puls et al. (1996)
	315	37 500 ± 1000	3.50 ± 0.10	3.62	0.120 ± 0.030	...	...	...	...	...	Herrero et al. (1992)
	300	34 500 ± 1000	3.50 ± 0.10	$3.60^{+0.09}_{-0.08}$	0.091 ± 0.017	...	...	...	...	...	Repolust et al. (2004)
	...	34 500 ± 1700	...	3.60 ± 0.10	0.167	...	...	...	...	...	Repolust et al. (2005)[b]
	300 ± 10	34 000 ± 1000	3.60 ± 0.15	...	...	8.20 ± 0.11	8.20 ± 0.19	...	0.00	...	Martins et al. (2015a)
HD 210839 (λCep)	214 ± 15	36 000 ± 1500	3.50 ± 0.15	3.56 ± 0.15	0.113 ± 0.030	7.83 ± 0.27	8.74 ± 0.34	8.13 ± 0.21	0.91 ± 0.43	0.61 ± 0.40	This work
	100	38 000	3.60	3.65	0.091	...	...	...	...	...	Puls et al. (1996)
	250	37 000 ± 1500	3.55 ± 0.10	...	0.250 ± 0.030	...	...	...	...	...	Herrero et al. (2000)
	200	36 000 ± 1500	3.55 ± 0.10	3.58 ± 0.09	0.091 ± 0.017	...	...	...	...	...	Repolust et al. (2004)
	210	36 000 ± 1000	...	3.54 ± 0.10	0.107	8.22 ± 0.21	8.70 ± 0.15	8.48 ± 0.14	0.48	0.22	Bouret et al. (2012)
	210 ± 10	36 000 ± 1000	3.50 ± 0.15	...	...	7.78 ± 0.15	$8.78^{+0.14}_{-0.09}$	8.40 ± 0.35	1.00	0.38	Martins et al. (2015a)
HD 228841	305 ± 15	34 000 ± 1500	3.50 ± 0.15	3.62 ± 0.15	0.112 ± 0.030	7.48 ± 0.27	8.74 ± 0.34	8.67 ± 0.21	1.26 ± 0.43	0.07 ± 0.40	This work
	317	34 500 ± 1000	3.50 ± 0.10	3.62	...	...	8.73 ± 0.22	...	...	...	Mahy et al. (2015)

Appendix E: Comparison with CMFGEN spectra

This appendix provides a comparison between the observations of the hotter stars and their best-fit CMFGEN models. Lines useful for the abundance derivations are indicated (see Sect. 4.3.2 for details on the fitting procedure and Table B.1 for the actual list of lines used for each star). Finally, in the caption we mention the remaining fitting imperfections for each star. In this context, we recall that the wind parameters were not derived, explaining why wind-sensitive lines (e.g. N III 4634–4643, He II 4686) may not be perfectly fitted.

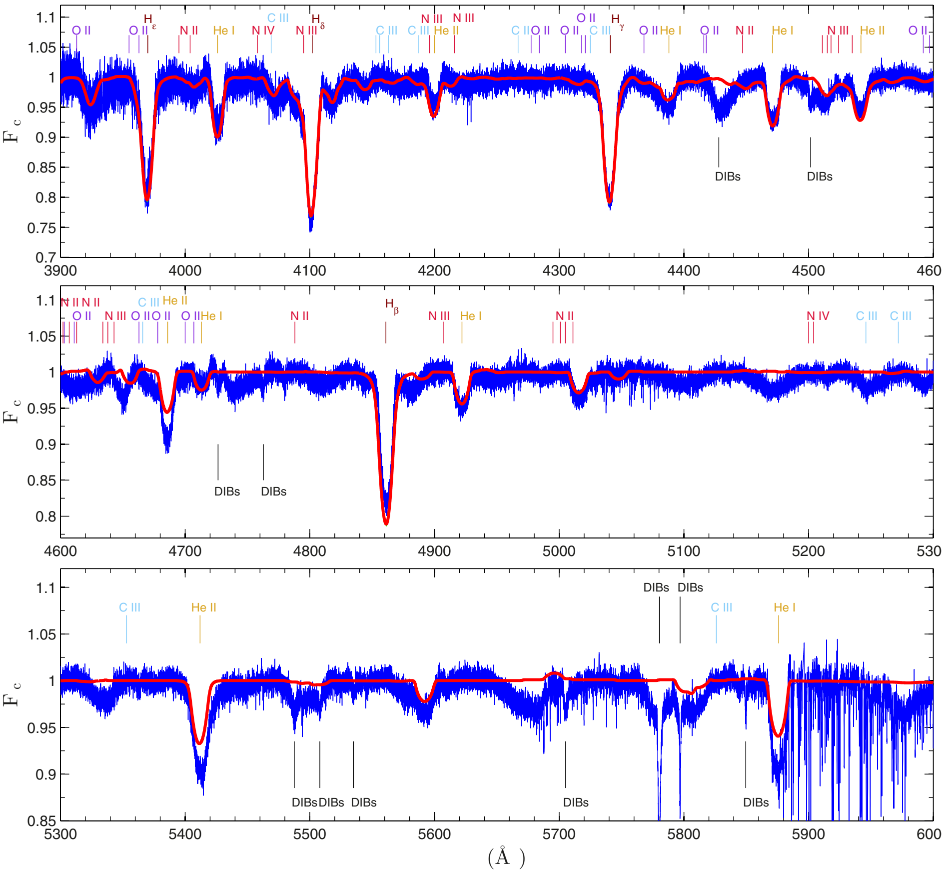

Fig. E.1. Best-fit CMFGEN model (red) compared to the observed spectrum (blue) of BD +34°1058 (O8nn; $v\sin i$ = 424 km s^{-1}). Diagnostic lines are indicated. The He I 5876 line appears too strong compared to the best-fit model, while the fit of He II 4686 and He II 5412 is imperfect, probably because of normalisation problems.

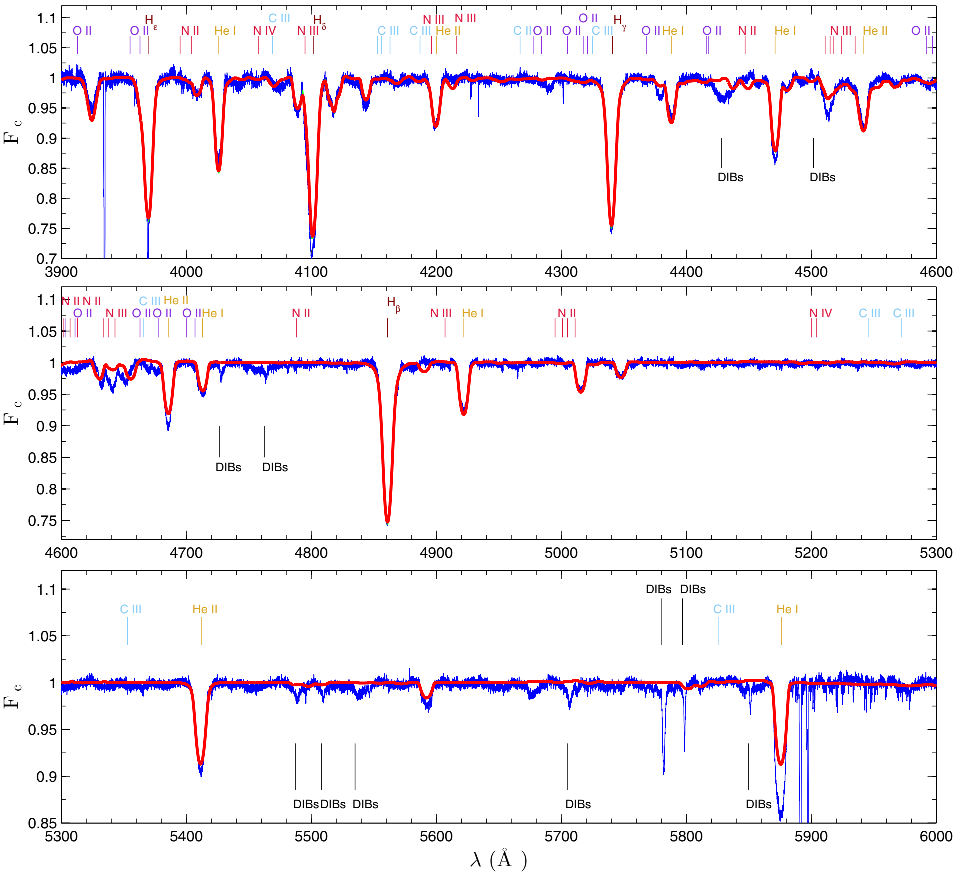

Fig. E.2. Same as Fig. E.1, but for HD 13268 (ON8.5IIIn; $v \sin i = 301$ km s^{-1}). He I lines are generally well fitted, except He I 5876. Some nitrogen lines, e.g. N III 4634–4643, are not perfectly fitted.

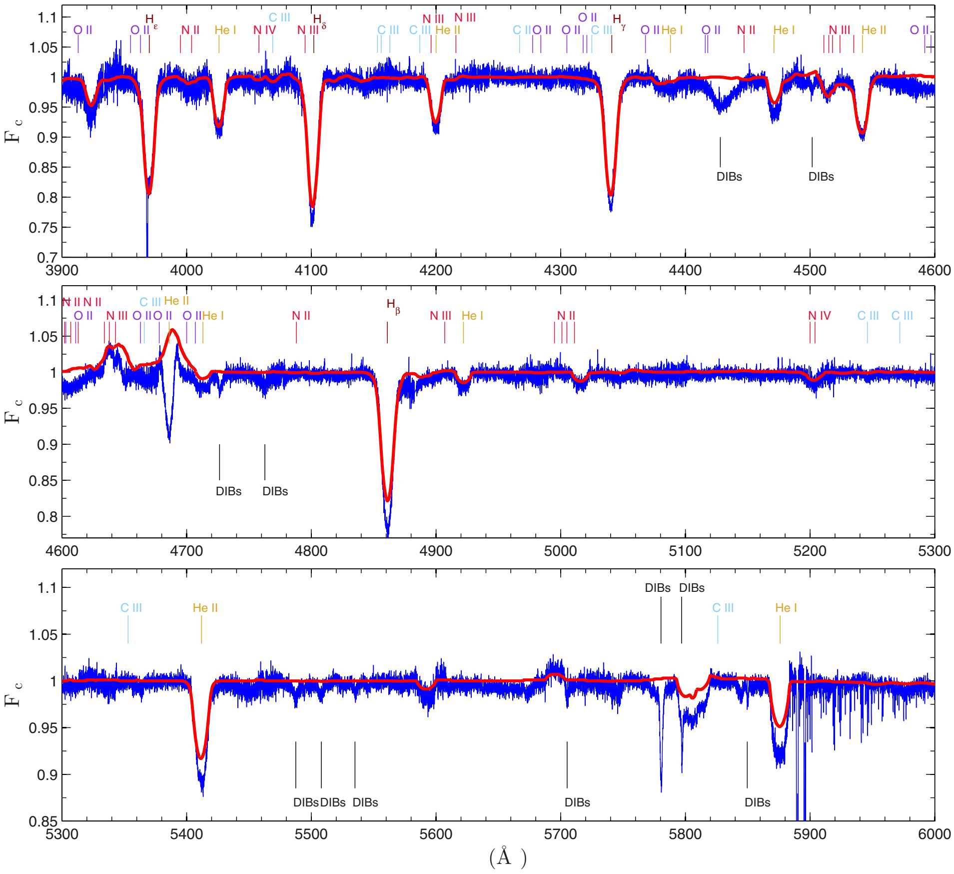

Fig. E.3. Same as Fig. E.1, but for HD 14434 (O5.5Vnn((f))p; $v \sin i = 408$ km s^{-1}). He I lines are generally well fitted, except He I 5876; some local normalisation problems explain the apparently imperfect fit to Hβ and He II 5412. Because wind parameters were not derived, the wind-sensitive line He II 4686 is not well reproduced as too much emission is seen for the best-fit model.

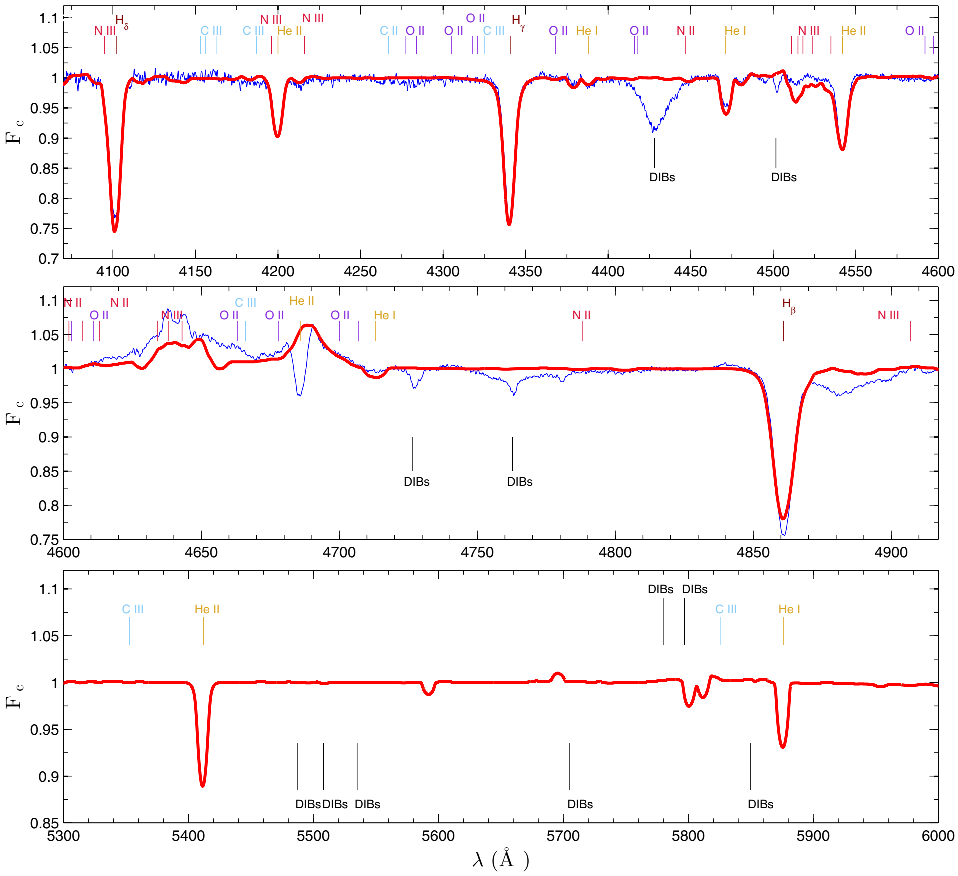

Fig. E.4. Same as Fig. E.1, but for HD 14442 (O5n(f)p; $v \sin i$ = 285 km s^{-1}). Because wind parameters were not derived, wind-sensitive lines are not well reproduced: too much emission is seen in He II 4686 for the best-fit model, but too little emission for the neighbouring N III 4634–4643 lines.

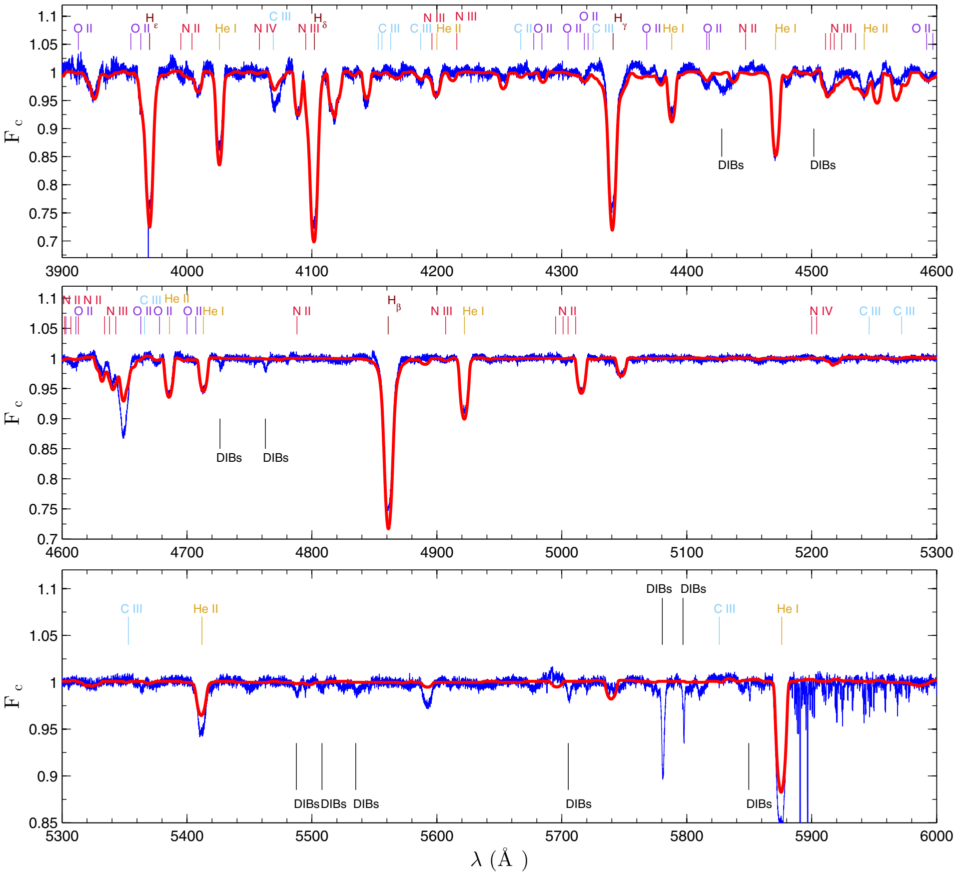

Fig. E.5. Same as Fig. E.1, but for HD 15137 (O9.5II-IIIn; $\upsilon \sin i$ = 267 km s^{-1}). The wings of Hγ are affected by a normalisation problem. He II 5412 and He I 5876 appear somewhat too weak in the model.

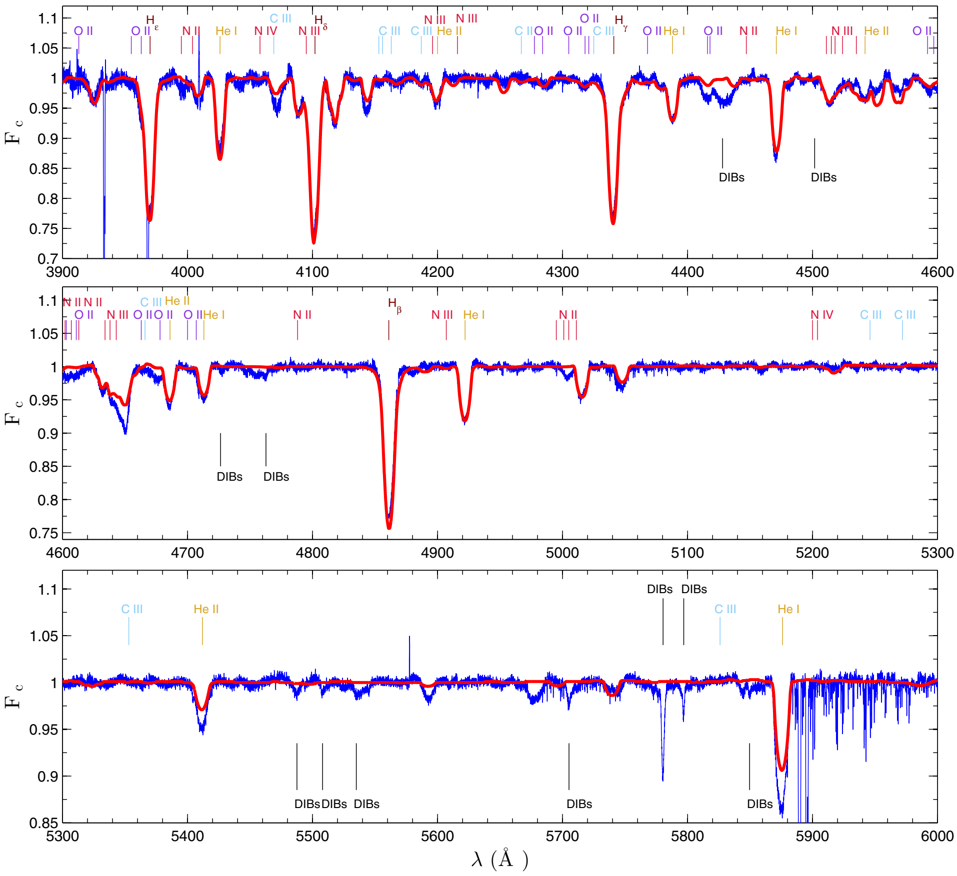

Fig. E.6. Same as Fig. E.1, but for HD 15642 (O9.5II-IIIn; $v \sin i$ = 335 km s^{-1}). While other He lines appear well fitted, He II 5412 and He I 5876 are too weak in the model.

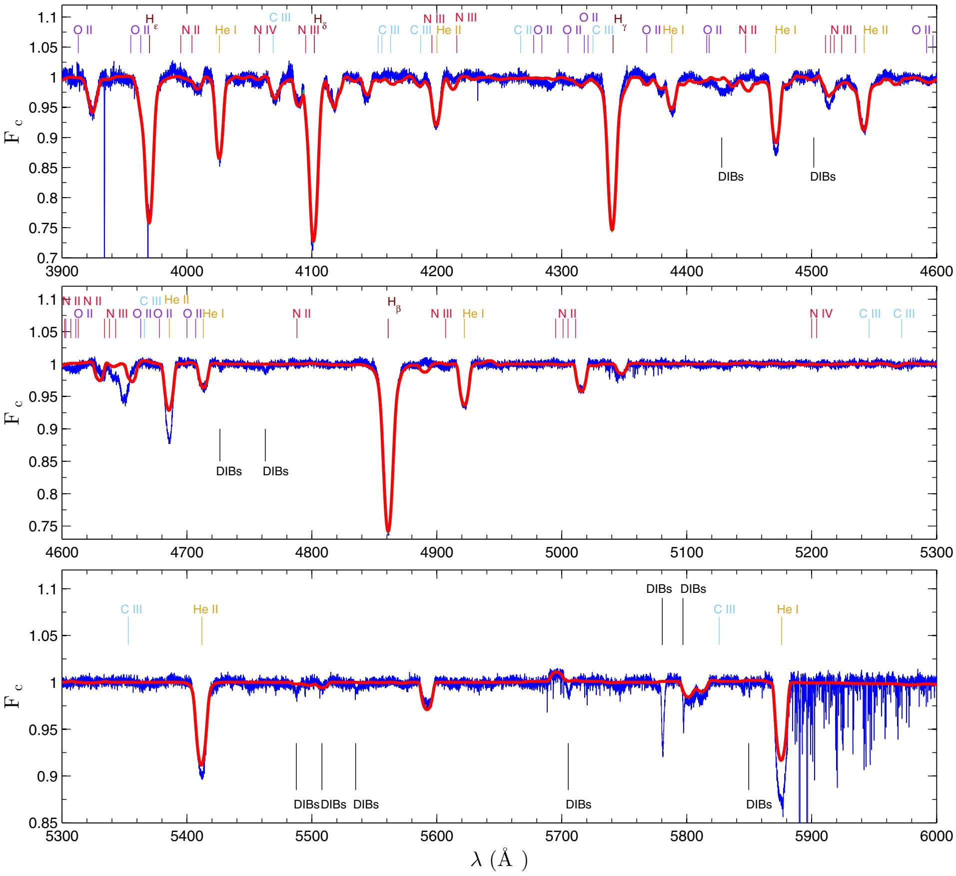

Fig. E.7. Same as Fig. E.1, but for HD 41161 (O8Vn; $v \sin i = 303$ km s^{-1}). While other He lines appear well fitted, He II 4686 and He I 5876 are too weak in the model.

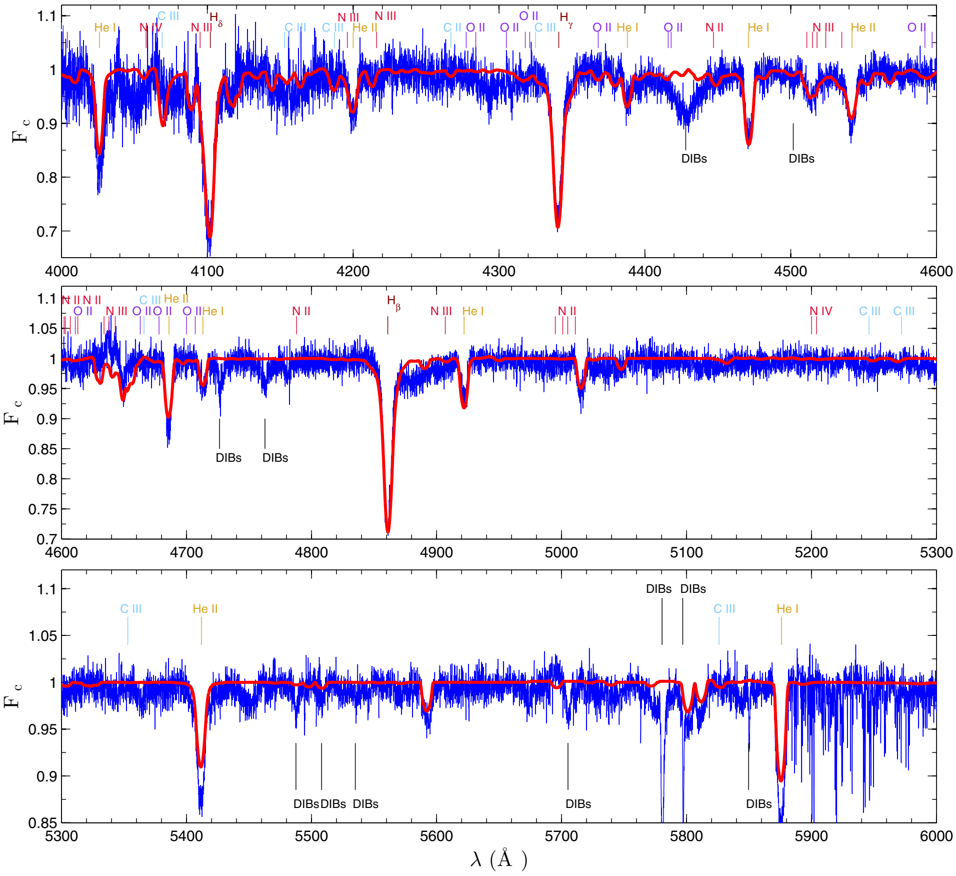

Fig. E.8. Same as Fig. E.1, but for HD 41997 (O7.5Vn((f)); $v \sin i = 247$ km s^{-1}). Our sole ELODIE spectrum of this star has a low S/N, rendering the fitting more uncertain. While other He lines appear well fitted, He II 5412 and He I 5876 are too weak in the model.

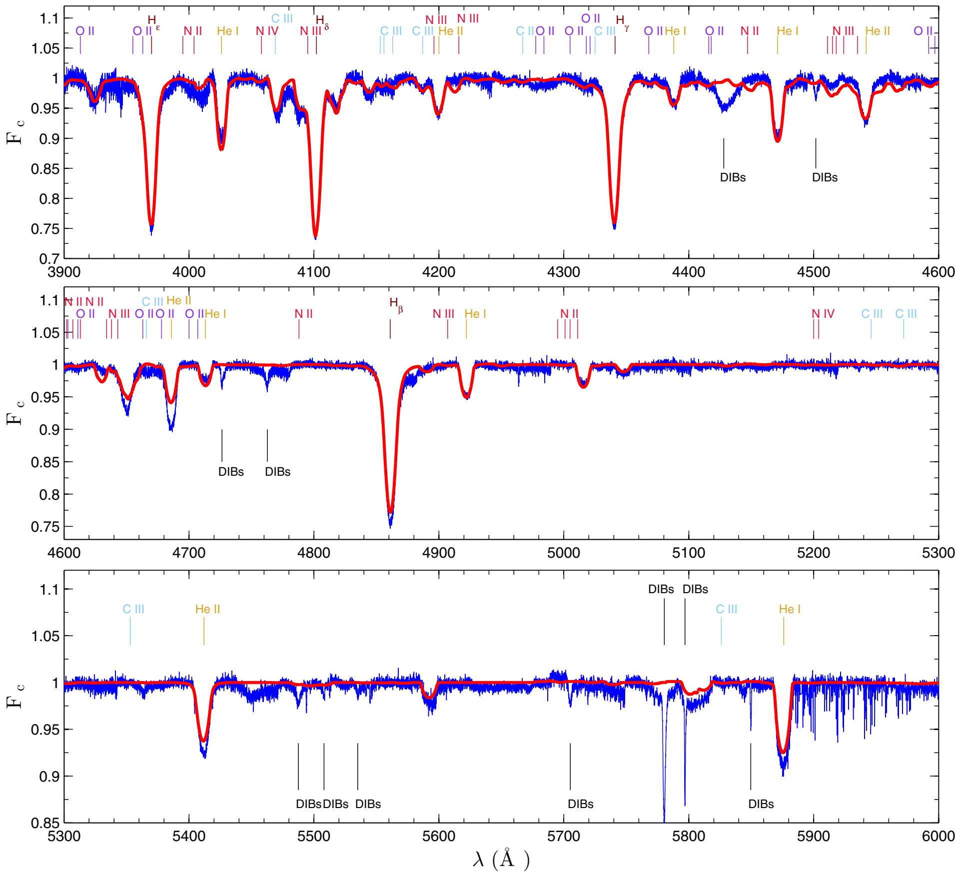

Fig. E.9. Same as Fig. E.1, but for HD 46056 (O8Vn; $\upsilon \sin i$ = 350 km s^{-1}). While other He lines appear well fitted, He II 4686 is too weak in the model, which is explained by the fact that wind parameters were not derived (see Sect. 4.3.2).

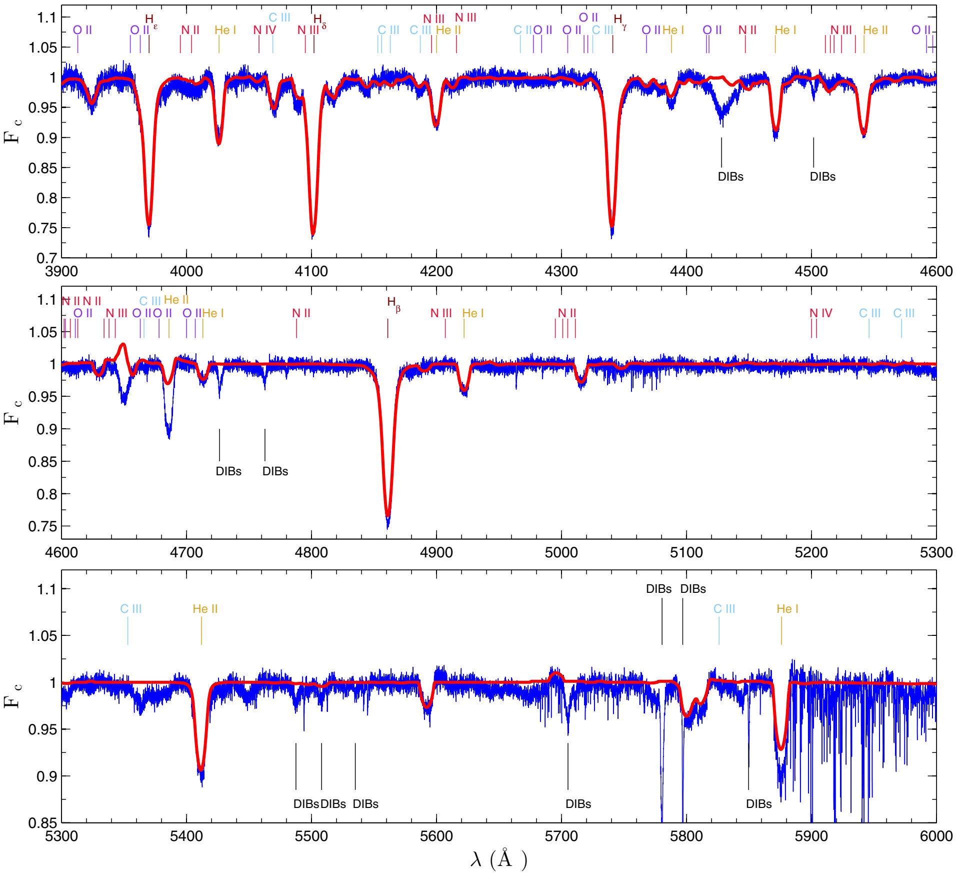

Fig. E.10. Same as Fig. E.1, but for HD 46485 (O7V((f))nz; $\upsilon \sin i = 315$ km s^{-1}). The He I 5876 and He II 4686 lines appear too strong compared to the best-fit model.

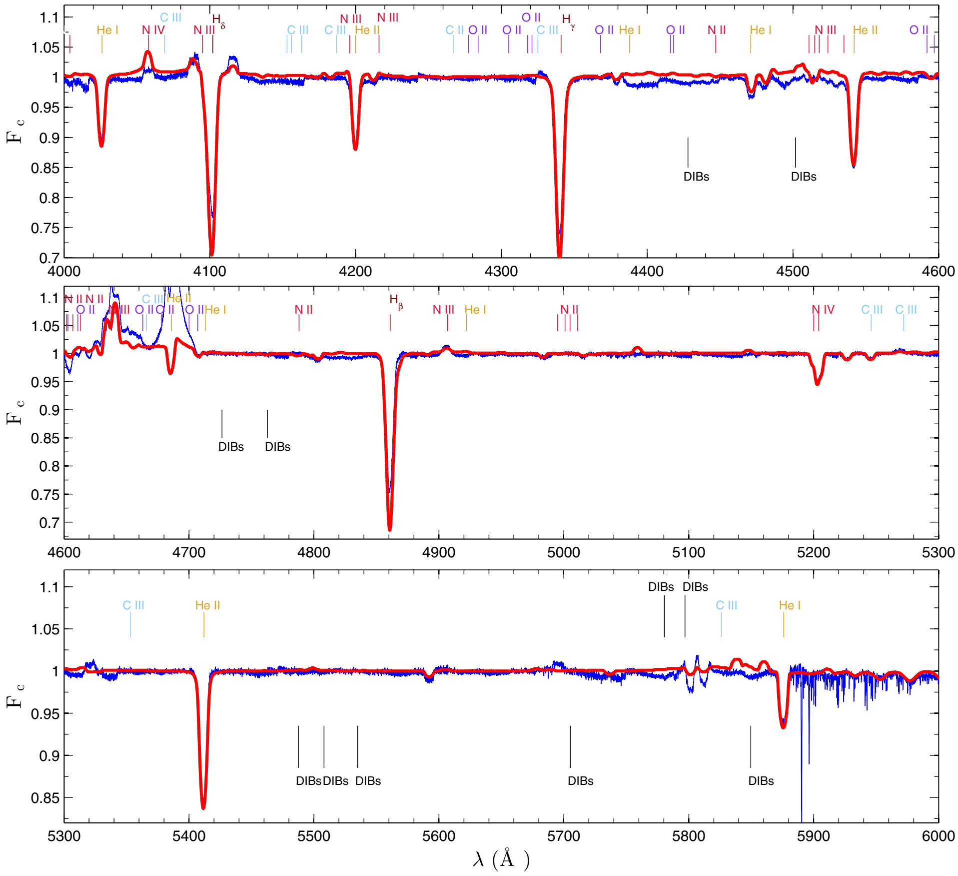

Fig. E.11. Same as Fig. E.1, but for HD 66811 (O4I(n)fp; $v \sin i = 225$ km s^{-1}). The normalisation around Hβ is imperfect, leading to some slight mismatch between the observation and the fit; the emission of the He II 4686 line is not reproduced in the model, but we recall that wind parameters were not derived (see Sect. 4.3.2).

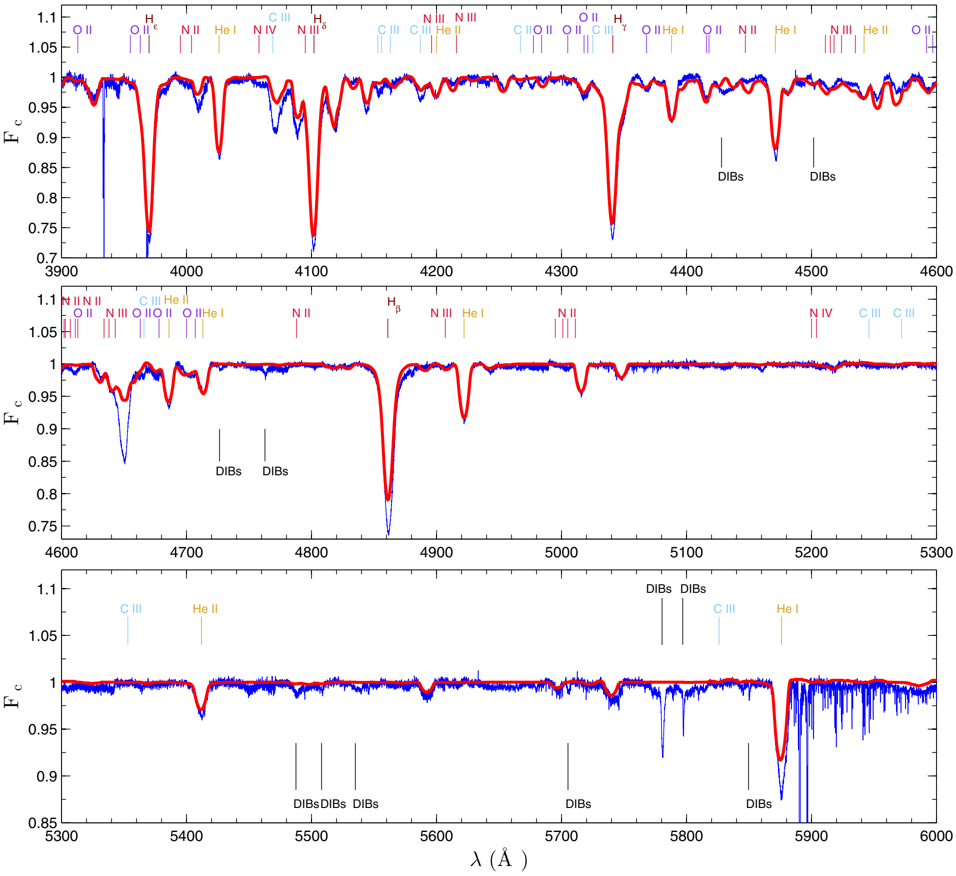

Fig. E.12. Same as Fig. E.1, but for HD 69106 (O9.7IIn; $\upsilon \sin i$ = 306 km s^{-1}). The Hβ and He I 5876 lines appear too strong compared to the best-fit model.

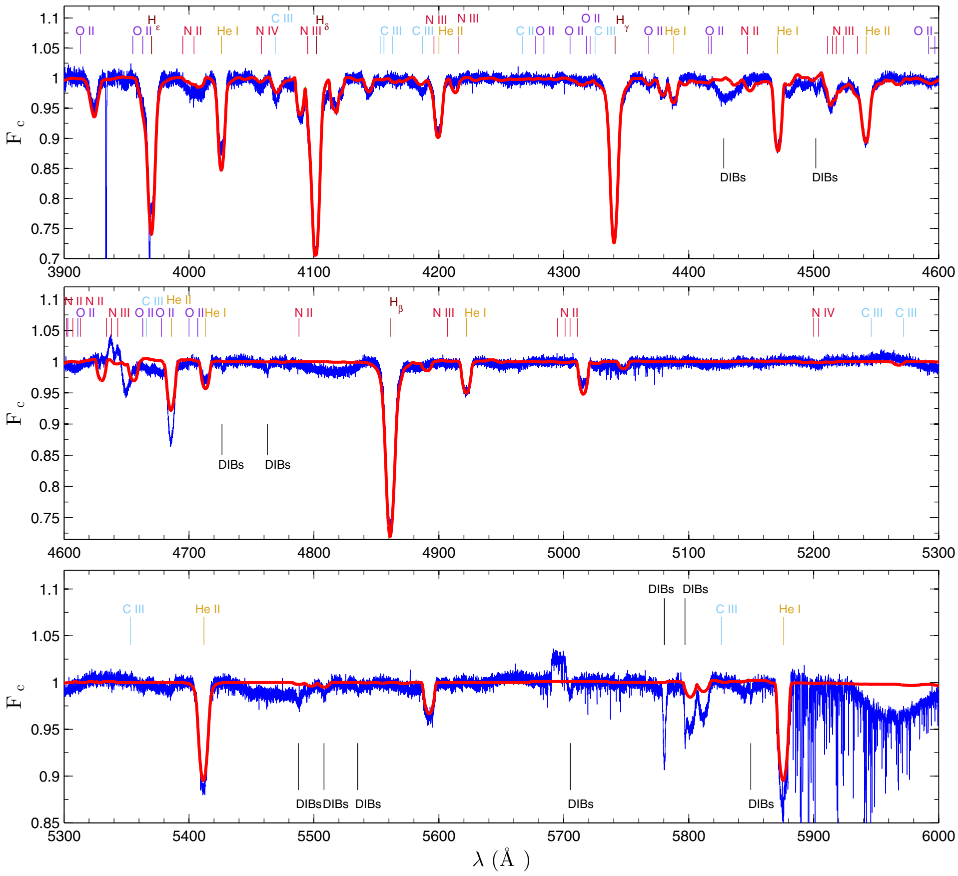

Fig. E.13. Same as Fig. E.1, but for HD 74920 (O7.5IVn((f)); $v \sin i = 274$ km s^{-1}). The He II 4686 line appears too strong compared to the best-fit model, but this mismatch may be due to a normalisation issue.

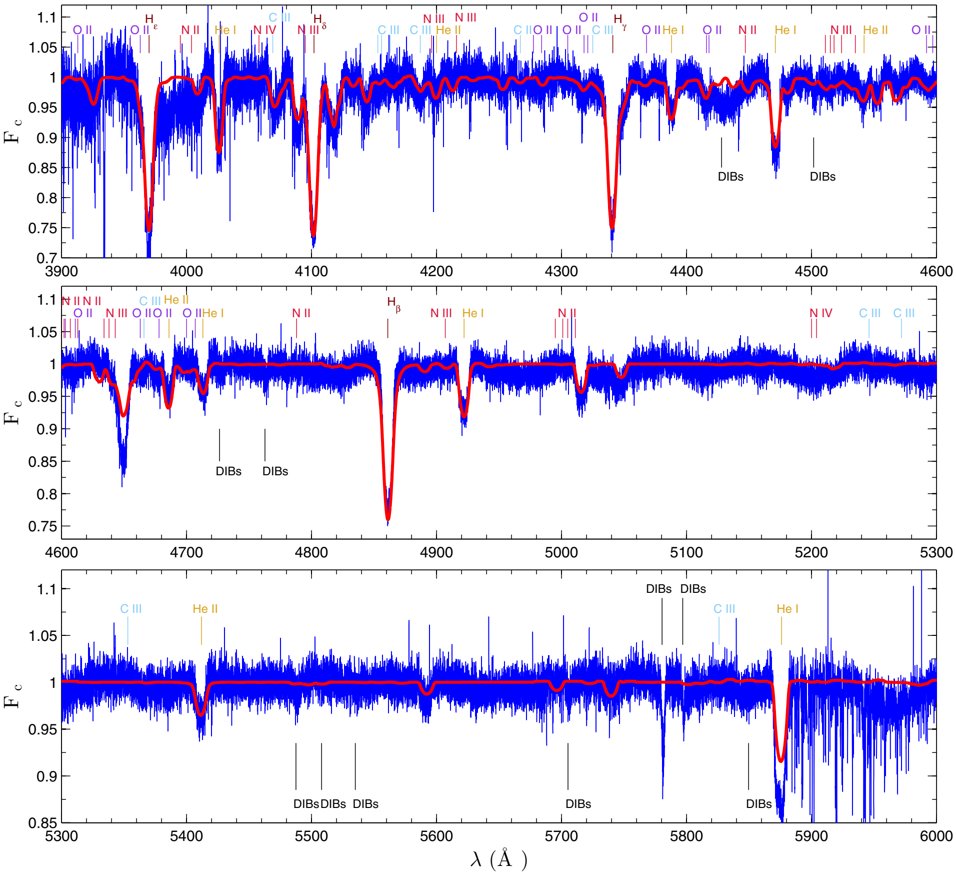

Fig. E.14. Same as Fig. E.1, but for HD 92554 (O9.5III; $v \sin i$ = 303 km s^{-1}). Our CORALIE spectra of this star have a low S/N, rendering the fitting more uncertain. Despite a good fit of the He lines, He I 5876 appears weaker than observed.

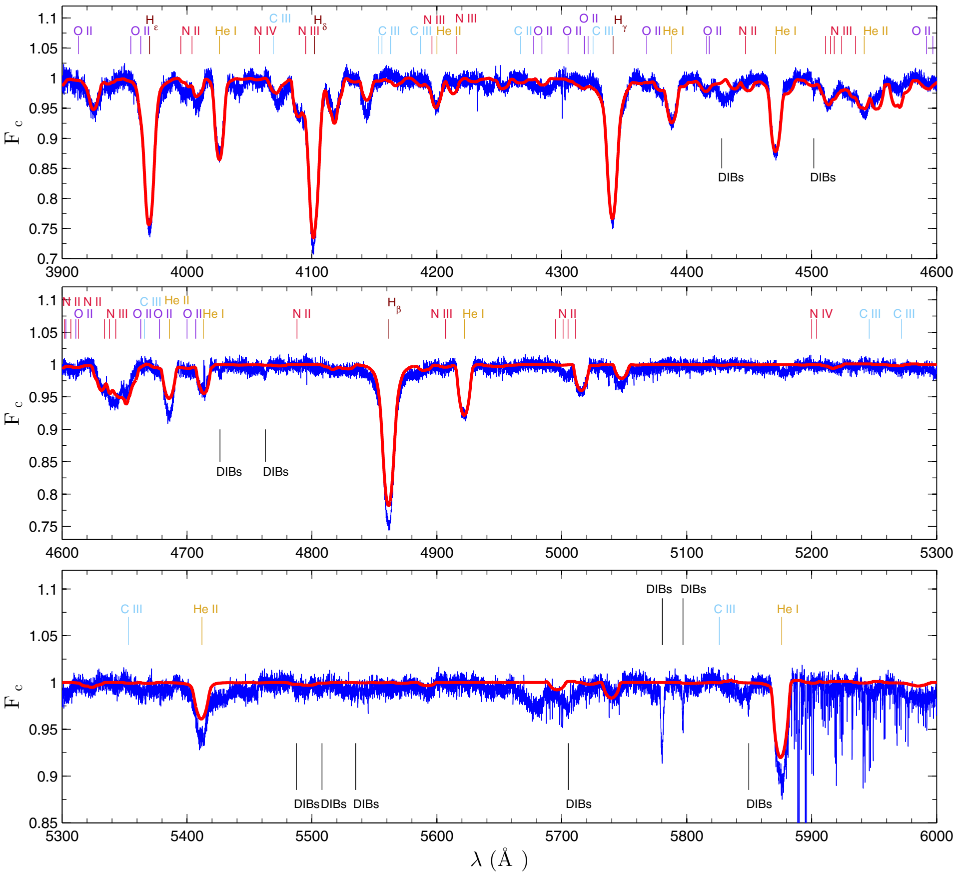

Fig. E.15. Same as Fig. E.1, but for HD 117490 (ON9.5IIInn; $v \sin i$ = 361 km s^{-1}). Some small mismatches between the model and observation for Hβ and He II 5412 are mainly due to normalisation imperfections.

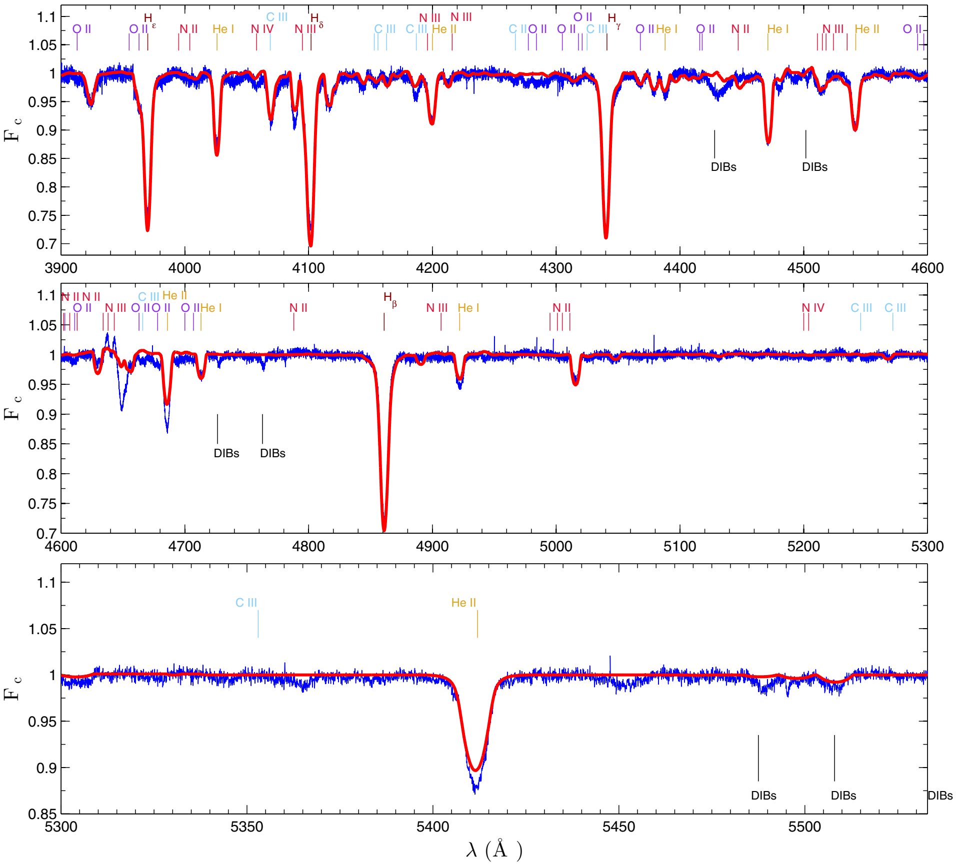

Fig. E.16. Same as Fig. E.1, but for HD 124979 (O7.5IV(n)((f)); $v \sin i$ = 246 km s^{-1}). Despite a good fit of the He lines, He II 4686 and He II 5412 appear weaker than observed; however, the normalisation is imperfect near 4686 Å.

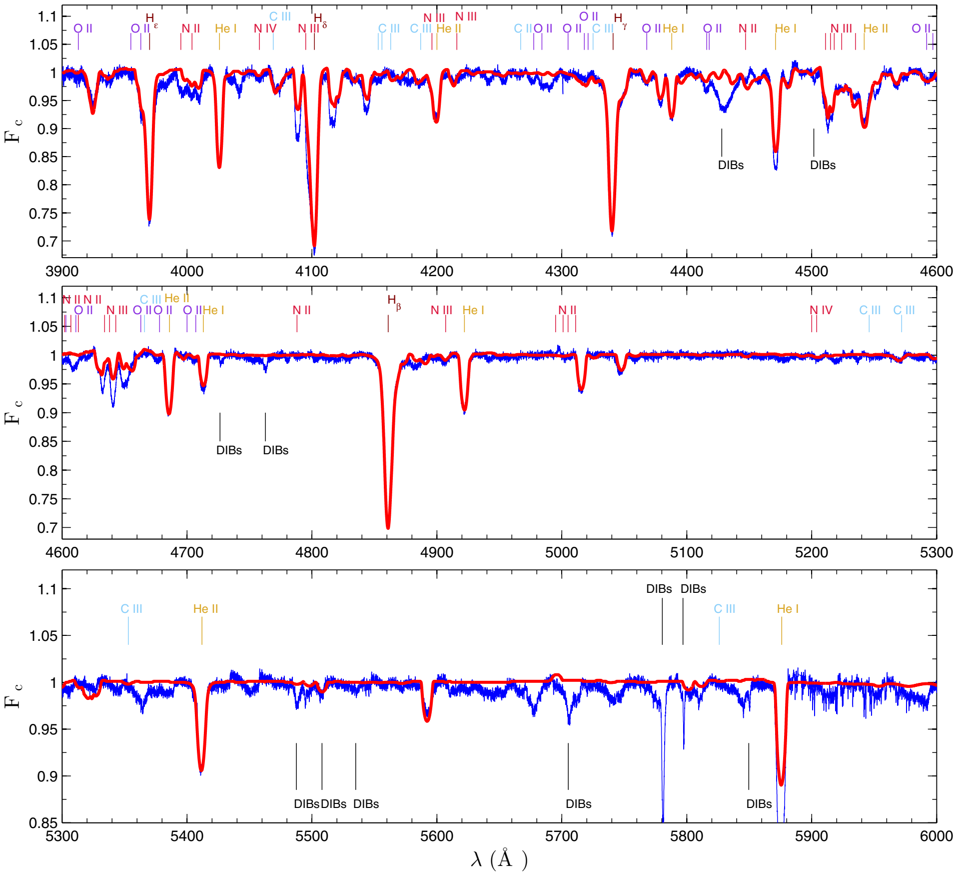

Fig. E.17. Same as Fig. E.1, but for HD 150574 (ON9III(n); $v \sin i = 233$ km s^{-1}). The observed He I 5876 line appears too strong compared to the model, despite a good fit of the other He lines.

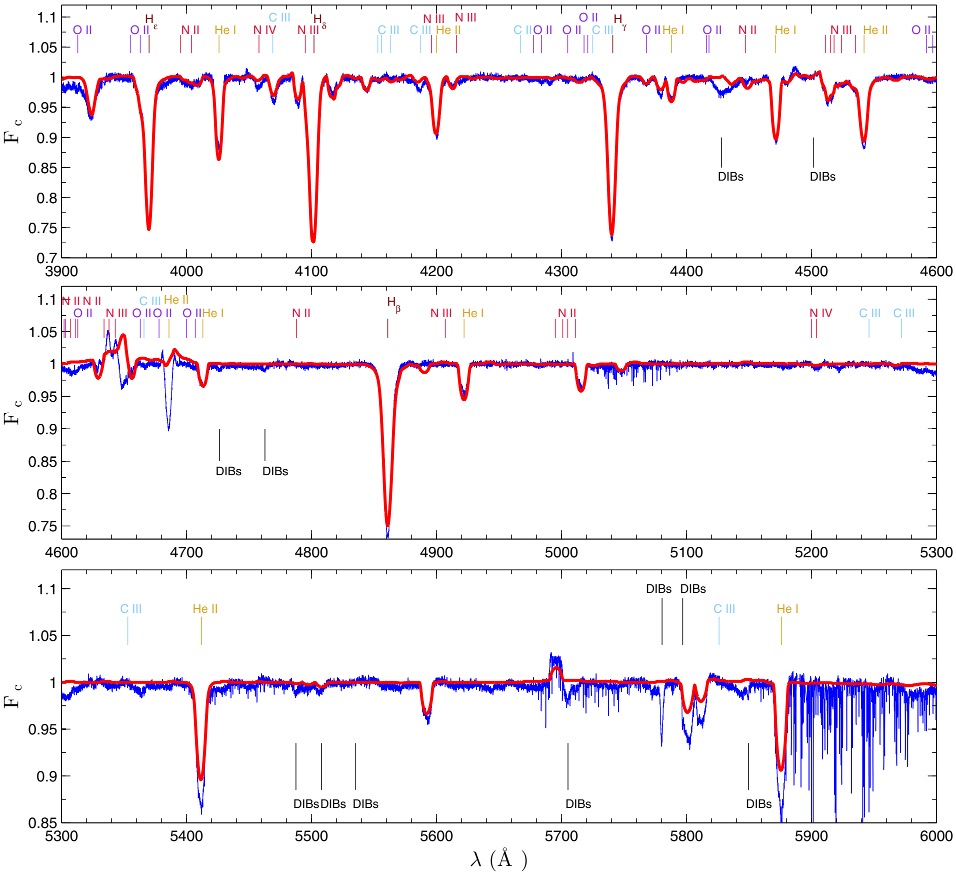

Fig. E.18. Same as Fig. E.1, but for HD 175876 (O6.5III(n)(f); $v \sin i$ = 265 km s^{-1}). There remains some mismatches in the wind-sensitive lines (but see Sect. 4.3.2), in particular He II 5412 (though an imperfect normalisation may have an impact) and He I 5876.

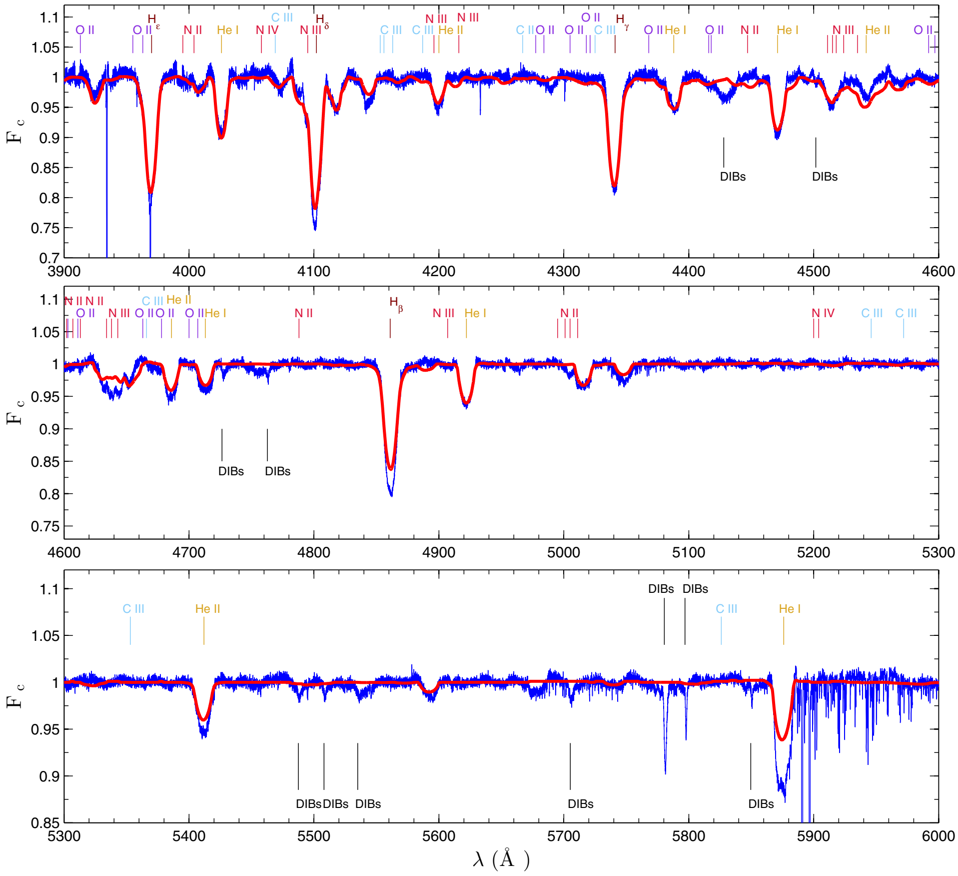

Fig. E.19. Same as Fig. E.1, but for HD 191423 (ON9II-IIInn; $v \sin i$ = 420 km s^{-1}). Despite an overall good fit of the H and He lines, some mismatches remain for Hβ and He I 5876.

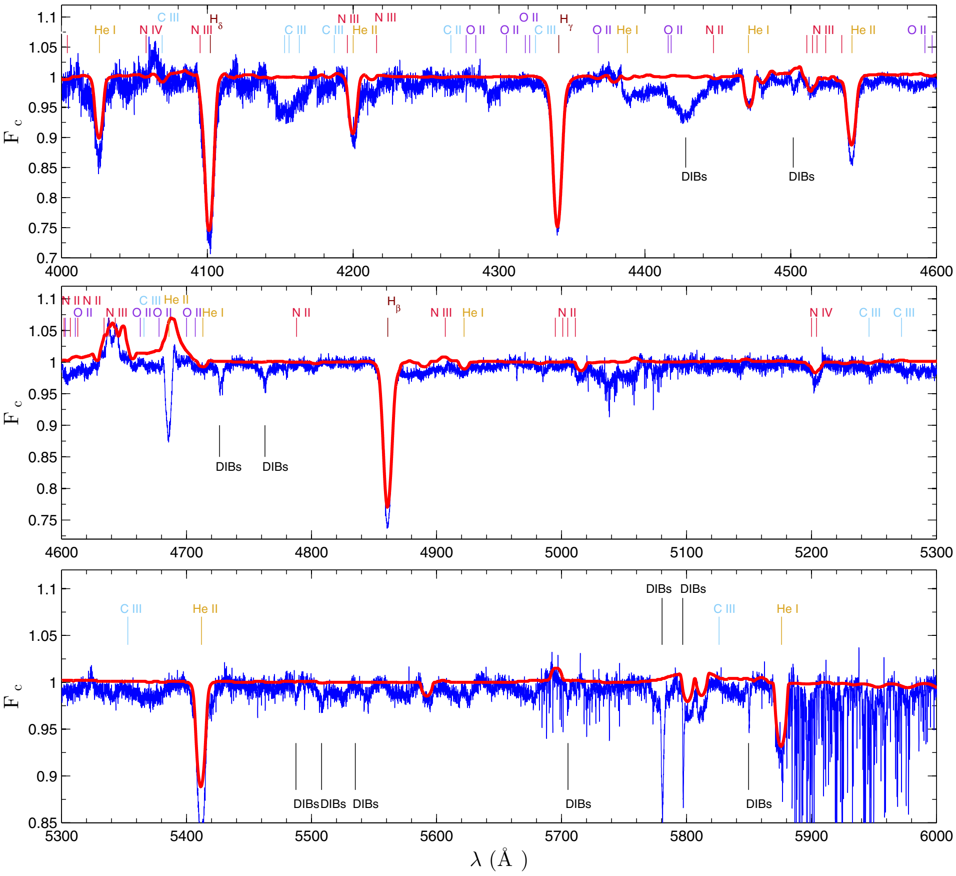

Fig. E.20. Same as Fig. E.1, but for HD 192281 (O4.5V(n)((f)); $\upsilon \sin i$ = 276 km s^{-1}). Our ELODIE spectra of this star have a rather low S/N, rendering the fitting more uncertain. Some mismatches remain, in particular for He II 5412 and the C III 4153–4163 complex. Because wind parameters were not derived, wind-sensitive lines are not well reproduced: too much emission is seen in He II 4686 and N III 4634–4643 for the best-fit model.

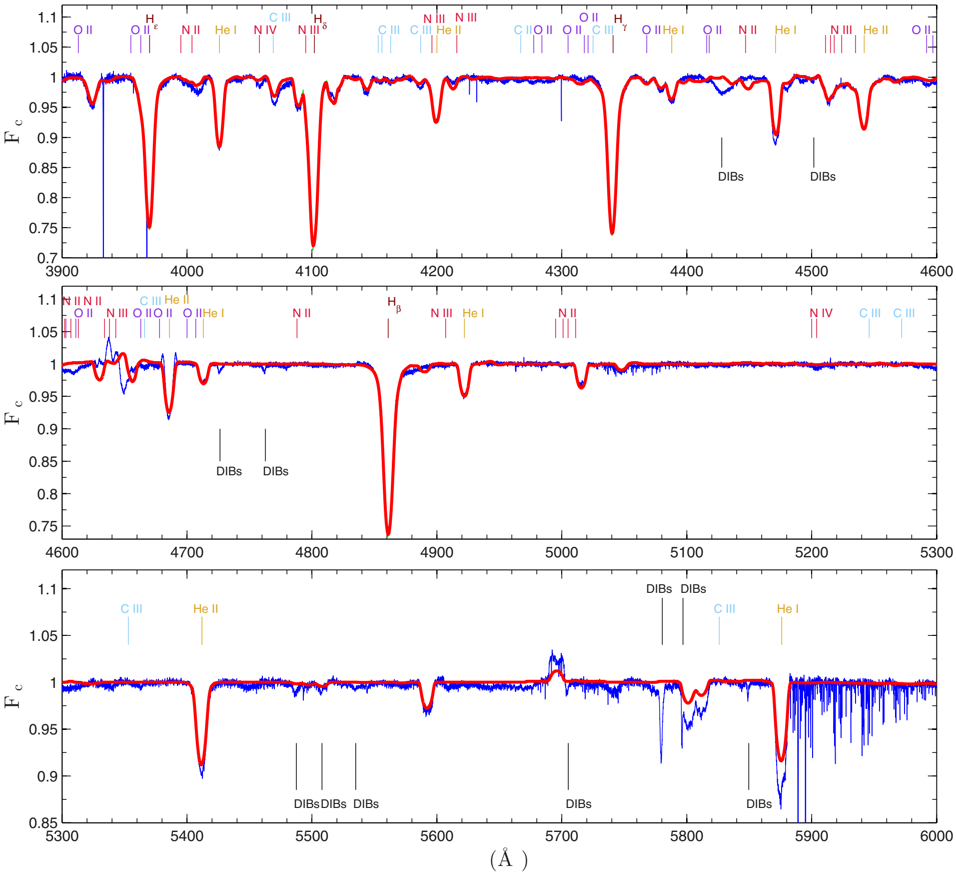

Fig. E.21. Same as Fig. E.1, but for HD 203064 (O7.5IIIn((f)); $v \sin i$ = 298 km s^{-1}). Despite an overall good fit of the He lines, a mismatch remains for He I 5876; some fitting imperfections are also spotted in the region of wind-sensitive lines (4600–4700 Å, see Sect. 4.3.2).

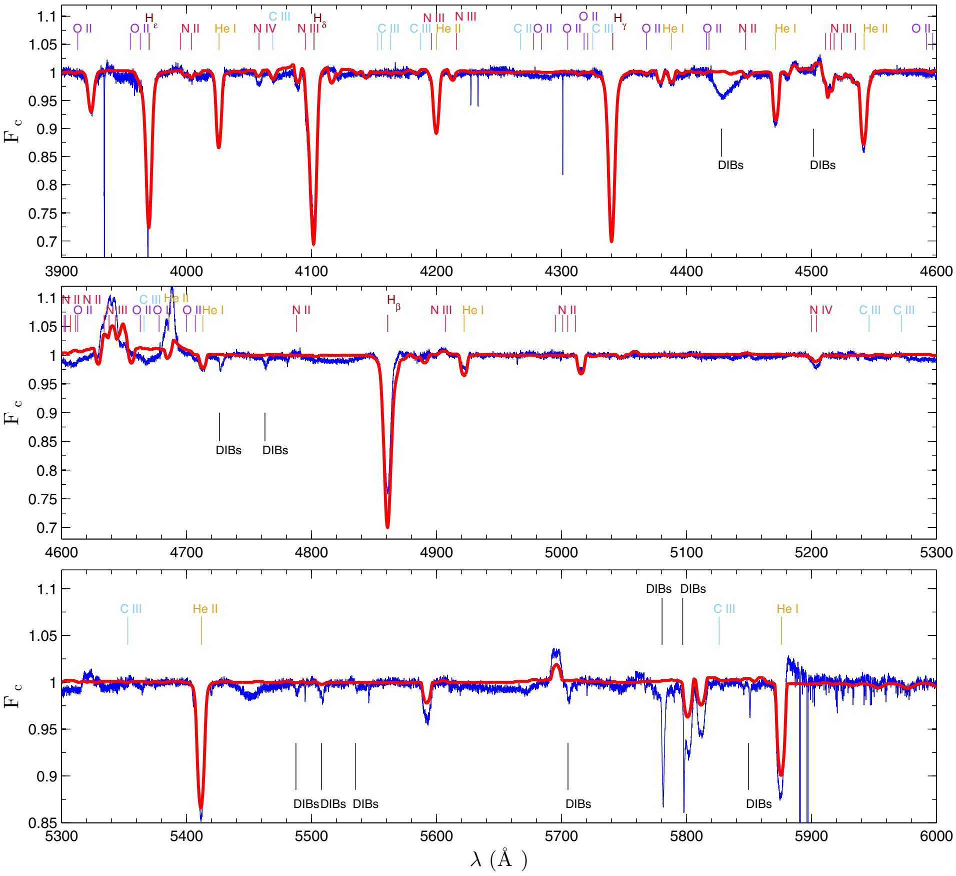

Fig. E.22. Same as Fig. E.1, but for HD 210839 (O6.5I(n)fp; $v \sin i$ = 214 km s^{-1}). Some normalisation imperfections remain, notably near Hβ, and the spectral domain encompassing wind-sensitive lines is not well fitted (4600-4700 Å, see Sect. 4.3.2).

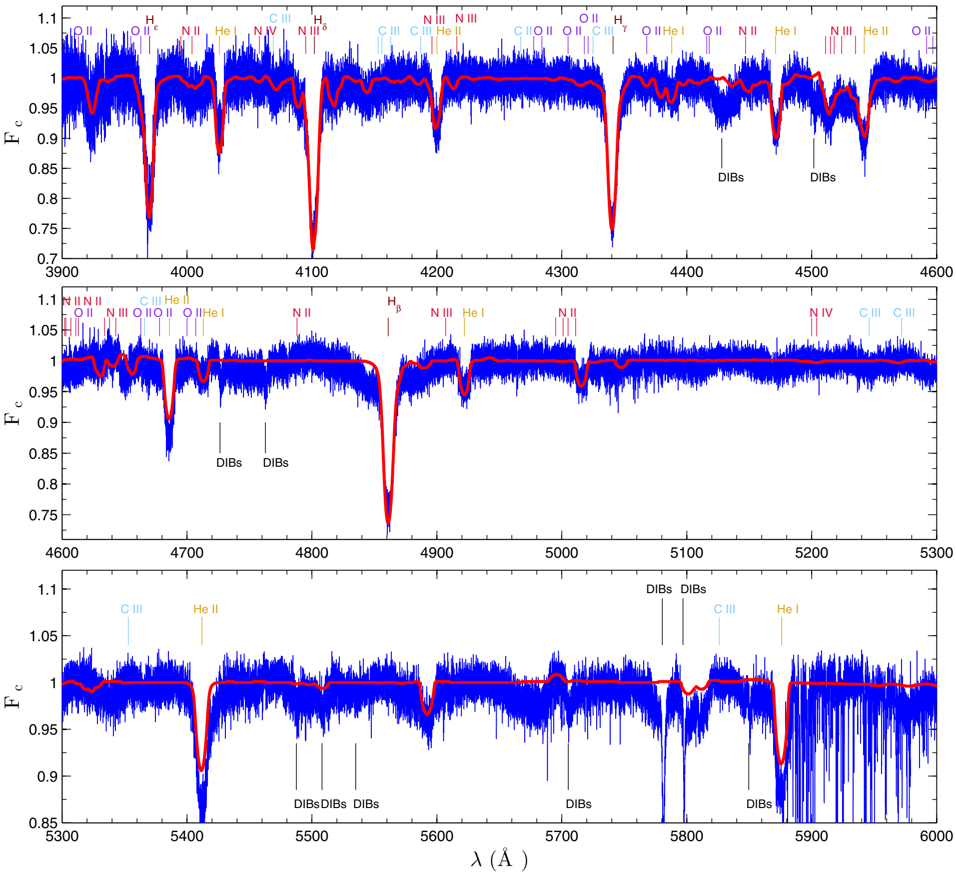

Fig. E.23. Same as Fig. E.1, but for HD 228841 (O6.5Vn((f)); $v \sin i = 305$ km s^{-1}). Our sole SOPHIE spectrum of this star has a low S/N, rendering the fitting more uncertain; a good match is found overall except maybe for He II 5412, which could be affected by normalisation problems.

Appendix F: Additional tables

Table F.1. Main characteristics of our targets, along with the source of data.

Name		Spectral type	Ref.	m_V	Number of spectra														
ALS/BD/HD	Other			[mag]	AU	C	EL	ESPa	ESPR	FE	FI	G		HA	HE	M	N	S	U
												Alb	B&C						
Slow rotators																			
HD 214680	10 Lac	O9V	1	4.88											1				
HD 46328	ξ^1 CMa	B0.5IV	2	4.33											1				
HD 57682		O9.2IV	1	6.43											5				
HD 149438	τ Sco	B0V	3	2.81											2				
Fast rotators																			
ALS 864		O9V	4	10.63												1			
ALS 18675		...	1	13.60												1			
BD +60° 594		O9V	3	9.30			1											1	
BD +34° 1058		O8nn	2	8.84														1	
HD 13268		ON8.5IIIn	1	8.18	62		2				3								
HD 14434		O5.5Vnn((f))p	1	8.49	6			8										1	
HD 14442		O5n(f)p	1	9.27	38														
HD 15137		O9.5II-IIIn	1	7.86			1				3								
HD 15642		O9.5II-IIIn	1	8.55							3								
HD 28446A	1 Cam A	B0IIIn	2	5.77											14				
HD 41161		O8Vn	1	6.76			1				3				22				
HD 41997		O7.5Vn((f))	5	8.46			1												
HD 46056		O8Vn	1	8.16				8	1										
HD 46485		O7V((f))nz	1	8.27			1			1									
HD 52266		O9.5IIIn	1	7.23						6	2		1						
HD 52533		O8.5IVn	1	7.68		1				2	2		1			1			
HD 53755	V569 Mon	B0.5V	6	6.49															1
HD 66811	ζ Pup	O4I(n)fp	1	2.25				2											
HD 69106		O9.7IIn	1	7.13		3		4					1						
HD 74920		O7.5IVn((f))	1	7.54		3							1						
HD 84567		B0.5IIIn	7	6.45		2													
HD 90087		O9.2III(n)	1	7.80						2									
HD 92554		O9.5III	8	9.50		2													
HD 93521		O9.5IIInn	1	7.03			20								2			1	
HD 102415		ON9IV:nn	1	9.28		1				4									
HD 117490		ON9.5IIInn	1	8.89						8									
HD 124979		O7.5IV(n)((f))	1	8.51						2									
HD 149757	ζ Oph	O9.2 IVnn	1	2.56			1			1				1					
HD 150574		ON9III(n)	1	8.50						2									
HD 163892		O9.5IV(n)	1	7.44		3				12	2								
HD 172367		B0V	3	9.54														1	
HD 175876		O6.5III(n)(f)	1	6.94		1				11									
HD 184915	κ Aql	B0.5III	3	4.96							4				3			1	
HD 188439	V819 Cyg	B0.5IIIpvar	3	6.28							4				5			1	
HD 191423		ON9II-IIInn	1	8.03	7		2		2		2	1							
HD 192281	V2011 Cyg	O4.5V(n)((f))	1	7.55	37		4											1	
HD 198781		B0.5V	2	6.45											5				
HD 203064	68 Cyg	O7.5IIIn((f))	1	5.00				1			3						4		
HD 210839	λ Cep	O6.5I(n)fp	1	5.05				1									6	1	
HD 228841		O6.5Vn((f))	1	9.01														1	

Notes. The slow rotators are used for validation purposes (see Sect. 6). Magnitudes in the *V* band are from the SIMBAD database. For data sources, AU corresponds to AURELIE, C to CORALIE, EL to ELODIE, ESPa to ESPaDOnS, ESPR to ESPRESSO, FE to FEROS, FI to FIES, G to GOSSS (Alb to Albireo and B&C to Boller & Chivens), HA to HARPS, HE to HEROS, M to MIKE, N to NARVAL, S to SOPHIE, and U to UCLES.

References. For spectral types: [1] Sota et al. (2011, 2014); [2] Lesh (1968); [3] Morgan et al. (1955); [4] Fitzgerald & Moffat (1975); [5] Blaauw (1961); [6] Murphy (1969); [7] Hiltner et al. (1969); [8] Humphreys (1973).

Table F.2. Stellar parameters derived for the stars in our sample and assumed wind parameters for our hotter stars.

Star	$v \sin i$	$v_{\rm mac}$	Multiplicity	Runaway?	$T_{\rm eff}$	$\log g$	$\log g_{\rm C}$	$\log(\dot{M})$	v_∞	β	y	$\log \epsilon$(C)	$\log \epsilon$(N)	$\log \epsilon$(O)			[N/C]	[N/O]
	[km s^{-1}]	[km s^{-1}]	from spectroscopy		[K]				[km s^{-1}]					4060–4082 Å	4691–4709 Å	Adopted		
Cooler stars (DETAIL/SURFACE)																		
ALS 864	249	<98	...	No	31 500	4.00	4.05	...	...	...	0.064	<7.86	7.64	8.26	7.98	8.12	>–0.22	–0.48
ALS 18675	236	<200	...	No	30 300	3.90	3.95	...	...	...	0.071	7.78	7.54	8.02	8.12	8.07	–0.24	–0.53
BD +60° 594	314	<197	RV var	No	33 200	4.00	4.04	...	...	...	0.131	7.66	<8.24	8.60	8.36	8.48	<0.58	<–0.24
HD 28446A	275	<169	RV var	No	29 400	3.70	3.78	...	...	...	0.126	8.30	7.48	8.76	8.28	8.52	–0.82	–1.04
HD 52266	285	<96	SB1	No	30 100	3.60	3.70	...	...	...	0.187	7.78	7.74	8.08	7.92	8.00	–0.04	–0.26
HD 52533	305	<180	SB1	...	34 100	4.10	4.16	...	...	...	0.065	7.76	<7.78	8.08	8.22	8.15	<0.02	<–0.37
HD 53755^{a}	285	<102	...	No	28 100	3.60	3.70	...	...	...	0.135	...	7.32	...	8.38	8.38	...	–1.06
HD 84567	261	<105	RV var	...	27 700	3.50	3.59	...	...	...	0.204	<7.84	7.98	8.62	8.16	8.39	>0.14	–0.41
HD 90087	276	<63	Pres. single	No	29 000	3.50	3.60	...	...	...	0.163	7.72	7.42	8.18	8.14	8.16	–0.30	–0.74
HD 93521	405	<88	Pres. single	...	30 000	3.60	3.78	...	...	...	0.166	7.68	8.10	8.50	8.16	8.33	0.42	–0.23
HD 102415 †	357	<72	Pres. single	No	32 900	4.10	4.19	...	...	...	0.158	<7.54	8.16	8.46	7.98	8.22	>0.62	–0.06
HD 149757 †	378	<104	Pres. single	Yes	31 500	3.87	3.99	...	...	...	0.135	8.07	7.85	8.47	8.27	8.37	–0.22	–0.52
HD 163892 †	205	<79	SB1	No	32 000	3.80	3.84	...	...	...	0.082	8.24	7.34	8.44	8.32	8.38	–0.90	–1.04
HD 172367	266	<107	...	No	27 600	3.60	3.69	...	...	...	0.140	<8.09	8.44	8.48	8.46	8.47	>0.35	–0.03
HD 184915	252	<62	Pres. single	No	27 800	3.70	3.77	...	...	...	0.183	<8.18	8.46	>8.86	8.62	8.62	>0.28	–0.16
HD 188439	281	<197	RV var	...	27 700	3.70	3.79	...	...	...	0.122	<8.09	8.16	>8.86	8.66	8.66	>0.07	–0.50
HD 198781	222	<103	Pres. single	No	29 100	3.90	3.94	...	...	...	0.230	<8.09	8.62	8.98	8.58	8.78	>0.53	–0.16
Typical errors	*15*	...	...	...	*1000*	*0.10*	*0.10*	...	...	...	*0.025*	*0.12*	*0.13*	...	...	*0.21*	*0.21*	*0.12*
Hotter stars (CMFGEN)																		
BD +34° 1058	424	<57	...	No	34 400	3.67	3.85	–7.0	2035	1.03	0.119	7.90	8.14	...	...	8.68	0.24	–0.54
HD 13268	301	<86	RV var	Yes	32 500	3.42	3.55	–6.6	2266	0.80	0.206	≤7.50	8.61	...	...	8.10	≥1.11	0.51
HD 14434	408	<44	Pres. single	No	40 000	3.89	4.03	–6.2	1960	0.84	0.103	7.96	8.81	...	...	≤8.10	0.85	≥0.71
HD 14442^{b}	285	<10	Pres. single	No	39 200	3.69	3.78	–6.2	1960	0.84	0.097	7.10	8.61	...	...	≤8.10	1.51	≥0.51
HD 15137	267	<76	RV var	Yes	29 500	3.18	3.31	–6.4	2575	0.89	0.112	7.63	8.27	...	...	≤8.30	0.64	≥–0.03
HD 15642	335	<128	Pres. single	No	29 700	3.28	3.47	–6.4	2575	0.89	0.150	≤7.55	8.43	...	...	7.93	≥0.88	0.50
HD 41161	303	<81	RV var	Yes	33 900	3.67	3.77	–7.0	2035	1.03	0.123	7.87	8.09	...	...	8.67	0.22	–0.58
HD 41997	247	<118	...	Yes	34 400	3.92	3.97	–6.8	2700	1.03	0.110	8.59	8.21	...	...	8.79	–0.38	–0.58
HD 46056	350	<48	Pres. single	No	34 500	3.90	4.00	–7.0	1305	1.03	0.088	8.34	7.78	...	...	8.32	–0.56	–0.54
HD 46485	315	<149	Pres. single	No	37 000	4.00	4.08	–6.6	1780	1.03	0.076	8.46	7.95	...	...	8.72	–0.51	–0.77
HD 66811	225	<124	Pres. single	Yes	41 000	3.55	3.62	–6.0	2485	0.92	0.148	≤7.00	8.94	...	...	8.20	≥1.94	0.74
HD 69106	306	<177	Pres. single	No	29 500	3.45	3.58	–6.1	2700	1.03	0.091	7.88	7.74	...	...	8.47	–0.14	–0.73
HD 74920	274	<111	Pres. single	No	34 100	3.85	3.92	–6.6	4410	1.20	0.134	7.78	8.34	...	...	8.51	0.56	–0.17
HD 92554	303	<99	...	Yes	30 000	3.41	3.54	–6.7	1260	0.99	0.091	7.57	7.30	...	...	8.53	–0.27	–1.23
HD 117490	361	<94	Pres. single	No	30 000	3.55	3.70	–6.1	2970	0.95	0.141	≤7.39	8.50	...	...	8.15	≥1.11	0.35
HD 124979	246	<215	RV var	Yes	34 100	3.85	3.91	–6.6	4410	1.20	0.091	8.48	7.92	...	...	8.74	–0.56	–0.82
HD 150574	233	< 61	Pres. single	No	31 500	3.32	3.41	–6.8	2960	0.90	0.172	7.48	≥9.08	...	...	≥8.93	≥1.60	...
HD 175876	265	<100	Pres. single	...	35 900	3.66	3.74	–6.3	2430	1.07	0.110	8.04	8.36	...	...	8.42	0.32	–0.06
HD 191423	420	<29	Pres. single	No	30 600	3.33	3.57	–6.4	600	0.99	0.134	≤7.24	8.33	...	...	≤8.33	≥1.09	≥0.00
HD 192281	276	<99	RV var	No	39 000	3.64	3.73	–6.2	1960	0.84	0.103	8.00	8.76	...	...	8.05	0.76	0.71
HD 203064	298	<104	SB1	Yes	35 000	3.73	3.82	–6.6	2340	1.03	0.076	7.92	8.23	...	...	8.46	0.31	–0.23
HD 210839	214	<82	SB1	Yes	36 000	3.50	3.56	–6.0	2600	1.03	0.113	7.83	8.74	...	...	8.13	0.91	0.61
HD 228841	305	<189	Pres. single	...	34 000	3.50	3.62	–7.1	2700	1.03	0.112	7.48	8.74	...	...	8.67	1.26	0.07
Typical errors	*15*	...	...	...	*1500*	*0.15*	*0.15*	...	...	...	*0.030*	*0.27*	*0.34*	...	...	*0.21*	*0.43*^{c}	*0.40*^{c}

Notes. Because macroturbulent velocities cannot be determined reliably for fast rotators (Sect. 4.2), all values in Col. 3 are upper limits. Column 4 provides the multiplicity status (see Sect. 4.1 for the classification criterion and Appendix C for the RV studies of each individual object). The runaway status is based on literature studies (references are given on a star-to-star basis in Appendix C). Columns 9–11 list the assumed wind parameters. For stars with the lowest temperatures (typically B0.5 stars), the carbon abundance cannot be firmly determined due to the weakness of the C III lines at these temperatures. Besides, N II lines may also be very weak for the hottest stars studied with DETAIL/SURFACE. In these cases, we provide upper limits for both carbon and nitrogen abundances. They correspond to predicted lines becoming detectable, i.e. having a depth significantly exceeding the local noise. Similarly, CMFGEN fits may converge towards very high or very low CNO abundances. In both cases, the upper or lower limits were determined from the χ^2 curves and correspond to the limit of their flat minimum. Since the CNO abundances are measured relative to the hydrogen content (assumed to be constant in our study), a correction should in principle be applied to the CNO abundances of stars that exhibit a very high helium abundance (and therefore have a reduced hydrogen abundance). However, we found this correction to be negligible (≲0.1 dex) even for the most He-rich stars. The last row of each table section gives the typical 1σ errors on the parameters. Stars studied with both DETAIL/SURFACE and CMFGEN (see Sect. 6.3) are flagged with †. [a] Because the UCLES spectrum only covers the wavelength range ~4350–6800 Å, neither Hϵ, Hδ, Hγ, He I 4026, nor the C and O lines in the 4060–4082 Å region were used. In order to check the reliability of our results, we determined the atmospheric parameters of HD 172367 (whose spectral type is similar to HD 53755) considering either only one (Hβ) or four (Hϵ, Hδ, Hγ, Hβ) Balmer lines. No significant differences were found between the two sets of results, ensuring that our parameter derivation for HD 53755 is secure. [b] Atmospheric parameters and surface abundances must be considered with caution, as they were derived from a low S/N spectrum that only ranges from 4075 to 4920 Å (i.e. with fewer diagnostic lines). [c] Quadratic sum of the CNO abundance uncertainties.

2.1.2.1 Complementary information

Projected rotational and macroturbulence velocities.

- **Distribution of the projected rotational velocities.** It has been suggested by evolutionary models of binary stars that the distribution of projected rotational velocities of massive stars is bimodal and that a peak may be present at $\sim$ 300 km s^{-1} (de Mink et al., 2013). The first peak at low velocities ($\lesssim$ 100 km s^{-1}) is essentially made of single stars and binary system components that have not experienced a Roche lobe overflow. The second peak may be due to post-interaction binaries (mergers or mass gainers in a mass-transfer event, Fig. 2.5; de Mink et al. 2013; Dufton et al. 2013). On the observational side, there is, however, no obvious evidence for this high-velocity peak in large samples of Galactic O-type stars (Holgado et al., 2017). While there is no evidence, solely based on the rotational velocities, that our sample stars are drawn from a specific population that underwent binary system interactions, this possibility cannot be ruled out and is discussed further in Paper II.

- **Macroturbulence velocity.** In addition to using the `iacob-broad` tool (Simón-Díaz & Herrero, 2014), we also derived the rotational and macroturbulence velocities ($v \sin i$ and $v_{\rm mac}$, respectively) by searching for a best-fit amongst model spectra that were convolved using the `rotin3` and `SPECTRUM` programmes (to take the broadening associated to $v \sin i$ and $v_{\rm mac}$, respectively, into account), the latter assuming a radial-tangential prescription (see Gray 2005 for a definition). This yields degenerate solutions (Fig. 2.6) as with `iacob-broad`. However, velocities values were similar in both methods. In Paper I, we thus provided results for $v_{\rm mac}$ from `iacob-broad` only as it is publicly available, facilitating further comparisons.

Atmospheric parameters and abundances. Figure 2.7 illustrates the DETAIL/SURFACE grid used to derive the atmospheric parameters and helium abundance of the cooler stars of our sample.

The Kurucz atmosphere models chosen to study these stars were computed with a solar helium abundance. We show in Table 2.2 that no significant difference is found in the atmospheric parameters ($T_{\rm eff}$, $\log g$) and He, C, N,

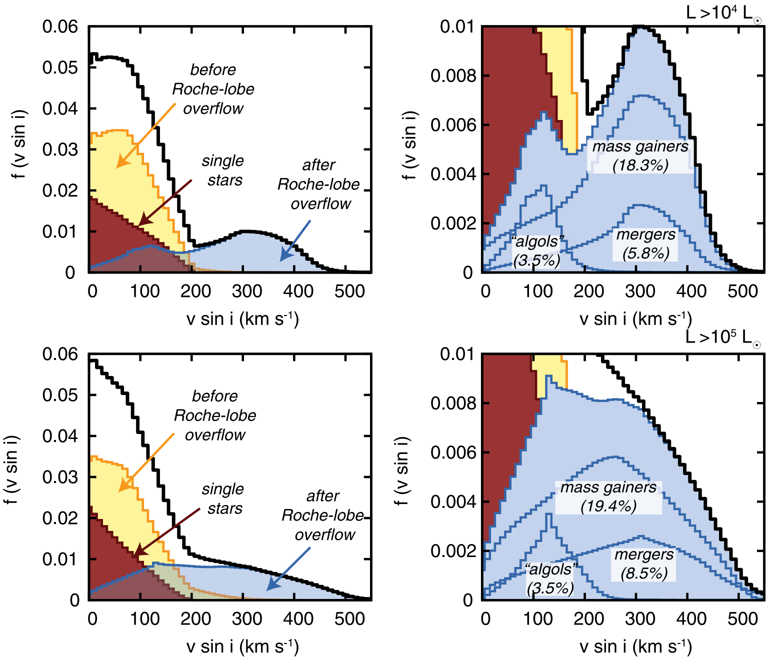

Figure 2.5: Predicted distribution of $v \sin i$ for MS massive stars assuming the binary properties of Sana et al. (2012). Results for objects brighter than 10^4 and 10^5 $L_\odot$ are illustrated in upper and lower panels, respectively. Right panels show a zoom-in of left panels, highlighting the contribution of post-interaction binaries. *Source:* de Mink et al. (2013).

O surface abundances when models with twice the solar helium abundance are considered.

We noticed that the scatter in oxygen abundances derived with the 4060 – 4082 Å spectral region is greater than that for the 4691 – 4709 Å region (∼ 1.0 vs ∼ 0.7 dex). This may be due to the fact that the O II lines in the 4060 – 4082 Å region are blended with C III lines, rendering the oxygen abundance slightly less precise (as, e.g., there may be a degeneracy issue in the abundance determinations, see Fig. 7 of Rauw et al. 2012). However, we chose to adopt the average value of the oxygen abundances derived in the two regions, when they have both been firmly determined. This is justified by the fact that – albeit being apparently less precise – the O abundances from the 4060 – 4082 Å region are on average larger than those from the 4691 – 4709 Å region and more in accord with the expected values for OB stars (namely roughly solar, Fig. 2.8). Averaging the results provided by the

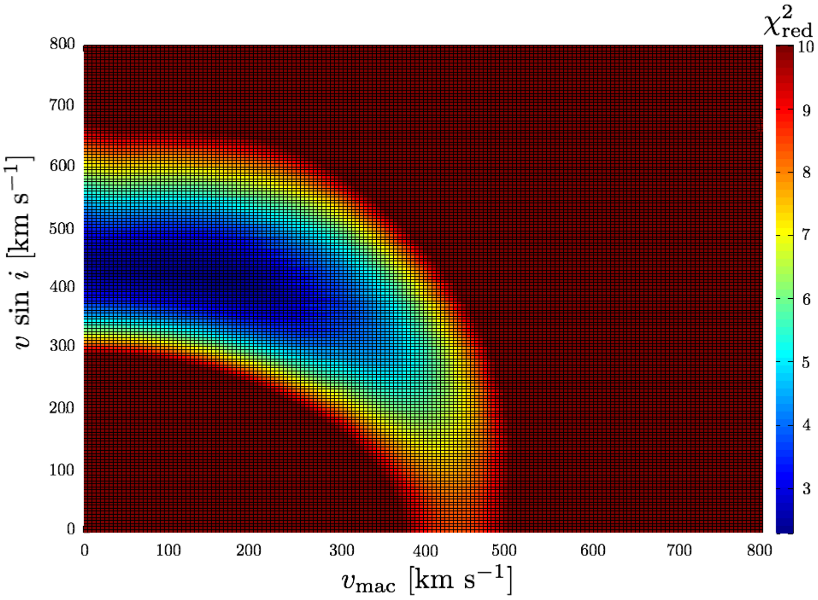

Figure 2.6: Illustration of the determination of v sin i and $v_{\rm mac}$ of HD 93521 thanks to spectral synthesis, using the He I 4921 line. DETAIL/SURFACE spectra were convolved with broadening functions (taking v sin i and $v_{\rm mac}$ into account; values between 0 and 800 km s^{-1} are considered). Colours represent the reduced χ^2 values.

Table 2.2: Changes in the atmospheric parameters and surface abundances when HD 163892 is analysed with Kurucz models using a helium abundance twice solar. (1) and (2) refer to the spectral regions 4060 – 4082 Å and 4691 – 4709 Å, respectively.

Parameter		Helium abundance		Difference
		Solar	Twice solar	
$T_{\rm eff}$ [K]		31 936	31 741	−195
$\log g$ [dex]		3.80	3.70	−0.10
y		0.082	0.079	−0.003
$\log \varepsilon$(C) [dex]		8.24	8.24	0
$\log \varepsilon$(N) [dex]		7.34	7.32	−0.02
$\log \varepsilon$(O) [dex]	(1)	8.44	8.46	+0.02
	(2)	8.32	8.30	−0.02

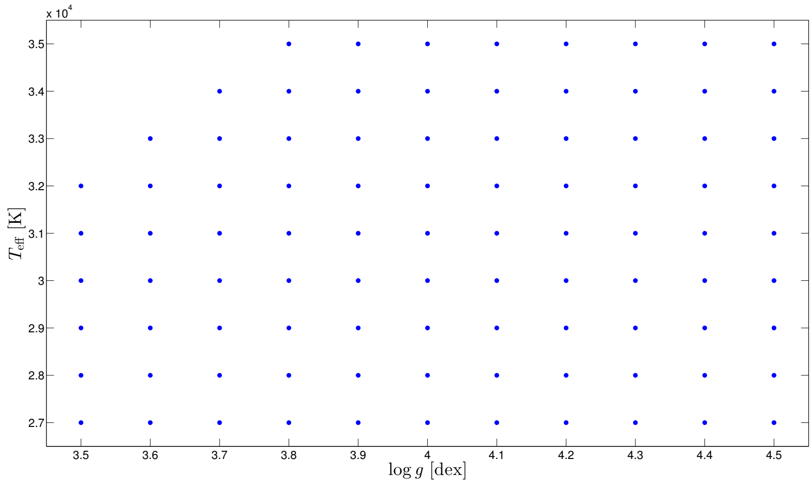

Figure 2.7: Grid of synthetic spectra used to derive the atmospheric parameters and helium abundance for the cooler stars. For each couple ($T_{\rm eff}$, $\log g$) the helium abundance varies from $y = 0.005$ to 0.250 with a step of 0.005.

two regions thus seemed a fair compromise between precision and accuracy. In addition, the lowest [N/O] abundance ratios computed with the average of the oxygen abundances nearly coincide with the solar values from Grevesse & Sauval (1998) and Asplund et al. (2009), as well as those adopted by evolutionary models on the ZAMS of the Bonn and Geneva evolutionary models (Fig. 2.8).

We have also assessed the impact of the variation of temperature (by typical values corresponding to the error bars for our cooler sample, i.e., ±1000 K) on CNO abundances. To this aim, we chose to consider HD 149757. Indeed, this star has been observed by different high-resolution spectrographs and making this exercise will also reveal potential instrumental differences. In that context, we assigned to HD 149757 effective temperatures equal to the derived ones but lowered or increased by 1000 K, and examined the differences in CNO abundances. Results are listed in Table 2.3. On average, a lower temperature increases the carbon abundance by 0.11 dex, decreases the nitrogen abundance by 0.17 dex and the oxygen abundance by 0.13 dex. A contrario, a higher temperature decreases the carbon abundance by 0.05 dex, increases the nitrogen abundance by 0.21 dex and the oxygen abundance by 0.15 dex. These differences are within the typical errors bars of the carbon and oxygen abundances, and within 2σ for the nitrogen abundance.

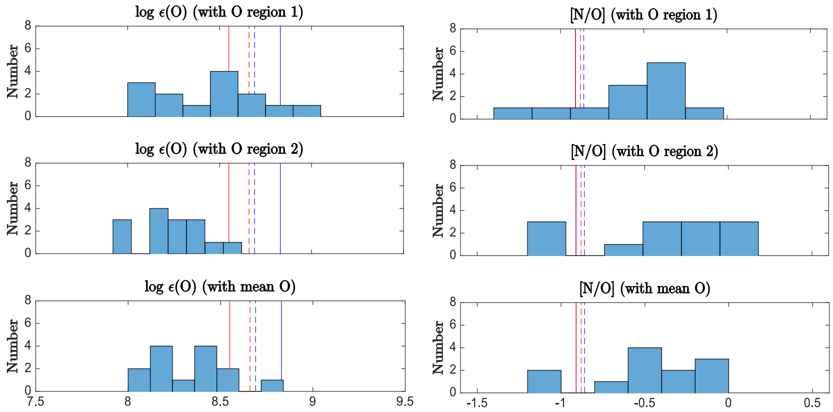

Figure 2.8: *Left*: Distribution of the oxygen abundances of our cooler stars derived in the 4060 – 4082 Å region (upper panel), in the 4691 – 4709 Å region (middle panel), and distribution of the average of the abundances derived in these two regions (lower panel). *Right*: Same as left panel but for [N/O] abundance ratios. Upper limits are ignored in all plots. The solar values of Grevesse & Sauval (1998) and Asplund et al. (2009) are shown in these panels as blue solid and blue dashed lines, respectively. The baseline values adopted in the Bonn and Geneva evolutionary models are shown as red solid and red dashed lines, respectively.

Table 2.3: Impact of the uncertainty in effective temperature on CNO abundances. For each instrument, the first and second columns give the differences in CNO abundances when the effective temperature is decreased or increased by 1000 K, respectively. (1) and (2) refer to the spectral regions 4060 – 4082 Å and 4691 – 4709 Å, respectively.

Instrument		ELODIE		FEROS		HARPS		Mean	
$\Delta T_{\rm eff}$ [K]		-1000	$+1000$	-1000	$+1000$	-1000	$+1000$	-1000	$+1000$
$\Delta \log \varepsilon(\mathrm{C})$ [dex]		$+0.08$	-0.06	$+0.08$	-0.04	$+0.18$	-0.06	$+0.11$	-0.05
$\Delta \log \varepsilon(\mathrm{N})$ [dex]		-0.18	$+0.20$	-0.18	$+0.18$	-0.16	$+0.24$	-0.17	$+0.21$
$\Delta \log \varepsilon(\mathrm{O})$ [dex]	(1)	-0.12	$+0.16$	-0.14	$+0.16$	-0.16	$+0.14$	-0.14	$+0.15$
	(2)	-0.12	$+0.14$	-0.12	$+0.16$	-0.12	$+0.14$	-0.12	$+0.15$

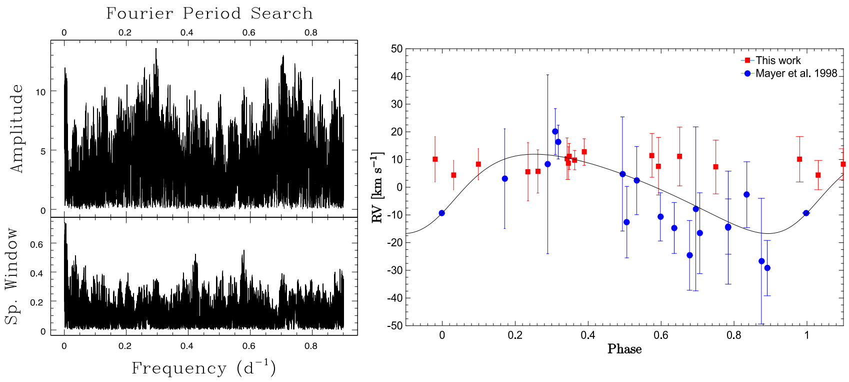

Figure 2.9: *Left*: Fourier periodogram derived from the RVs (our work + literature) of HD 28446A. Note the peak near 0.3 d^{-1}. *Right*: Phase diagram of the RV values of HD 28446A folded with a 3.37730 d period. The best-fit orbital solution (Table 2.4) is shown as a black curve.

Binarity. Two stars, HD 28446A and HD 41161 were found to have significantly variable RVs and had enough RVs to perform a period search. These searches suggested potential timescales, but the orbital solution then derived was unconvincing. They were thus excluded from Table C.1 of Paper I and these two stars were not flagged as SB1. Nevertheless, we provide here these results, to be taken with caution (Table 2.4, Figs. 2.9 and 2.10).

- **HD 28446A.** The noisy RV curve is shown in Fig. 2.9. Its amplitude is small and the scatter is quite large. Non-radial pulsations as well as a gravitationally bound companion might lead to such RV curves.
- **HD 44161.** The amplitude of the periodogram peak is very small: only 6 km s^{-1} (Fig. 2.10). This is not formally significant since peaks with this amplitude are typically found in periodograms calculated based on Monte Carlo simulations (based on the observing dates and observed noise). Besides, such a small amplitude could arise from line-profile variations.

X-ray emission of our targets. Information concerning the X-ray emission of our sample stars taken from literature are presented in Table 2.5. Such X-ray emission can in principle be used to determine whether our targets are part of a high mass X-ray binary (HMXB). However, as shown in Table 2.5, their X-ray emission is moderate, typical of OB stars ($L_{\rm X}/L_{\rm BOL} \sim 10^{-7}$), hence there is no need for a HMXB scenario.

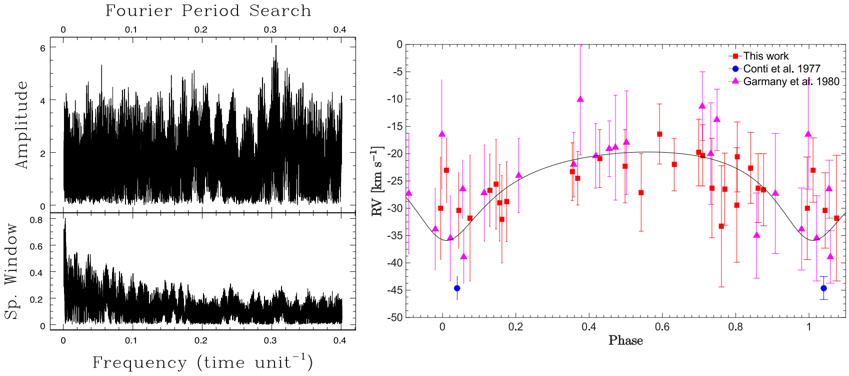

Figure 2.10: *Left*: Fourier periodiogram derived from the RVs (our work+literature) of HD 41161. Note the peak at 0.306 d^{-1}. *Right*: Phase diagram of the RV values of HD 41161 folded on a 3.26594 days period. The orbital solution derived for this star is represented with the black curve.

Table 2.4: Tentative orbital solutions, presented for completeness, obtained with the LOSP program for two stars of our sample. T_0 stands for the time of passage at periastron when $e \neq 0$ and at conjunction (primary in front) otherwise.

Elements	HD 28446 A	HD 41161
P [days]	3.37730 ± 0.00004	3.26594 ± 0.00006
T_0 [HJD–2400000]	49982.05 ± 0.40	50829.96 ± 0.29
e	0.25 ± 0.21	0.41 ± 0.24
ω [°]	241.4 ± 50.8	169.8 ± 39.6
$K_{\rm prim}$ [km s^{-1}]	14.3 ± 2.7	8.1 ± 1.3
$V_{\gamma,\rm pri}$ [km s^{-1}]	-0.7 ± 2.0	-24.50 ± 1.10
f(m) [M$_\odot$]	0.00093 ± 0.00054	0.000136 ± 0.000083
a sin i [R$_\odot$]	0.93 ± 0.18	0.48 ± 0.09
rms [km s^{-1}]	5.2	6.09

Star	X-ray properties	Source
HD 14434	$\log(L_{\rm X}) < 33.66$ erg s^{-1}	Chlebowski et al. (1989)
	$\log(L_{\rm X}/L_{\rm BOL}) < -5.25$	
HD 41161	$L_{\rm X} < 10^{34}$ erg s^{-1}	Cherepashchuk & Aslanov (1984)
	$\log(L_{\rm X}/L_{\rm BOL}) < -4.48$	Cherepashchuk & Aslanov (1984)†
HD 46056	$\log(L_{\rm X}) = 31.62$ erg s^{-1}	Berghöfer & Christian (2002)
	$\log(L_{\rm X}) < 32.49$ erg s^{-1}	Chlebowski et al. (1989)
	$\log(L_{\rm X}/L_{\rm BOL}) < -6.07$	
HD 46485	$\log(L_{\rm X}) < 31.42$ erg s^{-1}	Berghöfer & Christian (2002)
	$\log(L_{\rm X}/L_{\rm BOL}) < -7.26$	Berghöfer & Christian (2002)†
	$\log(L_{\rm X}) < 33.02$ erg s^{-1}	Chlebowski et al. (1989)
	$\log(L_{\rm X}/L_{\rm BOL}) < -5.74$	
HD 53755	$f_{\rm X} < 3.9\times10^{-13}$ erg cm^{-2} s^{-1}	Maggio et al. (1990)
	$\log(f_{\rm X}/f_{\rm BOL}) < -6.73$	Maggio et al. (1990)⋆
HD 66811	$\log(L_{\rm X}) = 32.42\pm0.21$ erg s^{-1}	
	$\log(L_{\rm X}/L_{\rm BOL}) = -7.00\pm0.18$	Chlebowski et al. (1989)
	$\log(L_{\rm X}/L_{\rm BOL}) = -6.85$	‡
HD 74920	$\log(L_{\rm X}) = 33.58 \pm 0.32$ erg s^{-1}	Chlebowski et al. (1989)
	$\log(L_{\rm X}/L_{\rm BOL}) = -5.68 \pm 0.31$	
HD 93521	$L_{\rm X} < 10^{34}$ erg s^{-1}	Cherepashchuk & Aslanov (1984)
	$\log(L_{\rm X}/L_{\rm BOL}) = -7.06 - -7.03$	Rauw et al. (2012)
HD 149757	$\log(L_{\rm X}) = 31.15$ erg s^{-1}	Oskinova (2005)
	$\log(L_{\rm X}/L_{\rm BOL}) = -7.30$	Oskinova (2005),Krtička et al. (2009b)
HD 175876	$\log(L_{\rm X}/L_{\rm BOL}) = -7.03$	Oskinova (2005)‡
	$L_{\rm X} < 10^{34}$ erg s^{-1}	Cherepashchuk & Aslanov (1984)
	$\log(L_{\rm X}/L_{\rm BOL}) < -5.07$	Cherepashchuk & Aslanov (1984)†
HD 192281	$\log(L_{\rm X}) = 32.49$ erg s^{-1}	Meurs et al. (2005)
	$\log(L_{\rm X}/L_{\rm BOL}) = -6.50$	Meurs et al. (2005)†
HD 203064	$\log(L_{\rm X}) = 32.30$ erg s^{-1}	Meurs et al. (2005)
	$\log(L_{\rm X}) = 31.76$ erg s^{-1}	Krtička & Kubát (2009a)
	$\log(L_{\rm X}/L_{\rm BOL}) = -7.18$	Krtička & Kubát (2009a)†
HD 210839	$\log(L_{\rm X}) = 32.30$ erg s^{-1}	Meurs et al. (2005)
	$\log(L_{\rm X}) = 31.92$ erg s^{-1}	Oskinova (2005)
	$\log(L_{\rm X}/L_{\rm BOL}) = -6.95$	Oskinova (2005)†
HD 228841	$\log(L_{\rm X}) = 32.75 \pm 0.36$ erg s^{-1}	Chlebowski et al. (1989)
	$\log(L_{\rm X}/L_{\rm BOL}) = -6.20 \pm 0.36$	

Table 2.5: Information on the X-ray emission for our targets. $f_{\rm X}$ and $L_{\rm X}$ stand for the X-ray flux and luminosity, respectively. Values of $L_{\rm X}/L_{\rm BOL}$ obtained using bolometric luminosities derived with the CMFGEN code are marked with †, while those derived from our estimates of the luminosity of HD 66811 and HD 149757 (see Paper I) are marked with ‡. The bolometric flux of HD 53755 (marked with ⋆) is derived with the formula $\log(f_{\rm BOL})$ = –4.61 – ($m_{\rm V}$ – 3.1 × E(B-V) + BC)/2.5 (Nazé, 2009), where the colour excess and bolometric correction are taken from Gudennavar et al. (2012) and Martins et al. (2005), respectively.

Difference with Martins' results. Figures 2.11 to 2.14 graphically show the difference between our results and those found by Martins et al. (2015a,b), both obtained with CMFGEN, for the 11 stars in common. We did not find any significant correlations between these differences and stellar properties.

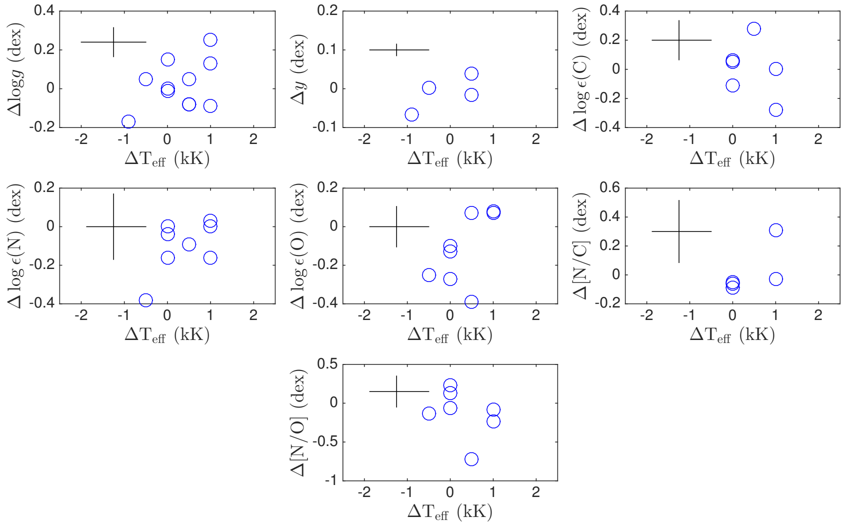

Figure 2.11: Difference between our parameter estimates and those found by Martins et al. (2015a,b) as a function of the difference in temperature (us – Martins). Crosses in each panel show our typical error bars.

2.2 Comparison with evolutionary models

2.2.1 Stellar models

Evolutionary models aim at explaining and predicting the properties of stars. Several groups have produced single star evolutionary models for massive stars, the two most popular ones being the Geneva and Bonn groups. A list of rotating models produced after 2000 and until 2014 is given in Table 2.6. Modern models of massive stars include essential inputs and ingredients, such as the initial mass, the chemical composition, convection (and overshooting),

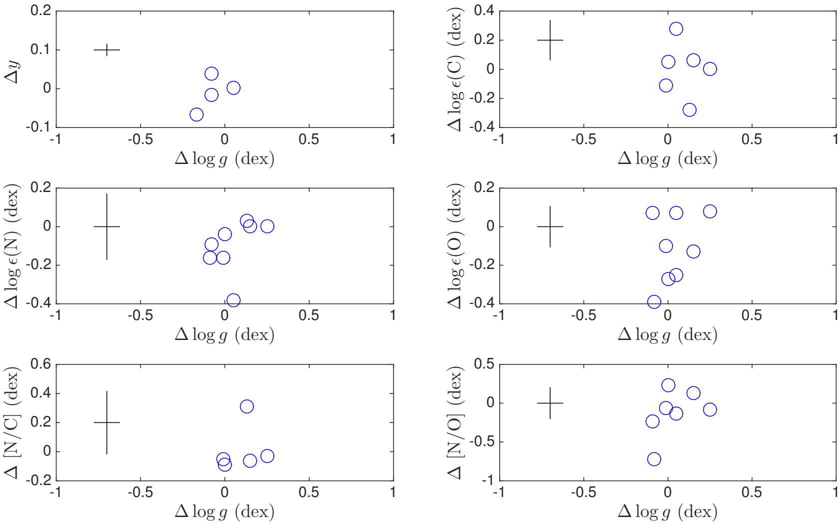

Figure 2.12: Difference between our parameter estimates and those found by Martins et al. (2015a,b) as a function of the difference in surface gravity (us – Martins). Crosses in each panel show our typical error bars.

rotation, as well as mass loss. Different assumptions are used, as the presence of internal or external magnetic fields. Geneva models do not include internal magnetic fields, unlike Bonn models. On the other hand, external magnetic fields are only implemented in some models of the Geneva group. We recall that internal and external fields have an effect on the distribution of chemical elements in the stellar interior (see Sect. 1.1.2.3). In our analysis, we also used models from the Liège group (Scuflaire et al., 2008).

The present thesis focuses on the study of Galactic stars, so we chose to consider models with a solar chemical composition, and fast rotation. Since a recent determination of the solar chemical composition (Asplund et al., 2009) provides a metal abundance of Z=0.0134±0.0008, for each family of models we chose to compare our results with the model that considers a metallicity closest to that value. Those are models of Georgy et al. (2013a) where $Z_\odot = 0.014$, complemented by unpublished computations with similar physical ingredients, but for higher masses. The models of Brott et al. (2011) with $Z_\odot$=0.0088 were also considered.

Choosing the most appropriate models to fit our targets' properties among those from Georgy et al. (2013a) and Brott et al. (2011) (hereafter called the

Group	Z	Mass range ($M_{\odot}$)	v_{ZAMS} (km s^{-1})	$\mathbf{B}_{\mathrm{int.}}$	$\mathbf{B}_{\mathrm{ext.}}$	Reference
Geneva	0	9 – 200	0 – 800	No	No	Ekström et al. (2008a)
	0	3 – 60	40 – 1423	No	No	Ekström et al. (2008b)
	0.00000001	9 – 85	500 – 800	No	No	Hirschi (2007)
	0.00001	3 – 60	39 – 1017	No	No	Ekström et al. (2008b)
	0.00001	2 – 60	0 – 400	No	No	Meynet & Maeder (2002)
	0.0005	20 – 120	0 – 800	No	No	Decressin et al. (2007)
	0.002	3 – 60	34 – 879	No	No	Ekström et al. (2008b)
	0.002	1.7 – 15	0 – 599	No	No	Georgy et al. (2013a)
	0.002	0.8 – 120	0 – 438	No	No	Georgy et al. (2013b)
	0.004	9 – 60	0 – 400	No	No	Maeder & Meynet (2001)
	0.004	30 – 120	300	No	No	Meynet & Maeder (2005)
	0.006	1.7 – 15	0 – 587	No	No	Georgy et al. (2013a)
	0.008	30 – 120	300	No	No	Meynet & Maeder (2005)
	0.014	10	200	No	Yes	Meynet et al. (2011)
	0.014	0.8 – 120	50 – 389	No	No	Ekström et al. (2012)
	0.014	1.7 – 15	0 – 556	No	No	Georgy et al. (2013a)
	0.02	9 – 120	0 – 300	No	No	Meynet & Maeder (2000)
	0.02	9 – 120	0 – 500	No	No	Meynet & Maeder (2003)
	0.02	12 – 60	0 – 300	No	No	Hirschi et al. (2004)
	0.02	3 – 60	28 – 732	No	No	Ekström et al. (2008b)
	0.04	20 – 120	0 – 300	No	No	Meynet & Maeder (2005)
Bonn	0.00001	20 – 60	230 – 605	Yes	No	Yoon & Langer (2005)
	0.00001	12 – 60	0 – 936	Yes	No	Yoon et al. (2006)
	0.001	40 – 60	479 – 522	Yes	No	Yoon & Langer (2005)
	0.001	12 – 60	0 – 747	Yes	No	Yoon et al. (2006)
	0.002	12 – 60	0 – 653	Yes	No	Yoon et al. (2006)
	0.0021	5 – 60	0 – 595	Yes	No	Brott et al. (2011)
	0.004	12 – 60	0 – 507	Yes	No	Yoon et al. (2006)
	0.0047	5 – 60	0 – 573	Yes	No	Brott et al. (2011)
	0.0088	5 – 60	0 – 595	Yes	No	Brott et al. (2011)
	0.02	40	408	Yes	No	Yoon & Langer (2005)
	0.02	16 – 40	210 – 556	Yes	No	Yoon et al. (2006)
Others	0.01345	13 – 120	300	No	No	Chieffi & Limongi (2013)
	0.02	8 – 25	200	No	No	Heger & Langer (2000a)
	0.02	8 – 25	0 – 474	No	No	Heger et al. (2000b)
	0.02	12 – 35	200	Yes and no	No	Heger et al. (2005)

Table 2.6: Rotating single stellar models, starting from 2000. Authors are associated to research groups and the studies are listed by increasing initial metallicity Z within each group. *Source:* inspired by Maeder & Meynet (2012).

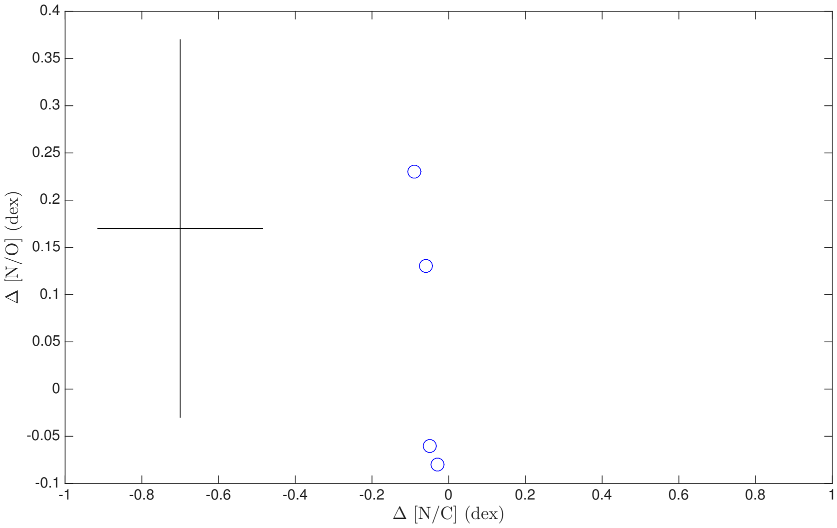

Figure 2.13: Difference between our [N/O] abundance ratio estimates and those found by Martins et al. (2015a,b) as a function of the difference in [N/C] (us – Martins). The cross shows our typical error bar.

Geneva and Bonn models, respectively) is not an easy task. We decided to use models corresponding to the typical $v \sin i$ of our targets, i.e., $\sim$ 300 km s^{-1}, assuming $i = 70^\circ$ (Zorec et al., 2002), at the middle of the MS phase ($\log g_{\rm C} \sim 3.80$ dex). This corresponds to Geneva models with $\Omega/\Omega_{\rm crit} = 0.8$. The predicted variation of $v \sin i$ as a massive star evolves is displayed in Fig. 2.15 for the Geneva and Bonn models.

We briefly compare hereafter the difference in the main ingredients and input parameters used in the Geneva and Bonn models. Before enumerating the differences between them, it is useful to recall the criteria for convective instability. Within stars, some small perturbations may, sometimes, grow and generate macroscopic motions. Some stability criteria can define whether these perturbations will develop or not. A criterion that can be used is the Ledoux stability one, that can formulated by

$$\nabla_{\rm rad} < \nabla_{\rm ad} + \frac{\phi}{\delta} \nabla_{\mu}, \tag{2.3}$$

where $\nabla \equiv \frac{d\ln T}{d\ln P}$ ($\nabla_{\rm ad}$ is the internal gradient when the moving cell does not exchange heat with the surrounding medium and $\nabla_{\rm rad}$ is the thermal

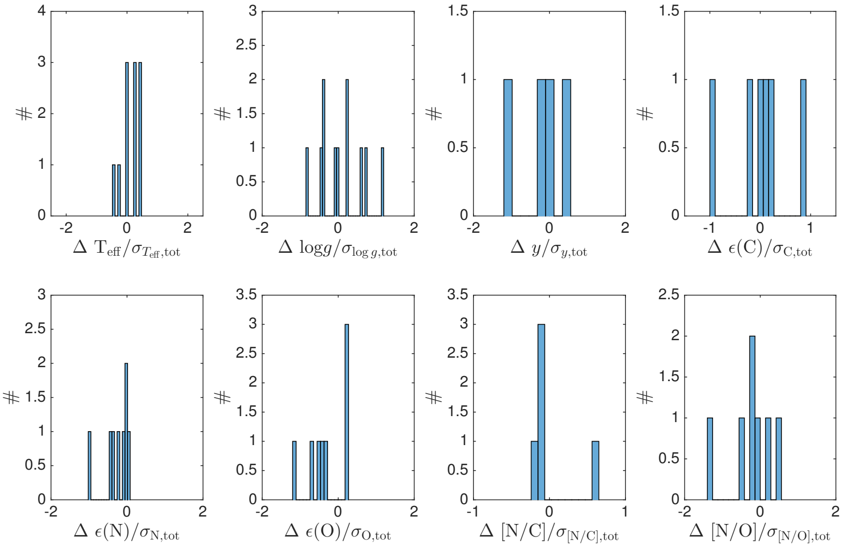

Figure 2.14: Histograms of the differences between our results and those derived by Martins et al. (2015a,b), normalised by the errors $\sigma_{\rm tot} = \sqrt{\sigma^2_{\rm this\,work} + \sigma^2_{\rm Martins}}$.

gradient necessary to carry the convective and radiative energies by radiation), $\nabla_\mu \equiv \frac{d\ln\mu}{d\ln P}$, $\delta = -\frac{\partial\ln\rho}{\partial\ln T}$, $\phi = \frac{\partial\ln\rho}{\partial\ln\mu}$, and μ the mean molecular weight. In the absence of a chemical gradient, $\nabla_\mu = 0$, and the Schwarzschild stability criterion is recovered ($\nabla_{\rm rad} < \nabla_{\rm ad}$).

Convection. In the Geneva models, the extent of the convective regions is dictated by the Schwarzschild criterion. The adopted mixing-length parameter, which is the distance over which the properties of a moving element are not modified (l) to the local pressure scale height ($H_{\rm p}$), is $\alpha_{\rm MLT}$ $=$ 1.6, except for star with a mass greater than 40 $M_\odot$, for which the local pressure scale height is no longer used in the calculation of this parameter, and is replaced by the density scale height with $\alpha_{\rm MLT} = 1$ following Maeder (1987). Enlargements of convective cores are made possible thanks to the effect of an overshooting parameter characterised by $d_{\rm over}/H_{\rm p}$ $=$ 0.1. No semi-convection is included in these models. In Bonn models, the extent of the convective regions is determined by the Ledoux criterion. The mixing-length parameter is chosen to be 1.5 in models of Brott et al. (2011). Furthermore, extensions of convective cores are generated by the inclusion of an overshooting parameter characterised by $d_{\rm over}/H_{\rm p}$ $=$ 0.335. Semi-convection is implemented according to Langer et al. (1983).

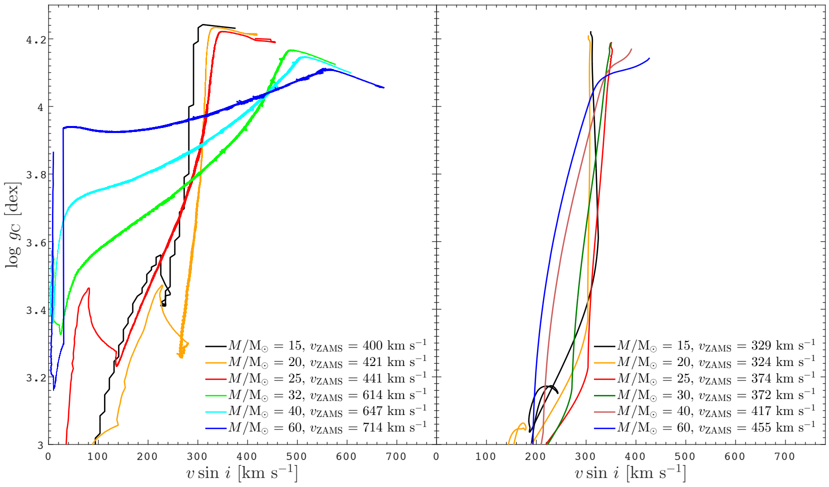

Figure 2.15: Predicted $v \sin i$ as a function of $\log g_\mathrm{C}$ by the Geneva (*left*) and Bonn (*right*) models. Initial stellar masses (in solar units) are indicated and rotational velocities at the ZAMS are listed in the bottom right corner of each panels.

Magnetic fields. The internal magnetic fields implemented in the Bonn models are due to the so-called Spruit-Taylor dynamo (Spruit, 2002), incorporated as described in Petrovic et al. (2005). This process can be produced in differentially rotating radiative stellar envelopes. The main constituent of the resulting magnetic field is toroidal and its effect is believed to create a torque coupling the rotation of the core with the one of the envelope, which effect is the transport of angular momentum in the opposite way as the angular momentum gradient. Theoretical support for the Spruit's model is provided by simplified magnetohydrodynamic models (Braithwaite, 2006), while Zahn et al. (2007) questioned the existence of the dynamo loop suggested by Spruit.

Solar chemical composition. The Geneva models use the solar chemical composition of Asplund et al. (2005), with a Ne abundance taken from Cunha et al. (2006). The Bonn models consider the reference chemical abundance of Asplund et al. (2005), but with different assumptions for the C, N, O, Mg, Si, and Fe abundances. These modifications are due to the fact that the authors consider tailored chemical composition appropriate for the Galactic sample of the VLT-FLAMES Survey of Massive Stars, hence the different Z values (Evans et al., 2005).

Mass loss. Wind prescriptions for both Bonn and Geneva models are the ones of Vink et al. (2000, 2001). Mass-loss rates in Geneva models are chosen to be in line with Maeder & Meynet (2000b).

Rotational mixing. Changes in the stellar structure due to rotation in Geneva models follow the prescriptions of Meynet & Maeder (1997). The rotation-induced transport of chemicals and angular momentum by meridional circulation and shears follows the description of Zahn (1992) and Maeder & Zahn (1998). Solid-body rotation is considered for convective regions. The considered depiction for the diffusion coefficients is from Zahn (1992) for $D_{\rm h}$ and from Maeder (1997) for $D_{\rm shear}$. In Bonn models, the formulation of Kippenhahn et al. (1970) is adopted for describing the changes in the stellar structure induced by rotation. The transport of chemicals and angular momentum initiated by rotation is dictated by the prescriptions of Endal & Sofia (1978) and Heger & Langer (2000a). The transport of these quantities is mainly ensured by the meridional circulation, shears, instabilities occuring in baroclinic stars[2] (the Goldreich-Schubert-Fricke or GSF instability). Two free parameters are used to adjust the efficiency of the rotational mixing on observations.

To a lesser extent, predictions for binary stars have also been considered. In the literature, binary models have mainly been produced:

- with the Modules for Experiments in Stellar Astrophysics (MESA) code (Paxton et al. 2011, 2013, 2015);
- with the Brussels binary evolutionary code which is based on the code developed by Paczyński (1967);
- with a modified version of the TWIN stellar evolution code originally developed by Peter Eggleton (Eggleton 1971; Eggleton & Kiseleva-Eggleton 2002);
- with the Binary Population and Spectral Synthesis code (BPASS, Eldridge & Stanway 2009);
- by Wellstein et al. (2001) who studied the evolution of close binary systems;
- by Glebbeek et al. (2013) who investigated the outcomes of stellar merging as a function of the masses of the initial components.

---

[2] A star is said to be baroclinic when, in the case of differential rotation, all quantities except the pressure change with colatitude on an isobar.

Predictions for the CNO surface abundances in binary systems are, however, not provided, except for the studies of Wellstein et al. (2001) and Glebbeek et al. (2013): our results were therefore compared only with predictions from these last two works.

The initial masses considered in the models of Glebbeek et al. (2013) range from 5 to 40 $M_\odot$ for the primary and from 0.5 to 40 $M_\odot$ for the secondary, while the models of Wellstein et al. (2001) considered initial primary masses between 12 and 25 $M_\odot$ and initial secondary masses in the range 6 to 24 $M_\odot$. The initial periods were selected such that the RLOF episode starts during the core hydrogen burning phase of the primary, or quickly after. All mass and angular momentum involved in the RLOF episode is assumed to be transferred to the secondary (conservative evolution) for contact-free systems, while this is not necessarily the case for systems that get into contact.

2.2.2 Published paper

Astronomy & Astrophysics manuscript no. ABUN_P2_15
June 20, 2017

Chemical abundances of fast-rotating massive stars

II. Interpretation and comparison with evolutionary models

Constantin Cazorla[1], Yaël Nazé⋆[1], Thierry Morel[1], Cyril Georgy[2], Mélanie Godart[1], and Norbert Langer[3]

[1] Space sciences, Technologies and Astrophysics Research (STAR) Institute, Université de Liège, Quartier Agora, Allée du 6 Août 19c, Bât. B5C, B4000-Liège, Belgium
[2] Observatoire de Genève, Université de Genève, Chemin des Maillettes 51, 1290 Versoix, Switzerland
[3] Argelander-Institut für Astronomie der Universität Bonn, Auf dem Hügel 71, 53121 Bonn, Germany
e-mail: `cazorla@astro.ulg.ac.be`

Received ... ; accepted ...

ABSTRACT

Aims. Past observations of fast-rotating massive stars exhibiting normal nitrogen abundances at their surface have raised questions about the rotational mixing paradigm. We revisit this question thanks to a spectroscopic analysis of a sample of bright fast-rotating OB stars, with the goal of quantifying the efficiency of rotational mixing at high rotation rates.

Methods. Our sample consists of 40 fast rotators on the main sequence, with spectral types comprised between B0.5 and O4. We compare the abundances of some key element indicators of mixing (He, CNO) with the predictions of evolutionary models for single objects and for stars in interacting binary systems.

Results. The properties of half of the sample stars can be reproduced by single evolutionary models, even in the case of probable or confirmed binaries that can therefore be true single stars in a pre-interaction configuration. The main problem for the rest of the sample is a mismatch for the [N/O] abundance ratio (we confirm the existence of fast rotators with a lack of nitrogen enrichment) and/or a high helium abundance that cannot be accounted for by models. Modifying the diffusion coefficient implemented in single-star models does not solve the problem as it cannot simultaneously reproduce the helium abundances and [N/O] abundance ratios of our targets. Since part of them actually are binaries, we also compared their chemical properties with predictions for post-mass transfer systems. We found that these models can explain the abundances measured for a majority of our targets, including some of the most helium-enriched, but fail to reproduce them in other cases. Our study thus reveals that some physical ingredients are still missing in current models.

Key words. Stars: abundances – Stars: early-type – Stars: fundamental parameters – Stars: massive – Stars: rotation – Stars: binaries

1. Introduction

Massive stars are generally fast rotators with projected rotational velocities that can amount to up to at least 400 km s^{-1} (e.g. Howarth et al. 1997; Dufton et al. 2011). Such rotation rates can be acquired during their formation or arise later on from interactions with a companion in a binary system (e.g. Packet 1981; de Mink et al. 2009, 2013). Stellar rotation has an impact on many facets of stellar physics. In particular, it transports material and angular momentum inside the star, affecting some surface chemical abundances. Observations in the framework of the VLT-FLAMES Survey of Massive Stars (Evans et al. 2008) has suggested that some fast-rotating, evolved B-type stars in the Large Magellanic Cloud (LMC) may exhibit surface abundances that cannot be explained by evolutionary models for single stars incorporating rotational mixing (Hunter et al. 2009; Brott et al. 2011b). A previous exchange of mass and/or angular momentum in an interacting binary system might be able to explain the observations (de Mink et al. 2009), but the binary status of these fast rotators is largely unknown.

To revisit this question, we have decided to undertake a project combining for the first time a detailed abundance analysis of Galactic fast rotators with a radial velocity (RV) study in order to establish the potential importance of binary effects (Cazorla et al. 2017; hereafter Paper I). Details of our analysis can be found in Paper I, and here we only briefly describe the methods followed to derive the properties of our sample, which is composed of 40 Galactic fast-rotating ($v \sin i > 200$ km s^{-1}) OB stars.

As a first step, we derived the RV associated with each stellar spectrum thanks to a cross-correlation technique, and calculated the projected rotational velocity through Fourier techniques (Gray 2005; Simón-Díaz & Herrero 2007). The RV measurements were complemented by literature values and were searched for variability to assess the multiplicity status of our targets: (1) if the maximum RV difference was larger than $4\,\sigma$ and above a threshold of 20 km s^{-1}, the star was considered as RV variable (RVVar thereafter), hence a possible binary; (2) period searches were applied to (large) RV datasets, leading to the derivation of SB1 orbital solutions in five cases. In parallel, two different tools, depending on the stellar temperature, were used to derive the atmospheric parameters (effective temperature $T_{\rm eff}$ and surface gravity $\log g$), as well as He, C, N, and O abundances: a cooler group of objects (with spectral types in the range B0.5-O9) was analysed with DETAIL/SURFACE (Butler & Giddings 1985; Giddings 1981), while a second group of hotter stars (O4-O9) was analysed with CMFGEN (Hillier & Miller 1998). We performed several validation checks to ensure the compati-

---

⋆ Research associate FNRS.

bility of the two methods. First, we verified that the [N/C] and [N/O] ratios follow the predictions for the CNO cycle, as expected for such massive stars (Przybilla et al. 2010). Second, as fast rotation may modify the stellar shape, we used the Code of Massive Binary Spectral Computation (CoMBISpeC; Palate & Rauw 2012; Palate et al. 2013) to verify that the abundances derived for flattened stars are, within errors, in good agreement with our results assuming no geometrical distortions and gravity darkening. Finally, we investigated a few stars showing different levels of nitrogen enrichment with both DETAIL/SURFACE and CMFGEN, demonstrating a good agreement, within errors, for the derived parameters. Hence, our dataset is, to first order, homogeneous and all the results can be discussed altogether.

Paper I provided the individual results for all the stars in our sample. This paper takes a more global view; the aim is to compare our observational results with theoretical predictions for single and binary massive stars. To compare our data to expectations for single stars, we employ two independent sets of models, those of Brott et al. (2011a) (with $Z_\odot = 0.0088$) and Georgy et al. (2013) (with $Z_\odot = 0.014$). The latter set has been complemented by unpublished calculations having similar physical ingredients as adopted in Georgy et al. (2013), but extending to higher masses. In the following the two sets of models will be referred to as the Bonn and the Geneva models, respectively.

This paper is organised as follows: Sect. 2 discusses the global characteristics of our sample, Sect. 3 compares these properties with predictions of single-star evolutionary models, while Sect. 4 considers these characteristics in the light of the stellar multiplicity status. Finally, Sect. 5 summarises our results and presents the conclusions of our project.

2. Global properties of our sample

We compare our CNO abundances with those found in some previous non-LTE studies of nearby OB stars (see Fig. 1) (Gies & Lambert 1992; Hunter et al. 2009; Nieva & Przybilla 2012; Martins et al. 2015a,b). These studies sample widely different domains in terms of rotation rate, mass, and evolutionary status. Indeed, the samples of Gies & Lambert (1992) and Nieva & Przybilla (2012) are only composed of slow rotators, whereas our stars are all fast rotators. Regarding evolutionary stages, we mostly concentrate on main-sequence (MS) stars with high mass, as in Martins et al. (2015a,b), while the Galactic stars studied by Hunter et al. (2009) typically have lower masses and span various evolutionary stages.

The three samples of (mostly) slow-rotating MS stars of Gies & Lambert (1992), Nieva & Przybilla (2012), and Martins et al. (2015a,b) differ in their chemical properties; the last sample, which is composed of higher mass stars, exhibits markedly higher $\log \epsilon(\mathrm{N})$, [N/C], and [N/O] values. Conversely, the abundance distributions are similar for our stars and those studied by Martins et al., which have comparable masses and evolutionary status but drastically different rotational velocities on average ($\langle v \sin i \rangle \sim 300$ km s^{-1} in our sample versus $\lesssim 100$ km s^{-1} for the vast majority of the Martins stars). However, caution must be taken when interpreting these results in the framework of single-star evolutionary models and, in particular, when trying to quantify the relative importance of the various parameters (e.g. mass, rotational velocity) controlling the amount of rotational mixing. For instance, because their masses differ, the stars in the studies of Gies & Lambert (1992) and Martins et al. (2015a,b) have suffered a different loss of angular momentum because of the stellar winds. As a result, the two samples may have had different rotational velocity distributions on the zero age main sequence (ZAMS) even though the present-day distributions are quite similar. Therefore, the different distributions in Fig. 1 may not only reflect the dependency of rotational mixing with mass. Also, the proportion of stars in the various samples for which binary effects are important is unknown (see discussion in Sect. 4).

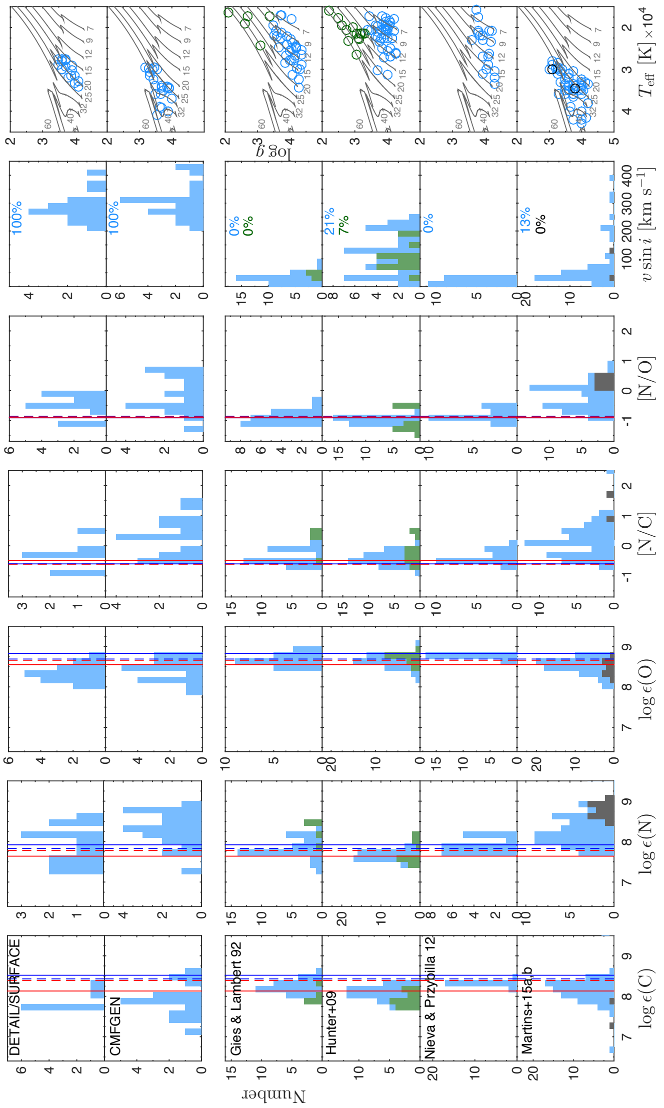

Fig. 1. Comparison between our results (cooler and hotter stars are depicted (from top to bottom) in Rows 1 and 2) and those of some previous non-LTE studies for nearby OB stars (Rows 3-6 for Gies & Lambert 1992, Hunter et al. 2009, Nieva & Przybilla 2012, and Martins et al. 2015a,b). Green histograms/symbols represent supergiant stars. The blue and black histograms/symbols in the bottom panels correspond to the sample of normal O and ON stars analysed by Martins et al. (2015a) and Martins et al. (2015b), respectively. Columns 1, 2, and 3 show the C, N, and O abundances, respectively, and Cols. 4 and 5 the [N/C] and [N/O] abundance ratios. Lower and upper limits are ignored in all plots. The solar values of Grevesse & Sauval (1998) and Asplund et al. (2009) are shown in these panels as blue solid and blue dashed lines, respectively. The baseline values adopted in the Bonn and Geneva evolutionary models are shown as red solid and red dashed lines, respectively. The two rightmost columns show the breakdown of $v \sin i$ values (the percentage of stars with $v \sin i \geq 200$ km s^{-1} in each sample is indicated) and the position of targets in the Kiel diagram. In the last column, evolutionary tracks from the Geneva group at solar metallicity and including rotation are overplotted with initial stellar masses (in M$_{\odot}$) indicated. Rotational velocities at the ZAMS for stellar masses higher than 12 M$_{\odot}$ are listed in Table 1; for 7, 9, and 12 M$_{\odot}$, the initial rotational velocities are 352, 381, and 404 km s^{-1}, respectively.

Figure 2 illustrates the dependence between the helium and nitrogen surface abundances for our study and previous non-LTE studies in various environments (Galaxy and Magellanic Clouds). A trend can be seen between the nitrogen and helium abundances of our sample stars; the two quantities seem to increase in parallel (this aspect is examined in a quantitative way in Sect. 3). This trend is also seen in some literature samples, especially in those of Rivero González et al. (2012a,b) and, to a lesser extent, Grin et al. (2017) which are both composed of LMC stars with on average lower $v \sin i$ but higher masses than ours. The nitrogen enrichment in the sample of Gies & Lambert (1992), composed of less massive slow rotators, is low, even if the helium abundance can be high in a few cases. The nitrogen excess is higher in the Galactic sample of Bouret et al. (2012), which is composed of high-mass stars with moderate $v \sin i$. The sample of Martins et al. (2015b), partially composed of fast rotators whose mass is ~ 25 $M_{\odot}$, exhibits strong helium and nitrogen enrichments. In contrast, the SMC stars of Bouret et al. (2013) generally show dramatic nitrogen overabundances without a helium abundance enhancement, even if their masses are high.

The aim of this paper is to compare the results of Paper I with models, and to assess whether the models can reproduce these results. The question then arising is the choice of the best observational diagnostics to perform this comparison. For example, are elemental abundances or abundance ratios the best indicators to use?

Figure 1 shows that mismatches exist between the derived abundances and the solar values of Grevesse & Sauval (1998) and Asplund et al. (2009), as well as the initial values adopted in the Bonn and Geneva evolutionary models. For carbon, there seems to be a systematic underabundance for all observational studies considered, while lower oxygen abundances are detected in our sample and those of Martins et al. (2015a,b). The nitrogen abundance displays a more varied behaviour in the samples in Fig. 1: underabundances and overabundances are both found.

The CNO abundances are affected by mixing and a depletion of carbon and, to a lesser extent, oxygen are expected. However, subsolar N abundances are unexpected. The C and O depletions also appear significantly higher than predicted by models. It is therefore likely that shortcomings in the data analysis are at play. It could be deficiencies in the modelling (e.g. Morel 2009) or technical issues (e.g. continuum level set too low in fast rotators because of the lack of continuum windows, which would lead to an underestimation of the strength of the spectral features). In this case, elemental CNO abundances may not be reliable diagnostics.

In contrast, the lowest [N/C] and [N/O] abundance ratios (which should correspond to unmixed objects) nearly coincide with the solar values and those adopted by evolutionary models on the ZAMS. There are only a few values appearing below (though well within 2σ in our case) and they can be explained by statistical fluctuations, considering Gaussian distributions. Abundance ratios thus appear much less affected by systematics. They are also more sensitive to mixing (Maeder et al. 2014): [N/C] should increase more rapidly than the nitrogen abundance in the CN cycle because the stellar core should be gradually depleted in carbon; in the ON cycle, the same behaviour is observed for [N/O], due to the depletion of oxygen that occurs in this regime. These abundance ratios are thus better indicators of transport processes. However, numerous [N/C] values in our study are lower limits, mostly because only upper limits could be derived for the carbon abundance in our coolest stars (since the diagnostic C III lines are then very weak): adopting this ratio would thus lead to the exclusion of many targets. Furthermore, there is a good correlation between [N/C] and [N/O] (see Fig. 7 of Paper I), and the conclusions presented in the following will be unchanged whatever the adopted ratio. Therefore, we consider the [N/O] abundance ratio as the main diagnostic of rotational mixing in the rest of this paper[1].

---

[1] The [N/O] abundance ratio of HD 150574 is, however, unavailable (see Paper I).

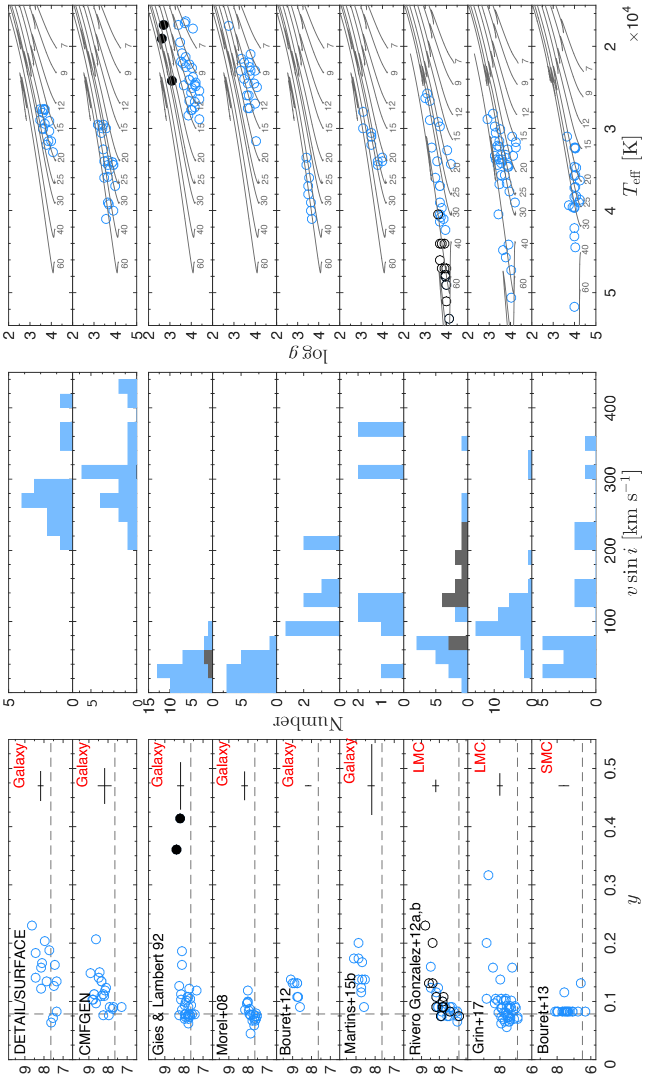

Fig. 2. *Left panels:* Nitrogen abundance as a function of the helium abundance (y = $\mathcal{N}$(He)/[$\mathcal{N}$(H) + $\mathcal{N}$(He)]) for this work (with cooler and hotter stars depicted in the first and second rows, respectively) and previous non-LTE studies in the literature (Gies & Lambert 1992; Morel et al. 2008; Bouret et al. 2012, 2013; Rivero González et al. 2012a,b; Martins et al. 2015b; Grin et al. 2017). The very He-rich stars of Gies & Lambert (1992) are highlighted as filled symbols. The helium data of Morel et al. (2008) are supplemented by results from Morel et al. (2006), Briquet & Morel (2007), Briquet et al. (2007), and Hubrig et al. (2008). Sample stars of Rivero González et al. (2012a) and Rivero González et al. (2012b) are shown in blue and black, respectively. Typical error bars are shown to the right of each panel. The dashed lines show the baseline abundances of Brott et al. (2011a) for the Galaxy and the Magellanic Clouds. *Central panels:* Breakdown of $v \sin i$ values. *Right panels:* Positions of the stars in the Kiel diagram. Evolutionary tracks from Brott et al. (2011a) for the relevant metallicity are overplotted. Initial stellar masses (in solar units) are indicated. Rotational velocities at the ZAMS of Galaxy models for stellar masses higher than 12 $M_\odot$ are listed in Table 1; for 7, 9, and 12 $M_\odot$, the initial rotational velocities are chosen to be close to that of the 15 $M_\odot$ model, i.e. 339, 333, and 331 km s^{-1}, respectively. Assumed rotational velocities at the ZAMS of Magellanic Cloud models are close to the ones of Galaxy models for each mass. Lower and upper limits are ignored in all plots.

The amount of mixing by rotation inside massive stars depends on several factors: rotational velocity, mass, but also age, metallicity, multiplicity, and possibly magnetic fields. Prior to comparing our results with model predictions, we will thus separate our sample into different subgroups. As the distance and thus the luminosity of our targets are usually not accurately known, their position in a $T_{\rm eff}$–$\log g_{\rm C}$[2] diagram is used to estimate their evolutionary status. The Kiel diagram is shown in Fig. 3 where the Bonn and Geneva evolutionary models are overplotted. All our targets are on the main sequence. Furthermore, all stars have masses comprised between 15 and ∼ 60 $M_\odot$; splitting the sample into groups of stars with similar masses may ease the comparison with models. To define such subsamples, we build [N/O] versus $\log g_{\rm C}$ diagrams (Fig. 4) and examine when significant changes in theoretical [N/O] occur. This was done considering Geneva models since there is no monotonic change with mass in the theoretical curves of the Bonn group for the chosen initial rotational velocities (Table 1). This slightly non-monotonic behaviour of the Bonn models might occur because mixing through composition barriers can depend (numerically) on spatial resolution (see Lau et al. 2014). Since the 15, 20, and 25 $M_\odot$ Geneva models predict similar [N/O] values during the MS phase, we can thus group all lower-mass targets. The increase of [N/O] for high-mass stars is expected to be significantly greater than for lower-mass stars. We thus define three subsamples: from 15 to 28 $M_\odot$, from 29 to 35 $M_\odot$, and above 35 $M_\odot$. In order to compare the properties of our stars with models of appropriate mass, our data and evolutionary tracks will be colour-coded as a function of the stellar mass in all diagrams of the following sections. As shown by Langer (1992), the evolutionary masses of helium-rich stars are overestimated compared to theoretical tracks computed for a solar He abundance, but neglecting this aspect is not expected to notably affect the breakdown of the stars in the various subsamples. A more significant effect is actually the choice of the evolutionary models; as can be seen, the Geneva and Bonn groups predict very different evolutionary paths in Fig. 3. For this reason, the population in each subsample is different depending on the chosen family of models.

Finally, a previous episode of mass transfer may also dramatically alter the chemical properties of components in a massive binary. In Paper I we derived the multiplicity status of our targets. We found 19 stars to be presumably single (47.5% of our sample); 9 stars with variable RVs, hence probable binaries (22.5% of our sample); and only 5 targets with SB1 orbital solution, hence confirmed binaries (12.5% of our sample). The binary status of 7 stars (17.5% of our sample) could not be determined because of a lack of observations. We note that confirmed double-lined spectroscopic binaries (SB2s) were initially discarded from our sample and that none of our targets were subsequently found to belong to this category. In parallel, a runaway status has been assigned to 10 targets (25% of the sample).

Our RV measurements are derived from our own observations and from a large body of spectra retrieved from public archives (see Paper I for details). In addition, our RV dataset is supplemented by results taken from the literature. Although the sampling of the RV time series varies drastically depending on the target considered, this approach generally provides a large number of measurements spread over a very long temporal baseline. Of particular interest is the fact that most stars have been monitored over a time span considerably exceeding ∼3 years, which implies that we are in principle sensitive to long orbital periods. For most of our targets, we therefore possess all the information necessary to examine the impact of multiplicity on the abundances. However, some caveats do exist and we discuss the consequences of potentially missed binaries in Sect. 4 .

Table 1. Assumed initial rotational velocities for Geneva and Bonn models.

Geneva		Bonn	
M ($M_\odot$)	$v_{\rm ZAMS}$ (km s^{-1})	M ($M_\odot$)	$v_{\rm ZAMS}$ (km s^{-1})
15	400	15	329
20	421	20	324
25	441	25	374
32	614	30	372
40	647	40	417
60	714	60	455

Notes. Values of the Bonn models were chosen to best represent the typical $v \sin i$ of our sample stars, i.e. ∼ 300 km s^{-1}, at the middle of the MS phase. In this context, we assume $i = 70°$ as, being fast rotators, our targets are preferentially seen close to equator on (see Appendix B and discussion in Sect. 3 for the inclination values found by BONNSAI; we also note that Zorec et al. 2002 obtained an average value of 68±18° for a sample of Be stars). We emphasise that another slightly different choice would not affect our conclusions. Geneva models have systematically greater initial rotational velocities than the Bonn models. This is due to the different treatment of rotation within the star: Geneva models assume a less strong coupling between the core and the envelope and the surface spin-down by stellar winds is more efficient than in Bonn models. Higher initial rotational velocities are therefore needed to reach fast rotation during the MS phase.

One can argue that the stars in our sample that we define as being RV variables may actually be pulsating stars. However, the "presumably single star" classification that we obtain for stars that have well-characterised pulsations (HD 93521, Rauw et al. 2008; HD 149757, Kambe et al. 1997) suggests that the number of pulsators incorrectly identified as binaries is low and that the criteria, inspired by those of Sana et al. (2013) and used in Paper I to establish whether the measured RVs are variable, generally excludes pulsators. However, we exclude HD 28446A and HD 41161 from the discussion in Sect. 4 as the origin of their RV variations is unclear (see Paper I).

3. Comparison with single-star evolution

In this section we confront our results with predictions for single star evolution from Geneva and Bonn models.

Internal magnetic fields induce the transport of chemical elements and angular momentum inside the star (e.g. Maeder & Meynet 2005)[3]. External magnetic fields generate a mechanical coupling between the stellar surface and the winds, taking away some angular momentum from the star (ud-Doula & Owocki 2002; ud-Doula et al. 2008) and producing a magnetic braking (ud-Doula et al. 2009; Meynet et al. 2011). The presence of magnetic fields is thus predicted to modify the amount of mixing in stellar interiors, hence to affect abundances at the stellar surface (e.g. Heger et al. 2005; Meynet et al. 2011; Potter at al. 2012). However, the abundance analyses of magnetic massive stars did

---

[2] $\log g_{\rm C}$ is the surface gravity corrected for the effects of centrifugal forces: $g_{\rm C} = g + (v \sin i)^2/R_*$, with R_* being the star radius (Repolust et al. 2004).

[3] The Bonn models do not consider the effect of magnetic fields on the transport of chemical elements; however, they do incorporate their effect on the distribution of angular momentum in the interior (Brott et al. 2011a).

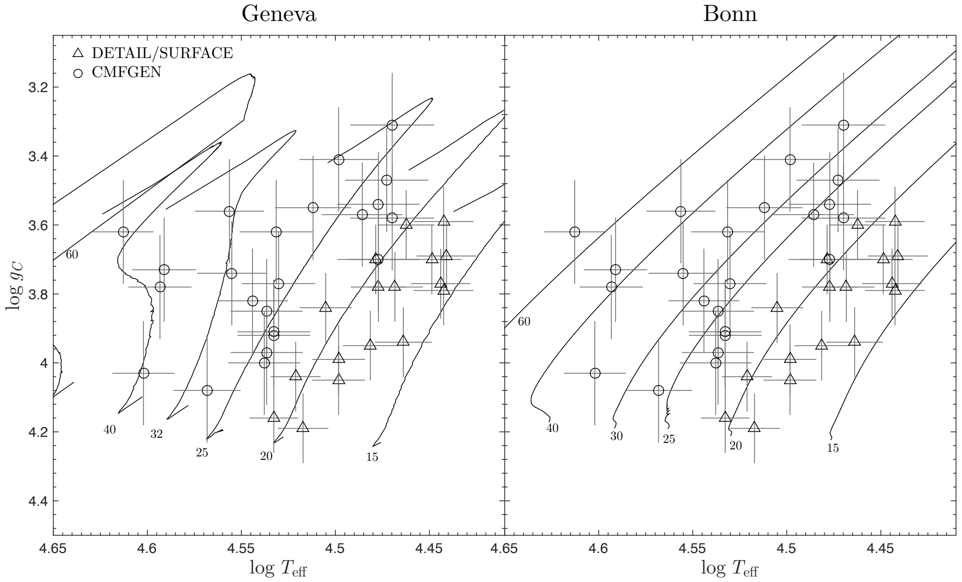

Fig. 3. Kiel diagrams comparing the position of our targets with evolutionary tracks (left-hand panel displays Geneva models; right-hand panel displays Bonn models). Only the predictions for the MS phase are illustrated. The initial stellar masses (in solar units) are indicated for each model. Rotational velocities at the ZAMS are listed in Table 1. Triangle and circle symbols represent the cooler stars studied with DETAIL/SURFACE and the hotter stars studied with CMFGEN, respectively.

not reveal a clear and systematic difference in their surface CNO properties compared to non-magnetic stars (Morel 2012; Martins et al. 2015a). Furthermore, the incidence of large-scale surface fields with a longitudinal component above ~ 100-200 G is only of the order of 10% in massive stars (Fossati et al. 2015; Grunhut et al. 2017). This proportion applies to large samples that combine different types of stars, but some categories of objects are known to behave very differently (see e.g. Wade et al. 2014). Are fast rotators also a special group in this respect? Assuming the magnetic fields to be fossil, we would not expect evolved fast rotators to host a field as magnetic braking would have spun them down significantly. On the other hand, considering magnetic field and fast rotation to both arise from a merger event (Ferrario et al. 2009), we could instead expect a large fraction of magnetic stars in our sample. It is thus difficult to speculate theoretically on the magnetic field incidence amongst fast rotators. There are, however, some observational constraints, as about a quarter of our targets have been observed in circular spectropolarimetry: HD 66811, HD 93521, and HD 149757 were studied by Hubrig et al. (2013, 2016); HD 46056 and HD 93521 were analysed in the framework of the BOB survey (Fossati et al. 2015); while HD 46056, HD 46485, HD 66811, HD 69106, HD 149757, HD 192281, HD 203064, and HD 210839 were observed as part of the MiMeS survey (Grunhut et al. 2017). No significant field detection was reported for any of those stars; however, this is not surprising as the vast majority of magnetic OB stars are slow rotators. Since there is no convincing evidence for a generalised strong magnetic character in fast rotators, and since evidence for CNO abundance peculiarities in magnetic massive stars is unconvincing, we will not consider the influence of internal or external magnetic fields in our comparison with evolutionary models.

Figure 4 shows the [N/O] values of our sample stars as a function of their log g_C, which we use as a proxy for their evolutionary status. In the Geneva models there is no increase of the [N/O] abundance ratios at the very beginning of the MS, but there is a gradual increase afterwards. The evolution of [N/O] is widely different in the Bonn models as they predict a faster increase of [N/O] when the star evolves off the ZAMS but then no significant change during the rest of the MS. Nevertheless, compared to these models, some of our targets exhibit higher or lower [N/O] abundance ratios than is predicted for their mass, rotational velocity, and evolutionary status. Of particular importance are the stars in our sample with an apparent lack of CNO-cycled material at their surface (they correspond to the anomalous group 1 of Hunter et al. 2007, 2009). In our sample, such objects tend to have a mass in the range 15–28 $M_\odot$. We note that these stars are a mixture of objects studied with DETAIL/SURFACE and CMFGEN. Their low [N/O] abundance ratio is therefore very unlikely to be an artefact of the data analysis (see comparison of the two methods for a few illustrative cases in Sect. 6.3 of Paper I). An interesting result is that the higher-mass stars display higher [N/O] abundance ratios, at any given value of the surface gravity, which is a trend predicted by the rotational mixing theory.

Fig. 5 shows the [N/O] abundance ratios as a function of the projected rotational velocities. The [N/O] of most stars can be explained by single-star models, but some stars show discrepant [N/O] values considering their mass and projected rotational velocity, especially when they are compared to Geneva models.

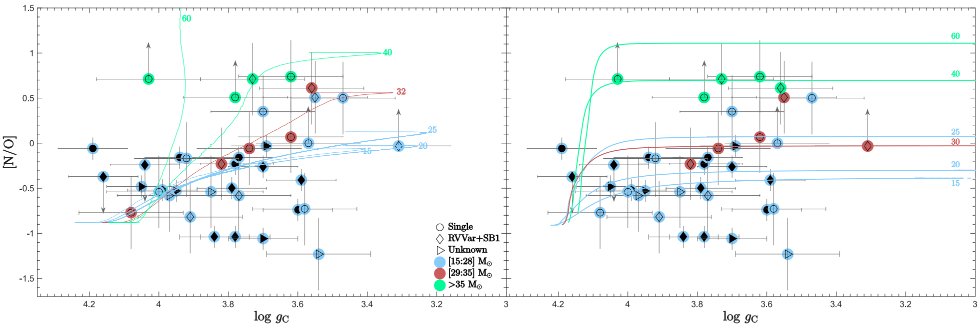

Fig. 4. Predicted [N/O] values as a function of log g_C by the Geneva (left) and Bonn (right) groups. Initial stellar masses (in solar units) are indicated. Rotational velocities at the ZAMS are listed in Table 1. Each panel shows the data for the presumably single stars (circles), RV variables and SB1s (diamonds), and stars with unknown multiplicity status (right oriented triangles). Black empty and filled symbols represent the hotter stars studied with CMFGEN and the cooler stars studied with DETAIL/SURFACE, respectively. Blue, brown, and green filled circles represent stars with masses comprised in the ranges from 15 to 28, from 29 to 35, and higher than 35 M$_\odot$, respectively.

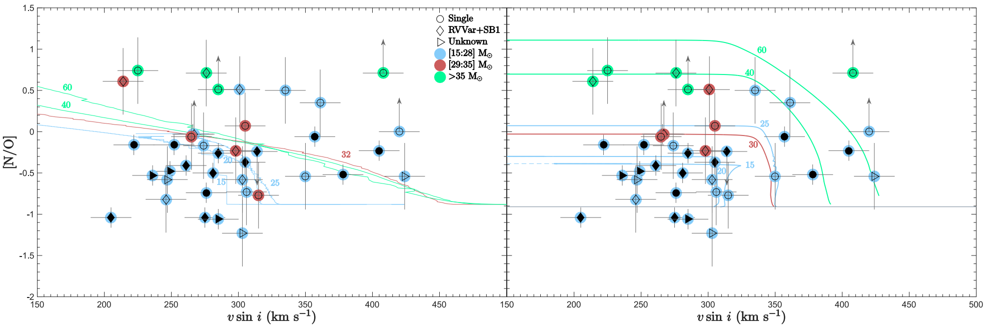

Fig. 5. [N/O] abundance ratio as a function of $v \sin i$. Theoretical predictions for different masses and rotational velocities are from the Geneva (left) and Bonn (right) groups. Initial stellar masses (in solar units) are indicated. Rotational velocities at the ZAMS are listed in Table 1. Predicted rotational velocities have been multiplied by sin(70°) to take the projection effect into account (see Table 1); however, a slightly different choice would not affect these plots in any significant way. Solid lines in both models represent the MS phase, while dashed lines for the Bonn models represent the supergiant phase. Symbols and related colours are the same as in Fig. 4.

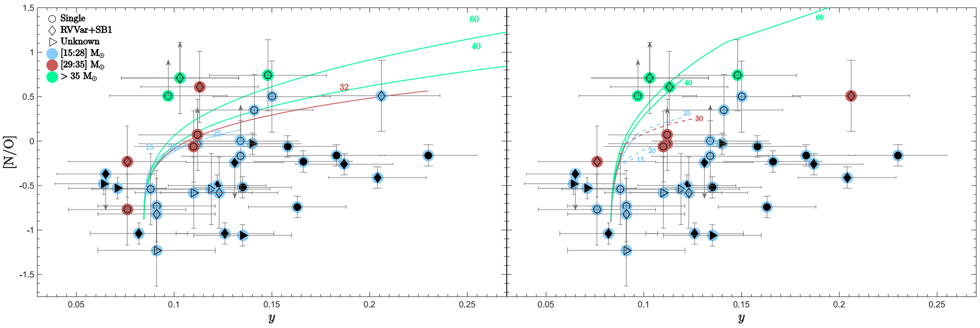

Fig. 6. [N/O] as a function of y. Graphical conventions are the same as in Figs. 4 and 5.

Fig. 6 shows the [N/O] abundance ratios as a function of the helium abundances. In order to investigate the likelihood of the presence of a positive correlation between the two quantities, we used the "bhk" and "spearman" tasks of the stsdas.statistics package in IRAF[4] that can take upper/lower limits into account. The highest significance levels are obtained with the "spearman" method, but they only amount to 4.4 and 2.6% when upper and lower limits in [N/O] are taken into account or not, respectively. This suggests that there is no statistically significant correlation between [N/O] and y; we simply note a lack of cases with both high y and low [N/O] ratio.

The majority of our targets are located to the right of the curves for MS stars predicted by the Geneva and Bonn models; specifically, they are more enriched in helium than is predicted by models. It should be noted in this context that the Kiel diagrams of our targets (Fig. 3) instead indicate that they are core-hydrogen burning stars.

Globally, a comparison with evolutionary tracks reveals general trends, but we also performed a more detailed, object-by-object comparison. To this end, we used the BONN Stellar Astrophysics Interface (BONNSAI; Schneider et al. 2014)[5], which relies on the Bonn evolutionary models (unfortunately, a similar tool making use of Geneva models is not available). We considered a Salpeter mass function (Salpeter 1955) as initial mass prior and a Gaussian initial rotational velocity prior with a mean of 372 km s^{-1} and a full width at half maximum (FWHM) of 57 km s^{-1}. This FWHM value was inferred from a Gaussian fit of the breakdown of the $v \sin i$ values of our sample stars, while the mean initial velocity was chosen to be the one for which the corresponding Bonn model predicts $v \sin i \sim 300$ km s^{-1} (with $i = 70°$) at the middle of the MS phase for a 30 M$_{\odot}$ star, which is typical of our sample (Fig. 3).

We first tried to use all available parameters ($T_{\rm eff}$, $\log g_{\rm C}$, $v \sin i$, y, C, N, and O abundances) as input parameters. In this case, BONNSAI finds a match between the model predictions and the observed input parameters in 21 cases out of 40. The values provided by BONNSAI are given in Table B.1. Of these stars, the atmospheric parameters and abundances of HD 66811 cannot be reproduced with our chosen initial rotational velocity prior, but can be explained when a flat distribution is considered. This may be due to the particular properties of this star since it is the highest-mass star in our sample (and notably has a very high mass-loss rate). It is interesting to note that success or failure to get a solution is not linked to projected rotational velocities (i.e. the stars for which BONNSAI found a result span the whole range of $v \sin i$) or to the multiplicity status (5 RV variables and 3 SB1s are amongst the 21 successes). However, some of the stars for which BONNSAI fails to converge have nitrogen or oxygen abundances that are out of the ranges considered by this tool (7.64 – 10.12 and 7.19 – 8.55 dex for $\log \epsilon$(N) and $\log \epsilon$(O), respectively).

This recalls the elemental abundance problem already mentioned in Sect. 2. However, abundance ratios cannot be entered as input for BONNSAI. To overcome this limitation, we performed a second analysis, ignoring the CNO abundances (i.e. the input parameters are $T_{\rm eff}$, $\log g_{\rm C}$, $v \sin i$, and y). In this case, the atmospheric parameters and abundances of 32 stars can be derived by BONNSAI and are given in Table B.2; the 8 remaining stars in our sample have a helium abundance that is too high, which cannot be reproduced by Bonn models. As a last exercise, we therefore used BONNSAI without considering any abundance parameters. Convergence is then reached for all targets and the values derived by BONNSAI are given in Table B.3.

When BONNSAI reaches a solution it does not mean that the observed properties (especially the [N/O] ratio and y) are well reproduced. We therefore compare the observed and predicted values of the helium abundances and [N/O] ratios (see Fig. 7). Table 2 provides the number of stars whose predicted and observed y and [N/O] values both differ by less than 1, 2, and 3σ. On average, the properties of 50% of our 40 targets can be explained by models within 3σ (~33% for 2σ and ~15% for 1σ). There is no tendency for our targets to present systematically higher (or lower) [N/O] values than the predictions of the Bonn models. However, as already pointed out above, we note a systematic excess in the observed helium abundance ($y - y_{\rm BONNSAI} > 0$) for the vast majority of the stars shown in Fig. 7 (84%) and a slight underabundance of helium ($y - y_{\rm BONNSAI} < 0$) for a minority of them (16%). More precisely, there is a significant (above 1σ) excess in helium for 56% of the stars in the first subsample, the deviation remaining within 1σ for 44% of them. There is no case of significant underabundance of helium.

In summary, while [N/O] ratios may or may not be reproduced depending on the object under consideration, single-star models and observations differ in a more systematic way for the helium abundance.

For very luminous stars, the outer layers can be peeled off because of strong mass loss. Helium-rich material would then be revealed at the surface. However, as shown by Bestenlehner et al. (2014) from LMC observations, it only occurs for $\log(\dot{\rm M}/{\rm M}) \gtrsim -6.5$. Current single-star models for Galactic stars using the mass-loss formalism of Vink et al. (2001) also do not predict strong helium enrichment for stars with masses below 60 M$_{\odot}$. This conclusion depends on the assumed overshooting parameter as a helium excess due to mass loss is expected in the stellar mass range 40–60 M$_{\odot}$ for high values (Castro et al. 2014). However, HD 66811 is the only star in our sample falling in this mass range.

Furthermore, it should be noted that in the case of very fast rotation, the mixing timescale becomes shorter than the nuclear timescale (Maeder 1987). No strong chemical gradients can then develop in the stellar interior and it will therefore be completely mixed. Thus, a fast-rotating MS star could exhibit a high helium abundance at its surface; however, as the opacity is reduced by the large fraction of helium at the surface, such a quasi-chemically homogeneous star will appear overluminous for its mass. This peculiarity can be revealed with the method of Langer & Kudritzki (2014) for stars exhibiting an excess in helium at their surface and with accurate distance estimates. It is the case for HD 66811 and HD149757, which have good Hipparcos parallaxes (van Leeuwen et al. 1997; Maíz Apellániz et al. 2008); in the case of HD 66811, we assume here that the helium excess at its surface arises from rotational mixing, and is not related to its strong mass loss. We evaluated their luminosities from the distances, reddenings (taken from Bastiaansen (1992) and Morton (1975) for HD 66811 and HD 149757, respectively), apparent magnitudes in the V band, and typical bolometric corrections for their spectral types (Martins et al. 2005). Evidence of an overluminosity is found for these two stars, which – independent of their evolutionary history – is consistent with their enhanced helium abundance (Langer 1992). In the context of single stars, this may indicate a quasi-chemically homogeneous evolution. An as-

---

[4] `IRAF` is distributed by the National Optical Astronomy Observatories, operated by the Association of Universities for Research in Astronomy, Inc., under cooperative agreement with the National Science Foundation.

[5] The BONNSAI web-service is available at `http://www.astro.uni-bonn.de/stars/bonnsai`.

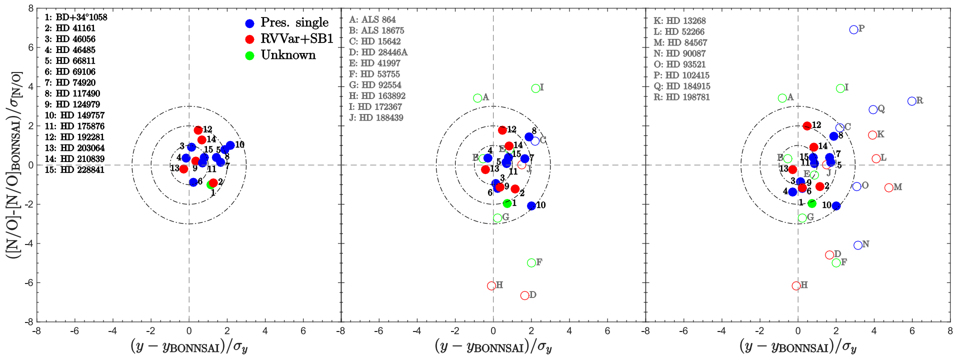

Fig. 7. Difference between the observed [N/O] ratio and that predicted by BONNSAI, normalised by the error derived for our objects, as a function of a similar difference for the abundance y. Stars with lower/upper limits in [N/O] are not included, explaining why there are fewer stars than indicated in Tables B.1-3. Filled circles represent the stars common to the three panels. The three dash-dotted circles delimitate the areas in which the differences are within 1, 2, and 3 σ. Colours represent the multiplicity status of our targets. The input parameters in BONNSAI are different for the three panels – left panel: full parameter set (T_{eff}, $\log g_{\mathrm{C}}$, $v \sin i$, He and CNO abundances); middle panel: T_{eff}, $\log g_{\mathrm{C}}$, $v \sin i$, and y; right panel: T_{eff}, $\log g_{\mathrm{C}}$, and $v \sin i$.

Table 2. Number of stars whose helium abundances and [N/O] ratios are both reproduced by Bonn models within 1, 2, and 3σ. Stars with lower/upper limits in [N/O] are not considered.

BONNSAI input parameters	$\leq 1\sigma$	$\leq 2\sigma$	$\leq 3\sigma$
T_{eff}, $\log g_{\mathrm{C}}$, $v \sin i$, y, CNO abundances	7	13	15
T_{eff}, $\log g_{\mathrm{C}}$, $v \sin i$, y	7	15	20
T_{eff}, $\log g_{\mathrm{C}}$, $v \sin i$	6	14	20

sessment of such overluminosities for the full sample must await further *Gaia* data releases.

Another way to examine the mismatch between the observations and the theoretical expectations is to investigate whether the efficiency of chemical element transport is different from what is assumed in the models. We therefore examined the role of turbulent diffusion. To this end, we used an updated version of the Code Liégeois d'Évolution Stellaire (CLÉS; Scuflaire et al. 2008) in which a turbulent diffusion has been implemented for every element following a decreasing law towards the stellar interior, and which is controlled by a constant diffusion coefficient D_{T} as a free input parameter in the models. Predicted helium abundance and [N/O] ratios are illustrated in Kiel diagrams (Fig. 8) for different diffusion rates, called diffusion 1 and 2, chosen according to their effect on the surface abundances. From these diagrams, it is found that helium and [N/O] enrichments can be explained in most stars by the diffusion 1 configuration, for which the diffusion coefficient is of the order of $D_{\mathrm{T}} \sim 10^7$ cm^2 s^{-1}. This diffusion coefficient, which had to be included in order to fit the observations, is quite large. Miglio et al. (2008) have shown that in a 6 M$_{\odot}$ model, a diffusion coefficient of D_{T} = 5000 cm^2 s^{-1} reproduces the main sequence evolutionary tracks of a 6 M$_{\odot}$ rotating model with an initial velocity of 25 km s^{-1}. In order to reproduce the helium abundance of the most helium-enriched star in our sample (HD 198781), we have to consider an even larger diffusion, which would lower the initial mass of the model to 6 M$_{\odot}$, though (standard) evolutionary tracks (Fig. 3) hint at a mass of ~15 M$_{\odot}$ for this star. Moreover, we note that the [N/O] ratio predicted by this model is too high compared to the observed value. Furthermore, we also tested the effect of combinations of overshooting and mass loss in models computed with the same evolutionary code but without diffusion. The only way to reproduce the observed enrichment in helium (and in [N/O]), as well as the position of our targets in the Kiel diagram, is by considering a very large parameter, such as α_{oversh} = 0.5, and a mass-loss rate 10 times larger than the predicted values of Vink et al. (2001) for 40 and 50 M$_{\odot}$ models. In conclusion, such enrichments in helium combined with high [N/O] ratios can only be achieved in models accounting for uncommonly large input parameters.

4. Comparison with binary star evolution

As shown in the previous section, many aspects of our observations cannot be explained by single-star evolutionary models. In the following, we therefore consider the possible influence of companions on the surface abundances of our targets.

The presence of close companions may modify the surface abundances and the rotation rates of massive stars, because of tidal effects (Zahn 1975; Hut 1981; de Mink et al. 2009, 2013; Song et al. 2013), mass accretion (Packet 1981; Pols et al. 1991; Podsiadlowski et al. 1992; Langer et al. 2003; Petrovic et al. 2005a,b; de Mink et al. 2009, 2013; Dervişoğlu et al. 2010) or even merging (de Mink et al. 2013; Tylenda et al. 2011). For example, Köhler et al. (2012) proposed that fast rotators with low surface nitrogen abundance (which cannot be explained by single-star evolutionary models) may have been slow rotators for most of their lives, and then experienced a non-conservative mass transfer in a binary system. In parallel, the enrichment in nitrogen and/or helium is considered a signature of a past Roche-

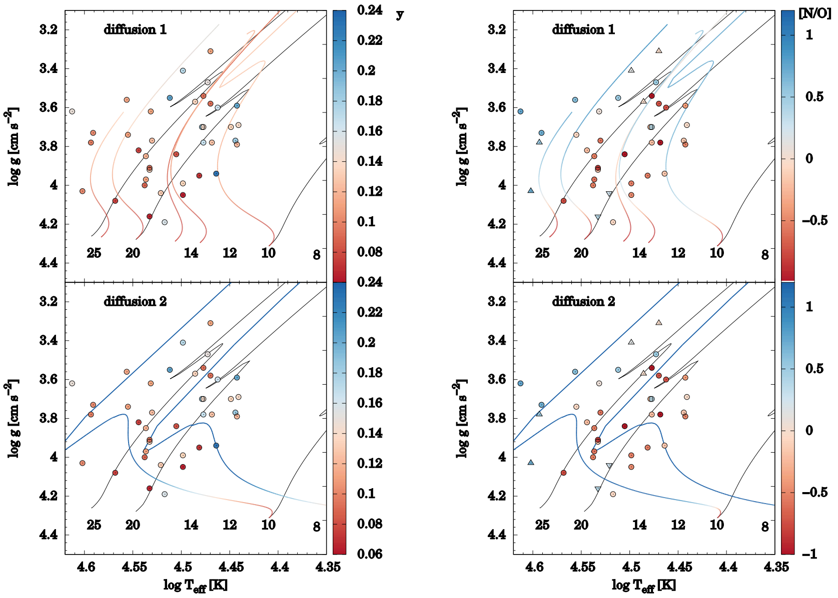

Fig. 8. Illustrative impact of the choice of the diffusion coefficients on the CLÉS evolutionary tracks, as well as the predicted helium abundances and [N/O] ratios. Black tracks stand for models without diffusion, while models with different diffusion coefficients are colour-coded according to helium abundance (left panel) or the [N/O] ratio (right). The first and second rows of panels show the tracks computed with diffusion 1 and 2 (see text), respectively. Circles stand for fixed values, upwards oriented triangles for lower limits, and downwards oriented triangles for upper limits in [N/O].

lobe overflow (RLOF) for the Plaskett's Star (Linder et al. 2008), θ Car (Hubrig et al. 2008), HD 149404 (Raucq et al. 2016), LSS 3074 (Raucq et al. 2017), as well as the X-ray binaries X Per (Lyubimkov et al. 1997) and BD +53° 2790 (Blay et al. 2006).

After such a mass-transfer episode, the gainer star may be "rejuvenated" (e.g. the blue straggler θ Car in IC 2602; Hubrig et al. 2008). The stars in clusters should thus appear younger than the other members. Two stars in our sample are confirmed cluster members, so their ages are known: HD 46056 and HD 46485 in NGC 2244 (Ogura & Ishida 1981). They are both presumably single stars. Using our last BONNSAI run, we estimated the ages of these stars (see Table B.3) and compared them with the age of their host cluster taken from Hensberge et al. (2000): 2.3 ± 0.2 Myrs. No significant difference is found.

While our sample contains several true or probable binaries, it also contains runaway stars; these objects can be the consequence of dynamical interactions in a cluster or the result of a(n) (asymmetric) supernova explosion. In the latter case, surface abundances of the surviving star may be affected. It is thus interesting to examine specifically the results obtained for runaway objects, whatever their multiplicity status. We note that, in dynamical interactions, ejection of a binary occurs in ~ 10% of the cases (Leonard & Duncan 1990), while ~ 20 to 40% of runaways resulting from a supernova explosion remain binary systems (Portegies Zwart 2000). However, ten of our objects – five of which are runaways, including the SB1 HD 210839 – have been searched for pulsed radio emission (Philp et al. 1996; Sayer et al. 1996), but none was found.

Figures A.1, A.2, and A.3 split the results shown in Figs. 4, 5, and 6, respectively, according to the multiplicity status of the targets derived in Paper I. The lack of clear differences between binaries (or runaways) and single stars may at first sight look surprising. However, it should be kept in mind that the classification of targets as presumably single suffers from some unavoidable limitations. For instance, an obvious observational bias is that several single stars lacking an extensive RV monitoring might have been detected as variable had more data been accumulated. Furthermore, some stars identified as presumably single might actually be the products of mass transfer in a binary. As noted by de Mink et al. (2014), the RV variation induced by the presence of a companion star will not be large enough to be detected in typically ~ 45% of all early B- and O-type stars. Indeed, models predict that post-mass exchange systems are relatively long-period binaries with a large mass ratio (e.g. Wellstein et al. 2001). The companion is thus expected to be much fainter than the actual primary and to reside in an orbit that is quite wide, which would induce low-amplitude RV variations of the mass gainer (typically ~ 10 km s^{-1} if the unseen companion is a stripped-down remnant; see e.g. Poeckert 1981, Peters et al. 2008, 2013, 2016). These expected RV variations are comparable to the precision that can be achieved for fast-rotating OB stars. To complicate matters further, stars that survive the supernova explosion of the former companion may not necessarily have a large peculiar velocity (Eldridge et al. 2011).

Furthermore, Sana et al. (2012) argued that the evolution of more than 70 % of massive stars is affected by binary effects, and de Mink et al. (2011) claimed that these effects mainly result in a single star (after a merging event that occurs, according to Sana et al. 2012, for $\sim$25% of O stars) or a look-alike star (for example one that has gained mass in a post mass-transfer event and which is associated with a very faint companion). Therefore, if we did not detect large differences between our subsamples on the basis of their multiplicity, it may simply be because several presumably single stars are binary products. It is thus worth comparing our results for all stars with those expected from binary evolutionary models.

First, Glebbeek et al. (2013) calculated the consequences of stellar merging, notably on the surface abundances exhibited by the resulting object. Figure 9 compares their results with those obtained for our presumably single stars. As can be seen, the observed [N/O] ratios agree with expectations for most of the lower-mass subsample, but disagree for the higher-mass objects. The reverse situation is found for the helium abundances. However, it must be noted that the models of Glebbeek et al. (2013) do not take the rotation of stars into account so their predictions of surface nitrogen and helium abundances should be considered as lower limits. This leads us to speculate that observations and predictions are in fact in better agreement than Fig. 9 suggests.

Second, we consider binary models that include mass and angular momentum transfer (Wellstein & Langer 1999; Wellstein et al. 2001). Figure 10 compares the predicted values for a mass gainer at the end of mass transfer assuming different initial masses, orbital periods, mass transfer cases, and semi-convective efficiency parameters. We see that binary models computed with a slow semi-convective mixing predict $y \lesssim 0.13$. Predictions by these models are very similar to those by Glebbeek et al. (2013) in the [N/O] versus y plane. On the other hand, the model adopting the Schwarzschild condition reaches $y \sim 0.19$. Binary models with fast semi-convective mixing can therefore explain the abundances of our most helium-enriched stars, and can also reproduce the effective temperature and surface gravity of two of them (HD 13268 and HD 150574) within the error bars. There are, however, a few data points in Fig. 10 located above the predictions of the binary models investigated here, i.e. stars with little helium enrichment but significant nitrogen excess. Three stars with both high y and low [N/O] values also exist in a region that does not comply with the theory of the CNO-cycle, and the region is thus not expected to be filled. There is no evidence that these abundances are related to artefacts in the data analysis, but a few outliers are expected on statistical grounds, as mentioned in Sect. 2, and they can be reconciled with models at 3σ.

5. Conclusion

Following the derivation of the individual stellar parameters and abundances of 40 fast rotators in Paper I, we have analysed the results in a global way.

Using BONNSAI, we found that the Brott et al. (2011a) models can reproduce the atmospheric parameters and abundances of half of our sample. Interestingly, we found that the atmospheric parameters and abundances can be reproduced by single-star evolutionary models whatever the multiplicity status of the targets. Some systems might thus be pre-interaction binaries (de Mink et al. 2011). We found a systematic underprediction of the helium abundance for our targets. Changing the diffusion coefficient in models does not solve this issue as both y and [N/O] ratios cannot be reproduced simultaneously.

As our sample contains known or probable binaries, as well as runaways, and since even presumably single stars may actually be binaries or have suffered from interactions with a companion, we have also compared our results with those from binary evolutionary models. We find that merger models of nonrotating objects (Glebbeek et al. 2013) are not readily able to reproduce the [N/O] abundance ratios of our higher-mass single stars and the helium abundances of our lower-mass single stars, but an agreement might be reached after stellar rotation is taken into account. On the other hand, binary models including mass and angular momentum transfer (through RLOF) appear to explain the [N/O] in most cases and can reproduce the helium abundances of some of our most helium-enriched stars, but have difficulties in explaining the properties of some of our stars.

In summary, we confirm the presence of fast massive rotators with no nitrogen enrichment for 10–20% of our targets (first reported by Hunter et al. 2009), but bring to light another unexpected problem: a quite common large abundance of helium at the stellar surface. Such features appear difficult to reproduce by single-star or binary evolutionary models, indicating that some fundamental physics ingredient is missing in (or is not well taken into account by) current models. On the observational side, future work should focus on fast rotators of the SMC and LMC, where the enhancement of the surface nitrogen abundance arising from rotational mixing is expected to be greater than in the Galaxy and which should thus reveal the abundance problems in even greater detail.

Acknowledgements. We are very grateful to the referee for providing useful comments. We thank Dr Fabian Schneider for helping us with BONNSAI, and Drs Nathan Grin and Pablo Marchant for providing useful comments. We also thank Prof. Arlette Grötsch-Noels and Dr. Richard Scuflaire for very fruitful discussions and for making the necessary modifications in the CLÉS evolutionary code for our paper. The Liège team acknowledges support from the Fonds National de la Recherche Scientifique (Belgium), the Communauté Française de Belgique, the PRODEX XMM and GAIA-DPAC contracts (Belspo), and an ARC grant for concerted research actions financed by the French community of Belgium (Wallonia-Brussels federation). ADS and CDS were used to prepare this document.

References

Asplund, M., Grevesse, N., Sauval, A. J., & Scott, P. 2009, ARA&A, 47, 481
Bastiaansen, P. A. 1992, A&AS, 93, 449
Bestenlehner, J. M., Gräfener, G., Vink, J. S., et al. 2014, A&A, 570, A38
Blay, P., Negueruela, I., Reig, P., et al. 2006, A&A, 446, 1095
Bouret, J.-C., Hillier, D. J., Lanz, T., & Fullerton, A. W. 2012, A&A, 544, A67
Bouret, J.-C., Lanz, T., Martins, F., et al. 2013, A&A, 555, A1
Briquet, M., & Morel, T. 2007, Communications in Asteroseismology, 150, 183
Briquet, M., Morel, T., Thoul, A., et al. 2007, MNRAS, 381, 1482
Brott, I., de Mink, S. E., Cantiello, M., et al. 2011a, A&A, 530, A115
Brott, I., Evans, C. J., Hunter, I., et al. 2011b, A&A, 530, A116
Butler, K., & Giddings, J. R. 1985, in Newsletter of Analysis of Astronomical Spectra, No. 9 (Univ. London)
Castro, N., Fossati, L., Langer, N., et al. 2014, A&A, 570, L13
Cazorla, C., Morel, T., Nazé, Y., et al. 2017, A&A, in press, arXiv:1703.05592 (Paper I)
de Mink, S. E., Cantiello, M., Langer, N., et al. 2009, A&A, 497, 243
de Mink, S. E., Langer, N., & Izzard, R. G. 2011, Bulletin de la Société Royale des Sciences de Liège, 80, 543
de Mink, S. E., Langer, N., Izzard, R. G., Sana, H., & de Koter, A. 2013, ApJ, 764, 166
de Mink, S. E., Sana, H., Langer, N., Izzard, R. G., & Schneider, F. R. N. 2014, ApJ, 782, 7
Dervişoğlu, A., Tout, C. A., & Ibanoğlu, C. 2010, MNRAS, 406, 1071
Dufton, P. L., Dunstall, P. R., Evans, C. J., et al. 2011, ApJ, 743, L22
Eldridge, J. J., Langer, N., & Tout, C. A. 2011, MNRAS, 414, 3501
Evans, C., Hunter, I., Smartt, S., et al. 2008, The Messenger, 131, 25
Ferrario, L., Pringle, J. E., Tout, C. A., & Wickramasinghe, D. T. 2009, MNRAS, 400, L71
Fossati, L., Castro, N., Schöller, M., et al. 2015, A&A, 582, A45
Georgy, C., Ekström, S., Granada, A., et al. 2013, A&A, 553, A24
Gies, D. R., & Lambert, D. L. 1992, ApJ, 387, 673
Giddings, J. R. 1981, Ph.D. Thesis

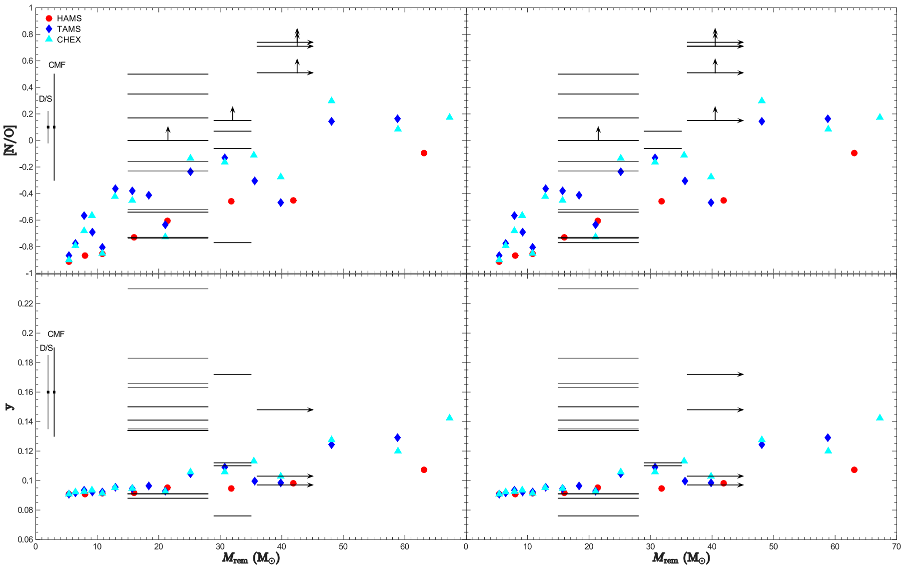

Fig. 9. [N/O] abundance ratios (upper panels) and helium abundance (lower panels) as a function of the total mass of merger remnants predicted by the models of Glebbeek et al. (2013). Symbols represent the evolutionary stages of the parent stars: solid red circles, blue diamonds, and cyan triangles stand for collisions halfway through the main-sequence lifetime (HAMS), at the terminal-age main sequence (TAMS), and at core hydrogen exhaustion (CHEX), respectively. [N/O] values for our presumably single stars are represented with thin and thick horizontal lines for the cooler and hotter samples, respectively, as a function of their typical masses derived with the Geneva (left panels) and Bonn models (right panels). Typical error bars for the DETAIL/SURFACE and CMFGEN analyses are indicated to the left of the diagrams.

Glebbeek, E., Gaburov, E., Portegies Zwart, S., & Pols, O. R. 2013, MNRAS, 434, 3497
Gray, D. F. 2005, "The Observation and Analysis of Stellar Photospheres", 3rd Edition, ISBN 0521851866, Cambridge University Press
Grin, N. J., Ramírez-Agudelo, O. H., de Koter, A., et al. 2017, A&A, 600, A82
Grunhut, J. H., Wade, G. A., Neiner, C., et al. 2017, MNRAS, 465, 2432
Grevesse, N., & Sauval, A. J. 1998, Space Sci. Rev., 85, 161
Heger, A., Woosley, S. E., & Spruit, H. C. 2005, ApJ, 626, 350
Hensberge, H., Pavlovski, K., & Verschueren, W. 2000, A&A, 358, 553
Hillier, D. J., & Miller, D. L. 1998, ApJ, 496, 407
Howarth, I. D., Siebert, K. W., Hussain, G. A. J., & Prinja, R. K. 1997, MNRAS, 284, 265
Hubrig, S., Briquet, M., Morel, T., et al. 2008, A&A, 488, 287
Hubrig, S., Schöller, M., Ilyin, I., et al. 2013, A&A, 551, A33
Hubrig, S., Kholtygin, A., Ilyin, I., Schöller, M., & Oskinova, L. M. 2016, ApJ, 822, 104
Hunter, I., Dufton, P. L., Smartt, S. J., et al. 2007, A&A, 466, 277
Hunter, I., Brott, I., Langer, N., et al. 2009, A&A, 496, 841
Hut, P. 1981, A&A, 99, 126
Kambe, E., Hirata, R., Ando, H., et al. 1997, ApJ, 481, 406
Köhler, K., Borzyszkowski, M., Brott, I., Langer, N., & de Koter, A. 2012, A&A, 544, A76
Langer, N. 1992, A&A, 265, L17
Langer, N., Wellstein, S., & Petrovic, J. 2003, A Massive Star Odyssey: From Main Sequence to Supernova, 212, 275
Langer, N., & Kudritzki, R. P. 2014, A&A, 564, A52
Lau, H. H. B., Izzard, R. G., & Schneider, F. R. N. 2014, A&A, 570, A125
Leonard, P. J. T., & Duncan, M. J. 1990, AJ, 99, 608
Linder, N., Rauw, G., Martins, F., et al. 2008, A&A, 489, 713
Lyubimkov, L. S., Rostopchin, S. I., Roche, P., & Tarasov, A. E. 1997, MNRAS, 286, 549
Maeder, A. 1987, A&A, 178, 159
Maeder, A., & Meynet, G. 2005, A&A, 440, 1041
Maeder, A., Przybilla, N., Nieva, M.-F., et al. 2014, A&A, 565, A39
Mahy, L., Martins, F., Machado, C., Donati, J.-F., & Bouret, J.-C. 2011, A&A, 533, A9
Maíz Apellániz, J., Alfaro, E. J., & Sota, A. 2008, arXiv:0804.2553
Martins, F., Schaerer, D., & Hillier, D. J. 2005, A&A, 436, 1049
Martins, F., Hervé, A., Bouret, J.-C., et al. 2015a, A&A, 575, A34
Martins, F., Simón-Díaz, S., Palacios, A., et al. 2015b, A&A, 578, A109
Meynet, G., Eggenberger, P., & Maeder, A. 2011, A&A, 525, L11
Miglio, A., Montalbán, J., Noels, A., & Eggenberger, P. 2008, MNRAS, 386, 1487
Morel, T., Butler, K., Aerts, C., Neiner, C., & Briquet, M. 2006, A&A, 457, 651
Morel, T., Hubrig, S., & Briquet, M. 2008, A&A, 481, 453
Morel, T. 2009, Communications in Asteroseismology, 158, 122
Morel, T. 2012, Proceedings of a Scientific Meeting in Honor of Anthony F. J. Moffat, 465, 54
Morton, D. C. 1975, ApJ, 197, 85
Nieva, M.-F., & Przybilla, N. 2012, A&A, 539, A143
Ogura, K., & Ishida, K. 1981, PASJ, 33, 149
Packet, W. 1981, A&A, 102, 17
Palate, M., & Rauw, G. 2012, A&A, 537, A119
Palate, M., Rauw, G., Koenigsberger, G., & Moreno, E. 2013, A&A, 552, A39
Peters, G. J., Gies, D. R., Grundstrom, E. D., & McSwain, M. V. 2008, ApJ, 686, 1280-1291
Peters, G. J., Pewett, T. D., Gies, D. R., Touhami, Y. N., & Grundstrom, E. D. 2013, ApJ, 765, 2
Peters, G. J., Wang, L., Gies, D. R., & Grundstrom, E. D. 2016, ApJ, 828, 47
Petrovic, J., Langer, N., Yoon, S.-C., & Heger, A. 2005a, A&A, 435, 247
Petrovic, J., Langer, N., & van der Hucht, K. A. 2005b, A&A, 435, 1013
Philp, C. J., Evans, C. R., Leonard, P. J. T., & Frail, D. A. 1996, AJ, 111, 1220
Podsiadlowski,P., Joss, P. C., & Hsu, J. J. L. 1992, ApJ, 391, 246
Poeckert, R. 1981, PASP, 93, 297
Pols, O. R., Cote, J., Waters, L. B. F. M., & Heise, J. 1991, A&A, 241, 419
Portegies Zwart, S. F. 2000, ApJ, 544, 437
Potter, A. T., Chitre, S. M., & Tout, C. A. 2012, MNRAS, 424, 2358
Przybilla, N., Firnstein, M., Nieva, M.-F., Meynet, G., & Maeder, A. 2010, A&A, 517, A38
Raucq, F., Rauw, G., Gosset, E., et al. 2016, A&A, 588, A10
Raucq, F., Gosset, E., Rauw, G., et al. 2017, A&A, in press, arXiv:1703.03247
Rauw, G., De Becker, M., van Winckel, H., et al. 2008, A&A, 487, 659

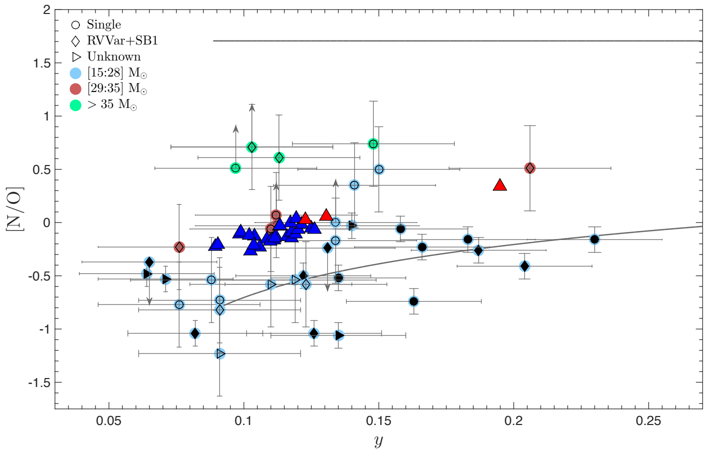

Fig. 10. [N/O] abundance ratio as a function of y for our sample stars and comparison with predicted values for mass gainers after a mass transfer, assuming that the mass donor has already exploded (triangles; Wellstein & Langer 1999; Wellstein et al. 2001). Our data are colour-coded as a function of the stellar mass defined by the Bonn models. Black empty and filled symbols represent the hotter stars studied with CMFGEN and the cooler stars studied with DETAIL/SURFACE, respectively. The mass gainers with initial masses of 8 – 25 M$_\odot$ which grow to 17 – 40 M$_\odot$ are shown in dark blue, while the mass gainers with initial masses of 22 – 24 M$_\odot$ which grow to ~40 M$_\odot$ are shown in red (a slow semi-convection mixing, $\alpha_{\rm sc} = 0.01$, and 0.04, has been considered for the two leftmost red triangles, while a fast semi-convection mixing Schwarzschild criterion, $\alpha_{\rm sc} = \infty$, has been considered for the rightmost one). The upper grey line shows the CNO equilibrium, while the lower grey line assumes that the extra helium at the surface contains the CNO-equilibrium distribution.

Repolust, T., Puls, J., & Herrero, A. 2004, A&A, 415, 349
Rivero González, J. G., Puls, J., Najarro, F., & Brott, I. 2012a, A&A, 537, A79
Rivero González, J. G., Puls, J., Massey, P., & Najarro, F. 2012b, A&A, 543, A95
Salpeter, E. E. 1955, ApJ, 121, 161
Sana, H., de Mink, S. E., de Koter, A., et al. 2012, Science, 337, 444
Sana, H., de Koter, A., de Mink, S. E., et al. 2013, A&A, 550, A107
Sayer, R. W., Nice, D. J., & Kaspi, V. M. 1996, ApJ, 461, 357
Schneider, F. R. N., Langer, N., de Koter, A., et al. 2014, A&A, 570, A66
Scuflaire, R., Théado, S., Montalbán, J., et al. 2008, Ap&SS, 316, 83
Simón-Díaz, S., & Herrero, A. 2007, A&A, 468, 1063
Song, H. F., Maeder, A., Meynet, G., et al. 2013, A&A, 556, A100
Tylenda, R., Hajduk, M., Kamiński, T., et al. 2011, A&A, 528, A114
ud-Doula, A., & Owocki, S. P. 2002, ApJ, 576, 413
ud-Doula, A., Owocki, S. P., & Townsend, R. H. D. 2008, MNRAS, 385, 97
ud-Doula, A., Owocki, S. P., & Townsend, R. H. D. 2009, MNRAS, 392, 1022
van Leeuwen, F., Evans, D. W., Grenon, M., et al. 1997, A&A, 323, L61
Vink, J. S., de Koter, A., & Lamers, H. J. G. L. M. 2001, A&A, 369, 574
Wade, G. A., et al., 2014, IAUS, 302, 265
Wellstein, S., & Langer, N. 1999, A&A, 350, 148
Wellstein, S., Langer, N., & Braun, H. 2001, A&A, 369, 939
Zahn, J.-P. 1975, A&A, 41, 329
Zorec, J., Frémat, Y., Hubert, A. M., & Floquet, M. 2002, IAU Colloq. 185: Radial and Nonradial Pulsations as Probes of Stellar Physics, 259, 244

Appendix A: Illustration of the results for our sample stars as a function of their multiplicity status

We present in Figs. A.1, A.2, and A.3 the results presented in Figs. 4, 5, and 6, respectively, but split according to the multiplicity status derived in Paper I. HD 28446 A and HD 41161 have been excluded because the origin of their RV variations is unclear (see Paper I).

Appendix B: Results obtained with BONNSAI

We present in Tables B.1, B.2, and B.3 the parameters and abundances derived by BONNSAI.

Table B.1. Results obtained with BONNSAI for stars for which atmospheric parameters and He, C, N, O abundances can be reproduced with Bonn models when $T_{\rm eff}$, $\log g_{\rm C}$, $v\sin i$, y, $\log \epsilon$(C), $\log \epsilon$(N), and $\log \epsilon$(O) are given as input to BONNSAI. Observed values of Paper I are indicated between parentheses.

Star	BD +34° 1058	BD +60° 594	HD 14434	HD 14442	HD 15137	HD 41161
$M_{\rm ini}$ (M$_\odot$)	$20.0^{+2.4}_{-1.6}$	$20.6^{+1.9}_{-1.7}$	$30.6^{+4.0}_{-3.3}$	$39.2^{+6.4}_{-4.5}$	$26.2^{+7.0}_{-3.7}$	$22.0^{+4.6}_{-3.0}$
$M_{\rm act}$ (M$_\odot$)	$20.0^{+2.2}_{-1.7}$	$20.6^{+1.6}_{-1.9}$	$30.0^{+3.9}_{-3.1}$	$36.0^{+5.7}_{-3.0}$	$25.0^{+6.1}_{-2.8}$	$21.8^{+4.2}_{-2.8}$
$\log L$ (L$_\odot$)	$4.7^{+0.1}_{-0.1}$	$4.7^{+0.2}_{-0.1}$	$5.2^{+0.1}_{-0.1}$	$5.5^{+0.1}_{-0.1}$	$5.4^{+0.1}_{-0.2}$	$4.9^{+0.3}_{-0.1}$
Age (Myr)	$1.6^{+1.9}_{-1.0}$	$4.0^{+0.6}_{-0.8}$	$1.3^{+0.8}_{-0.5}$	$2.9^{+0.4}_{-0.5}$	$4.6^{+1.4}_{-0.4}$	$4.1^{+0.9}_{-0.7}$
$\tau_{\rm MS}$	$0.2^{+0.2}_{-0.1}$	$0.5^{+0.1}_{-0.1}$	$0.2^{+0.1}_{-0.1}$	$0.6^{+0.1}_{-0.1}$	$0.8^{+0.0}_{-0.0}$	$0.6^{+0.1}_{-0.2}$
$v_{\rm ini}$ (km s^{-1})	$420.0^{+22.2}_{-19.3}$	$400.0^{+41.2}_{-23.2}$	$420.0^{+26.6}_{-14.8}$	$380.0^{+27.1}_{-33.4}$	$360.0^{+37.6}_{-33.3}$	$330.0^{+34.4}_{-25.4}$
$v\sin i$ (km s^{-1})	$420.0^{+12.9}_{-19.2}$ (424±15)	$320.0^{+13.1}_{-19.9}$ (314±15)	$400.0^{+16.9}_{-13.8}$ (408±15)	$280.0^{+18.3}_{-12.3}$ (285±15)	$270.0^{+14.1}_{-17.6}$ (267±15)	$300.0^{+18.4}_{-12.7}$ (303±15)
i (°)	90.0	53.1	77.3	74.9	74.6	75.4
y	$0.085^{+0.006}_{-0.000}$ (0.119±0.030)	$0.093^{+0.003}_{-0.003}$ (0.131±0.025)	$0.093^{+0.003}_{-0.003}$ (0.103±0.030)	$0.110^{+0.000}_{-0.014}\dagger$ (0.097±0.030)	$0.089^{+0.003}_{-0.003}$ (0.112±0.030)	$0.085^{+0.003}_{-0.003}$ (0.123±0.030)
$\log \epsilon$(C)	$7.91^{+0.14}_{-0.21}$ (7.90±0.27)	$7.72^{+0.12}_{-0.08}$ (7.66±0.12)	$7.70^{+0.18}_{-0.16}$ (7.96±0.27)	$7.39^{+0.22}_{-0.03}\dagger$ (7.10±0.27)	$7.80^{+0.12}_{-0.15}\dagger$ (7.63±0.27)	$7.90^{+0.06}_{-0.13}$ (7.87±0.27)
$\log \epsilon$(N)	$8.36^{+0.13}_{-0.26}$ (8.14±0.34)	$8.40^{+0.06}_{-0.11}$ (<8.24)	$8.50^{+0.06}_{-0.19}$ (8.81±0.34)	$8.61^{+0.02}_{-0.10}$ (8.61±0.34)	$8.34^{+0.14}_{-0.08}\dagger$ (8.27±0.34)	$8.26^{+0.10}_{-0.14}$ (8.09±0.34)
$\log \epsilon$(O)	$8.50^{+0.04}_{-0.09}$ (8.68±0.21)	$8.40^{+0.05}_{-0.05}$ (8.48±0.21)	$8.38^{+0.10}_{-0.08}$ (≤8.10)	$8.13^{+0.19}_{-0.03}\dagger$ (≤8.10)	$8.42^{+0.07}_{-0.05}\dagger$ (≤8.30)	$8.48^{+0.03}_{-0.06}$ (8.67±0.21)

Star	HD 46056	HD 46485	HD 52533	HD 66811	HD 69106	HD 74920
$M_{\rm ini}$ (M$_\odot$)	$20.6^{+2.4}_{-2.1}$	$24.4^{+3.2}_{-2.5}$	$21.4^{+1.7}_{-1.6}$	$60.0^{+14.6}_{-20.7}\dagger$	$18.0^{+3.3}_{-2.9}$	$22.2^{+3.7}_{-3.0}$
$M_{\rm act}$ (M$_\odot$)	$20.6^{+2.3}_{-2.1}$	$24.2^{+3.2}_{-2.4}$	$21.2^{+1.6}_{-1.5}$	$53.6^{+10.6}_{-17.5}\dagger$	$18.8^{+2.1}_{-3.6}$	$22.0^{+3.3}_{-2.8}$
$\log L$ (L$_\odot$)	$4.7^{+0.1}_{-0.1}$	$4.9^{+0.1}_{-0.1}$	$4.8^{+0.1}_{-0.1}$	$5.9^{+0.2}_{-0.2}$	$4.8^{+0.2}_{-0.2}$	$4.9^{+0.2}_{-0.2}$
Age (Myr)	$0.6^{+1.5}_{-0.6}$	$0.5^{+0.9}_{-0.5}$	$2.8^{+0.8}_{-0.7}$	$2.1^{+0.6}_{-0.4}$	$6.4^{+1.3}_{-0.8}$	$3.8^{+0.9}_{-0.8}$
$\tau_{\rm MS}$	$0.1^{+0.1}_{-0.1}$	$0.1^{+0.1}_{-0.1}$	$0.3^{+0.1}_{-0.1}$	$0.6^{+0.1}_{-0.1}$	$0.7^{+0.1}_{-0.1}$	$0.6^{+0.1}_{-0.2}$
$v_{\rm ini}$ (km s^{-1})	$350.0^{+32.8}_{-16.3}$	$330.0^{+32.9}_{-26.7}$	$390.0^{+51.7}_{-36.4}$	$380.0^{+29.0}_{-58.1}$	$320.0^{+33.6}_{-23.7}$	$340.0^{+55.5}_{-35.0}$
$v\sin i$ (km s^{-1})	$350.0^{+14.1}_{-17.8}$ (350±15)	$320.0^{+9.7}_{-21.5}$ (315±15)	$310.0^{+13.4}_{-19.1}$ (305±15)	$220.0^{+20.8}_{-10.5}$ (225±15)	$310.0^{+11.2}_{-20.4}$ (306±15)	$280.0^{+12.6}_{-19.5}$ (274±15)
i (°)	76.5	90.0	52.6	66.4	75.6	58.0
y	$0.085^{+0.000}_{-0.000}$ (0.088±0.030)	$0.081^{+0.000}_{-0.000}$ (0.076±0.030)	$0.089^{+0.003}_{-0.003}$ (0.065±0.025)	$0.105^{+0.010}_{-0.010}\dagger$ (0.148±0.030)	$0.085^{+0.003}_{-0.000}$ (0.091±0.030)	$0.085^{+0.003}_{-0.003}$ (0.134±0.030)
$\log \epsilon$(C)	$8.12^{+0.02}_{-0.13}$ (8.34±0.27)	$8.13^{+0.01}_{-0.11}$ (8.46±0.27)	$7.84^{+0.13}_{-0.12}$ (7.76±0.12)	$7.22^{+0.21}_{-0.09}$ (≤7.00)	$7.90^{+0.06}_{-0.08}$ (7.88±0.27)	$7.90^{+0.10}_{-0.15}$ (7.78±0.27)
$\log \epsilon$(N)	$7.64^{+0.41}_{-0.01}$ (7.78±0.34)	$7.64^{+0.35}_{-0.01}$ (7.95±0.34)	$8.32^{+0.11}_{-0.15}$ (<7.78)	$8.65^{+0.09}_{-0.08}$ (8.94±0.34)	$8.13^{+0.13}_{-0.09}$ (7.74±0.34)	$8.26^{+0.17}_{-0.14}$ (8.34±0.34)
$\log \epsilon$(O)	$8.55^{+0.01}_{-0.05}$ (8.32±0.21)	$8.55^{+0.00}_{-0.04}$ (8.72±0.21)	$8.45^{+0.05}_{-0.06}$ (8.15±0.21)	$8.06^{+0.23}_{-0.20}\dagger$ (8.20±0.21)	$8.51^{+0.02}_{-0.03}$ (8.47±0.21)	$8.49^{+0.04}_{-0.08}$ (8.51±0.21)

Star	HD 117490	HD 124979	HD 149757	HD 175876	HD 191423	HD 192281
$M_{\rm ini}$ (M$_\odot$)	$18.4^{+4.5}_{-1.9}$	$20.2^{+3.0}_{-2.3}$	$17.2^{+1.2}_{-1.3}$	$27.0^{+6.8}_{-3.4}$	$18.8^{+1.6}_{-1.9}$	$38.0^{+6.9}_{-5.6}$
$M_{\rm act}$ (M$_\odot$)	$18.6^{+3.8}_{-2.0}$	$20.0^{+3.0}_{-2.1}$	$17.2^{+1.2}_{-1.3}$	$26.8^{+5.5}_{-3.3}$	$18.4^{+1.6}_{-1.7}$	$35.2^{+6.2}_{-3.9}$
$\log L$ (L$_\odot$)	$4.9^{+0.2}_{-0.3}$	$4.7^{+0.2}_{-0.2}$	$4.5^{+0.1}_{-0.1}$	$5.3^{+0.1}_{-0.2}$	$4.8^{+0.1}_{-0.1}$	$5.5^{+0.1}_{-0.2}$
Age (Myr)	$6.1^{+1.0}_{-0.8}$	$3.5^{+0.8}_{-2.2}$	$1.7^{+1.0}_{-0.9}$	$3.4^{+0.6}_{-0.6}$	$6.8^{+1.0}_{-0.8}$	$2.8^{+0.4}_{-0.5}$
$\tau_{\rm MS}$	$0.8^{+0.1}_{-0.1}$	$0.2^{+0.3}_{-0.1}$	$0.2^{+0.1}_{-0.1}$	$0.6^{+0.1}_{-0.1}$	$0.7^{+0.1}_{-0.1}$	$0.6^{+0.1}_{-0.1}$
$v_{\rm ini}$ (km s^{-1})	$400.0^{+30.8}_{-34.4}$	$270.0^{+65.5}_{-23.2}$	$370.0^{+30.1}_{-16.9}$	$330.0^{+36.6}_{-36.7}$	$410.0^{+15.5}_{-15.4}$	$360.0^{+28.8}_{-33.5}$
$v\sin i$ (km s^{-1})	$360.0^{+16.9}_{-14.8}$ (361±15)	$240.0^{+23.8}_{-7.9}$ (246±15)	$370.0^{+20.4}_{-11.3}$ (378±15)	$270.0^{+12.0}_{-20.0}$ (265±15)	$410.0^{+18.3}_{-11.9}$ (420±15)	$270.0^{+19.4}_{-11.3}$ (276±15)
i (°)	76.6	62.7	76.8	74.6	77.5	74.6
y	$0.085^{+0.013}_{-0.000}\dagger$ (0.141±0.030)	$0.081^{+0.000}_{-0.000}$ (0.091±0.030)	$0.081^{+0.000}_{-0.000}$ (0.135±0.025)	$0.089^{+0.000}_{-0.003}$ (0.110±0.030)	$0.093^{+0.003}_{-0.003}\dagger$ (0.134±0.030)	$0.089^{+0.010}_{-0.003}$ (0.103±0.030)
$\log \epsilon$(C)	$7.82^{+0.04}_{-0.34}\dagger$ (≤7.39)	$8.12^{+0.02}_{-0.11}$ (8.48±0.27)	$8.07^{+0.04}_{-0.06}$ (8.07±0.12)	$7.81^{+0.16}_{-0.04}$ (8.04±0.27)	$7.61^{+0.08}_{-0.08}$ (≤7.24)	$7.67^{+0.19}_{-0.24}\dagger$ (8.00±0.27)
$\log \epsilon$(N)	$8.51^{+0.06}_{-0.20}\dagger$ (8.50±0.34)	$7.65^{+0.47}_{-0.01}\dagger$ (7.92±0.34)	$7.90^{+0.15}_{-0.13}$ (7.85±0.13)	$8.33^{+0.05}_{-0.20}$ (8.36±0.34)	$8.42^{+0.06}_{-0.07}\dagger$ (8.33±0.34)	$8.43^{+0.19}_{-0.13}\dagger$ (8.76±0.34)
$\log \epsilon$(O)	$8.48^{+0.02}_{-0.17}\dagger$ (8.15±0.21)	$8.55^{+0.00}_{-0.03}$ (8.74±0.21)	$8.54^{+0.01}_{-0.02}$ (8.37±0.21)	$8.43^{+0.07}_{-0.02}$ (8.42±0.21)	$8.40^{+0.02}_{-0.07}$ (≤8.33)	$8.43^{+0.03}_{-0.18}$ (8.05±0.21)

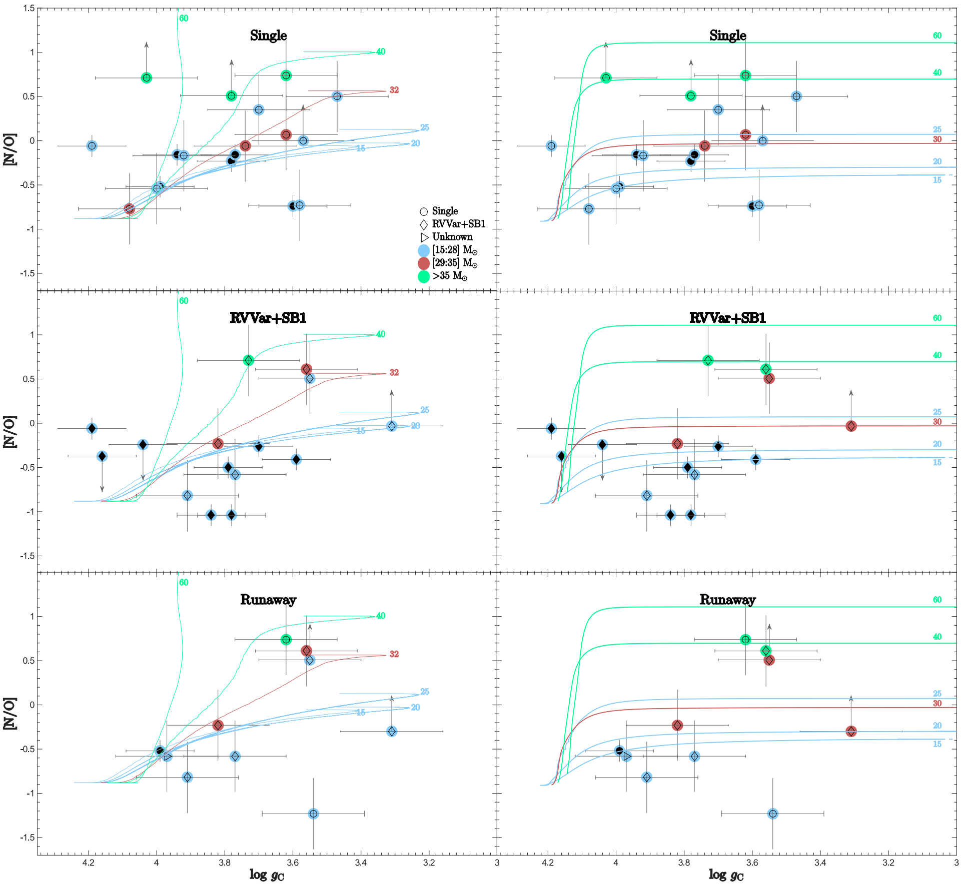

Fig. A.1. Same as Fig. 4, but for the different multiplicity status.

Table B.1. Continued.

Star	HD 203064	HD 210839	HD 228841
$M_{\rm ini}$ (M$_\odot$)	$23.6^{+5.1}_{-3.0}$	$37.8^{+16.7}_{-6.3}$	$25.8^{+6.6}_{-2.5}$
$M_{\rm act}$ (M$_\odot$)	$23.2^{+4.7}_{-2.6}$	$34.6^{+13.5}_{-4.1}$	$24.8^{+5.8}_{-1.9}$
log L (L$_\odot$)	$5.1^{+0.2}_{-0.3}$	$5.6^{+0.2}_{-0.2}$	$5.2^{+0.2}_{-0.1}$
Age (Myr)	$3.6^{+0.8}_{-0.7}$	$3.4^{+0.3}_{-0.8}$	$4.1^{+0.9}_{-0.4}$
$\tau_{\rm MS}$	$0.6^{+0.1}_{-0.2}$	$0.7^{+0.0}_{-0.1}$	$0.7^{+0.1}_{-0.1}$
$v_{\rm ini}$ (km s^{-1})	$330.0^{+37.9}_{-25.1}$	$360.0^{+31.4}_{-39.2}$	$380.0^{+30.8}_{-34.6}$
$v \sin i$ (km s^{-1})	$300.0^{+14.3}_{-16.9}$ (298±15)	$220.0^{+11.0}_{-20.3}$ (214±15)	$310.0^{+12.0}_{-19.5}$ (305±15)
i (°)	75.4	73.0	75.6
y	$0.085^{+0.003}_{-0.003}$ (0.076±0.030)	$0.093^{+0.007}_{-0.007}$ (0.113±0.030)	$0.089^{+0.007}_{-0.000}$ (0.112±0.030)
log ϵ(C)	$7.91^{+0.06}_{-0.14}$ (7.92±0.27)	$7.73^{+0.02}_{-0.37}$† (7.83±0.27)	$7.78^{+0.07}_{-0.19}$ (7.48±0.27)
log ϵ(N)	$8.33^{+0.05}_{-0.19}$ (8.23±0.34)	$8.43^{+0.20}_{-0.07}$† (8.74±0.34)	$8.34^{+0.15}_{-0.04}$ (8.74±0.34)
log ϵ(O)	$8.48^{+0.02}_{-0.07}$ (8.46±0.21)	$8.33^{+0.13}_{-0.15}$† (8.13±0.21)	$8.43^{+0.02}_{-0.11}$† (8.67±0.21)

Notes. $M_{\rm ini}$ and $M_{\rm act}$ are the initial and current stellar masses, respectively, L is the stellar bolometric luminosity, $\tau_{\rm MS}$ is the fractional MS age, i is the inferred stellar inclination from the actual and projected rotational velocities given by BONNSAI, and $v_{\rm ini}$ is the initial rotational velocity. Errors from BONNSAI correspond to 1 σ, except for values flagged with † for which the errors are slightly larger than 1 σ.

Table B.2. Same as Fig. B.1 but when $T_{\rm eff}$, $\log g_{\rm C}$, $v \sin i$, and y are given as input to BONNSAI.

Star	ALS 864	ALS 18675	BD +34° 1058	BD +60° 594	HD 14434	HD 14442
$M_{\rm ini}$ ($\rm M_\odot$)	$17.4^{+1.5}_{-1.4}$	$16.4^{+1.7}_{-1.4}$	$21.6^{+1.6}_{-2.1}$	$19.8^{+1.9}_{-1.5}$	$30.2^{+4.0}_{-3.5}$	$37.8^{+4.0}_{-8.2}$
$M_{\rm act}$ ($\rm M_\odot$)	$17.4^{+1.4}_{-1.4}$	$16.6^{+1.4}_{-1.5}$	$21.2^{+1.6}_{-1.9}$	$20.0^{+1.5}_{-1.7}$	$29.8^{+3.8}_{-3.5}$	$35.2^{+3.7}_{-6.1}$
$\log L$ ($\rm L_\odot$)	$4.5^{+0.1}_{-0.1}$	$4.5^{+0.1}_{-0.1}$	$4.9^{+0.1}_{-0.2}$	$4.7^{+0.1}_{-0.1}$	$5.2^{+0.1}_{-0.1}$	$5.5^{+0.1}_{-0.3}$
Age (Myr)	$3.8^{+1.1}_{-1.9}$	$5.3^{+1.0}_{-1.4}$	$5.0^{+1.2}_{-1.8}$	$3.6^{+1.0}_{-1.6}$	$1.2^{+0.9}_{-1.2}$	$2.7^{+0.6}_{-0.6}$
$\tau_{\rm MS}$	$0.4^{+0.1}_{-0.2}$	$0.5^{+0.1}_{-0.2}$	$0.6^{+0.1}_{-0.2}$	$0.4^{+0.1}_{-0.2}$	$0.3^{+0.1}_{-0.2}$	$0.6^{+0.1}_{-0.1}$
$v_{\rm ini}$ (km s^{-1})	$350.0^{+28.2}_{-94.3}$	$330.0^{+73.5}_{-48.1}$	$430.0^{+34.4}_{-19.7}$	$330.0^{+62.2}_{-25.5}$	$430.0^{+28.6}_{-26.3}$	$360.0^{+38.5}_{-48.4}$
$v \sin i$ (km s^{-1})	$250.0^{+16.3}_{-15.7}$ (249±15)	$240.0^{+14.4}_{-17.5}$ (236±15)	$420.0^{+14.2}_{-17.0}$ (424±15)	$320.0^{+11.2}_{-20.4}$ (314±15)	$400.0^{+17.6}_{-12.8}$ (408±15)	$280.0^{+18.8}_{-12.6}$ (285±15)
i (°)	44.0	36.9	90.0	75.9	77.3	74.9
y	$0.085^{+0.000}_{-0.000}$ (0.064±0.025)	$0.085^{+0.003}_{-0.000}$ (0.071±0.025)	$0.097^{+0.010}_{-0.007}$† (0.119±0.030)	$0.085^{+0.003}_{-0.000}$ (0.131±0.025)	$0.085^{+0.013}_{-0.000}$† (0.103±0.030)	$0.089^{+0.010}_{-0.003}$† (0.097±0.030)
$\log \epsilon$(C)	$8.12^{+0.01}_{-0.16}$ (<7.86)	$8.04^{+0.08}_{-0.14}$ (7.78±0.12)	$7.47^{+0.23}_{-0.30}$† (7.90±0.27)	$8.12^{+0.01}_{-0.26}$ (7.66±0.12)	$8.12^{+0.01}_{-0.67}$† (7.96±0.27)	$7.81^{+0.15}_{-0.38}$† (7.10±0.27)
$\log \epsilon$(N)	$7.65^{+0.42}_{-0.02}$ (7.64±0.13)	$7.97^{+0.30}_{-0.13}$ (7.54±0.13)	$8.57^{+0.13}_{-0.15}$ (8.14±0.34)	$8.16^{+0.24}_{-0.27}$ (<8.24)	$8.53^{+0.20}_{-0.28}$ (8.81±0.34)	$8.33^{+0.35}_{-0.10}$† (8.61±0.34)
$\log \epsilon$(O)	$8.54^{+0.02}_{-0.04}$ (8.12±0.21)	$8.54^{+0.02}_{-0.05}$ (8.07±0.21)	$8.32^{+0.12}_{-0.21}$ (8.68±0.21)	$8.55^{+0.01}_{-0.09}$ (8.48±0.21)	$8.54^{+0.01}_{-0.28}$ (≤8.10)	$8.43^{+0.08}_{-0.19}$ (≤8.10)

Star	HD 15137	HD 15642	HD 28446A	HD 41161	HD 41997	HD 46056
$M_{\rm ini}$ ($\rm M_\odot$)	$25.0^{+7.8}_{-3.2}$	$24.6^{+2.1}_{-5.2}$	$17.2^{+2.0}_{-1.8}$	$23.0^{+5.0}_{-3.2}$	$21.6^{+3.2}_{-2.9}$	$21.6^{+2.8}_{-2.5}$
$M_{\rm act}$ ($\rm M_\odot$)	$24.4^{+6.1}_{-3.0}$	$23.4^{+1.9}_{-4.3}$	$16.6^{+2.4}_{-1.2}$	$22.8^{+4.2}_{-3.1}$	$21.4^{+3.0}_{-2.7}$	$21.4^{+2.7}_{-2.4}$
$\log L$ ($\rm L_\odot$)	$5.3^{+0.2}_{-0.1}$	$5.2^{+0.1}_{-0.3}$	$4.7^{+0.2}_{-0.1}$	$5.1^{+0.2}_{-0.3}$	$4.8^{+0.2}_{-0.2}$	$4.8^{+0.2}_{-0.2}$
Age (Myr)	$4.5^{+1.7}_{-0.3}$	$6.2^{+1.1}_{-0.7}$	$6.4^{+0.9}_{-0.7}$	$4.2^{+1.0}_{-0.7}$	$3.6^{+1.1}_{-1.5}$	$3.5^{+1.0}_{-1.9}$
$\tau_{\rm MS}$	$0.8^{+0.0}_{-0.0}$	$0.8^{+0.1}_{-0.1}$	$0.7^{+0.1}_{-0.1}$	$0.7^{+0.1}_{-0.2}$	$0.5^{+0.1}_{-0.3}$†	$0.4^{+0.2}_{-0.2}$
$v_{\rm ini}$ (km s^{-1})	$360.0^{+54.2}_{-50.0}$	$390.0^{+53.0}_{-46.8}$	$290.0^{+96.9}_{-13.8}$	$340.0^{+61.9}_{-31.9}$	$350.0^{+66.0}_{-82.4}$†	$360.0^{+40.3}_{-21.9}$
$v \sin i$ (km s^{-1})	$270.0^{+13.7}_{-18.2}$ (267±15)	$330.0^{+19.6}_{-11.8}$ (335±15)	$280.0^{+11.9}_{-19.6}$ (275±15)	$300.0^{+19.8}_{-11.9}$ (303±15)	$250.0^{+14.9}_{-17.2}$ (247±15)	$350.0^{+15.1}_{-16.6}$ (350±15)
i (°)	74.6	76.1	74.9	69.6	45.6	76.5
y	$0.089^{+0.007}_{-0.003}$† (0.112±0.030)	$0.085^{+0.013}_{-0.000}$† (0.150±0.030)	$0.085^{+0.003}_{-0.003}$† (0.126±0.025)	$0.089^{+0.003}_{-0.003}$† (0.123±0.030)	$0.085^{+0.006}_{-0.000}$ (0.110±0.030)	$0.085^{+0.006}_{-0.000}$ (0.088±0.030)
$\log \epsilon$(C)	$7.80^{+0.14}_{-0.21}$† (7.63±0.27)	$7.83^{+0.06}_{-0.41}$† (≤7.55)	$7.97^{+0.05}_{-0.20}$† (8.30±0.12)	$7.88^{+0.11}_{-0.28}$† (7.87±0.27)	$8.13^{+0.01}_{-0.30}$ (8.59±0.27)	$8.12^{+0.02}_{-0.34}$ (8.34±0.27)
$\log \epsilon$(N)	$8.34^{+0.17}_{-0.15}$ (8.27±0.34)	$8.49^{+0.19}_{-0.22}$† (8.43±0.34)	$8.28^{+0.01}_{-0.33}$ (7.48±0.13)	$8.33^{+0.19}_{-0.17}$ (8.09±0.34)	$7.65^{+0.65}_{-0.02}$ (8.21±0.34)	$8.38^{+0.15}_{-0.35}$ (7.78±0.34)
$\log \epsilon$(O)	$8.42^{+0.09}_{-0.09}$ (≤8.30)	$8.48^{+0.03}_{-0.23}$ (7.93±0.21)	$8.52^{+0.02}_{-0.06}$ (8.52±0.21)	$8.42^{+0.10}_{-0.07}$ (8.67±0.21)	$8.54^{+0.02}_{-0.10}$ (8.79±0.21)	$8.54^{+0.02}_{-0.13}$ (8.32±0.21)

Star	HD 46485	HD 52533	HD 53755	HD 66811	HD 69106	HD 74920
$M_{\rm ini}$ ($\rm M_\odot$)	$25.0^{+3.8}_{-2.7}$	$20.6^{+1.6}_{-1.5}$	$16.6^{+2.0}_{-1.9}$	$50.0^{+26.5}_{-8.6}$	$18.8^{+4.5}_{-3.3}$	$21.6^{+3.7}_{-2.9}$
$M_{\rm act}$ ($\rm M_\odot$)	$24.8^{+3.6}_{-2.5}$	$20.6^{+1.6}_{-1.5}$	$15.6^{+2.8}_{-0.9}$	$41.4^{+22.8}_{-4.2}$	$18.8^{+3.7}_{-3.3}$	$21.4^{+3.4}_{-2.7}$
$\log L$ ($\rm L_\odot$)	$5.0^{+0.2}_{-0.1}$	$4.7^{+0.1}_{-0.1}$	$4.6^{+0.2}_{-0.1}$	$5.8^{+0.3}_{-0.1}$	$4.9^{+0.2}_{-0.3}$	$4.8^{+0.3}_{-0.2}$
Age (Myr)	$2.3^{+0.7}_{-1.6}$	$1.2^{+1.0}_{-1.2}$	$7.4^{+1.0}_{-0.9}$	$2.1^{+0.7}_{-0.3}$	$6.2^{+1.2}_{-0.9}$	$3.8^{+1.2}_{-1.1}$
$\tau_{\rm MS}$	$0.3^{+0.1}_{-0.3}$	$0.1^{+0.1}_{-0.1}$	$0.7^{+0.1}_{-0.1}$	$0.6^{+0.1}_{-0.1}$	$0.8^{+0.1}_{-0.1}$	$0.6^{+0.1}_{-0.2}$
$v_{\rm ini}$ (km s^{-1})	$330.0^{+56.5}_{-19.8}$	$320.0^{+57.8}_{-23.9}$	$300.0^{+91.2}_{-17.6}$†	$400.0^{+46.9}_{-52.8}$	$320.0^{+65.8}_{-18.4}$	$300.0^{+101.7}_{-15.7}$
$v \sin i$ (km s^{-1})	$320.0^{+11.4}_{-20.2}$ (315±15)	$310.0^{+12.2}_{-19.1}$ (305±15)	$290.0^{+11.7}_{-20.0}$ (285±15)	$230.0^{+11.4}_{-18.6}$ (225±15)	$310.0^{+12.5}_{-19.2}$ (306±15)	$280.0^{+12.1}_{-20.0}$ (274±15)
i (°)	75.9	75.6	69.3	73.4	75.6	74.9
y	$0.085^{+0.003}_{-0.000}$ (0.076±0.030)	$0.081^{+0.003}_{-0.000}$ (0.065±0.025)	$0.085^{+0.003}_{-0.000}$ (0.135±0.025)	$0.128^{+0.022}_{-0.019}$† (0.148±0.030)	$0.085^{+0.006}_{-0.000}$† (0.091±0.030)	$0.085^{+0.006}_{-0.003}$ (0.134±0.030)
$\log \epsilon$(C)	$8.12^{+0.02}_{-0.28}$ (8.46±0.27)	$8.13^{+0.01}_{-0.14}$ (7.76±0.12)	$7.95^{+0.05}_{-0.19}$ (...)	$7.12^{+0.17}_{-0.03}$† (≤7.00)	$7.88^{+0.09}_{-0.17}$† (7.88±0.27)	$8.13^{+0.01}_{-0.37}$ (7.78±0.27)
$\log \epsilon$(N)	$7.64^{+0.64}_{-0.01}$ (7.95±0.34)	$7.64^{+0.41}_{-0.01}$ (<7.78)	$8.06^{+0.33}_{-0.08}$† (7.32±0.13)	$8.75^{+0.09}_{-0.11}$ (8.94±0.34)	$8.24^{+0.16}_{-0.16}$ (7.74±0.34)	$8.18^{+0.36}_{-0.16}$ (8.34±0.34)
$\log \epsilon$(O)	$8.55^{+0.01}_{-0.11}$ (8.72±0.21)	$8.55^{+0.01}_{-0.05}$ (8.15±0.21)	$8.52^{+0.02}_{-0.06}$ (8.38±0.21)	$8.06^{+0.01}_{-0.59}$ (8.20±0.21)	$8.49^{+0.04}_{-0.08}$ (8.47±0.21)	$8.48^{+0.07}_{-0.08}$ (8.51±0.21)

Table B.2. Continued.

Star	HD 92554	HD 117490	HD 124979	HD 149757	HD 150574	HD 163892
$M_{\rm ini}$ (M$_\odot$)	$20.6^{+5.0}_{-3.7}$	$18.0^{+3.6}_{-2.6}$	$21.4^{+3.7}_{-3.0}$	$18.0^{+1.6}_{-1.4}$	$39.4^{+4.9}_{-17.3}$ †	$19.8^{+2.6}_{-1.9}$
$M_{\rm act}$ (M$_\odot$)	$20.8^{+4.0}_{-3.8}$	$18.0^{+3.2}_{-2.5}$	$21.2^{+3.4}_{-2.8}$	$17.8^{+1.6}_{-1.2}$	$34.4^{+3.5}_{-12.8}$ †	$20.2^{+1.8}_{-2.4}$
log L (L$_\odot$)	$5.0^{+0.3}_{-0.2}$	$4.7^{+0.3}_{-0.2}$	$4.8^{+0.3}_{-0.2}$	$4.6^{+0.1}_{-0.1}$	$5.6^{+0.1}_{-0.3}$	$4.8^{+0.1}_{-0.2}$
Age (Myr)	$6.0^{+1.0}_{-1.0}$	$6.2^{+1.2}_{-0.9}$	$3.7^{+1.1}_{-1.1}$	$4.7^{+1.0}_{-1.6}$	$4.1^{+2.1}_{-0.6}$†	$5.0^{+0.7}_{-0.7}$
$\tau_{\rm MS}$	$0.8^{+0.1}_{-0.1}$	$0.7^{+0.1}_{-0.1}$	$0.6^{+0.1}_{-0.2}$	$0.5^{+0.1}_{-0.2}$	$0.8^{+0.1}_{-0.1}$	$0.6^{+0.1}_{-0.1}$
$v_{\rm ini}$ (km s^{-1})	$330.0^{+62.1}_{-24.8}$	$360.0^{+56.7}_{-17.1}$	$350.0^{+36.8}_{-85.8}$	$380.0^{+35.7}_{-22.1}$	$400.0^{+80.0}_{-40.5}$	$350.0^{+42.1}_{-83.2}$
$v \sin i$ (km s^{-1})	$300.0^{+19.0}_{-12.6}$ (303±15)	$360.0^{+16.3}_{-15.4}$ (361±15)	$250.0^{+14.0}_{-18.1}$ (246±15)	$380.0^{+13.6}_{-18.1}$ (378±15)	$230.0^{+16.7}_{-15.5}$ (233±15)	$210.0^{+13.5}_{-19.3}$ (205±15)
i (°)	75.4	76.6	47.3	77.0	90.0	36.9
y	$0.085^{+0.006}_{-0.003}$ (0.091±0.030)	$0.085^{+0.006}_{-0.000}$ (0.141±0.030)	$0.081^{+0.006}_{-0.000}$ (0.091±0.030)	$0.085^{+0.003}_{-0.003}$ (0.135±0.025)	$0.089^{+0.029}_{-0.003}$ (0.172±0.030)	$0.085^{+0.003}_{-0.003}$ (0.082±0.025)
log ϵ(C)	$7.84^{+0.12}_{-0.14}$ (7.57±0.27)	$7.83^{+0.09}_{-0.28}$† (≤7.39)	$8.13^{+0.01}_{-0.30}$ (8.48±0.27)	$7.87^{+0.14}_{-0.19}$ (8.07±0.12)	$7.11^{+0.58}_{-0.05}$† (7.48±0.27)	$7.90^{+0.17}_{-0.10}$ (8.24±0.12)
log ϵ(N)	$8.33^{+0.13}_{-0.19}$ (7.30±0.34)	$8.25^{+0.24}_{-0.09}$ (8.50±0.34)	$8.17^{+0.28}_{-0.23}$ (7.92±0.34)	$8.22^{+0.24}_{-0.11}$ (7.85±0.13)	$8.73^{+0.13}_{-0.27}$† (≥9.08)	$8.19^{+0.18}_{-0.25}$ (7.34±0.13)
log ϵ(O)	$8.48^{+0.05}_{-0.09}$ (8.53±0.21)	$8.48^{+0.03}_{-0.12}$ (8.15±0.21)	$8.54^{+0.02}_{-0.10}$ (8.74±0.21)	$8.49^{+0.04}_{-0.08}$ (8.37±0.21)	$8.43^{+0.09}_{-0.75}$† (≥8.93)	$8.49^{+0.06}_{-0.04}$ (8.38±0.21)

Star	HD 172367	HD 175876	HD 188439	HD 191423	HD 192281	HD 203064
$M_{\rm ini}$ (M$_\odot$)	$16.0^{+2.1}_{-1.8}$	$26.4^{+8.6}_{-3.6}$	$14.8^{+1.9}_{-1.4}$	$20.4^{+1.5}_{-2.5}$	$39.0^{+5.0}_{-8.3}$	$23.6^{+5.2}_{-3.1}$
$M_{\rm act}$ (M$_\odot$)	$15.6^{+2.3}_{-1.3}$	$25.6^{+8.7}_{-2.6}$†	$15.6^{+0.9}_{-2.1}$	$20.0^{+1.2}_{-2.3}$	$36.0^{+4.3}_{-6.1}$	$23.4^{+4.5}_{-3.0}$
log L (L$_\odot$)	$4.6^{+0.2}_{-0.2}$	$5.2^{+0.3}_{-0.1}$	$4.5^{+0.2}_{-0.2}$	$4.9^{+0.1}_{-0.2}$	$5.5^{+0.1}_{-0.3}$	$5.1^{+0.2}_{-0.3}$
Age (Myr)	$8.0^{+1.0}_{-0.9}$	$3.5^{+0.7}_{-0.6}$	$7.7^{+1.1}_{-1.0}$	$7.0^{+0.9}_{-0.9}$	$2.8^{+0.5}_{-0.6}$	$3.7^{+0.9}_{-0.8}$
$\tau_{\rm MS}$	$0.7^{+0.1}_{-0.1}$	$0.7^{+0.1}_{-0.1}$	$0.7^{+0.1}_{-0.1}$	$0.8^{+0.1}_{-0.1}$	$0.6^{+0.1}_{-0.1}$	$0.6^{+0.1}_{-0.2}$
$v_{\rm ini}$ (km s^{-1})	$360.0^{+29.1}_{-95.9}$	$350.0^{+52.2}_{-52.3}$	$290.0^{+94.7}_{-12.3}$†	$420.0^{+40.6}_{-22.4}$	$360.0^{+43.8}_{-45.4}$	$330.0^{+53.9}_{-27.9}$
$v \sin i$ (km s^{-1})	$270.0^{+13.8}_{-17.6}$ (266±15)	$270.0^{+11.5}_{-20.3}$ (265±15)	$280.0^{+17.3}_{-14.0}$ (281±15)	$420.0^{+12.0}_{-19.4}$ (420±15)	$270.0^{+19.6}_{-11.6}$ (276±15)	$300.0^{+14.7}_{-16.9}$ (298±15)
i (°)	45.3	74.6	64.6	90.0	74.6	75.4
y	$0.085^{+0.003}_{-0.000}$ (0.140±0.025)	$0.089^{+0.007}_{-0.003}$ (0.110±0.030)	$0.085^{+0.003}_{-0.000}$ (0.122±0.025)	$0.089^{+0.013}_{-0.003}$ (0.134±0.030)	$0.089^{+0.013}_{-0.003}$† (0.103±0.030)	$0.089^{+0.003}_{-0.003}$ (0.076±0.030)
log ϵ(C)	$7.96^{+0.05}_{-0.21}$ (<8.09)	$7.81^{+0.19}_{-0.25}$† (8.04±0.27)	$7.96^{+0.06}_{-0.16}$ (<8.09)	$7.61^{+0.12}_{-0.30}$† (≤7.24)	$7.82^{+0.13}_{-0.40}$ (8.00±0.27)	$7.91^{+0.10}_{-0.19}$ (7.92±0.27)
log ϵ(N)	$8.03^{+0.47}_{-0.09}$† (8.44±0.13)	$8.34^{+0.22}_{-0.20}$† (8.36±0.34)	$8.03^{+0.27}_{-0.08}$† (8.16±0.13)	$8.52^{+0.12}_{-0.14}$ (8.33±0.34)	$8.43^{+0.20}_{-0.19}$† (8.76±0.34)	$8.34^{+0.13}_{-0.21}$ (8.23±0.34)
log ϵ(O)	$8.53^{+0.01}_{-0.07}$ (8.47±0.21)	$8.43^{+0.09}_{-0.10}$ (8.42±0.21)	$8.53^{+0.01}_{-0.05}$ (8.66±0.21)	$8.38^{+0.07}_{-0.17}$ (≤8.33)	$8.43^{+0.08}_{-0.25}$† (8.05±0.21)	$8.48^{+0.04}_{-0.09}$ (8.46±0.21)

Star	HD 210839	HD 228841
$M_{\rm ini}$ (M$_\odot$)	$40.0^{+12.3}_{-12.5}$	$25.0^{+6.6}_{-2.7}$
$M_{\rm act}$ (M$_\odot$)	$35.2^{+11.1}_{-7.9}$	$24.2^{+5.8}_{-2.1}$
log L (L$_\odot$)	$5.6^{+0.3}_{-0.2}$	$5.2^{+0.2}_{-0.1}$
Age (Myr)	$3.4^{+0.4}_{-0.9}$	$4.1^{+0.9}_{-0.5}$
$\tau_{\rm MS}$	$0.7^{+0.1}_{-0.1}$	$0.7^{+0.1}_{-0.1}$
$v_{\rm ini}$ (km s^{-1})	$370.0^{+45.2}_{-60.2}$	$360.0^{+51.8}_{-37.1}$
$v \sin i$ (km s^{-1})	$220.0^{+10.7}_{-20.1}$ (214±15)	$310.0^{+10.9}_{-20.7}$ (305±15)
i (°)	73.0	75.6
y	$0.089^{+0.023}_{-0.003}$† (0.113±0.030)	$0.089^{+0.007}_{-0.003}$ (0.112±0.030)
log ϵ(C)	$7.33^{+0.63}_{-0.01}$† (7.83±0.27)	$7.78^{+0.15}_{-0.19}$ (7.48±0.27)
log ϵ(N)	$8.65^{+0.12}_{-0.41}$† (8.74±0.34)	$8.34^{+0.18}_{-0.11}$ (8.74±0.34)
log ϵ(O)	$8.43^{+0.10}_{-0.33}$† (8.13±0.21)	$8.42^{+0.07}_{-0.10}$ (8.67±0.21)

Table B.3. Same as Fig. B.1 but when $T_{\rm eff}$, $\log g_{\rm C}$, and $v \sin i$ are given as input to BONNSAI.

Star	ALS 864	ALS 18675	BD +34° 1058	BD +60° 594	HD 13268	HD 14434
$M_{\rm ini}$ (M$_\odot$)	$17.4^{+1.5}_{-1.4}$	$16.4^{+1.7}_{-1.4}$	$21.4^{+1.8}_{-2.0}$	$19.8^{+1.7}_{-1.6}$	$25.0^{+5.6}_{-3.9}$	$30.2^{+3.9}_{-3.6}$
$M_{\rm act}$ (M$_\odot$)	$17.4^{+1.5}_{-1.4}$	$16.6^{+1.4}_{-1.5}$	$21.0^{+1.7}_{-1.8}$	$19.6^{+1.8}_{-1.4}$	$24.0^{+5.0}_{-3.0}$	$29.8^{+3.8}_{-3.7}$
$\log L$ (L$_\odot$)	$4.5^{+0.1}_{-0.1}$	$4.5^{+0.2}_{-0.1}$	$4.8^{+0.1}_{-0.1}$	$4.7^{+0.1}_{-0.1}$	$5.2^{+0.2}_{-0.2}$	$5.2^{+0.1}_{-0.1}$
Age (Myr)	$3.8^{+1.1}_{-1.8}$	$5.3^{+1.0}_{-1.4}$	$4.9^{+1.3}_{-2.1}$	$3.4^{+1.0}_{-1.6}$	$4.8^{+0.8}_{-0.7}$	$0.8^{+1.4}_{-0.8}$
$\tau_{\rm MS}$	$0.4^{+0.1}_{-0.2}$	$0.5^{+0.1}_{-0.1}$	$0.6^{+0.1}_{-0.3}$	$0.4^{+0.1}_{-0.2}$	$0.8^{+0.1}_{-0.1}$	$0.2^{+0.2}_{-0.1}$
$v_{\rm ini}$ (km s^{-1})	$350.0^{+72.4}_{-94.1}$†	$330.0^{+75.8}_{-47.1}$	$430.0^{+30.8}_{-22.3}$	$330.0^{+53.3}_{-26.2}$	$360.0^{+46.4}_{-42.9}$	$420.0^{+39.0}_{-17.8}$
$v \sin i$ (km s^{-1})	$250.0^{+16.3}_{-15.7}$ (249±15)	$240.0^{+14.4}_{-17.6}$ (236±15)	$420.0^{+14.0}_{-17.3}$ (424±15)	$320.0^{+10.9}_{-20.6}$ (314±15)	$300.0^{+16.5}_{-14.9}$ (301±15)	$400.0^{+17.7}_{-12.7}$ (408±15)
i (°)	44.0	36.9	90.0	75.9	75.4	77.3
y	$0.085^{+0.003}_{-0.000}$ (0.064±0.025)	$0.085^{+0.003}_{-0.000}$ (0.071±0.025)	$0.097^{+0.007}_{-0.013}$ (0.119±0.030)	$0.085^{+0.003}_{-0.000}$ (0.131±0.025)	$0.089^{+0.007}_{-0.003}$ (0.206±0.030)	$0.085^{+0.013}_{-0.003}$ (0.103±0.030)
$\log \epsilon$(C)	$8.12^{+0.01}_{-0.17}$ (<7.86)	$8.04^{+0.08}_{-0.15}$ (7.78±0.12)	$7.52^{+0.27}_{-0.30}$ (7.90±0.27)	$8.12^{+0.01}_{-0.22}$ (7.66±0.12)	$7.78^{+0.15}_{-0.19}$† (≤7.50)	$8.11^{+0.02}_{-0.62}$ (7.96±0.27)
$\log \epsilon$(N)	$7.65^{+0.44}_{-0.02}$ (7.64±0.13)	$7.97^{+0.31}_{-0.12}$ (7.54±0.13)	$8.56^{+0.14}_{-0.19}$ (8.14±0.34)	$8.12^{+0.21}_{-0.27}$ (<8.24)	$8.33^{+0.19}_{-0.11}$ (8.61±0.34)	$8.54^{+0.21}_{-0.31}$ (8.61±0.34)
$\log \epsilon$(O)	$8.54^{+0.02}_{-0.04}$ (8.12±0.21)	$8.54^{+0.02}_{-0.05}$ (8.07±0.21)	$8.32^{+0.24}_{-0.10}$ (8.68±0.21)	$8.55^{+0.01}_{-0.07}$ (8.48±0.21)	$8.43^{+0.07}_{-0.09}$ (8.10±0.21)	$8.54^{+0.01}_{-0.28}$ (≤8.10)

Star	HD 14442	HD 15137	HD 15642	HD 28446A	HD 41161	HD 41997
$M_{\rm ini}$ (M$_\odot$)	$38.2^{+3.7}_{-8.6}$	$26.0^{+6.7}_{-4.4}$	$21.6^{+3.8}_{-3.7}$	$17.2^{+2.0}_{-1.9}$	$22.6^{+5.2}_{-3.2}$	$21.4^{+3.3}_{-2.8}$
$M_{\rm act}$ (M$_\odot$)	$35.6^{+3.2}_{-6.7}$	$24.4^{+6.1}_{-3.0}$	$20.6^{+3.8}_{-2.7}$	$16.4^{+2.6}_{-1.1}$	$22.4^{+4.5}_{-2.9}$	$21.4^{+2.9}_{-2.8}$
$\log L$ (L$_\odot$)	$5.5^{+0.1}_{-0.3}$	$5.3^{+0.2}_{-0.2}$	$5.0^{+0.2}_{-0.2}$	$4.7^{+0.2}_{-0.2}$	$5.1^{+0.1}_{-0.3}$	$4.8^{+0.2}_{-0.2}$
Age (Myr)	$2.8^{+0.6}_{-0.7}$	$4.6^{+1.6}_{-0.3}$	$6.3^{+1.0}_{-0.8}$	$6.4^{+0.9}_{-0.7}$	$4.1^{+1.0}_{-0.7}$	$3.5^{+1.1}_{-1.6}$
$\tau_{\rm MS}$	$0.6^{+0.1}_{-0.2}$	$0.8^{+0.0}_{-0.0}$	$0.8^{+0.1}_{-0.1}$	$0.7^{+0.1}_{-0.1}$	$0.7^{+0.1}_{-0.1}$	$0.5^{+0.1}_{-0.2}$
$v_{\rm ini}$ (km s^{-1})	$360.0^{+43.6}_{-50.5}$	$350.0^{+57.3}_{-44.8}$	$360.0^{+50.6}_{-29.7}$	$290.0^{+88.0}_{-14.7}$	$330.0^{+60.8}_{-24.6}$	$350.0^{+36.4}_{-89.2}$
$v \sin i$ (km s^{-1})	$280.0^{+18.7}_{-12.8}$ (≤8.10)	$270.0^{+13.5}_{-18.3}$ (267±15)	$330.0^{+19.1}_{-12.6}$ (335±15)	$280.0^{+11.9}_{-19.7}$ (275±15)	$300.0^{+19.4}_{-12.1}$ (303±15)	$250.0^{+14.9}_{-17.1}$ (247±15)
i (°)	74.9	74.6	76.1	74.9	69.6	47.3
y	$0.089^{+0.010}_{-0.003}$ (0.097±0.030)	$0.089^{+0.003}_{-0.003}$ (0.112±0.030)	$0.085^{+0.010}_{-0.003}$ (0.150±0.030)	$0.085^{+0.003}_{-0.000}$ (0.126±0.025)	$0.089^{+0.003}_{-0.003}$ (0.123±0.030)	$0.085^{+0.006}_{-0.000}$ (0.110±0.030)
$\log \epsilon$(C)	$7.82^{+0.15}_{-0.39}$ (7.10±0.27)	$7.80^{+0.15}_{-0.20}$† (7.63±0.27)	$7.83^{+0.08}_{-0.24}$ (≤7.55)	$7.97^{+0.05}_{-0.16}$ (8.30±0.12)	$7.90^{+0.09}_{-0.23}$† (7.87±0.27)	$8.12^{+0.01}_{-0.28}$ (8.59±0.27)
$\log \epsilon$(N)	$8.34^{+0.32}_{-0.09}$ (8.61±0.34)	$8.35^{+0.16}_{-0.17}$† (8.27±0.34)	$8.22^{+0.31}_{-0.05}$† (8.43±0.34)	$8.03^{+0.24}_{-0.07}$ (7.48±0.13)	$8.34^{+0.14}_{-0.20}$ (8.09±0.34)	$8.16^{+0.27}_{-0.30}$ (8.21±0.34)
$\log \epsilon$(O)	$8.43^{+0.09}_{-0.25}$† (≤8.10)	$8.42^{+0.10}_{-0.07}$ (≤8.30)	$8.48^{+0.03}_{-0.17}$† (7.93±0.21)	$8.52^{+0.02}_{-0.05}$ (8.52±0.21)	$8.48^{+0.05}_{-0.10}$ (8.67±0.21)	$8.54^{+0.02}_{-0.09}$ (8.79±0.21)

Star	HD 46056	HD 46485	HD 52266	HD 52533	HD 53755	HD 66811
$M_{\rm ini}$ (M$_\odot$)	$21.6^{+2.8}_{-2.5}$	$25.0^{+3.8}_{-2.6}$	$19.2^{+2.9}_{-2.1}$	$20.6^{+1.7}_{-1.5}$	$16.4^{+2.1}_{-1.8}$	$50.0^{+21.5}_{-10.6}$
$M_{\rm act}$ (M$_\odot$)	$21.4^{+2.7}_{-2.3}$	$24.8^{+3.6}_{-2.5}$	$19.4^{+2.2}_{-2.4}$	$20.6^{+1.6}_{-1.5}$	$15.6^{+2.7}_{-1.0}$	$42.4^{+18.6}_{-6.1}$
$\log L$ (L$_\odot$)	$4.8^{+0.2}_{-0.2}$	$5.0^{+0.2}_{-0.1}$	$4.9^{+0.2}_{-0.2}$	$4.7^{+0.1}_{-0.1}$	$4.6^{+0.2}_{-0.1}$	$5.8^{+0.3}_{-0.1}$
Age (Myr)	$3.5^{+1.0}_{-2.0}$	$2.4^{+0.8}_{-1.6}$	$6.0^{+0.8}_{-0.6}$	$1.2^{+1.0}_{-1.2}$	$7.4^{+1.0}_{-0.8}$	$2.1^{+0.6}_{-0.4}$
$\tau_{\rm MS}$	$0.4^{+0.2}_{-0.3}$	$0.4^{+0.1}_{-0.2}$	$0.7^{+0.1}_{-0.1}$	$0.1^{+0.1}_{-0.1}$	$0.7^{+0.1}_{-0.1}$	$0.6^{+0.1}_{-0.1}$
$v_{\rm ini}$ (km s^{-1})	$360.0^{+41.8}_{-22.2}$	$330.0^{+60.6}_{-19.7}$	$310.0^{+67.0}_{-26.4}$	$320.0^{+60.5}_{-23.9}$	$300.0^{+82.3}_{-20.7}$†	$370.0^{+58.4}_{-57.3}$
$v \sin i$ (km s^{-1})	$350.0^{+15.2}_{-16.5}$ (350±15)	$320.0^{+11.6}_{-20.1}$ (315±15)	$290.0^{+12.4}_{-19.6}$ (285±15)	$310.0^{+12.3}_{-19.1}$ (305±15)	$290.0^{+11.7}_{-20.0}$ (285±15)	$230.0^{+11.2}_{-19.2}$ (225±15)
i (°)	76.5	75.9	75.2	75.6	69.3	73.4
y	$0.085^{+0.006}_{-0.003}$ (0.088±0.030)	$0.085^{+0.003}_{-0.003}$ (0.076±0.030)	$0.085^{+0.003}_{-0.003}$ (0.187±0.025)	$0.081^{+0.003}_{-0.000}$ (0.065±0.025)	$0.085^{+0.003}_{-0.000}$ (0.135±0.025)	$0.097^{+0.027}_{-0.010}$† (0.148±0.030)
$\log \epsilon$(C)	$8.13^{+0.01}_{-0.36}$ (8.34±0.27)	$8.13^{+0.01}_{-0.31}$ (8.46±0.27)	$7.93^{+0.06}_{-0.15}$† (7.78±0.12)	$8.13^{+0.01}_{-0.15}$ (7.76±0.12)	$7.95^{+0.05}_{-0.15}$ (...)	$7.11^{+0.35}_{-0.03}$ (≤7.00)
$\log \epsilon$(N)	$8.34^{+0.20}_{-0.31}$ (7.78±0.34)	$8.33^{+0.18}_{-0.39}$ (7.95±0.34)	$8.22^{+0.12}_{-0.20}$† (7.74±0.13)	$7.64^{+0.42}_{-0.01}$ (<7.78)	$8.06^{+0.21}_{-0.07}$ (7.32±0.13)	$8.74^{+0.11}_{-0.21}$ (8.94±0.34)
$\log \epsilon$(O)	$8.54^{+0.02}_{-0.13}$ (8.32±0.21)	$8.55^{+0.01}_{-0.12}$ (8.72±0.21)	$8.52^{+0.02}_{-0.08}$ (8.00±0.21)	$8.55^{+0.01}_{-0.05}$ (8.15±0.21)	$8.52^{+0.02}_{-0.05}$ (8.38±0.21)	$8.06^{+0.43}_{-0.44}$† (8.20±0.21)

Table B.3. Continued.

Star	HD 69106	HD 74920	HD 84567	HD 90087	HD 92554	HD 93521
$M_{\rm ini}$ (M$_\odot$)	$18.8^{+4.5}_{-3.3}$	$21.2^{+3.7}_{-2.8}$	$17.4^{+2.5}_{-2.1}$	$19.2^{+3.2}_{-2.3}$	$20.6^{+5.1}_{-3.7}$	$18.0^{+1.9}_{-1.7}$
$M_{\rm act}$ (M$_\odot$)	$18.8^{+3.8}_{-3.3}$	$21.2^{+3.3}_{-2.7}$	$17.4^{+2.0}_{-2.3}$	$19.0^{+2.9}_{-2.1}$	$20.8^{+4.0}_{-3.8}$	$17.8^{+1.7}_{-1.6}$
log L (L$_\odot$)	$4.9^{+0.3}_{-0.3}$†	$4.8^{+0.2}_{-0.2}$	$4.8^{+0.2}_{-0.2}$	$4.9^{+0.2}_{-0.2}$	$5.0^{+0.3}_{-0.2}$	$4.7^{+0.2}_{-0.1}$
Age (Myr)	$6.2^{+1.3}_{-0.9}$	$3.8^{+1.1}_{-1.3}$	$7.7^{+0.9}_{-1.1}$	$6.5^{+0.9}_{-0.7}$	$6.0^{+1.0}_{-0.9}$	$6.5^{+0.8}_{-0.7}$
$\tau_{\rm MS}$	$0.8^{+0.1}_{-0.1}$	$0.6^{+0.1}_{-0.2}$	$0.8^{+0.1}_{-0.1}$	$0.8^{+0.0}_{-0.1}$	$0.8^{+0.1}_{-0.1}$	$0.7^{+0.1}_{-0.1}$
$v_{\rm ini}$ (km s^{-1})	$320.0^{+66.7}_{-19.0}$	$300.0^{+83.7}_{-20.9}$	$280.0^{+95.6}_{-14.9}$	$300.0^{+78.8}_{-19.5}$	$330.0^{+63.5}_{-25.5}$	$400.0^{+26.3}_{-22.2}$
$v \sin i$ (km s^{-1})	$310.0^{+12.5}_{-19.2}$ (306±15)	$280.0^{+12.2}_{-19.9}$ (274±15)	$260.0^{+18.5}_{-13.3}$ (261±15)	$280.0^{+13.4}_{-18.5}$ (276±15)	$300.0^{+19.0}_{-12.6}$ (303±15)	$400.0^{+17.4}_{-13.9}$ (405±15)
i (°)	75.6	74.9	68.2	74.9	75.4	77.3
y	$0.085^{+0.006}_{-0.000}$ (0.091±0.030)	$0.085^{+0.006}_{-0.000}$ (0.134±0.030)	$0.085^{+0.003}_{-0.000}$ (0.204±0.025)	$0.085^{+0.003}_{-0.003}$ (0.163±0.025)	$0.085^{+0.006}_{-0.003}$ (0.091±0.030)	$0.089^{+0.003}_{-0.003}$ (0.166±0.025)
log ϵ(C)	$7.88^{+0.09}_{-0.17}$† (7.88±0.27)	$7.93^{+0.20}_{-0.10}$ (7.78±0.27)	$7.94^{+0.06}_{-0.15}$ (<7.84)	$7.92^{+0.06}_{-0.16}$† (7.72±0.12)	$7.87^{+0.09}_{-0.22}$† (7.57±0.27)	$7.74^{+0.09}_{-0.16}$ (7.68±0.12)
log ϵ(N)	$8.23^{+0.17}_{-0.16}$ (7.74±0.34)	$8.18^{+0.26}_{-0.24}$ (8.34±0.34)	$8.26^{+0.02}_{-0.29}$ (7.98±0.13)	$8.26^{+0.08}_{-0.24}$† (7.42±0.13)	$8.33^{+0.14}_{-0.19}$ (7.30±0.34)	$8.33^{+0.14}_{-0.07}$ (8.10±0.13)
log ϵ(O)	$8.49^{+0.04}_{-0.08}$ (8.47±0.21)	$8.50^{+0.06}_{-0.06}$ (8.51±0.21)	$8.53^{+0.01}_{-0.06}$ (8.39±0.21)	$8.51^{+0.03}_{-0.07}$ (8.16±0.21)	$8.48^{+0.05}_{-0.09}$ (8.53±0.21)	$8.43^{+0.05}_{-0.07}$ (8.33±0.21)

Star	HD 102415	HD 117490	HD 124979	HD 149757	HD 150574	HD 163892
$M_{\rm ini}$ (M$_\odot$)	$19.0^{+1.5}_{-1.4}$	$17.8^{+3.1}_{-2.6}$	$21.4^{+3.7}_{-3.0}$	$18.0^{+1.5}_{-1.5}$	$28.4^{+9.5}_{-5.5}$	$19.8^{+2.6}_{-1.9}$
$M_{\rm act}$ (M$_\odot$)	$19.0^{+1.5}_{-1.3}$	$17.2^{+3.4}_{-1.9}$	$21.2^{+3.4}_{-2.7}$	$17.8^{+1.5}_{-1.3}$	$28.4^{+6.5}_{-5.2}$	$20.2^{+1.8}_{-2.4}$
log L (L$_\odot$)	$4.6^{+0.1}_{-0.1}$	$4.7^{+0.2}_{-0.2}$	$4.8^{+0.3}_{-0.2}$	$4.6^{+0.1}_{-0.1}$	$5.4^{+0.3}_{-0.2}$	$4.8^{+0.1}_{-0.2}$
Age (Myr)	$0.0^{+2.2}_{-0.0}$	$6.2^{+1.2}_{-0.9}$	$3.7^{+1.2}_{-1.2}$	$4.6^{+1.0}_{-1.7}$	$4.1^{+1.3}_{-0.5}$	$5.0^{+0.7}_{-0.7}$
$\tau_{\rm MS}$	$0.1^{+0.2}_{-0.1}$	$0.7^{+0.1}_{-0.1}$	$0.6^{+0.1}_{-0.2}$	$0.5^{+0.1}_{-0.2}$	$0.8^{+0.0}_{-0.1}$	$0.6^{+0.1}_{-0.1}$
$v_{\rm ini}$ (km s^{-1})	$360.0^{+37.7}_{-19.9}$	$360.0^{+41.3}_{-19.0}$	$350.0^{+37.4}_{-87.0}$	$380.0^{+29.1}_{-22.6}$	$350.0^{+56.1}_{-53.9}$	$350.0^{+46.8}_{-84.7}$
$v \sin i$ (km s^{-1})	$360.0^{+12.4}_{-20.1}$ (357±15)	$360.0^{+15.8}_{-15.8}$ (361±15)	$250.0^{+14.0}_{-18.0}$ (246±15)	$380.0^{+12.8}_{-18.7}$ (378±15)	$230.0^{+18.6}_{-13.4}$ (233±15)	$210.0^{+13.3}_{-19.3}$ (205±15)
i (°)	76.6	76.6	47.3	77.0	73.4	36.9
y	$0.085^{+0.000}_{-0.000}$ (0.158±0.025)	$0.085^{+0.003}_{-0.003}$ (0.141±0.030)	$0.085^{+0.006}_{-0.000}$ (0.091±0.030)	$0.085^{+0.003}_{-0.003}$ (0.135±0.025)	$0.089^{+0.007}_{-0.003}$ (0.172±0.030)	$0.085^{+0.003}_{-0.003}$ (0.082±0.025)
log ϵ(C)	$8.13^{+0.01}_{-0.15}$ (<7.54)	$7.83^{+0.09}_{-0.17}$† (≤7.39)	$8.01^{+0.12}_{-0.19}$ (8.48±0.27)	$7.87^{+0.16}_{-0.14}$ (8.07±0.12)	$7.81^{+0.20}_{-0.27}$† (7.48±0.27)	$7.90^{+0.17}_{-0.11}$ (8.24±0.12)
log ϵ(N)	$7.66^{+0.41}_{-0.02}$ (8.16±0.13)	$8.24^{+0.17}_{-0.10}$ (8.50±0.34)	$8.18^{+0.28}_{-0.25}$ (7.92±0.34)	$8.22^{+0.20}_{-0.14}$ (7.85±0.13)	$8.35^{+0.22}_{-0.20}$† (≥9.08)	$8.19^{+0.20}_{-0.25}$ (7.34±0.13)
log ϵ(O)	$8.55^{+0.01}_{-0.05}$ (8.22±0.21)	$8.48^{+0.03}_{-0.07}$ (8.15±0.21)	$8.54^{+0.02}_{-0.10}$ (8.74±0.21)	$8.49^{+0.06}_{-0.04}$ (8.37±0.21)	$8.43^{+0.10}_{-0.13}$ (≥8.93)	$8.49^{+0.07}_{-0.05}$ (8.38±0.21)

Star	HD 172367	HD 175876	HD 184915	HD 188439	HD 191423	HD 192281
$M_{\rm ini}$ (M$_\odot$)	$15.8^{+2.1}_{-1.7}$	$26.8^{+7.9}_{-4.0}$	$15.2^{+1.8}_{-1.6}$	$14.8^{+1.8}_{-1.4}$	$19.6^{+1.9}_{-2.2}$	$39.2^{+4.6}_{-8.7}$
$M_{\rm act}$ (M$_\odot$)	$15.4^{+2.3}_{-1.2}$	$26.2^{+7.4}_{-3.2}$	$15.6^{+1.2}_{-2.0}$	$15.6^{+0.8}_{-2.2}$	$19.8^{+1.2}_{-2.5}$	$35.6^{+4.4}_{-6.2}$
log L (L$_\odot$)	$4.6^{+0.2}_{-0.2}$	$5.2^{+0.2}_{-0.2}$	$4.5^{+0.2}_{-0.2}$	$4.5^{+0.2}_{-0.2}$	$4.9^{+0.1}_{-0.2}$	$5.5^{+0.1}_{-0.3}$
Age (Myr)	$7.9^{+1.0}_{-0.9}$	$3.5^{+0.7}_{-0.6}$	$7.7^{+1.0}_{-0.9}$	$7.7^{+1.1}_{-0.9}$	$7.0^{+0.9}_{-0.9}$	$2.8^{+0.6}_{-0.6}$
$\tau_{\rm MS}$	$0.7^{+0.1}_{-0.1}$	$0.7^{+0.1}_{-0.1}$	$0.7^{+0.1}_{-0.1}$	$0.7^{+0.1}_{-0.1}$	$0.7^{+0.1}_{-0.1}$	$0.6^{+0.1}_{-0.1}$
$v_{\rm ini}$ (km s^{-1})	$280.0^{+94.2}_{-13.4}$	$340.0^{+56.1}_{-47.8}$	$340.0^{+35.7}_{-84.5}$	$290.0^{+92.1}_{-14.1}$†	$420.0^{+29.6}_{-26.5}$	$360.0^{+46.9}_{-49.8}$
$v \sin i$ (km s^{-1})	$270.0^{+13.7}_{-17.9}$ (266±15)	$270.0^{+11.4}_{-20.3}$ (265±15)	$260.0^{+10.3}_{-21.9}$ (252±15)	$280.0^{+17.3}_{-14.1}$ (281±15)	$420.0^{+11.2}_{-20.3}$ (420±15)	$270.0^{+19.4}_{-11.8}$ (276±15)
i (°)	54.9	74.6	49.9	64.6	90.0	74.6
y	$0.085^{+0.003}_{-0.000}$ (0.140±0.025)	$0.085^{+0.006}_{-0.003}$ (0.110±0.030)	$0.085^{+0.003}_{-0.000}$ (0.183±0.025)	$0.085^{+0.003}_{-0.000}$ (0.122±0.025)	$0.089^{+0.010}_{-0.003}$ (0.134±0.030)	$0.089^{+0.013}_{-0.003}$ (0.103±0.030)
log ϵ(C)	$7.96^{+0.04}_{-0.16}$ (<8.09)	$7.81^{+0.20}_{-0.19}$ (8.04±0.27)	$7.98^{+0.05}_{-0.17}$ (<8.18)	$7.96^{+0.06}_{-0.14}$ (<8.09)	$7.67^{+0.07}_{-0.28}$ (≤7.24)	$7.81^{+0.14}_{-0.45}$† (8.00±0.27)
log ϵ(N)	$8.03^{+0.23}_{-0.07}$† (8.44±0.13)	$8.34^{+0.18}_{-0.22}$ (8.36±0.34)	$8.03^{+0.23}_{-0.11}$ (8.46±0.13)	$8.03^{+0.23}_{-0.08}$ (8.16±0.13)	$8.41^{+0.18}_{-0.09}$† (8.33±0.34)	$8.34^{+0.33}_{-0.08}$ (8.76±0.34)
log ϵ(O)	$8.53^{+0.01}_{-0.06}$ (8.47±0.21)	$8.43^{+0.10}_{-0.10}$† (8.42±0.21)	$8.53^{+0.02}_{-0.05}$ (8.62±0.21)	$8.53^{+0.01}_{-0.05}$ (8.66±0.21)	$8.40^{+0.06}_{-0.14}$ (≤8.33)	$8.43^{+0.08}_{-0.25}$ (8.05±0.21)

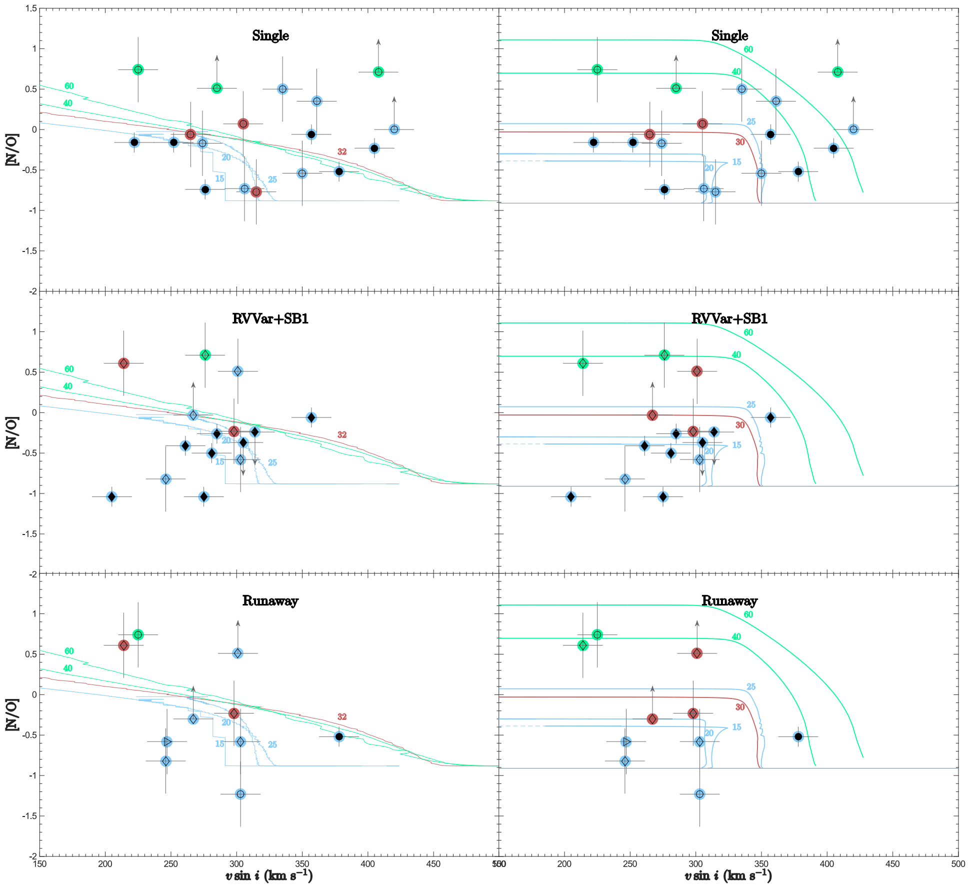

Fig. A.2. Same as Fig. 5, but for the different multiplicity status.

Table B.3. Continued.

Star	HD 198781	HD 203064	HD 210839	HD 228841
$M_{\rm ini}$ (M$_\odot$)	$15.2^{+1.5}_{-1.4}$	$23.8^{+5.1}_{-3.2}$	$40.0^{+11.4}_{-12.4}$	$25.4^{+6.2}_{-3.2}$
$M_{\rm act}$ (M$_\odot$)	$15.2^{+1.5}_{-1.3}$	$23.4^{+4.6}_{-2.9}$	$35.2^{+10.2}_{-8.2}$	$24.8^{+5.2}_{-2.8}$
log L (L$_\odot$)	$4.4^{+0.1}_{-0.1}$	$5.1^{+0.2}_{-0.3}$	$5.6^{+0.3}_{-0.2}$	$5.2^{+0.2}_{-0.2}$
Age (Myr)	$6.1^{+1.2}_{-1.5}$	$3.7^{+1.0}_{-0.7}$	$3.4^{+0.4}_{-0.9}$	$4.1^{+0.9}_{-0.5}$
$\tau_{\rm MS}$	$0.5^{+0.1}_{-0.1}$	$0.6^{+0.1}_{-0.2}$	$0.7^{+0.1}_{-0.1}$	$0.7^{+0.1}_{-0.1}$
$v_{\rm ini}$ (km s^{-1})	$370.0^{+24.6}_{-97.3}$	$330.0^{+59.8}_{-28.0}$	$350.0^{+65.5}_{-50.9}$	$360.0^{+46.2}_{-40.3}$
$v \sin i$ (km s^{-1})	$220.0^{+20.5}_{-12.1}$ (222±15)	$300.0^{+14.8}_{-16.8}$ (298±15)	$220.0^{+10.6}_{-20.3}$ (214±15)	$300.0^{+20.6}_{-11.0}$ (305±15)
i (°)	36.5	75.4	73.0	69.6
y	$0.081^{+0.003}_{-0.000}$ (0.230±0.025)	$0.085^{+0.006}_{-0.003}$ (0.076±0.030)	$0.089^{+0.020}_{-0.003}$ (0.113±0.030)	$0.089^{+0.003}_{-0.003}$ (0.112±0.030)
log ϵ(C)	$8.03^{+0.08}_{-0.15}$ (≤8.09)	$7.91^{+0.09}_{-0.24}$ (7.92±0.27)	$7.12^{+0.00}_{-0.00}$† (7.83±0.27)	$7.78^{+0.15}_{-0.18}$† (7.48±0.27)
log ϵ(N)	$7.98^{+0.27}_{-0.15}$† (8.62±0.34)	$8.34^{+0.15}_{-0.21}$ (8.23±0.34)	$8.69^{+0.08}_{-0.47}$† (8.74±0.34)	$8.34^{+0.17}_{-0.12}$ (8.74±0.34)
log ϵ(O)	$8.53^{+0.02}_{-0.04}$ (8.78±0.21)	$8.48^{+0.05}_{-0.10}$ (8.46±0.21)	$8.45^{+0.08}_{-0.35}$† (8.13±0.21)	$8.42^{+0.07}_{-0.09}$† (8.67±0.21)

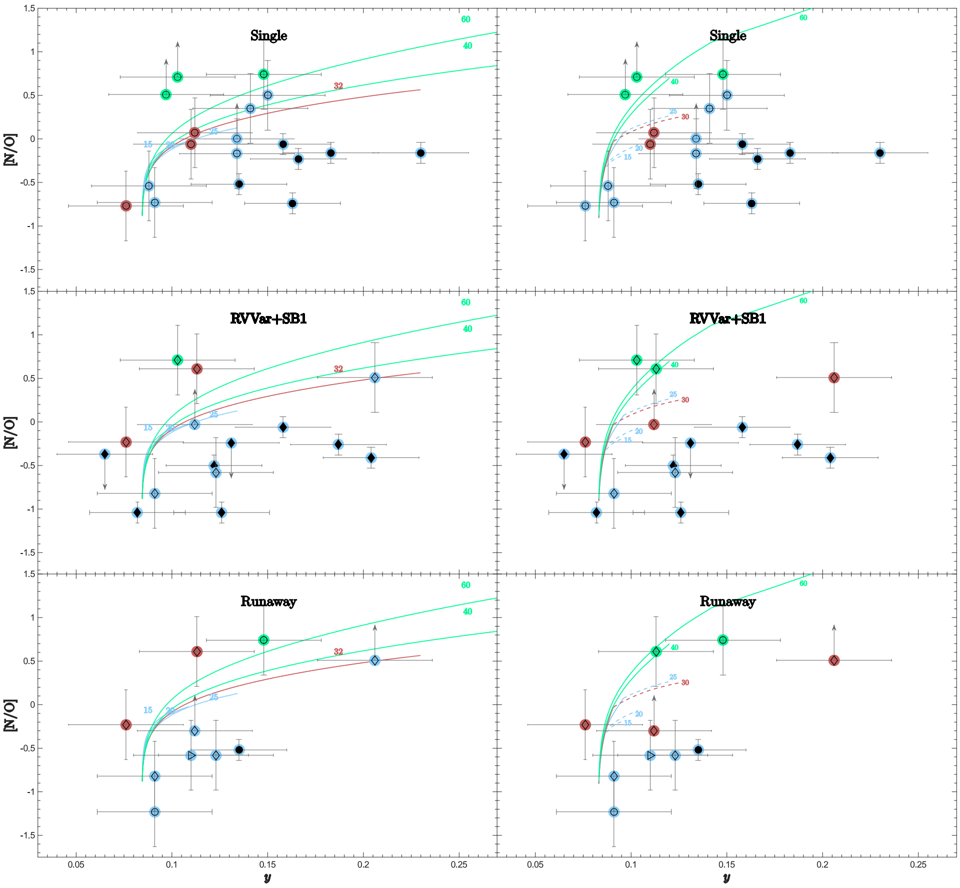

Fig. A.3. Same as Fig. 6, but for the different multiplicity status.

2.2.2.1 Complementary information

Additional information to the analysis presented in Paper II are given in this section.

Abundance peculiarities. Table 2.7 compares our helium and [N/O] abundance ratio estimates with the ones predicted by BONNSAI when the three following sets of input parameters are used:

1. $T_{\rm eff}$, $\log g_{\rm C}$, $v \sin i$, y, C, N, and O abundances;
2. $T_{\rm eff}$, $\log g_{\rm C}$, $v \sin i$, and y;
3. $T_{\rm eff}$, $\log g_{\rm C}$, and $v \sin i$.

We have noticed a clear excess of helium for a great majority of our stars, as well as [N/O] peculiarities for some of our targets. Figure 2.16 shows that there is no significant trend between the difference in the predicted [N/O] abundance ratios and the difference in the predicted y by BONNSAI when different input parameters are used.

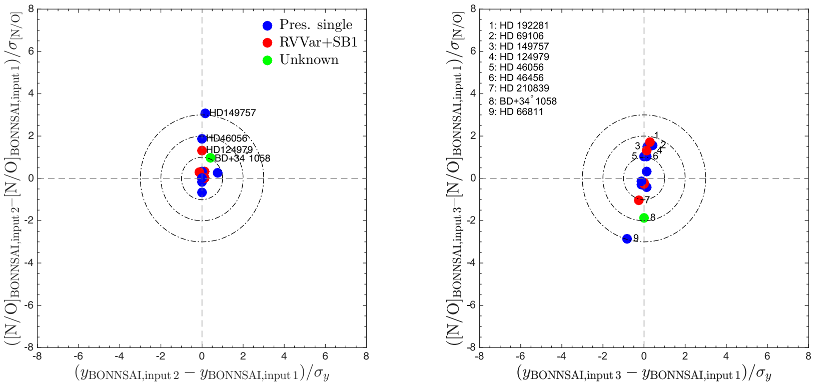

(a) **(b)**

Figure 2.16: Difference between the predicted [N/O] abundance ratios by BONNSAI when first and second sets **(a)** and first and third sets **(b)** of input parameters are used as a function of difference between the predicted y by BONNSAI.

Star	$y_{\rm obs}$	$y_{\rm BONN}$ input 1	$y_{\rm BONN}$ input 2	$y_{\rm BONN}$ input 3	$[\rm N/O]_{\rm obs}$	$[\rm N/O]_{\rm BONN}$ input 1	$[\rm N/O]_{\rm BONN}$ input 2	$[\rm N/O]_{\rm BONN}$ input 3
ALS 864	0.064±0.025	...	$0.085^{+0.000}_{-0.000}$	$0.085^{+0.003}_{-0.000}$	–0.48±0.12	...	–0.89	–0.89
ALS 18675	0.071±0.025	...	$0.085^{+0.003}_{-0.000}$	$0.085^{+0.003}_{-0.000}$	–0.53±0.12	...	–0.57	–0.57
BD +60° 594	0.131±0.025	$0.093^{+0.003}_{-0.003}$	$0.085^{+0.003}_{-0.000}$	$0.085^{+0.003}_{-0.000}$	<–0.24	0.00	–0.39	–0.43
HD 28446A	0.126±0.025	...	$0.085^{+0.003}_{-0.003}$	$0.085^{+0.003}_{-0.000}$	–1.04±0.12	...	–0.24	–0.49
HD 52266	0.187±0.025	...	...	$0.085^{+0.003}_{-0.003}$	–0.26±0.12	...	...	–0.30
HD 52533	0.065±0.025	$0.089^{+0.003}_{-0.003}$	$0.081^{+0.003}_{-0.000}$	$0.081^{+0.003}_{-0.000}$	<–0.37	–0.13	–0.91	–0.91
HD 53755	0.135±0.025	...	$0.085^{+0.003}_{-0.000}$	$0.085^{+0.003}_{-0.000}$	–1.06±0.12	...	–0.46	–0.46
HD 84567	0.204±0.025	...	...	$0.085^{+0.003}_{-0.000}$	–0.41±0.12	...	...	–0.27
HD 90087	0.163±0.025	...	...	$0.085^{+0.003}_{-0.003}$	–0.74±0.12	...	...	–0.25
HD 93521	0.166±0.025	...	...	$0.089^{+0.003}_{-0.003}$	–0.23±0.12	...	...	–0.10
HD 102415	0.158±0.025	...	...	$0.085^{+0.000}_{-0.000}$	–0.06±0.12	...	...	–0.89
HD 149757	0.135± 0.025	$0.081\ ^{+0.000}_{-0.000}$	$0.085^{+0.003}_{-0.003}$	$0.085^{+0.003}_{-0.000}$	–0.52± 0.12	–0.64	–0.27	–0.27
HD 163892	0.082±0.025	...	$0.085^{+0.003}_{-0.003}$	$0.085^{+0.003}_{-0.003}$	–1.04±0.12	...	–0.30	–0.30
HD 172367	0.140±0.025	...	$0.085^{+0.003}_{-0.000}$	$0.085^{+0.003}_{-0.000}$	–0.03±0.12	...	–0.50	–0.50
HD 184915	0.183±0.025	...	...	$0.085^{+0.003}_{-0.000}$	–0.16±0.12	...	...	–0.50
HD 188439	0.122±0.025	...	$0.085^{+0.003}_{-0.000}$	$0.085^{+0.003}_{-0.000}$	–0.50±0.12	...	–0.50	–0.50
HD 198781	0.230± 0.025	...	...	$0.081^{+0.003}_{-0.000}$	–0.16± 0.12	...	...	–0.55

Table 2.7: Comparison between the observed helium abundance and [N/O] abundance ratios with predicted values by BONNSAI, as a function of input parameters.

Star	$y_{\rm obs}$	$y_{\rm BONN}$ input 1	$y_{\rm BONN}$ input 2	$y_{\rm BONN}$ input 3	[N/O]$_{\rm obs}$	[N/O]$_{\rm BONN}$ input 1	[N/O]$_{\rm BONN}$ input 2	[N/O]$_{\rm BONN}$ input 3
BD +34° 1058	0.119±0.030	$0.085^{+0.006}_{-0.000}$	$0.097^{+0.010}_{-0.007}$	$0.097^{+0.007}_{-0.013}$	–0.54±0.40	–0.14	0.25	0.24
HD 13268	0.206±0.030	...	...	$0.089^{+0.007}_{-0.003}$	0.51±0.40	...	...	–0.10
HD 14434	0.103±0.030	$0.093^{+0.003}_{-0.003}$	$0.085^{+0.013}_{-0.000}$	$0.085^{+0.013}_{-0.003}$	$\geq$0.71	0.12	–0.01	0.00
HD 14442	0.097±0.030	$0.110^{+0.000}_{-0.014}$	$0.089^{+0.010}_{-0.003}$	$0.085^{+0.003}_{-0.013}$	$\geq$0.51	0.48	–0.10	–0.09
HD 15137	0.112±0.030	$0.089^{+0.003}_{-0.003}$	$0.089^{+0.007}_{-0.003}$	$0.089^{+0.003}_{-0.003}$	$\geq$–0.03	–0.08	–0.08	–0.07
HD 15642	0.150±0.030	...	$0.085^{+0.013}_{-0.000}$	$0.085\ ^{+0.010}_{-0.000}$	0.50±0.40	...	0.01	–0.26
HD 41161	0.123±0.030	$0.085^{+0.003}_{-0.003}$	$0.089^{+0.003}_{-0.003}$	$0.089^{+0.003}_{-0.003}$	–0.58±0.40	–0.22	–0.09	–0.14
HD 41997	0.110±0.030	...	$0.085^{+0.007}_{-0.000}$	$0.085\ ^{+0.006}_{-0.000}$	–0.58±0.40	...	–0.89	–0.38
HD 46056	0.088±0.030	$0.085^{+0.000}_{-0.000}$	$0.085^{+0.006}_{-0.000}$	$0.085^{+0.006}_{-0.003}$	–0.54±0.40	–0.91	–0.16	–0.20
HD 46485	0.076±0.030	$0.081^{+0.000}_{-0.000}$	$0.085^{+0.003}_{-0.000}$	$0.085^{+0.003}_{-0.003}$	–0.77±0.40	–0.91	–0.91	–0.22
HD 66811	0.148±0.030	$0.105^{+0.010}_{-0.010}$	$0.128^{+0.022}_{-0.018}$	$0.097^{+0.027}_{-0.010}$	0.74±0.40	0.59	0.69	0.68
HD 69106	0.091±0.030	$0.085^{+0.003}_{-0.000}$	$0.085^{+0.006}_{-0.000}$	$0.085^{+0.006}_{-0.000}$	–0.73±0.40	–0.38	–0.25	–0.26
HD 74920	0.134±0.030	$0.085^{+0.003}_{-0.003}$	$0.085^{+0.006}_{-0.003}$	$0.085^{+0.006}_{-0.000}$	–0.17±0.40	–0.23	–0.30	–0.32
HD 92554	0.091±0.030	...	$0.085\ ^{+0.006}_{-0.003}$	$0.085\ ^{+0.006}_{-0.003}$	–1.23±0.40		–0.15	–0.15
HD 117490	0.141±0.030	$0.085^{+0.013}_{-0.000}$	$0.085^{+0.006}_{-0.000}$	$0.085^{+0.003}_{-0.003}$	0.35±0.40	0.03	–0.23	–0.24
HD 124979	0.091±0.030	$0.081^{+0.000}_{-0.000}$	$0.081^{+0.006}_{-0.000}$	$0.085^{+0.006}_{-0.000}$	–0.82±0.40	–0.90	–0.37	–0.36
HD 150574	0.172±0.030	...	$0.089^{+0.029}_{-0.003}$	$0.089^{+0.007}_{-0.003}$	...	...	0.30	–0.08
HD 175876	0.110±0.030	$0.089^{+0.000}_{-0.003}$	$0.089^{+0.007}_{-0.003}$	$0.085^{+0.006}_{-0.003}$	–0.06±0.40	–0.10	–0.09	–0.09
HD 191423	0.134±0.030	$0.093^{+0.003}_{-0.003}$	$0.089^{+0.013}_{-0.003}$	$0.089^{+0.010}_{-0.003}$	$\geq$0.00	0.02	0.14	0.01
HD 192281	0.103±0.030	$0.089^{+0.010}_{-0.003}$	$0.089^{+0.013}_{-0.003}$	$0.089^{+0.013}_{-0.003}$	0.71±0.40	0.00	0.00	–0.09
HD 203064	0.076±0.030	$0.085^{+0.003}_{-0.003}$	$0.089^{+0.003}_{-0.003}$	$0.085^{+0.006}_{-0.003}$	–0.23±0.40	–0.15	–0.14	–0.14
HD 210839	0.113±0.030	$0.093^{+0.007}_{-0.007}$	$0.089^{+0.023}_{-0.003}$	$0.089^{+0.020}_{-0.003}$	0.61±0.40	0.10	0.22	0.24
HD 228841	0.112±0.030	$0.089^{+0.007}_{-0.000}$	$0.089^{+0.006}_{-0.003}$	$0.089^{+0.003}_{-0.003}$	0.07±0.40	–0.09	–0.08	–0.08

Table 2.7: Continued.

3

X-RAY STUDY

"The history of astronomy is a history of receding horizons."

— Edwin Powell Hubble

This third chapter introduces some X-ray emission properties of B-type stars and compares their abundances derived in the X-ray domain with the ones found in the optical domain.

The second part of our project focuses on the X-ray study of a sample of early B-type stars thanks to high-resolution data. The observatories used in the framework of our X-ray study are described hereafter.

3.1 Used X-ray facilities

XMM-*Newton* (for X-ray Multi-Mirror Mission-*Newton*), is one of the cornerstone missions of the European Space Agency (ESA) in its Horizon 2000 programme. Launched on 10th December 1999, it is one of the most powerful facilities for studying X-rays that has ever been put into orbit around the Earth. Its wide eccentric orbit allows to perform continuous observations over 40 hours (the satellite crossing the Van Allen radiation belts during the eight remaining hours of the orbit).

The XMM-*Newton* observatory harbours three X-ray telescopes, each having 58 Wolter I grazing-incidence mirrors[1] made of nickel and covered with gold. The largest mirror in each telescope has a diameter of 60 cm. The combined area of the mirrors of the three X-ray telescopes is 4650 cm^2 at 1 keV. In addition, a small UV/optical telescope with a diameter of 30 cm (the optical monitor, OM) allows to perform multiwavelength observations.

The european facility comprises five X-ray instruments: three EPIC (for European Photon Imaging Camera) cameras (two Metal Oxide Semi-conductor, MOS, and one pn cameras) and two Reflection Grating Spectrometers (RGS). In fact, each X-ray telescope is equipped with an EPIC camera, which provides 30' diameter images in the energy range 0.15 – 12 keV, as well as low-resolution spectroscopy $(E/\Delta E \sim 20-50)$[2]. The spatial resolution[3] of MOS1 and MOS2 amounts to 6.0 and 4.5" FWHM at 1.5 keV, respectively, while it is 6.6" FWHM for the pn camera, which currently is the largest X-ray detector in orbit. The two telescopes in front of the MOS detectors have structures on their mirror modules, called the Reflection Grating Arrays

---

[1] The only way X-rays can be reflected by a mirror is in a grazing-incidence configuration since the X-ray wavelengths are shorter than or close to the interatomic distances. Focal lengths are therefore extremely long. In order to reduce them, a combination of a parabolic and hyperbolic mirrors are used, which constitutes the Wolter I configuration.

[2] *Source:* ESA – XMM-*Newton* Science Operations Centre, XMM-*Newton* Users Handbook, Issue 2.14, 2016.

[3] *Source:* ESA – XMM-*Newton*, Instruments, European Photon Imaging Camera (EPIC), `http://sci.esa.int/science-e/www/object/index.cfm?fobjectid=31281&fbodylongid=774`

(RGAs), that scatter some incident radiation towards a secondary focal plane in which CCD (Charge Coupled Device) cameras are located. The combination of the RGA and the cameras form the two high-resolution spectrometers called RGS. These RGS cover a spectral region from 5 to 35 Å, which contains the radiative transitions associated to the K layer of the carbon, nitrogen, oxygen, neon, magnesium, and silicon, as well as the radiative transitions relative to the L layer of iron.

Chandra Chandra is a mission proposed by the National Aeronautics and Space Administration (NASA) that was launched on 23rd July 1999. Its orbital orbit around the Earth is 64.2 hours. Chandra is above the radiation belts for 85% of its orbital period, allowing in principle continuous observations for 55 hours.

The X-ray telescope of Chandra is composed of eight Wolter I grazing-incidence mirrors, with a total effective area of 800 cm^2 at 0.25 keV. The largest mirror in each telescope has a diameter of 122 cm. This telescope is characterised by an angular resolution of 0.5" FWHM. Four instruments are on-board Chandra : the Advanced CCD Imaging Spectrometer (ACIS), the High Resolution Camera (HRC), the Low Energy Transmission Grating Spectrometer (LETGS), and the High Energy Transmission Grating Spectrometer (HETGS). ACIS is sensitive in the energy domain 0.2 – 10 keV, while the LETGS and HETGS cover the ranges 0.08 – 2 keV and 0.4 – 10 keV, respectively. The HETGS contains two sets of gratings: the Medium Energy Grating (MEG) that is sensitive to the 0.4 – 5.0 keV range, and the High Energy Grating (HEG) that covers the 0.8 – 10.0 keV range.

The spectral resolutions are 40 – 2000 and 60 – 1000 for LETGS and HETGS, respectively. The effective area of LETGS (with the HRC spectroscopic array, HRC-S) is $\sim$ 35 cm^2 at 1.5 keV, while the one of HETGS is $\sim$ 120 cm^2 at 1.5 keV[4].

ROSAT (for Röntgensatellit), was an observatory developed by the United States, the United Kingdom, and Germany. ROSAT was launched on 1st June 1990 and ended its activities on 12th February 1999. The mission was split into two parts. The first part consisted of a survey that lasted 6 months (the so-called ROSAT All-Sky Survey, RASS), while the second part was devoted to the observations of specific X-ray sources.

---

[4] *Source:* The Chandra Proposers' Observatory Guide, version 19.0, `http://cxc.harvard.edu/proposer/POG/pdf/MPOG.pdf`

ROSAT was composed of an X-ray Telescope (XRT), two Position Sensitive Proportional Counters (PSPC, named B and C), a High Resolution Imager (HRI), and a Wide Field Camera (WFC). The X-ray telescope was composed of four Wolter I grazing-incidence mirrors of which the largest mirror had a diameter of 84 cm. This telescope was sensitive in the energy range 0.1 – 2.4 keV, and its angular resolution was below 5". The PSPCs had a low energy resolution ($\Delta E/E = 0.43 \times \sqrt{0.93/E}$), an effective area of 400 cm^2 at 1 keV and a high spatial resolution ($\sim$ 25' at 1 keV)[5].

3.2 Some X-ray properties of stars

In the Universe, some plasmas are the source of X-ray photons which do not further interact with the emitting plasmas (that are called optically thin), the resulting spectra being thus rich in emission lines. The origin of the X-ray emission is different for the low-mass and massive stars. The atmosphere of the former stars has a tenuous hot gas (the so-called X-ray emitting corona) that is heated in confined loops that are formed after the action of a magnetic field. Moreover, low-mass pre-main sequence (PMS) stars, such as T Tauri stars that are surrounded or not by a thick disk for classical and weak-line T Tauri stars, respectively, are also X-ray emitters. The origin of the X-ray emission of T Tauri stars can be linked to a magnetic activity similar to the one of the Sun, or due to a magnetic interaction with the surrounding disk. This emission is frequently variable and, during flare events, can rise rapidly, this increase being then followed by a slowly decay. Massive stars do not have coronae. Their intrinsic X-ray emission instead originates from shocks between dense shells of gas that occur within their strong wind (the so-called embedded wind shocks; Lucy & White 1980; Lucy 1982). Additional X-ray emissions can be produced in colliding wind shocks in binary stars and in magnetically-confined wind shocks (MCWS) in the case of magnetic stars. In the latter case, the stellar wind is guided to the equatorial plane, where there is a collision with the stream from the other hemisphere, the resulting hot plasma then generating an X-ray emission.

The region where the X-ray emission arises can be constrained thanks to the study of some spectral lines, especially the so-called fir triplets, that result

---

[5] *Sources:* The ROSAT PSPC, `https://heasarc.gsfc.nasa.gov/docs/rosat/pspc.html` and ESA – XMM-*Newton* Science Operations Centre, XMM-*Newton* Users Handbook, Issue 2.14, 2016.

from the transitions between the first excited levels and the ground state of He-like ions (C V, N VI, O VII, Ne IX, Mg XI, and Si XIII). They comprise a resonance (r; $^1\mathrm{P}_1$ – $^1\mathrm{S}_0$), two intercombination (i; $^3\mathrm{P}_{1,2}$ – $^1\mathrm{S}_0$), and a forbidden (f; $^3\mathrm{S}_1$ – $^1\mathrm{S}_0$) lines. The density influences the ratio between the f and i fluxes, $\mathscr{R} = f/i$ (Gabriel & Jordan, 1969). This is due to the fact that, if the electron collision rate is high enough, the ions in the upper level of the forbidden transition ($^3\mathrm{S}_1$) do not go back to the ground state ($^1\mathrm{S}_0$), and instead populate, thanks to collisions, the upper level of the intercombination transitions ($^3\mathrm{P}_{1,2}$). In addition, ions can also be radiatively excited to this level. An approximation of the ratio $\mathscr{R}$ is thus given by

$$\mathscr{R} = \frac{f}{i} = \mathscr{R}_0 \frac{1}{1 + n_\mathrm{e}/N_\mathrm{c} + \phi/\phi_\mathrm{c}},$$

where $\mathscr{R}_0$ is the limiting flux ratio at low densities and low UV fluxes, n_e the electron density, and ϕ the photoexcitation rate linked to the photospheric UV radiation (which is diluted as the distance to the star increases). N_c and ϕ_c are the critical density and photoexcitation rate, respectively. This ratio can be used to provide coronal density estimates in low-mass stars or the position of the X-ray emitting plasma with respect to the UV source (the photosphere) in massive stars as $\mathscr{R}$ decreases when n_e or ϕ are large. The influence of the density can be neglected for massive stars as their circumstellar density is generally low but the excitation of ions from the $^3\mathrm{S}_1$ level to the $^3\mathrm{P}_{1,2}$ level initiated by the UV radiation is significant in those stars. Another interest of the fir triplets is the computation of the $\mathscr{G} = (f + i)/r$ ratio, which can be used as an indicator of the temperature. An independent estimate of the temperature can also be provided by the ratio of H-like to He-like line fluxes.

As the X-rays arise in the outflowing winds, the X-ray lines of massive stars are also Doppler broadened. In addition, these lines should be asymmetric. Indeed, they are formed in the outflowing wind but this wind is also able to absorb X-rays. Therefore, the output flux is reduced, and even more so if the path is longer, as in the case of X-rays emitted behind the star (as viewed from Earth), i.e., in the redshifted part of the line. X-ray lines from massive stars were therefore expected to appear broad and skewed (Ignace 2001; Owocki & Cohen 2001). However, observations in the last two decades showed rather symmetric lines, demonstrating that the absorption by the winds were less important than initially thought, hence the mass-loss rates were revised downwards (Waldron & Cassinelli, 2007).

For the other origins of X-ray emission in massive stars, such as wind-wind collisions or MCWS, the situation is different: in the former case, lines are narrow, symmetric, and $\mathscr{R}$ is low as X-rays arise close to the photosphere; in the latter case, lines are broad and symmetric with large $\mathscr{R}$ as X-rays arise far from the photosphere. High-resolution data thus enable to probe the origin of the X-ray emission of massive stars.

Pottasch (1963) found substantially higher abundances of Mg, Si, and Fe in the corona of the Sun than in its photosphere. It is now established that elements with first ionisation potential (FIP) lower than 10 eV (i.e., Mg, Si, Ca, Fe, Ni, *called-FIP elements*), are more enhanced in the corona and the winds than in the photosphere; this effect being called the *FIP effect* (Feldman, 1992). Low-FIP elements are ionised in the chromosphere, while high-FIP elements (C, N, O, Ne, Ar, and to some extent S) are essentially neutral. These elements are thus affected in a different way by electric and magnetic fields. An inverse trend has been noticed within magnetically active stars, the *inverse FIP effect*, in which low-FIP abundances are systematically depleted compared to high-FIP elements (Brinkman et al., 2001). The FIP and IFIP effects reflects the two extreme evolutionary status of the corona: the IFIP effect weakens with the magnetic activity (i.e., when the coronal temperature decreases) and a FIP trend is finally obtained for less active stars.

This phenomenon is, however, not seen in massive stars as they do not have X-rays arising from a corona but from winds, and the wind and photospheric abundances should be identical. In this context, we have studied the abundances of B-type stars thanks to high-resolution X-ray spectra in order to compare them with the ones found in the optical domain. Unlike in the first part of this thesis, in which we focused on fast rotators only, we studied here some massive stars regardless of their projected rotational velocity, only one star being fast-rotating (Table 3.1). Indeed, the X-ray line width is determined by the wind velocity, where the emission takes place: it is unrelated to the stellar rotation itself. The abundances of fast rotators can therefore be determined without encountering the issues (e.g., line crowding) associated with the derivation in the optical domain. Our results were presented in Cazorla et al. (2017c).

Table 3.1: List of our studied massive X-ray emitters. References for projected rotational velocities are [1]: Abt et al. (2002), [2]: Simón-Díaz & Herrero (2014) (values obtained with the Fourier transform are reported), [3]: Uesugi & Fukuda (1970).

Star	$v \sin i$ [km s^{-1}]	Reference
HD 34816 (λ Lep)	25	[1]
HD 35468 (γ Ori)	52	[2]
HD 36512 (υ Ori)	15	[2]
HD 36960	23	[2]
HD 38771 (κ Ori)	54	[2]
HD 44743 (β CMa)	26	[2]
HD 52089 (ε CMa)	25	[1]
HD 63922 (P Pup)	25	[3]
HD 79351 (a Car)	0	[3]
HD 144217 (β^1 Sco)	88	[2]
HD 158926 (λ Sco)	237	[3]

3.3 Published paper

The last paper of our thesis aims at investigating the X-ray properties of B-type stars thanks to high-resolution spectra.

Astronomy & Astrophysics manuscript no. bstars
August 16, 2017

B-stars seen at high resolution by XMM-*Newton*[⋆]

Constantin Cazorla and Yaël Nazé[⋆⋆]

Groupe d'Astrophysique des Hautes Energies, STAR, Université de Liège, Quartier Agora (B5c, Institut d'Astrophysique et de Géophysique), Allée du 6 Août 19c, B-4000 Sart Tilman, Liège, Belgium
e-mail: `naze@astro.ulg.ac.be`

August 16, 2017

ABSTRACT

We report on the properties of 11 early B-stars observed with gratings onboard XMM-*Newton* and *Chandra*, doubling the number of B-stars analysed at high-resolution. The spectra typically appear soft, with temperatures of 0.2–0.6 keV, and moderately bright ($\log[L_X/L_{BOL}] \sim -7$, with lower values for later-type stars). In line with previous studies, we also find an absence of circumstellar absorption, negligible line broadening, no line shift, and formation radii in the range $2 - 7$ $R_\star$. From the X-ray brightnesses, we derive the quantity of "hot" mass-loss rate for each of our targets and compared them to predictions or values derived in the optical domain: in some cases, the hot fraction of the wind can be non-negligible. The derived X-ray abundances were compared to values obtained from the optical data with a fair agreement between them. Finally, half of the sample is found to present temporal variations, either on long-term, short-term, or both. In particular, HD 44743 is found to be the second example of an X-ray pulsator, and we detect a flare-like activity in the binary HD 79351, which also displays a high-energy tail and one of the brightest X-ray emission in the sample.

Key words. stars: early-type – X-rays: stars

1. Introduction

The advent of the first high-resolution X-ray spectrographs, onboard XMM-*Newton* and *Chandra*, profoundly modified our understanding of high-energy phenomena. Indeed, high-resolution spectra provide a wealth of detailed information. For massive stars, the X-ray emission comes from optically-thin, hot plasma, hence lines dominate the X-ray spectra. Their relative strengths closely constrain the plasma temperature and composition. The ratios between forbidden and intercombination lines of He-like ions further pinpoint where X-rays arise (Porquet et al. 2001). Finally, their line profiles provide unique information on the stellar wind, its opacity and its velocity field (Macfarlane et al. 1991; Owocki & Cohen 2001).

Analyses of the high-resolution spectra of O-stars have revealed winds to be less opaque than initially thought, and have helped constraining the properties of high-energy interactions (colliding winds in binaries, magnetically confined winds in strongly magnetic objects). However, much fewer B-stars were observed at high-resolution. To further advance the understanding of X-rays associated to early B-stars, we present in this paper the X-ray observations of 11 additional targets, thereby doubling the number of such stars observed at high-resolution. Section 2 presents the selection of targets, their properties, and their observations. Sections 3 and 4 report our analyses of spectra and lightcurves, respectively, while Sect. 5 summarises and concludes this paper.

2. Target selection and observations

Performing a spectroscopic X-ray survey of early-type B stars at high resolution can only be done if the X-ray emission is sufficiently bright, even with XMM-*Newton*, which is the most sensitive facility currently available. A target selection was therefore done, using the *ROSAT* All-Sky Survey (RASS): objects with RASS count rates larger than 0.1 cts s^{-1} yield usable RGS spectra within relatively short (still, for the great majority of the observations, greater than 20 ks) exposure times. There are 20 such B-stars in the catalog of Berghöfer et al. (1996), but one (HD 152234) actually is an O+O binary (for an analysis of its XMM-*Newton* low-resolution data, see Sana et al. 2006) and the high-resolution spectra of 8 stars have been previously analysed: the strongly magnetic stars HD 205021 (β Cep, B1III+B6–8+A2.5V, Favata et al. 2009) and HD 149438 (τ Sco, B0.2V, Cohen et al. 2003; Mewe et al. 2003; Waldron & Cassinelli 2007; Zhekov & Palla 2007), as well as HD 122451 (β Cen, B1III, Raassen et al. 2005), HD 111123 (β Cru, B0.5III+B2V+PMS Zhekov & Palla 2007; Waldron & Cassinelli 2007; Cohen et al. 2008), HD 93030 (θ Car, B0.2V, Nazé & Rauw 2008), HD 116658 (Spica, B1III-IV, Zhekov & Palla 2007; Miller 2007), HD 37128 (ϵ Ori, B0I, Waldron & Cassinelli 2007; Zhekov & Palla 2007), and the peculiar Be star HD 5394 (γ Cas, Lopes de Oliveira et al. 2010). This leaves 11 stars, which we analyse here using observations taken by XMM-*Newton* or *Chandra* (see Table 1 for the observing log). This table also presents the main properties of the targets. Amongst them, four are known binaries (HD 63922, HD 79351, HD 144217, HD 158926 – see Table 1) while two are known β Cephei pulsators (HD 44743, HD 158926 – see Sect. 4 for more details). Six targets were also searched for the presence of magnetic fields: HD 36512 (Bagnulo et al. 2006; Grunhut et al. 2017), HD 36960 (Bagnulo et al. 2006; Bychkov et al. 2009),

---

[⋆] Based on observations collected with the ESA science mission XMM-*Newton*, an ESA Science Mission with instruments and contributions directly funded by ESA Member States and the USA (NASA).

[⋆⋆] F.R.S.-FNRS Research Associate.

HD 79351 (Hubrig et al. 2007) and HD158926 (Bychkov et al. 2009) seem non-magnetic while HD 44743 and HD 52089 may present very weak fields (<100 G, Fossati et al. 2015; Neiner et al. 2017) – no strongly magnetic star is thus known in our sample. Finally, there is no Be star amongst them, hence none can belong to the class of peculiar, X-ray bright γ-Cas objects. We will thus refrain from comparing our targets to such objects in the following, especially since their X-ray emission has a completely different origin than for "normal" B-stars (for a review, see Smith et al. 2016). Comparisons with the published analyses of the 7 other B-stars will however be made.

2.1. XMM-*Newton*

The XMM-*Newton* data were reduced with SAS (Science Analysis Software) v16.0.0 using calibration files available in Spring 2016 and following the recommendations of the XMM-*Newton* team[1].

After the initial pipeline processing, the EPIC (European Photon Imaging Camera) observations were filtered to keep only the best-quality data (PATTERN 0–12 for MOS and 0–4 for pn). Lightcurves for events beyond 10 keV were calculated for the full cameras and, whenever background flares were detected, the corresponding time intervals were discarded (using thresholds of 0.2 cts s^{-1} for MOS, 0.5 cts s^{-1} for pn in full frame mode and 0.04 cts s^{-1} for pn in small window mode). We extracted EPIC spectra using the task *especget* in circular regions of 50″ radius for MOS and 35″ for pn (to avoid CCD gaps) centred on the Simbad positions of the targets except for HD 36960 and HD 144217, for which the radii were reduced to 25″ and 7.5″ respectively, due to the presence of neighbouring sources. Dedicated ARF (Ancillary Response File) and RMF (Redistribution Matrix File) response matrices, which are used to calibrate the flux and energy axes, respectively, were also calculated by this task. EPIC spectra were grouped with *specgroup* to obtain an oversampling factor of five and to ensure that a minimum signal-to-noise ratio of 3 (i.e., a minimum of 10 counts) was reached in each spectral bin of the background-corrected spectra; unreliable bins below 0.25 keV were discarded. EPIC light curves were extracted in the same regions as the spectra, for time bins of 100 s and 1 ks, and in the 0.3–10.0 keV energy band. They were further processed by the task *epiclccorr*, which corrects for the loss of photons due to vignetting, off-axis angle, or other problems such as bad pixels. In addition, to avoid very large errors, we discarded bins displaying effective exposure time lower than 50% of the time bin length.

RGS (Reflection Grating Spectrometer) data were also locally processed using the initial SAS pipeline. As for EPIC data, a flare filtering was then applied (using a threshold of 0.1 cts s^{-1}). For HD 36960 and HD 144217, close companions exist at a distance of 0.14–0.62' and 0.2', respectively, perpendicular to the dispersion axis. The extraction region was thus reduced to 45% and 50% of the PSF radius, respectively, to avoid contamination. Furthermore, the background was extracted after excluding regions within 98% of the PSF size from the source and the neighbours. Dedicated response files were calculated for both orders and both RGS instruments, and were subsequently attached to the source spectra for analysis. The two RGS datasets of HD 44743 were combined using *rgscombine*. For individual line analyses, no grouping and no background were considered (the local background around the lines was simply fitted using a flat power law). For global fits, background spectra were considered and a grouping was performed to reach at least 10 cts per bin and to get emissions of each He-like (fir) triplet in a single bin. The latter step is needed because global spectral fitting does not take into account the possible depopulation of the upper level of the f-line in triplets in favour of the i-lines' upper levels.

2.2. *Chandra*

The *Chandra* data of HD 38771 were reprocessed locally using CIAO 4.9 and CALDB 4.7.3. Since all *Chandra* data were taken within 10 days, orders +1 and –1 were added and the four exposures combined using *combine_grating_spectra* to get the final HEG and MEG spectra. For each exposure, 0th order spectra of the source were also extracted in a circle of 2.5″ radius around its Simbad position, while the associated background spectra were extracted in the surrounding annulus with radii 2.5 and 7.4″. Dedicated response matrices were calculated using the task *specextract*, and the individual spectra and matrices were then combined using the task *combine_spectra* to get a single spectrum for HD 38771. The resulting HEG, MEG, and 0th order spectra were grouped in the same way as the XMM-*Newton* spectra. For each exposure, lightcurves were extracted considering the same regions as the spectra, for time bins of 100 s and 1 ks, and in the 0.3–10.0 keV energy band.

3. Spectra

We performed two types of fitting: individual analyses of the lines and global analyses. All these analyses were performed within Xspec v 12.9.0i.

3.1. Line fits

Figure 1 displays the high-resolution spectra of our targets. Lines from H-like and He-like ions of C, N, O, Ne, Mg, and Si, as well as lines from ionised Fe, are readily detected, demonstrating the thermal nature of the X-ray emissions. In general, the triplet from He-like ions appear stronger than Lyα lines, as expected for late-type massive stars (Walborn et al. 2009), but we find no clear, systematic dependence with the spectral types of our targets.

An examination of the line profiles reveals no obvious asymmetry, hence we decided to fit them by simple Gaussian profiles. We relied on Cash statistics and therefore used unbinned spectra without background correction. We fitted only the lines which were sufficiently intense to provide a meaningful fit. In case of doublets (the two components of Lyman lines of H-like ions) or triplets (the fir components of He-like ions), the individual components were forced to share the same velocity and the same width. Furthermore, the flux ratios between the two Lyman components as well as the flux ratios between the two i lines of Si and Mg[2] were fixed to the theoretical ones in ATOMDB[3]. The derived line properties are listed in Table 2, with 1σ errors determined using the *error* command under Xspec. Whenever the fitted width was reaching a null value, a second fitting was performed with the width fixed to zero, and Table 2 provides the results of this second fitting.

Comparing for each target the results obtained for the different lines, we detect no significant and coherent line shifts

---

[1] SAS threads, see http://xmm.esac.esa.int/sas/current/documentation/threads/

[2] For N, O, and Ne, the second i component is >30 times less intense, hence can be neglected.

[3] See, e.g., http://www.atomdb.org/Webguide/webguide.php

Table 1. Journal of the observations and physical properties of the sample stars.

Target name	Sp. type	d (pc)	$\log(L_{\rm BOL}/L_{\odot})$	$R_\star$ ($R_\odot$)	$T_{\rm eff}$ (K)	$N_{\rm H}^{ism}$ ($10^{22}\,{\rm cm}^{-2}$)	ObsID (Rev)	Obs. mode	PI	Start date	Flare?	Duration (ks)
HD 34816 (λ Lep)	B0.5 V [1] *	261	4.22	4.7	30400	1.66e-2	0690200601 (2415)	ff+thick	Nazé	2013-02-15@07:41:26	N	26.5
HD 35468 (γ Ori)	B2 IV–III [2] *	77	3.87	6.4	21250	1.82e-3	0690680501 (2342)	ff+thick	Waldron	2012-09-22@19:27:17	Y	42.0
HD 36512 (υ Ori)	B0 V [1] *	877	5.21	12.1	33400	1.95e-2	0690200201 (2326)	ff+thick	Nazé	2012-08-22@02:46:15	Y	20.2
HD 36960	B0.7 V [1] *	495	4.58	7.8	29000	2.24e-2	0690200501 (2433)	ff+thick	Nazé	2013-03-23@08:57:52	Y	28.2
HD 38771 (κ Ori)	B0.5 Ia [3]	198	4.72	12.5	24800	3.39e-2	9940	ACIS-S	Waldron	2008-12-26@23:50:00		234.2
							10846	+HETG,		2008-12-30@02:53:17		
							9939	faint		2009-01-03@03:00:24		
							10839			2009-01-05@18:25:49		
HD 44743 (β CMa)	B1 II–III [4]	151	4.41	8.8	24700	2.00e-4	0503500101 (1509)	ff+thick	Waldron	2008-03-06@15:33:36	Y	10.6
							0761090101 (2814)	ff+thick	Oskinova	2015-04-21@06:44:53	Y	78.0
HD 52089 (ϵ CMa)	B1.5 II [4]	124	4.35	9.9	22500	1.00e-4	0069750101 (0234)	ff(MOS)/sw(pn)+thick	Cohen	2001-03-19@12:05:51	Y	31.2
HD 63922 (P Pup)	B0.2 III+? [1,5] *	505	4.95	10.4	31200	6.71e-2	0720390601 (2552)	ff+thick	Nazé	2013-11-15@02:11:45	N	46.5
HD 79351 (a Car)	B2.5 V+? [6,7] *	137	3.60	5.8	19150	6.04e-2	0690200701 (2393)	ff+thick	Nazé	2013-01-02@00:12:30	N	47.1
HD 144217 (β^1 Sco)	B0.5IV-V+B1.5V [8] *	124	4.44	6.1	30400	1.37e-1	0690200301 (2425)	ff+thick	Nazé	2013-03-06@16:04:28	N	26.6
HD 158926 (λ Sco)	B1.5 IV+ (DA.79 or PMS)+B [9,10] *	175	4.73	15.3	22500	2.51e-3	0690200101 (2424)	ff+thick	Nazé	2013-03-04@15:37:29	N	17.8

Notes. References for spectral types: [1] Nieva (2013); [2] Morel et al. (2008); [3] Lennon et al. (1992); [4] Fossati et al. (2015); [5] Nieva & Przybilla (2014); [6] Slettebak (1982); [7] Buscombe & Morris (1960); [8] Holmgren et al. (1997); [9] Holberg et al. (2013); [10] Uytterhoeven et al. (2004a). Distances, based on Hipparcos, come from van Leeuwen (2007) and interstellar absorbing columns $N_{\rm H}^{ism}$ were taken from Table 2 (the most recent values) of Gudennavar et al. (2012), except for HD 36960 (for which there is no available value in Gudennavar et al. 2012 so the adopted value is taken from Diplas & Savage 1994) and HD 63922, for which only the color excess is known ($E(B-V) = 0.11$, Katyal et al. 2013) – it was converted into an absorbing column using the relation of Gudennavar et al. (2012). Bolometric luminosities (for the primary star if binary) were calculated using their Simbad V magnitudes, Hipparcos distances, reddenings from Gudennavar et al. (2012, except for HD 63922, see above), and bolometric corrections of Nieva (2013) for non-supergiant stars (identified by *) and the scale of Cox (2002) for HD 38771. Effective temperatures $T_{\rm eff}$ were also taken from the latter two references with the addition of Fossati et al. (2015) for HD 44743 and HD 52089 (they also provided their $L_{\rm BOL}$, which is quoted here). Radii were calculated from $L_{\rm BOL} = 4\pi R_\star^2\,\sigma\,T_{\rm eff}^4$. For the EPIC cameras, "ff" and "sw" correspond to full frame and small window modes, respectively – note that the thick filter was always needed to reject optical/UV light, in view of the (optical) brightness of the targets. The durations in the last column correspond to exposure times after flare filtering for EPIC-pn or ACIS-S (0th order). The κ Ori data, taken within 10 days, were combined, so that only the total duration is provided.

Table 2. Results of the individual line fitting by Gaussians.

	HD 34816	HD 35468	HD 36512	HD 36960	HD 38771	HD 44743	HD 52089	HD 63922	HD 79351	HD 144217	HD 158926
He-like triplets											
Si XIII λ6.648,6.685,6.688,6.740Å											
v (km s^{-1})					136±90						
$FWHM$ (km s^{-1})					1201±182						
F_r					2.72±0.33						
F_i					0.62±0.19						
F_f					1.29±0.23						
f/i					2.08±0.74						
$(f+i)/r$					0.70±0.14						
T_{fir} (keV)					1.30±0.81						
Mg XI λ9.169,9.228,9.231,9.314Å											
v (km s^{-1})					–34±57						
$FWHM$ (km s^{-1})					1132±108						
F_r					5.45±0.55						
F_i					3.00±0.48						
F_f					2.87±0.45						
f/i					0.96±0.21						
$(f+i)/r$					1.08±0.16						
T_{fir} (keV)					0.25±0.08						
R_{fir} ($R_\star$)					2.38±0.44						
Ne IX λ13.447,13.553,13.699Å											
v (km s^{-1})			–160±67		–54±44	–95±110	24±130	–54±109		–37±86	
$FWHM$ (km s^{-1})			0 (fixed)		1310±71	732±309	830±291	369±441		0 (fixed)	
F_r			22.9±4.5		50.1±3.0	17.3±2.4	33.8±4.6	17.5±2.5		38.0±7.4	
F_i			26.7±4.7		31.7±2.9	11.2±2.2	19.5±4.2	12.1±2.4		41.5±8.4	
F_f			6.53±3.38		7.97±1.62	3.28±1.47	0.46±2.59	5.56±1.89		4.36±4.56	
O VII λ21.602,21.804,22.098Å											
v (km s^{-1})	1±146	142±111	0±57	–254±98	–2±47	–31±31	0±60	79±61		–135±61	0±108
$FWHM$ (km s^{-1})	0 (fixed)	0 (fixed)	361±353	313±406	1353±80	426±198	0 (fixed)	1033±144		0 (fixed)	845±391
F_r	66.0±8.3	18.7±4.1	161±17	44.1±9.9	300±27	84.5±6.8	107±8	102±8		204±19	82.9±10.0
F_i	73.1±8.6	28.8±4.7	175±20	53.8±10.3	238±24	107±7	117±9	90.6±7.9		210±20	57.2±9.9
F_f	2.87±3.95	0 (fixed)	3.08±6.03	0.20±4.65	25.2±10.3	0.±0.73	6.80±3.95	1.18±3.13		4.59±6.96	8.65±5.94
f/i	0.04±0.05	0 (fixed)	0.02±0.03	0.0±0.09	0.11±0.04	0.000±0.007	0.06±0.03	0.01±0.03		0.02±0.03	0.15±0.11
$(f+i)/r$	1.15±0.20	1.55±0.42	1.11±0.17	1.22±0.38	0.88±0.12	1.26±0.13	1.16±0.13	0.90±0.11		1.05±0.14	0.79±0.17
T_{fir} (keV)	0.09±0.05	<0.09	0.10±0.03	0.09±0.08	0.22±0.08	<0.09	0.09±0.03	0.18±0.06		0.12±0.05	0.26±0.18
R_{fir} ($R_\star$)	<10.1		<8.3	<9.8	7.4±2.3	<2.1	4.5±2.4	<6.9		<7.6	7.3±6.5
N VI λ28.787,29.084,29.535Å											
v (km s^{-1})							–127±76				
$FWHM$ (km s^{-1})							685±182				
F_r							42.8±5.9				
F_i							49.3±9.2				
F_f							0.0±3.1				
f/i							0.00±0.06				
$(f+i)/r$							1.15±0.28				
T_{fir} (keV)							0.09±0.08				
R_{fir} ($R_\star$)							<3.7				

Table 2. Continued

	HD 34816	HD 35468	HD 36512	HD 36960	HD 38771	HD 44743	HD 52089	HD 63922	HD 79351	HD 144217	HD 158926
Lyman doublets											
Mg xii λ8.419,8.425Å											
v (km s^{-1})					–222±200						
$FWHM$ (km s^{-1})					1046±475						
F					0.91±0.21						
He-to-H ratio					12.5±3.1						
$T_{He/H}$ (keV)					0.42±0.02						
Ne x λ12.132,12.137Å											
v (km s^{-1})				1±314	–72±43	1±147	4±192		283±80		
$FWHM$ (km s^{-1})				1111±836	1037±93	0 (fixed)	0 (fixed)		0 (fixed)		
F				24.9±4.1	19.4±1.3	13.4±1.7	25.8±3.1		18.5±2.7		
O viii Lyα λ18.967,18.973Å											
v (km s^{-1})	–2±69	144±379	0±31	–292±194	–144±36	0±27	–33±33	27±53	112±120	–87±41	–127±156
$FWHM$ (km s^{-1})	583±322	1750±1750	0 (fixed)	0 (fixed)	1267±69	0 (fixed)	283±247	709±190	0 (fixed)	0 (fixed)	760±759
F	57.1±4.2	12.3±2.2	126±8	42.2±5.4	261±11	97.0±3.2	159±5	109±5	22.4±3.2	218±13	32.4±4.2
He-to-H ratio	2.49±0.28	3.85±0.85	2.69±0.27	2.33±0.47	2.16±0.17	1.97±0.12	1.45±0.09	1.78±0.14		1.92±0.17	4.59±0.76
$T_{He/H}$ (keV)	0.193±0.004	0.18±0.01	0.189±0.004	0.19±0.01	0.198±0.004	0.207±0.004	0.22±0.01	0.202±0.005		0.189±0.004	0.168±0.004
O viii Lyβ λ16.006,16.007Å											
v (km s^{-1})			–228±152		–130±145	0±279	160±60	84±206		–171±171	
$FWHM$ (km s^{-1})			0 (fixed)		1296±159	1087±429	0 (fixed)	933±602		0 (fixed)	
F			14.7±3.6		34.0±3.3	11.3±1.8	26.0±3.4	14.4±2.5		34.0±4.5	
N vii λ24.779,24.785Å											
v (km s^{-1})	–73±133		–299±107		92±131	2±123	85±83	–4±118			
$FWHM$ (km s^{-1})	439±495		0 (fixed)		1838±233	0 (fixed)	1264±254	729±535			
F	23.4±4.8		37.2±8.2		158±15	19.5±2.7	72.0±5.9	24.8±4.4			
He-to-H ratio							1.28±0.19				
$T_{He/H}$ (keV)							0.15±0.01				
C vi λ33.734,33.740Å											
v (km s^{-1})			64±86			0±60	–122±49				122±91
$FWHM$ (km s^{-1})			470±469			268±267	328±328				0 (fixed)
F			127±17			84.1±8.1	91.1±8.4				79.9±13.6
Fe xvii λ15.014,15.261Å											
v (km s^{-1})			1±50		–115±36	9±49	0±56	188±130	0±65	104±166	
$FWHM$ (km s^{-1})			0 (fixed)		1192±81	707±185	0 (fixed)	927±477	0 (fixed)	1385±482	
F			38.7±5.2		96.2±4.4	51.6±2.5	112±5	33.0±3.4	26.4±2.8	84.5±8.2	
Fe xvii λ16.780,17.051,17.096Å											
v (km s^{-1})			–373±154		–585±42	–474±58	–602±26	–490±86	–614±147	–665±56	
$FWHM$ (km s^{-1})			937±632		989±90	0 (fixed)	0 (fixed)	504±504	0 (fixed)	0 (fixed)	
$F_{16.780}$			17.1±3.9		40.2±4.2	18.8±1.9	40.3±3.5	8.28±2.07	5.42±2.03	21.6±4.9	
$F_{both\,17}$			54.1±8.1		107±6	49.4±3.0	115±5	33.7±3.3	27.7±3.0	79.7±8.1	

Notes. Fluxes are given in units 10^{-6} ph cm^{-2} s^{-1}, and correspond to fluxes for all components of Lyman doublets or of iron line groups. The provided ratios are uncorrected for interstellar absorption; since the f flux of O vii was set to zero for HD 35468, no R_{fir} was derived in this case. For the He-like triplet of Neon, the presence of multiple iron lines in the area may render the line fluxes unreliable because of blending with iron lines, hence they are provided for information only and the ratios are not indicated. Errors correspond to 1σ uncertainties – if asymmetric, the larger value is given.

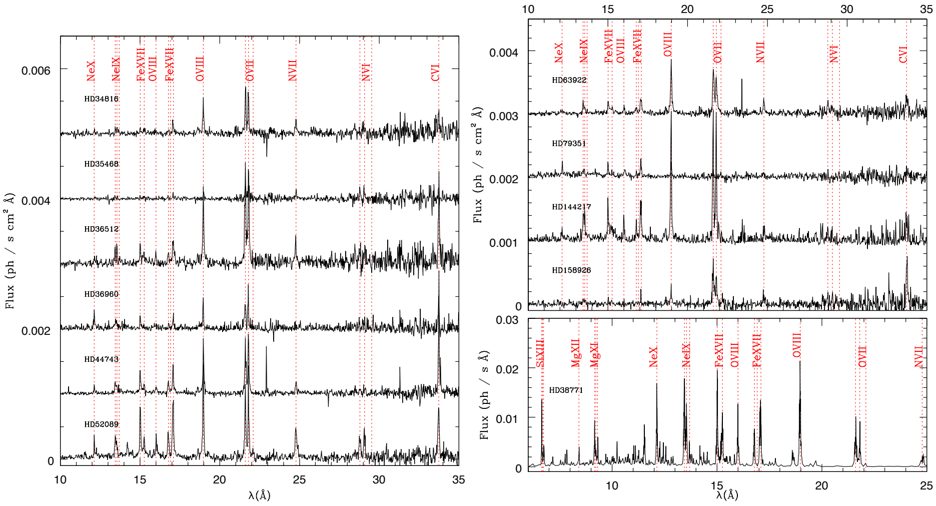

Fig. 1. RGS and MEG spectra of our targets, with the main lines identified and their position indicated by the dotted lines.

for any of them. Similarly, the line widths appear overall compatible with zero for each target except HD 38771, for which $FWHM \sim 1250\,\mathrm{km\,s^{-1}}$, a value close to the wind terminal velocity (Crowther et al. 2006; Searle et al. 2008). While other stars were observed using the RGS, which has a poorer spectral resolution than HEG/MEG, it should be noted that $FWHM$ larger than $1000\,\mathrm{km\,s^{-1}}$ would have been detected, considering the errors and instrumental broadening. The X-ray lines thus appear quite narrow, confirming the results found for other B-stars (e.g., Waldron & Cassinelli 2007; Cohen et al. 2008; Favata et al. 2009).

We now turn to the line ratios: $(f + i)/r$ in He-like triplets and flux ratios between He-like and H-like lines are indicators of temperature while $\mathcal{R} = f/i$ is a probe of the formation radius of the X-ray emission. Correcting for the energy-dependent interstellar absorption is unnecessary for ratios involving the closely spaced fir lines, but such a correction needs to be performed for the He-to-H-like flux ratios since the lines are more distant in this case. However, since our targets are nearby, their interstellar absorptions are small (Table 1), hence these corrections are of very limited amplitude.

As in Nazé et al. (2012), we used ATOMDB, though with the newer version 3.0.8, to compute the expected ratios He-to-H-like flux ratios and $(f + i)/r$ ratios as a function of temperatures, and compared them to the observed values (see results in Table 2). The derived temperatures, typically $\log(T) \sim 6.35$, are in line with the lowest ones found in global fits (see next section) and are also comparable to temperatures observed in "normal" B-stars (e.g., Waldron & Cassinelli 2007; Zhekov & Palla 2007, – see also further below).

The negligible f lines indicate that the emission from He-like triplets arises close to a source of UV, i.e., close to the stellar photosphere (e.g., Porquet et al. 2001). In fact, for massive stars, $\mathcal{R} = f/i = \mathcal{R}_0/(1 + \phi/\phi_C)$. The $\mathcal{R}_0$ values were derived from ATOMDB calculations, and taken at the temperature indicated by the $(f + i)/r$ ratio (see above and Table 3). The ϕ_C values were taken from Blumenthal et al. (1972). Finally, we used TLUSTY spectra (Lanz & Hubeny 2003, 2007) in the UV domain with solar abundances to get the stellar fluxes in the velocity interval [–2000; 0] km s^{-1} near the rest wavelengths of the $2^3\mathrm{S}_1 \rightarrow 2^3\mathrm{P}_{1,2}$ transition (for a similar approach, see Leutenegger et al. 2006). The TLUSTY models with the closest temperatures to the ones listed in Table 1 and the closest surface gravities predicted by Nieva (2013) for the different spectral types of non-supergiant stars – for HD 38771, HD 44743, and HD 52089, the surface gravities derived by Touhami et al. (2010) and Fossati et al. (2015) were considered. A microturbulence velocity of ξ=10 km s^{-1}, which is a value adapted to our target types (e.g., Hunter et al. 2009), was considered, unless models with the required temperatures and surface gravities were not available within the TLUSTY grid associated to ξ=10 km s^{-1} (i.e., for HD 35468, HD 44743, HD 52089, and HD 158926). In this case, TLUSTY models with ξ=2 km s^{-1} were taken into account. We performed tests to check the consistency of our choice: using these two microturbulence velocities resulted in similar formation radii, within error bars, for an effective temperature of 22000 K and a surface gravity of 3.00 dex. Since these UV fluxes are diluted, which can be represented by the dilution factor $W(r) = 0.5\,\{1 - [1 - (R_\star/r)^2]^{1/2}\}$ to get ϕ values, the $\mathcal{R}$ ratios constrain the position of the emitting plasma (see R_{fir} in Table 2). Note that UV TLUSTY spectra only cover the 900 – 3200 Å wavelength range, which therefore excludes the analysis of the Si XIII triplet lines, hence R_{fir} is not indicated in that case, but this concerned only HD 38771. Focusing on the formation radii derived from O VII lines (since they are available for all but one star), values ranging from ~ 2 to $\sim 8\,R_\star$ are found. This is in good agreement with values determined for the studied B-star mentioned in Sect. 2: for HD 205021, Favata et al. (2009) derived a formation radius in the range $\simeq 3 - 5\,R_\star$; for HD 122451, Raassen et al. (2005) estimated a formation radius $\lesssim 5.7\,R_\star$; Nazé & Rauw (2008) gave a formation radius $< 20\,R_\star$ for HD 93030; Miller (2007) derived a formation radius in the range

$5-8\,R_\star$ for HD 116658; Mewe et al. (2003) estimated the formation radius of HD 149438 to be $\lesssim 10\,R_\star$; for HD 37128, Waldron & Cassinelli (2007) provided a formation radius of $10.2\pm2.6\,R_\star$.

3.2. Global fits

Having both low-resolution, broad-band spectra (EPIC, ACIS-S 0th order) and high-resolution, narrower-band spectra (RGS, HEG/MEG) allows us to investigate the full X-ray spectra in detail, deriving not only temperatures and absorptions, but also abundances. However, caution must be taken since abundances may vary wildly when all parameters are relaxed in one step. Therefore, we have performed global fits in several steps. First, we have fitted the low-resolution spectra with absorbed thermal emission models with fixed solar abundances (Asplund et al. 2009). One thermal component was never sufficient to achieve a good fit, but two components were usually adequate, except for HD 36960, HD 79351, and HD 144217, for which three components were needed to fit a high-energy tail. Fits with absorption in addition to the interstellar one were tried, but either the additional absorbing column reached a null value or the χ^2 was worse than without such a column. This absence of (detectable) local absorption is quite usual for B-stars (Nazé et al. 2011; Rauw et al. 2015) and for the final fits we therefore considered only the interstellar contributions (see Table 1 for their values). Second, we fitted the high-resolution spectra with the same thermal models, but fixing the temperatures while releasing abundances. Only if lines of one element are clearly observed (and measured, see Table 2) is the abundance of that element allowed to vary. In the third step, the temperatures were released, again for fitting the high-resolution spectra. Finally, in the fourth step, a simultaneous fitting of both low-resolution and high-resolution spectra was performed, with the same model than in the third step. The final results are provided in Table 3. We note that the abundances found in the last two steps are similar, but they sometimes differ from those found in the second step, indicating that the formal error bars might actually be underestimated.

In general, the X-ray spectra appear very soft and the associated temperatures are low, i.e., 0.2–0.6 keV, in line with results from Raassen et al. (2005); Zhekov & Palla (2007); Nazé & Rauw (2008); Gorski & Ignace (2010) for optically bright, nearby B-stars observed at high-resolution in X-rays. However, in large surveys relying on low-resolution X-ray spectra, many B-stars present higher temperatures (Nazé 2009; Nazé et al. 2011), though the contamination by companions or magnetically confined winds cannot be excluded in such cases. In our sample, only three targets appear harder, with a hotter component: HD 36960, HD 79351, and HD 144217. The last two are binaries, and we may suspect that this plays a role in their properties – though only longer observations, including a full monitoring throughout the orbital period, would be able to reveal the exact origin of the hard X-rays (emission from the companion or due to an interaction with it?). For HD 36960, however, there is no obvious reason for such a hardness: it is not a binary nor a magnetic object. Further investigation will thus be needed to clarify this issue.

The X-ray luminosities of massive stars are generally compared to their bolometric ones (see penultimate line of Table 3). For single and non-magnetic O-type stars in clusters, the ratio $\log(L_X/L_{BOL})$ is close to -7, with a dispersion of about 0.2 dex (e.g., Nazé et al. 2011). The situation appears more complex for early B-stars: surveys show a large scatter with ratios between –8 and –6 and some "levering" of the X-ray emission for the optically faintest objects (Berghöfer et al. 1996; Nazé et al. 2011, 2014; Rauw et al. 2015) – again, contamination of the X-ray emission by companions cannot be excluded. Furthermore, while magnetic O-stars systematically appear brighter than their non-magnetic counterparts, this is not the case of magnetic B-stars (with $\log[L_X/L_{BOL}] \sim -7.6$ for the faintest case, in Fig. 4 and Table 7 of Nazé et al. 2014), which further blurs the picture. However, our sample is rather "clean" in this respect, as the chosen B-stars are nearby and not strongly magnetic (see Sect. 2). Our earliest B-type stars (B0–0.7) display ratios between –6.8 and –7.4, in line with the O-star relationship. This confirms previous results for such objects (Rauw et al. 2015, and references therein). Four of the five latest B-type stars (B1–2.5) have ratios < -7.4, confirming the lower level of intrinsic X-ray emission of such (non-magnetic) stars found in *ROSAT* data (Cohen et al. 1997), and attributed to their weakest stellar winds. However, the last one, HD 79351, appears overluminous. This can probably be explained by its binarity – note also the occurence of a flare during the observation of this star (see next section).

In massive stars, X-rays are linked to stellar winds. The amount of X-ray emission can therefore be used to estimate the amount of mass-loss heated to high temperatures. This is an important information since, in the tenuous winds of B- and late O-stars, cooling times are long, hence the plasma remains hot once heated. Estimating mass-loss rates from optical/UV diagnostics may thus lead to underestimations. This was clearly demonstrated by Huenemoerder et al. (2012) for the late O-star HD 38666 (see also a similar discussion for HD 111123 in Cohen et al. 2008). We have used the best-fit normalisation factors (Table 3) to calculate the total emission measures *EM*s (since $norm = 10^{-14}\,EM/[4\,\pi\,d^2]$), summing those of individual components (Table 4). These values were converted into rates of "hot" mass loss considering Eq. 1 of Huenemoerder et al. (2012) and its equivalent for constant velocity on p. 1868 of Cohen et al. (2008, correcting by the different stellar radii of our targets). This was done considering terminal wind velocities of 500, 1000, and 1500 km s^{-1}, and the formation radius derived for O VII lines (Table 2). The derived range of values are provided in Table 4. We also computed mass-loss rates from the formulae of Vink et al. (2001, listed in Table 4), using the temperature and bolometric luminosities of our targets listed in Table 1, as well as typical masses for our targets' spectral types, taken from Cox (2002). Finally, mass-loss estimates derived from the analysis of optical spectra are also provided in Table 4, when available. Comparing all these values, we find two categories. The hot plasma constitutes a small (or even negligible) part of the wind for HD 36512, HD 38771, HD 44743, HD 63922, and HD 158926, or about half of the sample. For the other stars, the hot plasma appears as the dominant component of the circumstellar environment, as in HD 38666 (Huenemoerder et al. 2012). The variability character (see next section) or the multiplicity does not influence the membership to the former of the latter category. However, the three stars displaying a hotter component in their X-ray spectrum all belong to the second category. For such stars, the *EM* may not perfectly reflect the intrinsic X-ray emission as there may be contamination by X-rays arising in a companion, in an interaction with it, or a still unknown phenomenon (see above). More investigation is thus needed to ascertain that most of their wind is hot. In any case, our analysis suggests that some B-stars have their winds in the X-ray emitting regime, so that using only optical/UV data could lead to underestimation of their actual mass-loss rate. We caution, however, that this result is preliminary, as detailed analysis of the optical/UV spectra are often not available for those stars.

Table 3. Results of the global fitting using models of the type $tbabs(ism) \times \sum vapec_i$.

	HD 34816	HD 35468	HD 36512	HD 36960	HD 38771*	HD 44743	HD 52089	HD 63922	HD 79351	HD 144217	HD 158926
kT_1	0.186±0.004	0.172±0.004	0.116±0.008	0.081±0.001	0.215±0.010	0.197±0.001	0.199±0.002	0.190±0.002	0.223±0.016	0.188±0.003	0.174±0.006
$norm_1$	8.63±0.42	2.91±0.10	19.8±3.7	13.6±0.78	46.5±4.3	7.66±0.28	9.93±0.40	13.3±0.5	4.07±0.23	27.6±1.21	5.37±0.40
kT_2	0.41±0.07	0.59±0.03	0.291±0.004	0.459±0.015	0.52±0.02	0.558±0.006	0.579±0.004	0.488±0.017	0.74±0.02	0.481±0.019	0.48±0.06
$norm_2$	0.46±0.30	0.19±0.02	7.00±0.55	1.20±0.04	7.30±0.82	1.91±0.05	5.78±0.13	1.78±0.13	3.73±0.09	4.18±0.35	0.43±0.09
kT_3				2.50±0.08					1.60±0.03	4.4±6.2	
$norm_3$				2.85±0.07					3.73±0.09	0.32±0.10	
χ^2_ν (dof)	1.39(454)	1.04(463)	1.31 (476)	1.35 (463)	1.08 (521)	1.54 (1414)	1.44 (1139)	1.21 (798)	1.40 (1020)	1.20 (377)	1.12 (312)
A_C			0.61±0.16			1.69±0.16	1.26±0.13				1.61±0.35
A_N	1.07±0.13		1.03±0.17		1.05±0.33	1.27±0.09	2.28±0.15	1.21±0.11			
A_O	0.54±0.03	0.45±0.03	0.97±0.11	2.74±0.15	0.33±0.03	0.78±0.03	0.76±0.03	0.69±0.03	0.34±0.03	0.78±0.04	0.74±0.07
A_N/A_C			1.69±0.52			0.75±0.09	1.81±0.22				
A_N/A_O	1.98±0.26		1.06±0.21		3.18±1.04	1.62±0.13	3.00±0.23	1.75±0.18			
A_{Ne}			1.41±0.12	5.40±0.32	0.65±0.07	1.79±0.08	1.67±0.07	1.29±0.06	1.99±0.42	1.73±0.10	
A_{Fe}			0.83±0.06		0.40±0.04	1.00±0.03	0.85±0.02	0.87±0.04	0.78±0.04	0.93±0.06	
A_O/A_{Fe}			1.17±0.16		0.83±0.11	0.78±0.04	0.89±0.04	0.79±0.05	0.44±0.04	0.84±0.07	
F_X^{obs}	0.42±0.02	0.135±0.003	1.08±0.03	0.83±0.06	2.10±0.06	0.926±0.005	1.80±0.01	0.788±0.006	1.037±0.007	1.47±0.02	0.343±0.010
$\log(L_X/L_{BOL})$	−7.24 ± 0.02	−8.48 ± 0.01	−6.77 ± 0.01	−6.76 ± 0.03	−7.26 ± 0.01	−7.597 ± 0.002	−7.421 ± 0.002	−7.044 ± 0.003	−6.767 ± 0.003	−7.38 ± 0.01	−8.21 ± 0.01
eq. *ROSAT* c.r.	0.134	0.095	0.397	0.176	0.326	0.341	0.537	0.091	0.102	0.142	0.178

Notes. Temperatures are in keV, normalisation factors in 10^{-4} cm^{-5}, fluxes in the 0.5–10.0 keV energy band in 10^{-12} erg cm^{-2} s^{-1}, abundances A_i in number, with respect to Hydrogen, and with respect to solar values (Asplund et al. 2009). Errors, derived from the Xspec "error" command for parameters and from "flux err" for fluxes, correspond to 1σ uncertainties – if asymmetric, the larger value is given here. EPIC spectra were fitted above 0.25 keV and ACIS-S 0th order spectra above 0.35 keV.

*For HD 38771, there are three additional parameters: $A_{Mg} = 0.44\pm0.06$, $A_{Si} = 0.52\pm0.08$, and the gaussian smoothing ("gsmooth", convolved to the thermal model) with $\sigma = (1.23\pm0.05)\times10^{-3}$ keV at 6 keV, corresponding to $FWHM = 145 \pm 6$ km s^{-1}. This smaller value, compared to individual line fits, may be explained by the grouping used for global fits, which blurs the line profiles.

Table 4. Derived mass loss from optical studies and estimates, from different prescriptions, of the "hot" mass loss derived with our X-ray data.

Target name	$\log(\dot{M}_{\rm literature})$ ($\mathrm{M}_\odot\ \mathrm{yr}^{-1}$)	$\log(\dot{M}_{\rm Vink+01})$ ($\mathrm{M}_\odot\ \mathrm{yr}^{-1}$)		EM ($10^{52}\ \mathrm{cm}^{-3}$)	$\log(\dot{M}_{\rm Huenemoerder+12})$ ($\mathrm{M}_\odot\ \mathrm{yr}^{-1}$)	$\log(\dot{M}_{\rm Cohen+08})$ ($\mathrm{M}_\odot\ \mathrm{yr}^{-1}$)
		Low $T_{\rm eff}$	High $T_{\rm eff}$			
HD 34816			-8.50 ± 0.06	74.1 ± 4.2	<-8.1 to <-7.6	<-8.0 to <-7.6
HD 35468		-8.33 ± 0.09		2.20 ± 0.07	-10.0 to $-8.4\ ^a$	-9.3 to $-8.4\ ^a$
HD 36512			-6.22 ± 0.06	2466 ± 344	<-7.2 to <-6.7	<-7.1 to <-6.6
HD 36960			-7.79 ± 0.07	159 ± 23	<-7.8 to <-7.3	<-7.8 to <-7.3
HD 38771	-6.05 [1], $-5.92^{+0.11}_{-0.07}$ [2]	-6.80 ± 0.08	-8.01 ± 0.07	252 ± 21	-7.7 to -7.2	-7.6 to -7.2
HD 44743		-7.33 ± 0.08	-8.55 ± 0.08	26.1 ± 0.8	<-8.6 to <-8.2	<-8.5 to <-8.0
HD 52089	-9 [3], -8 [4]	-7.53 ± 0.08		28.9 ± 0.8	-8.3 to -7.8	-8.3 to -7.8
HD 63922			-6.93 ± 0.06	460 ± 16	<-7.6 to <-7.1	<-7.6 to <-7.1
HD 79351		-8.71 ± 0.10		25.9 ± 0.6	-9.5 to $-7.9\ ^a$	-8.7 to $-7.8\ ^a$
HD 144217			-8.04 ± 0.06	59.1 ± 2.3	<-8.1 to <-7.7	<-8.1 to <-7.6
HD 158926		-6.50 ± 0.08		19.8 ± 1.5	-8.2 to -7.7	-8.1 to -7.7

Notes. The second column lists the mass-loss rate value derived in recent optical studies using atmosphere models: [1]: Crowther et al. (2006), [2]: Searle et al. (2008), [3]: Hamann et al. (priv. comm. with Fossati et al. 2015), [4]: Najarro et al. (1996). The third and fourth columns provide the mass-loss estimates by Vink et al. (2001) when the adopted $T_{\rm eff}$ is in the range 12500 – 22500 K (cool side of the bi-stability jump) and 27500 − 50000 K (hot side of the bi-stability jump), respectively. When the adopted $T_{\rm eff}$ (Table 1) is in the range 22500 − 27500 K (in the bi-stability jump), mass-loss estimates for both the cool and hot sides of the bi-stability jump are provided. The fifth column yields the total X-ray emission measures, estimated from the normalisation factors of the spectral fittings (Table 3). The last two columns provide the mass-loss rates predicted by Eq. 1 of Huenemoerder et al. (2012, with b=0.97) and the formula on p. 1868 of Cohen et al. (2008), respectively. In these columns only a range of mass-loss rates are given: the lower values correspond to a terminal wind velocity of 500 km s^{-1}, while the highest values correspond to a terminal wind velocity of 1500 km s^{-1}. ^{a}: These values were derived assuming R_{fir} = 1 to 7 $R_\star$, in line with the formation radii derived in Sect. 3.1.

The abundances of our sample stars derived from our X-ray fits are listed in Table 3 and those determined in optical studies from the literature are listed in Table 5. Figure 2 provides a graphical comparison for the main elements (N, O, and Fe) for the stars in common. Except for the high O enrichment derived in X-rays for HD 36960, which is not confirmed in the optical domain, the agreement between the derived abundances is fair (within 3σ in the worst cases). Indeed, the formal fit errors are known to be smaller than the actual ones (e.g., de Plaa et al. 2017, submitted). An example of disagreement can also be found in the subsolar abundances found by Cohen et al. (2008) and Zhekov & Palla (2007) for HD 111123: despite analysing the same dataset, Zhekov & Palla (2007) abundances of O, Ne, and Mg are a factor of two smaller than those of Cohen et al. (2008) – the origin of this discrepancy is unknown. We also note disagreements between optical studies, e.g., for HD 38771 or HD 52089, showing that improvements are required there too. In any case, not many comparisons between X-ray and optical abundances can be found in the literature. For HD 205021, Favata et al. (2009) derived O, Si, and Fe abundances which are depleted compared to photospheric abundances. Nazé & Rauw (2008) confirmed the depletion in C and O of HD 93030 as well as its enrichment in N reported in the optical domain by Hubrig et al. (2008). In fact, X-ray determinations would benefit from higher S/N data – e.g., the X-ray abundances of HD 66811, derived from very high quality spectra, could be better constrained (Hervé et al. 2013).

4. Lightcurves

We have finally examined the temporal evolution of the X-ray brightnesses of our targets. The lightcurves in the 0.3–10. keV energy band are shown in Fig. 3. We first performed χ^2 tests for three different null hypotheses (constancy, linear variation, quadratic variation). The improvement of the χ^2 when increasing the number of parameters in the model (e.g., linear trend vs constancy) was also determined by means of Snedecor F tests (nested models, see Sect. 12.2.5 in Lindgren 1976). As threshold for significance, we used 1% and we consider that a threshold of 10% indicates only marginal evidence. This yields the following results.

Two stars are clearly compatible with constancy: HD 34816 and HD 38771. For the latter, only the ACIS-S lightcurve with 1ks bins could be analysed, as there are not enough counts in each bin for a meaningful χ^2 test of the 100s-binned lighcurves. The lightcurves of each *Chandra* exposure were also analysed using the appropriate CIAO tool[4], and the variability index was found to be zero ("definitely not variable") for ObsID 9939, 10839, and 10846, and 2 ("probably not variable") for ObsID 9940, which confirms the χ^2 results. The combination of the four individual lightcurves was also tested by χ^2 tests, with the same null result as for individual lightcurves.

Four stars reveal marginal variability (i.e., presence of trends and/or rejection of constancy at the 1–10% level): HD 35468, HD 44743, HD 63922, and HD 144217. HD 35468 is detected to be variable for the MOS2 lightcurves, but it is only marginally variable for pn and it appears compatible with constancy in MOS1. For HD 44743, trends provide better fits for pn data in Rev. 1509 and for MOS1 and pn data for Rev. 2814. A marginal variability is further detected for all instruments in Rev. 2814, and when the two datasets are combined. The 100s-bin lightcurves of HD 144217 are better fitted by trends.

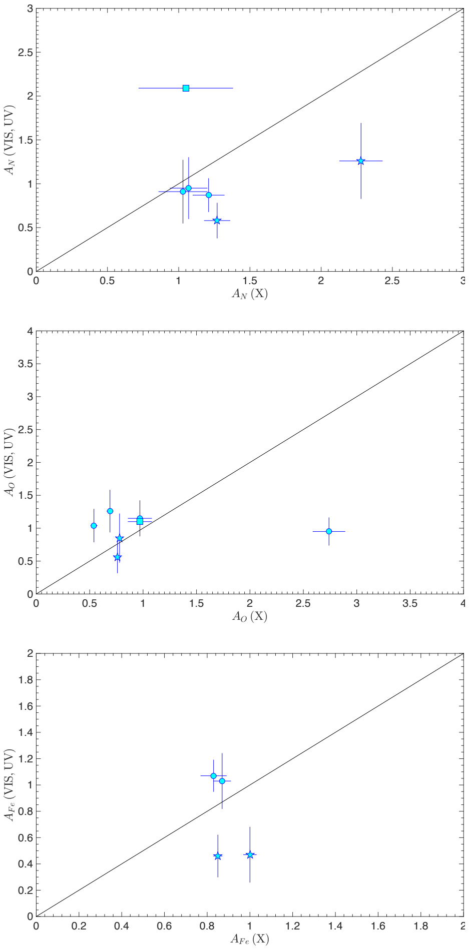

Fig. 2. Comparison between our N (upper panel), O (middle panel), and Fe (lower panel) abundance estimates and recent literature values obtained by optical studies. Circles, triangles, diamonds, squares, and star symbols represent values obtained by Nieva & Przybilla (2012), Venn et al. (2002), Valdes et al. (2004), Searle et al. (2008), and Morel et al. (2006, 2008), respectively.

Five stars exhibit a clear variability (significance level of <1%): HD 36512, HD 36960, HD 52089, HD 79351, and HD 158926. HD 36512 is detected to be variable for the 100s-bin pn lightcurve, and a trend provides a clearly better fit than a constant for MOS2 and pn. HD 36960 appears significantly variable for all instruments, with trends – especially parabolic ones – always providing better fits. Indeed, the lightcurve presents a large oscillation, with maxima at the beginning and end of the exposure, and a minimum in-between. This change in bright-

---

[4] http://cxc.harvard.edu/ciao/threads/variable/index.html#glvary

Table 5. Stellar abundances from optical studies.

	HD 34816	HD 35468	HD 36512	HD 36960	HD 38771
A_C	0.68 [1], 0.89±0.15 [2]	0.71 [3], 0.74 [1]	0.83±0.28 [2], 0.85±0.31 [7], 0.89±0.31 [6]	0.74±0.18 [9], 0.83±0.20 [2]	0.11 [10], 0.20 [11]
A_N	0.68 [1], 0.95±0.35 [2]	1.82 [3], 2.00 [1]	0.89±0.31 [6], 0.91±0.36 [2], 1.00±0.26 [7]	0.76±0.16 [9], 0.78±0.22 [2]	0.35±0.13, 2.69±0.92 [10], 2.09 [11]
A_O	1.04±0.25 [2], 1.15 [1]		1.05±0.34 [8], 1.06±0.41 [6], 1.15±0.27 [2]	0.95±0.21 [2], 1.07±0.21 [9]	1.10 [11], 1.29±0.38 [10]
A_N/A_C	1.00 [1], 1.07±0.43 [2]	2.56 [3], 2.70 [1]	1.10±0.57 [2], 1.00±0.49 [6], 1.18±0.53 [7]	0.94±0.35 [2], 1.03±0.33 [9]	3.18±1.18;24.5±8.4 [10], 10.45 [11]
A_N/A_O	0.59 [1], 0.91±0.40 [2]		0.84±0.44 [6], 0.79±0.36 [2]	0.71±0.20 [9], 0.82±0.39 [2]	0.27±0.13;2.09±0.94 [10], 1.90 [11]
A_{Ne}	1.77±0.16 [2]	1.12±0.26 [4]	1.52±0.43 [2], 1.70±0.55 [7]	1.59±0.54 [2]	
A_{Fe}	1.10±0.20 [2]	0.83 [5]	1.07±0.12 [2], 1.12±0.12 [7]	0.96±0.22 [2]	
A_O/A_{Fe}	0.95±0.28 [2]		1.07±0.28 [2]	0.99±0.32 [2]	
A_{Mg}					0.40 [10]
A_{Si}					0.45 [10]

	HD 44743	HD 52089	HD 63922
A_C	0.54±0.15 [12], 0.60 [1], 0.63 [3], 0.78±0.20 [14]	0.46±0.14 [12], 0.74±0.15 [14]	0.74±0.15 [2]
A_N	0.58±0.20 [12], 0.76 [1], 0.79 [3], 0.83±0.24 [14]	0.81 [15], 1.26±0.43 [12], 2.15±0.42 [14]	0.87±0.19 [2]
A_O	0.85±0.37 [12], 1.15 [1], 1.23 [3], 1.10±0.28 [14]	0.56±0.24 [12], 1.02±0.30 [14]	1.26±0.32 [2]
A_N/A_C	1.07±0.48 [12], 1.27 [1], 1.25 [3], 1.06±0.41 [14]	2.74±1.25 [12], 2.91±0.82 [14]	1.18±0.35 [2]
A_N/A_O	0.68±0.38 [12], 0.66 [1], 0.64 [3], 0.75±0.29 [14]	2.25±1.23 [12], 2.11±0.74 [14]	0.69±0.23 [2]
A_{Ne}	0.91±0.34 [4]	0.85±0.24 [4]	1.37±0.39 [2]
A_{Fe}	0.47±0.21 [13]	0.46±0.16 [12]	1.03±0.21 [2]
A_O/A_{Fe}		1.22±0.67 [12]	1.22±0.40 [2]

Notes. Abundances are in number, with respect to Hydrogen, and with respect to solar values, as for the X-ray ones in Table 3. References: [1] Gies & Lambert (1992), [2] Nieva & Przybilla (2012), [3] Venn et al. (2002), [4] Morel & Butler (2008), [5] Valdes et al. (2004), [6] Martins et al. (2015), [7] Nieva & Simón-Díaz (2011), [8] Simón-Díaz (2010), [9] Kilian (1992), [10] Lennon et al. (1991), [11] Searle et al. (2008), [12] Morel et al. (2008), [13] Morel et al. (2006), [14] Fossati et al. (2015), [15] Fraser et al. (2010).

ness is only marginally accompanied by a change in hardness (see Fig. 4), however. HD 52089 appears variable in pn data, and a trend provides a clearly better fit than a constant. HD 79351 appears significantly variable for all instruments. Indeed, the lightcurve steedily increase at first, then slightly decrease, and finally present a flare-like activity. Furthermore, when it brightens, HD 79351 also becomes harder (see Fig. 4). HD 158926 is detected to be significantly variable for all instruments when considering 100s bins, with trends providing a better fit to pn data.

Next, we applied period search algorithms (Heck et al. 1985; Graham et al. 2013) to the lightcurves with 100s bins, for each EPIC camera, but no peak stands out both clearly and coherently (i.e., for all instruments) from the periodograms.

Two types of specific timescales exist for our targets: orbital periods and pulsation periods. The former ones are usually long compared to the exposure length (5.9 d for HD 158926, Berghöfer et al. 2000; 6.745 d for HD 79351, Buscombe & Morris 1960; 6.83 d for HD144217, Holmgren et al. 1997), hence cannot be tested with the current dataset. However, we may still examine whether binarity may explain the flare-like behaviour of HD 79351. Indeed, Buscombe & Morris (1960) derived a mass function of 0.00663565 for this system: assuming the mass taken from Cox (2002, $\sim 10\,M_{\odot}$) for the primary star, we find a minimum mass of $\sim 0.7 M_{\odot}$ for the secondary star. It may thus be a PMS star, which could have underwent a flare during the observation. Indeed, the average X-ray luminosity of HD 79351 is $\sim 3{\times}10^{30}$ erg s^{-1} (Table 3) and its brightness increased by less than a factor of 2 during the flare (Fig. 3), which remains compatible with PMS flaring luminosities (Güdel & Nazé 2009). However, a better knowledge of the HD 79351 system is needed before its X-ray properties can be fully understood.

Regarding the latter timescales, it should be noted that two targets are known β Cephei: HD 44743 (3 closely-spaced frequencies with the strongest one at $f = 3.9793 \pm 0.0001\,\mathrm{d}^{-1}$, Shobbrook et al. 2006) and HD 158926 (dominant frequency at $f = 4.679410 \pm 0.000013\,\mathrm{d}^{-1}$, Uytterhoeven et al. 2004b). For HD 44743, a peak exists close to that dominant timescale in the periodogram of EPIC data taken in Rev. 2814 (top of Fig. 5): its amplitude is not very high but it is present and in fact, if the background flares are not discarded hence more data are available, it appears much more clearly. In this context, it should be remembered that the known pulsators HD 205021 (β Cep), HD 122451 (β Cen), HD 116658 (Spica), and HD 160578 (κ Sco) do not display X-ray variations linked to their pulsations (Raassen et al. 2005; Miller 2007; Favata et al. 2009; Oskinova et al. 2015), but HD 46328 (ξ^1 CMa) does (Oskinova et al. 2014; Nazé 2015) and β Cru may (Cohen et al. 2008, though see refutation in Oskinova et al. 2015). Therefore, even if periodograms do not show very strong peaks at these periods, we performed a folding using these known frequencies as a last check (bottom of Fig. 5). For HD 44743, the presence of a modulation is clearly confirmed, with a peak-to-peak amplitude of 14% (corresponding to 5 times the error on individual bins); it is not accompanied by significant hardness changes, but neither did HD 46328. The case of HD 158926 appears less convincing as the changes are not coherent from one instrument to the other, and the combination of all three EPIC instruments only leads to a slight modulation (the peak-to-peak variation is only 3σ), clearly calling for confirmation before detection can be claimed.

As a final exercise, we folded our before best-fit spectral models (Table 3) through the *ROSAT* response matrices, and derived the equivalent *ROSAT* count rates of our targets (reported in the last line of Table 3). Comparing to values tabulated by Berghöfer et al. (1996), we find negligible ($< 3\sigma$) differences for all but three targets: HD 35468 and HD 158926 have fainted by a factor of two, while HD 36512 has brightened by 50%. These three stars thus appear variable on both long and short timescales. While this could probably be linked to binarity for HD 158926, there is no clear explanation for the other two. A monitoring of all three stars will then be needed to better understand their behaviour, in particular searching for a putative periodicity.

5. Discussion and Conclusion

In this paper, we analysed the X-ray data of 11 early B-stars. Combined with 8 other B-stars previously analysed, our results provide the first X-ray luminosity-limited survey at high-resolution, thereby constituting a legacy project.

In this work, we have performed line-by-line fitting, global spectral fitting (with temperatures, abundances, and brightnesses as free parameters), and variability analyses.

In many ways, our results confirm previous studies: B-stars typically display soft and moderately intense X-ray emissions, their X-ray lines appear rather narrow and unshifted, and the X-ray emission arises at a few stellar radii from the photospheres.

The abundances we derived are in fair agreement with those found in optical data, taking errors into account. The X-ray brightnesses could be used to evaluate the total quantity of hot material surrounding the stars. Compared to expected mass-loss rates or values derived from the analysis of optical data, we find that at least in half of the cases, the "hot" mass-loss constitutes only a small fraction of the wind.

A quarter of our sample (3/11) display a high-energy tail and half of our targets (6/11) display significant variations on short or long timescales. These properties are not mutually exclusive as two targets (HD 36960 and HD 79351) combine both specificities. Three out of the four binaries present these peculiarities, which thus appear not restricted to, but more common in, binaries.

Finally, we have also analysed in detail the temporal behaviour of two β Cephei pulsators. HD 158926 presents flux changes on both short and long timescales, but they cannot be undoubtly assigned to the pulsational activity. On the contrary, HD 44743 appears marginally variable in χ^2 tests, but folding its lightcurve clearly reveals coherent variations with the optical period. This makes the star the second secure case of X-ray pulsator after HD 46328.

Much remains to be done: longer monitoring of the variable sources and more precise estimates of the parameters (formation radii, abundances). In this context, the advent of the Advanced Telescope for High-ENergy Astrophysics/X-ray Integral Field Unit (ATHENA/X-IFU) will certainly provide higher quality high-resolution spectra of B-stars, which will further advance our understanding of their X-ray properties.

Acknowledgements. We thank Thierry Morel and Gregor Rauw for their useful comments. We acknowledge support from the Fonds National de la Recherche Scientifique (Belgium), the Communauté Française de Belgique, the PRODEX XMM-*Newton* contract, and an ARC grant for concerted research actions financed by the French community of Belgium (Wallonia-Brussels Federation). ADS and CDS were used in preparing this document.

References

Asplund, M., Grevesse, N., Sauval, A.J., & Scott, P. 2009, ARA&A, 47, 481
Bagnulo, S., Landstreet, J. D., Mason, E., et al. 2006, A&A, 450, 777
Berghöfer, T. W., Schmitt, J. H. M. M., & Cassinelli, J. P. 1996, A&AS, 118, 481

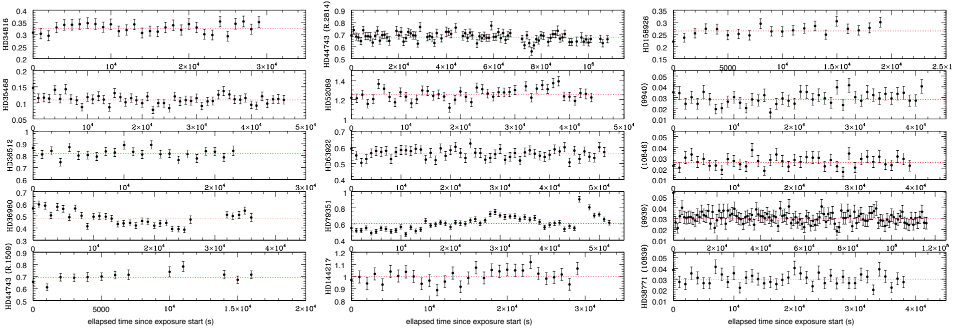

Fig. 3. Lightcurves in units cts s^{-1} from low-resolution data (EPIC-pn, ACIS-S 0th order) for the different targets in the 0.3–10.0 keV energy band and with 1ks bins. The weighted average is shown by the dotted red line.

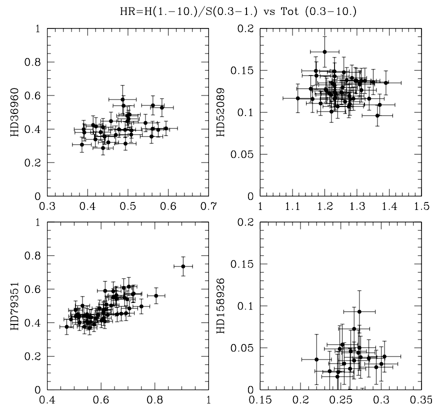

Fig. 4. Hardness ratios as a function of the count rates, in the 0.3–10.0 keV energy band and in units cts s^{-1}, for four clearly variable sources (for EPIC-pn and for 1ks bins). The hardness ratios are defined as the ratios between count rates in the 1.0–10.0 keV and 0.3–1.0 keV energy bands. The correlation coefficients amount to 40% for HD 36960, -9% for HD 52089, 81% for HD 79351, and 5% for HD 158926.

Berghöfer, T. W., Vennes, S., & Dupuis, J. 2000, ApJ, 538, 854
Blumenthal, G. R., Drake, G. W. F., & Tucker, W. H. 1972, ApJ, 172, 205
Buscombe, W., & Morris, P. M. 1960, MNRAS, 121, 263
Bychkov, V. D., Bychkova, L. V., & Madej, J. 2009, MNRAS, 394, 1338
Cohen, D. H., Cassinelli, J. P., & MacFarlane, J. J. 1997, ApJ, 487, 867
Cohen, D. H., de Messières, G. E., MacFarlane, J. J., et al. 2003, ApJ, 586, 495
Cohen, D. H., Kuhn, M. A., Gagné, M., Jensen, E. L. N., & Miller, N. A. 2008, MNRAS, 386, 1855
Cox, A. N. 2002, Allen's Astrophysical Quantities, fourth edition, Springer-AIP Press (New York)
Crowther, P. A., Lennon, D. J., & Walborn, N. R. 2006, A&A, 446, 279
Diplas, A., & Savage, B. D. 1994, ApJS, 93, 211
Favata, F., Neiner, C., Testa, P., Hussain, G., & Sanz-Forcada, J. 2009, A&A, 495, 217
Fossati, L., Castro, N., Morel, T., et al. 2015, A&A, 574, A20
Fraser, M., Dufton, P. L., Hunter, I., & Ryans, R. S. I. 2010, MNRAS, 404, 1306
Gies, D. R., & Lambert, D. L. 1992, ApJ, 387, 673
Gorski, M., & Ignace, R. 2010, Journal of the Southeastern Association for Research in Astronomy, 4, 12
Graham, M. J., Drake, A. J., Djorgovski, S. G., Mahabal, A. A., & Donalek, C. 2013, MNRAS, 434, 2629
Grunhut, J. H., Wade, G. A., Neiner, C., et al. 2017, MNRAS, 465, 2432
Gudennavar, S. B., Bubbly, S. G., Preethi, K., & Murthy, J. 2012, ApJS, 199, 8
Güdel, M., & Nazé, Y. 2009, A&A Rev., 17, 309
Heck, A., Manfroid, J., & Mersch, G. 1985, A&AS, 59, 63
Hervé, A., Rauw, G., & Nazé, Y. 2013, A&A, 551, A83
Holberg, J. B., Oswalt, T. D., Sion, E. M., Barstow, M. A., & Burleigh, M. R. 2013, MNRAS, 435, 2077
Holmgren, D., Hadrava, P., Harmanec, P., Koubsky, P., & Kubat, J. 1997, A&A, 322, 565
Hubrig, S., Yudin, R. V., Pogodin, M., Schöller, M., & Peters, G. J. 2007, Astronomische Nachrichten, 328, 1133
Hubrig, S., Briquet, M., Morel, T., et al. 2008, A&A, 488, 287
Huenemoerder, D. P., Oskinova, L. M., Ignace, R., et al. 2012, ApJ, 756, L34
Hunter, I., Brott, I., Langer, N., et al. 2009, A&A, 496, 841
Katyal, N., Gupta, R., & Vaidya, D. B. 2013, PASP, 125, 1443
Kilian, J. 1992, A&A, 262, 171
Lanz, T., & Hubeny, I. 2003, ApJS, 146, 417
Lanz, T., & Hubeny, I. 2007, ApJS, 169, 83
Lennon, D. J., Becker, S. T., Butler, K., et al. 1991, A&A, 252, 498
Lennon, D. J., Dufton, P. L., & Fitzsimmons, A. 1992, A&AS, 94, 569
Leutenegger, M. A., Paerels, F. B. S., Kahn, S. M., & Cohen, D. H. 2006, ApJ, 650, 1096
Lindgren, B.W. 1976, Statistical theory - third edition, McMillan Pub. (New York)
Lopes de Oliveira, R., Smith, M. A., & Motch, C. 2010, A&A, 512, A22
Martins, F., Hervé, A., Bouret, J.-C., et al. 2015, A&A, 575, A34
Macfarlane, J. J., Cassinelli, J. P., Welsh, B. Y., et al. 1991, ApJ, 380, 564
Mewe, R., Raassen, A. J. J., Cassinelli, J. P., et al. 2003, A&A, 398, 203
Miller, N. A. 2007, Active OB-Stars: Laboratories for Stellare and Circumstellar Physics, 361, 77
Morel, T., & Butler, K. 2008, A&A, 487, 307
Morel, T., Butler, K., Aerts, C., Neiner, C., & Briquet, M. 2006, A&A, 457, 651
Morel, T., Hubrig, S., & Briquet, M. 2008, A&A, 481, 453
Najarro, F., Kudritzki, R. P., Cassinelli, J. P., Stahl, O., & Hillier, D. J. 1996, A&A, 306, 892
Nazé, Y., & Rauw, G. 2008, A&A, 490, 801
Nazé, Y. 2009, A&A, 506, 1055
Nazé, Y., Broos, P. S., Oskinova, L., et al. 2011, ApJS, 194, 7
Nazé, Y., Zhekov, S. A., & Walborn, N. R. 2012, ApJ, 746, 142
Nazé, Y., Petit, V., Rinbrand, M., et al. 2014, ApJS, 215, 10 (erratum 2016, ApJS, 224, 13)
Nazé, Y. 2015, IAUS New Windows on Massive Stars, 307, 455
Neiner, C., Oksala, M. E., Georgy, C., et al. 2017, arXiv:1707.00560
Nieva, M.-F. 2013, A&A, 550, A26
Nieva, M.-F., & Simón-Díaz, S. 2011, A&A, 532, A2
Nieva, M.-F., & Przybilla, N. 2012, A&A, 539, A143
Nieva, M.-F., & Przybilla, N. 2014, A&A, 566, A7
Oskinova, L. M., Nazé, Y., Todt, H., et al. 2014, Nature Communications, 5, 4024
Oskinova, L. M., Todt, H., Huenemoerder, D. P., et al. 2015, A&A, 577, A32
Owocki, S. P., & Cohen, D. H. 2001, ApJ, 559, 1108
Porquet, D., Mewe, R., Dubau, J., Raassen, A. J. J., & Kaastra, J. S. 2001, A&A, 376, 1113

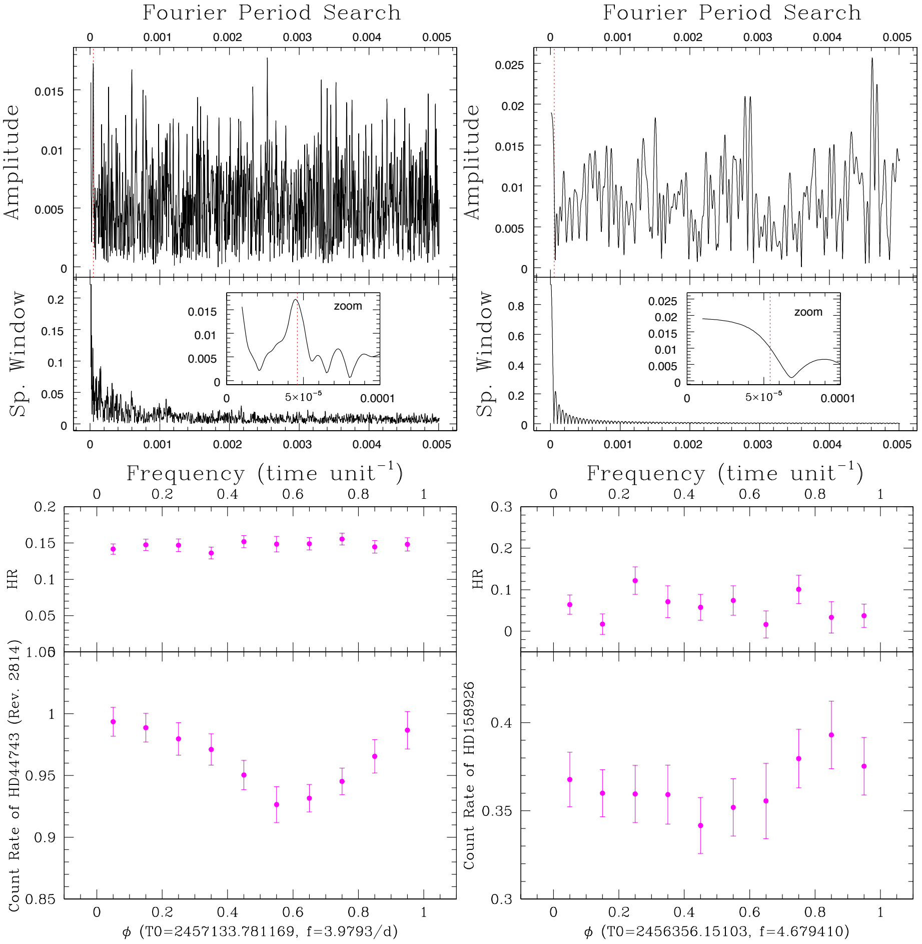

Fig. 5. *Top:* Periodograms based on the pn lightcurves with 100s bins of HD 44743 (Rev. 2814) and HD 158926, along with their associated spectral window. An inset provides a zoom on the lowest frequencies, with the β Cephei pulsation frequencies shown by the red dotted lines. *Bottom:* Lightcurves of HD 44743 (middle, for Rev. 2814) and HD158926 (right) folded using their dominant β Cephei frequency (see text). T_0 are arbitrary, they were chosen to correspond to the start time of the XMM-*Newton* observations (Table 1). The count rates corresponds to EPIC values (i.e., the addition of MOS1, MOS2, and pn count rates) while the hardness ratios correspond to means (i.e., [HR(MOS1)+HR(MOS2)+HR(pn)]/3). The phasing was here performed on lightcurves with 1ks bins – the 100s-binned lightcurves provide similar but slightly noisier results.

Raassen, A. J. J., Cassinelli, J. P., Miller, N. A., Mewe, R., & Tepedelenlioğlu, E. 2005, A&A, 437, 599
Rauw, G., Nazé, Y., Wright, N. J., et al. 2015, ApJS, 221, 1
Sana, H., Rauw, G., Nazé, Y., Gosset, E., & Vreux, J.-M. 2006, MNRAS, 372, 661
Searle, S. C., Prinja, R. K., Massa, D., & Ryans, R. 2008, A&A, 481, 777
Simón-Díaz, S. 2010, A&A, 510, A22
Shobbrook, R. R., Handler, G., Lorenz, D., & Mogorosi, D. 2006, MNRAS, 369, 171
Slettebak, A. 1982, ApJS, 50, 55
Smith, M. A., Lopes de Oliveira, R., & Motch, C. 2016, Advances in Space Research, 58, 782
Touhami, Y., Richardson, N. D., Gies, D. R., et al. 2010, PASP, 122, 379
Uytterhoeven, K., Willems, B., Lefever, K., et al. 2004a, A&A, 427, 581
Uytterhoeven, K., Telting, J. H., Aerts, C., & Willems, B. 2004b, A&A, 427, 593
Valdes, F., Gupta, R., Rose, J. A., Singh, H. P., & Bell, D. J. 2004, ApJS, 152, 251
van Leeuwen, F. 2007, A&A, 474, 653
Venn, K. A., Brooks, A. M., Lambert, D. L., et al. 2002, ApJ, 565, 571
Vink, J. S., de Koter, A., & Lamers, H. J. G. L. M. 2001, A&A, 369, 574
Walborn, N. R., Nichols, J. S., & Waldron, W. L. 2009, ApJ, 703, 633
Waldron, W. L., & Cassinelli, J. P. 2007, ApJ, 668, 456 (+erratum ApJ, 680, 1595)
Zhekov, S. A., & Palla, F. 2007, MNRAS, 382, 1124

4

CONCLUSIONS AND PERSPECTIVES

"When I have a terrible need of – shall I say the word — of religion, then I go out at night and paint the stars."

— Vincent van Gogh

This chapter concludes by summarising our findings and pointing future investigation alleys to further improve our knowledge of massive stars.

Massive stars, whose spectral types are O and B, are the true "cosmic engines" of our Universe. They are the most luminous stars and can ionise the interstellar medium through their strong ultraviolet radiation. Besides, they eject considerable amounts of material throughout their life, which influences their evolutionary path, the formation of neighbouring stars, the structure of the interstellar medium, and the chemical enrichment of their surroundings. These stars produce helium in their core from hydrogen though the CNO cycle. Due to a limiting reaction in this cycle, an excess of nitrogen atoms and a depletion of carbon or oxygen (depending on the initial stellar mass) atoms are generated in the stellar core. In parallel, these stars have high rotational velocities, typically more than a hundred times the Sun's rotational velocity. Such fast rotation can be acquired during the formation process or following an interaction with a companion. The theory of rotational mixing predicts that the transport of elements from the core to the surface increases with the rotational velocity of the star, so that the fastest rotating stars should naturally exhibit the largest enhancement in nitrogen and depletion in carbon/oxygen at their surface. A way to test this basic prediction is to study the chemical composition of the fastest rotators.

The work presented in this thesis aims at improving our understanding of the abundances of massive stars thanks to a multiwavelength study. It was split into two parts. The first part made use of observations taken in the optical domain to study the abundances of fast-rotating massive stars, a population that was rarely studied up to now. The starting point of this study was the discovery, through the VLT-FLAMES Survey of Massive Stars, of fast rotators exhibiting an unenriched nitrogen composition at their surface. This finding, that does not appear to be due to selection effects affecting the survey, is at odds with predictions from single-star evolutionary models including rotation. However, two aspects hamper a clear interpretation of these observations. First, the derived nitrogen abundances are frequently upper limits and are based on only a few lines. Furthermore, no or little information is available for other key elements (e.g., helium, carbon) which should also be affected by the rotational mixing. Finally, the binary status of the studied stars is generally unknown. Comparing the observational data with the predictions of evolutionary models for single stars could hence be misleading. Any claims about the (in)ability of rotation-related phenomena to reproduce the data without knowing the multiplicity status should thus be regarded as premature. Indeed, mass-transfer processes in massive stars may be much more prevalent than initially thought and such phenomena may dramatically affect the angular momentum history, as well as changing the surface abundances in some cases. In particular, mass transfer can in some cases lead to stars rotating at speeds comparable to breakup velocity, but which would appear roughly normal in terms of surface abundances. Our project therefore combines, for the first time, a detailed abundance analysis with a radial-velocity study. It considers a sample of 40 bright, OB stars from our Galaxy which have projected rotational velocities above 200 km s^{-1}. Our study relies on high-resolution spectra taken from instrument archives or acquired thanks to dedicated observational compaigns. We first determined the radial velocities of the targets by using cross-correlation techniques, and statistical tests were then applied to determine whether radial velocities vary. We also employed period-search techniques and derived orbital solutions whenever possible. This radial-velocity study reveals an important fraction ($\sim$ 40%) of binaries or candidate binaries within our sample, confirming previous findings of a large multiplicity fraction amongst massive stars. Then, state-of-the-art model atmosphere codes DETAIL/SURFACE or CMFGEN were used (depending on the spectral type of our targets) to derive stellar parameters, i.e., the effective temperatures and surface gravities, and the helium, carbon, nitrogen, and oxygen surface abundances of our sample stars. Our abundance study reveals a correlation between the helium and nitrogen abundances of our sample stars, which is predicted by the rotational mixing theory. What also emerges from our analysis is that a non-negligible fraction ($\sim$ 10 – 20%) of our targets shows no enhancement of the [N/O] abundance ratio (thus no nitrogen enrichment at the stellar surface), confirming the results found within the framework of the VLT-FLAMES Survey of Massive Stars. In order to interpret our results, we compared our observational data to predictions from single-star evolutionary models (from the Bonn, Geneva, and Liège groups) and from binary-star models (considering mass-transfer episodes or merging events). To this aim, we use [N/O] abundance ratios, since it is the indicator the least affected by any possible zero-point difference between the actual initial abundances of the observed stars and the initial abundances of the models, while being a very sensitive indicator of rotational mixing. We found that single-star models can reproduce the atmospheric parameters and surface abundances of half of our sample, whatever the multiplicity status of our targets. In fact, there is no difference in abundance patterns between single and multiple stars. However, we also found an unexpected overabundance of helium for most of our targets. Modifying the diffusion coefficient in single-star models could not lead to a simultaneous agreement of both helium abundances and [N/O] abundance ratios. Furthermore, we found that models of non-rotating mergers cannot explain the [N/O] abundance ratios of our higher-mass single stars as well as the helium abundances of our lower-mass single stars. Models that take fast semi-convective mixing into account for stars that underwent a mass and angular momentum transfer through a Roche Lobe overflow can reproduce the [N/O] abundance ratios of the majority of our targets, as well as the helium abundances of some of the most helium-enriched targets, but cannot reproduce the little helium enrichment combined to large [N/O] values of some stars. Therefore, these comparisons show that some features of massive stars cannot be explained by single- or binary-star models, and suggest that current models lack some physical ingredients.

Future work should aim at studying fast rotators of the Magellanic Clouds. This will allow us not only to increase the sample of fast rotators with well-determined metal content but also to study cases for which the rotational mixing effects should be larger than in the Galaxy (Sect. 1.1.2.3), providing another sensitive test. There are, however, some observational difficulties since these extragalactic stars are much fainter than Galactic ones. Therefore, the use of telescopes with large light-collecting area is required to obtain high-quality data for such a study. An example of such telescopes is the Extremely Large Telescope (ELT) that will use a 40m-class primary mirror. Compared to the 8m-class VLT telescopes, the exposure times for observations of fast rotators from the Magellanic Clouds should be significantly reduced (more than 20 times), which would greatly ease the acquisition of high-resolution data and multi-epoch observations in order to probe the RV evolution of these stars, hence their multiplicity status. The largest projects that aimed at the study of massive stars in the MCs found 66 fast-rotating stars (with a projected rotational velocity larger than 200 km s^{-1}) earlier than B0.5 in the SMC clusters NGC 330, NGC 346 (Hunter et al. 2008), as well as in the clusters NGC 2004, NGC 2060 and the regions 30 Dor and N 11 of the LMC (Hunter et al. 2008; Ramírez-Agudelo et al. 2013). The detailed abundance patterns of these stars should be obtained and confronted to our results found for Galactic stars.

Abundance studies would also benefit from access to a UV spectroscopic mission – such as the proposed Arago or Pollux missions. Indeed, not only UV provides access to strong resonance lines, but it gives access to other elements. For example, studying boron would be very interesting because that element is easily destroyed, at much lower temperatures than the ones required for the CNO cycle, by warm protons and even mixing in shallow layers can affect the observed abundance at the surface. Moreover, this depletion in boron at the surface is expected to happen before any enhancement of surface nitrogen abundance.

In parallel, improvements in evolutionary models should be performed to understand why massive stars exhibit an unexpected common overabundance in helium at their surface.

The second part of this thesis aimed at studying the X-ray properties of early B-stars. The intrinsic X-ray emission from massive stars directly arises from their winds. Indeed, the wind driving process is intrinsically unstable, giving rise to strong shocks hence to X-ray emission. The shape and variability of the X-ray lines therefore provide a direct diagnostics of the wind properties, improving their knowledge as well as constraining their abundances which reflect the photospheric ones. We studied 11 early B-stars thanks to two X-ray facilities, doubling the number of B-stars analysed at high-resolution in the X-ray domain. Individual line analyses as well as global spectral fittings were performed. Our study allowed us to confirm results from previous studies. We indeed found that the X-ray lines of early B-stars are emitted at a few stellar radii (2 – 7 $R_{\rm star}$) from the photosphere. Those lines, which are narrow and unshifted are born in a warm plasma (of typically 0.2 – 0.6 keV), with only few cases showing the presence of hotter plasma (of 1.6 – 4.4 keV). We also derived abundances in the X-ray domain that are in fair agreement with the ones of the photosphere that are derived in the optical domain. Finally, the X-ray emission appears to vary for half of our sample stars on short and/or long timescales, this latter finding being not initially expected. In this context, we found that the X-ray variability of HD 44743 can be undoubtedly associated to the pulsational activity of this β Cephei star, making it the second case only of X-ray "pulsator" after HD 46328. Three out of the four binaries of our sample combine variations with the presence of a hot component. In those cases, the emission of a companion or the emission associated to an interaction with it may actually contaminate the recorded X-rays. In particular, HD 79351 has a PMS star companion and its X-ray emission displays a quick rise followed by a slow decay and the luminosity of this flare is compatible with the ones of PMS stars.

The advent of the Advanced Telescope for High-energy Astrophysics/X-ray Integral Field Unit (ATHENA/X-IFU) will provide higher quality data that will undoubtedly improve our knowledge on the X-ray properties of massive stars. While the spectral resolution of ATHENA/X-IFU is expected to be similar to the ones of XMM-*Newton* and Chandra below 7 keV, its sensitivity should be significantly better than that of XMM-*Newton* and Chandra, as the mirror effective area of ATHENA/X-IFU is expected to be more than $\sim$ 3 and $\sim$ 27 larger than for XMM-*Newton* and Chandra, respectively. This eases the monitoring of X-ray emitters, hence will greatly help the study of massive stars winds and their properties (clumping, magnetic confinement, wind-wind collision, large-scale structures, ...).

5

ACKNOWLEDGEMENTS

First, I am thankful to the members of the jury who have accepted to read and review my work.

I would like to express my gratitude to the people that gave me support during the last four years.

I want to thank my supervisors, Drs Yaël Nazé and Thierry Morel, for guiding me and helping me from my Master work to the present achievement. I am so grateful for all the time that they granted me to answer my questions, for their patience, their advice, and for sharing their passion of massive stars with me.

I also want to express my thanks to Pr Gregor Rauw for giving me the opportunity to carry out a PhD project within the GAPHE group

I am very thankful to Alain Detal for the time spent in fixing my computer issues and to the stellar group of the Observatório Nacional of Rio de Janeiro, especially to Pr Simone Daflon, for their hospitality during my stay in Rio.

I am grateful to all the collaborators involved in my work, in particular Pr Norbert Langer for helping me clarifying some theoretical concepts.

I would like to say a particular thank to Françoise and Lindsay for answering to all my questions so kindly.

I am extremely thankful to Maxime for all the coffee breaks and for being such a good friend.

I can never thank Justine enough for supporting me in everyday life during the whole period of this thesis.

Finally, my heartfelt thanks go to Marie-Paule Adam and Romuald Lunebach for instilling in me the love of sciences.

BIBLIOGRAPHY

Abt, H. A., Levato, H., & Grosso, M. 2002, ApJ, **573**, 359

Aerts, C. 2015, Astronomische Nachrichten, **336**, 477

Ahmed, A., & Sigut, T. A. A. 2017, arXiv:1707.03009

Asplund, M., Grevesse, N., & Sauval, A. J. 2005, Cosmic Abundances as Records of Stellar Evolution and Nucleosynthesis, **336**, 25

Asplund, M., Grevesse, N., Sauval, A. J., & Scott, P. 2009, ARA&A, **47**, 481

Babel, J., & Montmerle, T. 1997a, ApJ, **485**, L29

Babel, J., & Montmerle, T. 1997, A&A, **323**, 121

Berghöfer, T. W., & Christian, D. J. 2002, A&A, **384**, 890

Bouret, J.-C., Hillier, D. J., Lanz, T., & Fullerton, A. W. 2012, A&A, **544**, A67

Braithwaite, J. 2006, A&A, **449**, 451

Brinkman, A. C., Behar, E., Güdel, M., et al. 2001, A&A, **365**, L324

Brott, I., de Mink, S. E., Cantiello, M., et al. 2011, A&A, **530**, A115

Butler, K., & Giddings, J. R. 1985, in Newsletter of Analysis of Astronomical Spectra, No. 9 (Univ. London)

Cantiello, M., Langer, N., Brott, I., et al. 2009, A&A, **499**, 279

Carciofi, A. C., Domiciano de Souza, A., Magalhães, A. M., Bjorkman, J. E., & Vakili, F. 2008, ApJ, **676**, L41

Cazorla, C., Morel, T., Nazé, Y., et al. 2017, A&A, **603**, A56 (Paper I)

Cazorla, C., Nazé, Y., Morel, T., Georgy, C., Godart, M., Langer, N. 2017b, A&A, accepted (Paper II)

Cazorla, C., Nazé, Y., Rauw, G., Morel, T. 2017c, A&A, submitted (Paper III)

Chaboyer, B., & Zahn, J.-P. 1992, A&A, **253**, 173

The Chandra Proposers' Observatory Guide, version 19.0, http://cxc.harvard.edu/proposer/POG/pdf/MPOG.pdf

Cherepashchuk, A. M., & Aslanov, A. A. 1984, Ap&SS, **102**, 97

Chieffi, A., & Limongi, M. 2013, ApJ, **764**, 21

Chlebowski, T., Harnden, F. R., Jr., & Sciortino, S. 1989, ApJ, **341**, 427

Collins, G. W., II 1963, ApJ, **138**, 1134

Conti, P. S., Leep, E. M., & Lorre, J. J. 1977, ApJ, **214**, 759

Cunha, K., Hubeny, I., & Lanz, T. 2006, ApJ, **647**, L143 de Koter, A. 2006, Stellar Evolution at Low Metallicity: Mass Loss, Explosions, Cosmology, **353**, 99

de Mink, S. E., Langer, N., Izzard, R. G., Sana, H., & de Koter, A. 2013, ApJ, **764**, 166

Decressin, T., Meynet, G., Charbonnel, C., Prantzos, N., & Ekström, S. 2007, A&A, **464**, 1029

Dufton, P. L., Langer, N., Dunstall, P. R., et al. 2013, A&A, **550**, A109

Domiciano de Souza, A., Kervella, P., Jankov, S., et al. 2003, A&A, **407**, L47

Eddington, A. S. 1925, The Observatory, **48**, 73

Eggleton, P. P. 1971, MNRAS, **151**, 351

Eggleton, P. P., & Kiseleva-Eggleton, L. 2002, ApJ, **575**, 461

Ekström, S., Meynet, G., Chiappini, C., Hirschi, R., & Maeder, A. 2008a, A&A, **489**, 685

Ekström, S., Meynet, G., Maeder, A., & Barblan, F. 2008b, A&A, **478**, 467

Ekström, S., Georgy, C., Eggenberger, P., et al. 2012, A&A, **537**, A146

Eldridge, J. J., & Stanway, E. R. 2009, MNRAS, **400**, 1019

Endal, A. S., & Sofia, S. 1978, ApJ, **220**, 279

ESA – XMM-Newton, Instruments, European Photon Imaging Camera (EPIC), http://sci.esa.int/science-e/www/object/index.cfm?fobjectid=31281&fbodylongid=774

ESA – XMM-Newton Science Operations Centre, XMM-Newton Users Handbook, Issue 2.14, 2016

Espinosa Lara, F., & Rieutord, M. 2011, A&A, **533**, A43

Evans, C. J., Smartt, S. J., Lee, J.-K., et al. 2005, A&A, **437**, 467

Evans, C. J., Taylor, W. D., Hénault-Brunet, V., et al. 2011, A&A, **530**, A108

Feldman, U. 1992, Phys. Scr, **46**, 202

Fliegner, J., Langer, N., & Venn, K. A. 1996, A&A, **308**, L13

Gabriel, A. H., & Jordan, C. 1969, MNRAS, **145**, 241

Garmany, C. D., Conti, P. S., & Massey, P. 1980, ApJ, **242**, 1063

Georgy, C., Ekström, S., Granada, A., et al. 2013a, A&A, **553**, A24

Georgy, C., Ekström, S., Eggenberger, P., et al. 2013b, A&A, **558**, A103

Glebbeek, E., Gaburov, E., Portegies Zwart, S., & Pols, O. R. 2013, MNRAS, **434**, 3497

Gray, D. F. 2005, "The Observation and Analysis of Stellar Photospheres", 3rd Edition, ISBN 0521851866, Cambridge University Press

Giddings, J. R. 1981, Ph.D. Thesis

Grevesse, N., & Sauval, A. J. 1998, Space Sci. Rev., **85**, 161

Grin, N. J., Ramírez-Agudelo, O. H., de Koter, A., et al. 2017, A&A, **600**, A82

Groh, J. H., Hillier, D. J., Damineli, A., et al. 2009, ApJ, **698**, 1698

Güdel, M., & Nazé, Y. 2009, A&A Rev., **17**, 309

Gudennavar, S. B., Bubbly, S. G., Preethi, K., & Murthy, J. 2012, ApJS, **199**, 8

Hamann, W.-R., & Gräfener, G. 2004, A&A, **427**, 697

Heger, A., & Langer, N. 2000a, ApJ, **544**, 1016

Heger, A., Langer, N., & Woosley, S. E. 2000b, ApJ, **528**, 368

Heger, A., Woosley, S. E., & Spruit, H. C. 2005, ApJ, **626**, 350

Hillier, D. J., & Miller, D. L. 1998, ApJ, **496**, 407

Hillier, D. J., & Lanz, T. 2001, Spectroscopic Challenges of Photoionized **247**, 343

Hirschi, R. 2007, A&A, **461**, 571

Hirschi, R., Meynet, G., & Maeder, A. 2004, A&A, **425**, 649

Holgado, G., Simón-Díaz, S., & Barbá, R. 2017, Highlights on Spanish Astrophysics IX, 394

Huang, S.-S. 1966, ARA&A, **4**, 35

Huang, W., & Gies, D. R. 2006, ApJ, **648**, 580

Huang, W., Gies, D. R., & McSwain, M. V. 2010, ApJ, **722**, 605

Hubeny, I., & Lanz, T. 1995, ApJ, **439**, 875

Hunter, I., Lennon, D. J., Dufton, P. L., et al. 2008, A&A, **479**, 541

Hunter, I., Brott, I., Langer, N., et al. 2009, A&A, **496**, 841

Iglesias, C. A., & Rogers, F. J. 1996, ApJ, **464**, 943

Iglesias, C. A., Rogers, F. J., & Wilson, B. G. 1992, ApJ, **397**, 717

Ignace, R. 2001, ApJ, **549**, L119

Kippenhahn, R., Meyer-Hofmeister, E., & Thomas, H. C. 1970, A&A, **5**, 155

Krtička, J., & Kubát, J. 2009a, MNRAS, **394**, 2065

Krtička, J., Feldmeier, A., Oskinova, L. M., Kubát, J., & Hamann, W.-R. 2009b, A&A, **508**, 841

Kurtz, M. J., & Mink, D. J. 1998, PASP, **110**, 934

Kurucz, R. 1993, ATLAS9 Stellar Atmosphere Programs and 2 km/s grid. Kurucz CD-ROM No. 13. Cambridge, Mass.: Smithsonian Astrophysical Observatory

Lamers, H. J. G. L. M., Snow, T. P., & Lindholm, D. M. 1995, ApJ, **455**, 269

Lamers, H. J. G. L. M., & Cassinelli, J. P. 1999, Introduction to Stellar Winds, by Henny J. G. L. M. Lamers and Joseph P. Cassinelli, pp. 452. ISBN 0521593980, Cambridge University Press

Langer, N. 2012, ARA&A, **50**, 107

Langer, N., Fricke, K. J., & Sugimoto, D. 1983, A&A, **126**, 207

Langer, N., Cantiello, M., Yoon, S.-C., et al. 2008, Massive Stars as Cosmic Engines, **250**, 167

Levenhagen, R. S., & Leister, N. V. 2006, MNRAS, **371**, 252

Lucy, L. B. 1982, ApJ, **255**, 286

Lucy, L. B., & White, R. L. 1980, ApJ, **241**, 300

Maeder, A. 1987, A&A, **178**, 159

Maeder, A. 1997, A&A, **321**, 134

Maeder, A. 2003, A&A, **399**, 263

Maeder, A. 2009b, Physics, Formation and Evolution of Rotating Stars: Astronomy and Astrophysics Library, ISBN 978-3-540-76948-4, Springer Berlin Heidelberg

Maeder, A., & Meynet, G. 2000b, A&A, **361**, 159

Maeder, A., & Meynet, G. 2001, A&A, **373**, 555

Maeder, A., & Meynet, G. 2005, A&A, **440**, 1041

Maeder, A., & Meynet, G. 2012, Reviews of Modern Physics, **84**, 25

Maeder, A., & Zahn, J.-P. 1998, A&A, **334**, 1000

Maeder, A., Meynet, G., Ekström, S., & Georgy, C. 2009, Communications in Asteroseismology, **158**, 72

Maggio, A., Vaiana, G. S., Haisch, B. M., et al. 1990, ApJ, **348**, 253

Mahy, L., Rauw, G., De Becker, M., Eenens, P., & Flores, C. A. 2015, A&A, **577**, A23

Martins, F., Schaerer, D., Hillier, D. J., & Heydari-Malayeri, M. 2004, A&A, **420**, 1087

Martins, F., Schaerer, D., & Hillier, D. J. 2005, A&A, **436**, 1049

Martins, F., Mahy, L., Hillier, D. J., & Rauw, G. 2012a, A&A, **538**, A39

Martins, F., Hervé, A., Bouret, J.-C., et al. 2015a, A&A, **575**, A34

Martins, F., Simón-Díaz, S., Palacios, A., et al. 2015b, A&A, **578**, A109

Mathis, S., Palacios, A., & Zahn, J.-P. 2004, A&A, **425**, 243

Mayer, P., Hanna, M. A., Wolf, M., & Chochol, D. 1998, Ap&SS, **262**, 163

Meurs, E. J. A., Fennell, G., & Norci, L. 2005, ApJ, **624**, 307

Meynet, G., & Maeder, A. 1997, A&A, **321**, 465

Meynet, G., & Maeder, A. 2000, A&A, **361**, 101

Meynet, G., & Maeder, A. 2002, A&A, **390**, 561

Meynet, G., & Maeder, A. 2003, A&A, **404**, 975

Meynet, G., & Maeder, A. 2005, A&A, **429**, 581

Meynet, G., Eggenberger, P., & Maeder, A. 2011, A&A, **525**, L11

Monnier, J. D., Zhao, M., Pedretti, E., et al. 2007, Science, **317**, 342

Morel, T. 2012, Proceedings of a Scientific Meeting in Honor of Anthony F. J. Moffat, **465**, 54

Nazé, Y. 2009, A&A, **506**, 1055

Nazé, Y., Broos, P. S., Oskinova, L., et al. 2011, ApJS, **194**, 7

Nieva, M. F., & Przybilla, N. 2007, A&A, **467**, 295

Oskinova, L. M. 2005, MNRAS, **361**, 679

Owocki, S. P., & Rybicki, G. B. 1984, ApJ, **284**, 337

Owocki, S. P., & Cohen, D. H. 2001, ApJ, **559**, 1108

Packet, W. 1981, A&A, **102**, 17

Paczyński, B. 1967, Acta Astron., **17**, 193

Paxton, B., Bildsten, L., Dotter, A., et al. 2011, ApJS, **192**, 3

Paxton, B., Cantiello, M., Arras, P., et al. 2013, ApJS, **208**, 4

Paxton, B., Marchant, P., Schwab, J., et al. 2015, ApJS, **220**, 15

Petrovic, J., Langer, N., Yoon, S.-C., & Heger, A. 2005, A&A, **435**, 247

Porquet, D., Mewe, R., Dubau, J., Raassen, A. J. J., & Kaastra, J. S. 2001, A&A, **376**, 1113

Pottasch, S. R. 1963, ApJ, **137**, 945

Przybilla, N., Nieva, M.-F., & Butler, K. 2011, Journal of Physics Conference Series, **328**, 012015

Puls, J., Urbaneja, M. A., Venero, R., et al. 2005, A&A, **435**, 669

Ramírez-Agudelo, O. H., Simón-Díaz, S., Sana, H., et al. 2013

Rauw, G., Morel, T., & Palate, M. 2012, A&A, **546**, A77

Repolust, T., Puls, J., & Herrero, A. 2004, A&A, **415**, 349

Rieutord, M. 1992, A&A, **259**, 581

Rieutord, M., & Zahn, J.-P. 1997, ApJ, **474**, 760

The ROSAT PSPC, https://heasarc.gsfc.nasa.gov/docs/rosat/pspc.html

Rybicki, G. B., & Hummer, D. G. 1991, A&A, **245**, 171

Sana, H., de Mink, S. E., de Koter, A., et al. 2012, Science, **337**, 444

Santolaya-Rey, A. E., Puls, J., & Herrero, A. 1997, A&A, **323**, 488

Schulz, N. S., Canizares, C., Huenemoerder, D., & Tibbets, K. 2003, ApJ, **595**, 365

Schulz, N. S., Testa, P., Huenemoerder, D. P., Ishibashi, K., & Canizares, C. R. 2006, ApJ, **653**, 636

Scuflaire, R., Théado, S., Montalbán, J., et al. 2008, Ap&SS, **316**, 83

Shu, F. H., & Lubow, S. H. 1981, ARA&A, **19**, 277

Simón-Díaz, S., & Herrero, A. 2007, A&A, **468**, 1063

Simón-Díaz, S., & Herrero, A. 2014, A&A, **562**, A135

Simón-Díaz, S., Godart, M., Castro, N., et al. 2017, A&A, **597**, A22

Smith, N., Vink, J. S., & de Koter, A. 2004, ApJ, **615**, 475

Song, H. F., Maeder, A., Meynet, G., et al. 2013, A&A, **556**, A100

Sota, A., Maíz Apellániz, J., Walborn, N. R., et al. 2011, ApJS, **193**, 24

Sota, A., Maíz Apellániz, J., Morrell, N. I., et al. 2014, ApJS, **211**, 10

Spruit, H. C. 2002, A&A, **381**, 923

Stothers, R. B., & Chin, C.-W. 1993, ApJ, **408**, L85

Struve, O. 1963, PASP, **75**, 207

Sweet, P. A. 1950, MNRAS, **110**, 548

Talon, S., & Zahn, J.-P. 1997, A&A, **317**, 749

Townsend, R. H. D., Owocki, S. P., & Howarth, I. D. 2004, MNRAS, **350**, 189

Uesugi, A., & Fukuda, I. 1970, Contributions from the Institute of Astrophysics and Kwasan Observatory, Institute of Astrophysics

ud-Doula, A., & Owocki, S. P. 2002, ApJ, **576**, 413

ud-Doula, A., Owocki, S. P., & Townsend, R. H. D. 2008, MNRAS, **385**, 97

ud-Doula, A., Owocki, S. P., & Townsend, R. H. D. 2009, MNRAS, **392**, 1022

van den Heuvel, E. P. J. 1976, Structure and Evolution of Close Binary Systems, **73**, 35

Villamariz, M. R., Herrero, A., Becker, S. R., & Butler, K. 2002, A&A, **388**, 940

Villamariz, M. R., & Herrero, A. 2005, A&A, **442**, 263

Vink, J. S., de Koter, A., & Lamers, H. J. G. L. M. 2000, A&A, **362**, 295

Vink, J. S., de Koter, A., & Lamers, H. J. G. L. M. 2001, A&A, **369**, 574

Vink, J. S., & de Koter, A. 2002, A&A, **393**, 543

Wade, G. A., Folsom, C. P., Grunhut, J., Landstreet, J. D., & Petit, V. 2015, New Windows on Massive Stars, **307**, 401

Waldron, W. L., & Cassinelli, J. P. 2007, ApJ, **668**, 456 (+ erratum ApJ, 680, 1595)

Wellstein, S., Langer, N., & Braun, H. 2001, A&A, **369**, 939

Yoon, S.-C., & Langer, N. 2005, A&A, **443**, 643

Yoon, S.-C., Langer, N., & Norman, C. 2006, A&A, **460**, 199

Yudin, R. V. 2001, A&A, **368**, 912

Zahn, J.-P. 1992, A&A, **265**, 115

Zahn, J.-P., Brun, A. S., & Mathis, S. 2007, A&A, **474**, 145

Zorec, J., Frémat, Y., Hubert, A. M., & Floquet, M. 2002, IAU Colloq. 185: Radial and Nonradial Pulsations as Probes of Stellar Physics, **259**, 244

A

PROCEEDINGS AND POSTER

Proceedings following the presentation of my results
obtained thanks to optical data, during IAU
Symposium 307 (Geneva, 23rd – 27th June 2014)

New windows on massive stars: asteroseismology, interferometry,
and spectropolarimetry
Proceedings IAU Symposium No. 307, 2014
G. Meynet, C. Georgy, J.H. Groh & Ph. Stee, eds.

DOI: 00.0000/X000000000000000X

Chemical abundances of fast-rotating OB stars

Constantin Cazorla[1], **Thierry Morel**[1], **Yaël Nazé**[1], **and Gregor Rauw**[1]

[1]Institut d'astrophysique, géophysique et océanographie, University of Liège, Belgium
email: `cazorla@astro.ulg.ac.be`

Abstract. Fast rotation in massive stars is predicted to induce mixing in their interior, but a population of fast-rotating stars with normal nitrogen abundances at their surface has recently been revealed (Hunter et al. 2009; Brott et al. 2011, but see Maeder et al. 2014). However, as the binary fraction of these stars is unknown, no definitive statements about the ability of single-star evolutionary models including rotation to reproduce these observations can be made. Our work combines for the first time a detailed surface abundance analysis with a radial-velocity monitoring for a sample of bright, fast-rotating Galactic OB stars to put strong constraints on stellar evolutionary and interior models.

Keywords. stars: abundances, stars: fundamental parameters, stars: rotation.

1. Introduction

By determining the abundances of the key elements expected to be affected by mixing (i.e., He, C, N, O) for a large sample of fast-rotating ($v \sin i > 200$ km s^{-1}), bright O8-B0 dwarfs in our Galaxy, our project aims at addressing the efficiency of rotational mixing in these objects. Several facilities are used: mainly el TIGRE (HEROS), complemented with archival data from the 1.93m telescope at the Observatoire de Haute-Provence (SOPHIE, ELODIE), various ESO telescopes (FEROS, UVES), NOT, and AAT. In addition, XMM-*Newton* data will also be used to validate the results obtained in the optical and to give access to elements such as Ne, Si, Mg, and Fe that are not easily measured in the optical.

2. Parameters and CNO abundance determination

Prior to any determination of the atmospheric parameters, radial velocities and projected rotational velocities, $v \sin i$, are estimated. The effective temperature T_{eff}, surface gravity $\log g$, and helium abundance by number $y = N(\mathrm{He})/[N(\mathrm{H}) + N(\mathrm{He})]$, are derived by finding the best match between a set of observed H and He line profiles, and a grid of rotationally-broadened, synthetic profiles. These have been computed using the non-LTE line-formation code DETAIL/SURFACE and Kurucz models. A microturbulence of 10 km s^{-1} was adopted. An iterative scheme is used: the effective temperature is taken as the value providing the best fit to the He I and He II lines with the same weight given to these two ions, the surface gravity is determined by fitting the wings of the Balmer lines, and the helium abundance is determined by fitting the He I features.

After determining the effective temperature and the surface gravity, CNO abundances are estimated by fitting synthetic profiles to three spectral domains in which the contribution of other elements can be neglected (see Rauw et al. 2012).

3. Results

A slowly-rotating star, 10 Lac (O9 V), was analysed to validate the procedure used to derive the atmospheric parameters and abundances. This star has its parameters and abundances derived from standard, curve-of-growth techniques (see Rauw et al. 2012, for another validation test involving two other stars).

As seen in Fig. 1, the N enrichment and C depletion detected in some stars are consistent with the appearance of CNO-cycled material at their surface. The photosphere of HD 102415 appears to be nitrogen overabundant at a level expected for a red supergiant. A single star analysis is thus inappropriate to describe this main-sequence star, raising the possibility of a mass transfer in a binary (see, e.g., Ritchie et al. 2012).

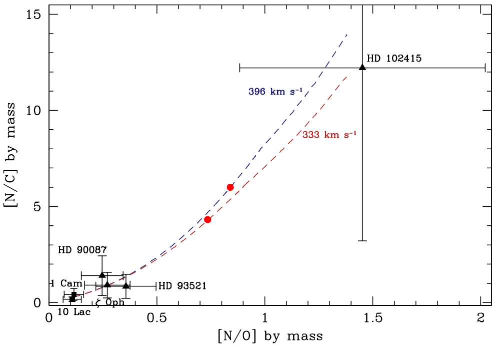

Figure 1. Dependence between the [N/C] and [N/O] abundance ratios (by mass). Except for 10 Lac, solid black symbols denote fast-rotating stars. Solid triangles and squares: archival and el TIGRE data, respectively. Dashed lines show the predictions of Geneva models (Georgy et al. 2013) for 15 $M_\odot$, $Z = 0.014$, and two initial rotational velocities. Solid circles indicate the beginning of the red supergiant phase.

4. Future work

New el TIGRE data are being acquired (up to 34 time-resolved spectra per star) in order to enlarge the sample of studied stars. Results will be compared to the predictions of models to investigate the relevance of the conclusions presented by Hunter et al. (2009). We will also account for the non-spherical shape due to fast rotation and the resulting gravity darkening. Moreover, a radial-velocity monitoring will be performed.

Acknowledgement

This research was funded through the ARC grant for Concerted Research Actions, financed by the Federation Wallonia-Brussels.

References

Brott, I., Evans, C. J., Hunter, I., et al. 2011, *A&A* 530, A116
Georgy, C., Ekström, S., Granada, A., et al. 2013, *A&A* 553, A24
Hunter, I., Brott, I., Langer, N., et al. 2009, *A&A* 496, 841
Maeder, A., Przybilla, N., Nieva, M.-F., et al. 2014, *A&A* 565, A39
Rauw, G., Morel, T., & Palate, M. 2012, *A&A* 546, A77
Ritchie, B. W., Stroud, V. E., Evans, C. J., et al. 2012, *A&A* 537, A29

Poster exhibiting my results obtained thanks to X-ray data, during XMM-Newton X-ray Universe 2017 Symposium (Rome, 6th – 9th June 2017)

A legacy survey of early B-stars using the RGS

Introduction:

- While many O-stars have been the subject of studies at high-resolution, much less B-stars have been examined.

- There are 20 B-stars with RASS count rate > 0.1 cts/s hence easily studied at high spectral resolution
    - 8 were already analyzed and one is O+O binary
    - remaining 11: some archival exposures (XMM, Chandra) + our dedicated XMM-RGS legacy survey

- Standard reduction with SAS v 16 and CIAO 4.9, filtering for solar flares, discarding nearby companions (extraction in a smaller area in such cases), combining when several exposures

Results: *(Cazorla et al. 2017, A&A, in prep)*

1) Lines

- He triplets larger than Lyα, in line with late-type massive stars results
- Gaussian fittings:
    - No significant line shift
    - No significant line broadening, except for HD38771 where HETG data indicate FWHM~1250km/s
- Line ratios:
    - Temperatures = low, typically log(T)~6.35

3) Lightcurves

- χ^2 tests
    - Constant objects: HD34816 & HD38771
    - Marginally variable cases: HD35468, HD44743, HD63922, & HD144217
    - Significantly variable targets: HD36512, HD36960 (~parabola), HD52089, HD79351 (~flare), & HD158926
- Period searches
    - Nothing coherent
- Known periods: orbits (but long) & pulsations
    - Folding reveals a clear modulation for HD44743 but only a moderate one for HD158926
- Long-term : comparison with ROSAT count rates
    - Only three cases with significantly different fluxes (HD35468, HD36512, & HD158926) : due to binarity ?

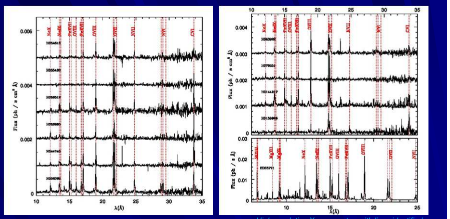

High-resolution X-ray spectra, with lines identified.

2) Global fits

- Step-by-step fits : low-res only, then high-res only freeing abundances of elements with detectable lines, then all data together
- Absorptions: no circumstellar absorption needed, as usual for “normal” B stars
- Temperatures: rather low (0.2-0.6keV), except for HD36960, HD79351 and HD144217 where a component with kT > 1keV exists
- Log(Lx/Lbol): for earliest types = -6.75..-7.37, for latest types, <-7.3 except for HD79351 (which underwent a flare: companion?)
- Abundances: best match with optical determinations for HD36512, but often different values…

X-ray lightcurves, with the mean shown by the red dotted line.

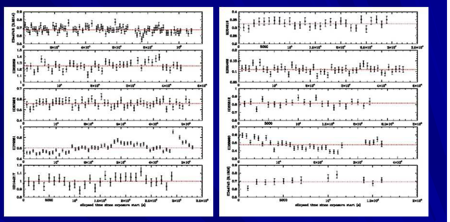

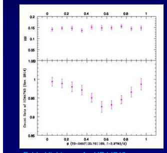

Folded lightcurve for HD44743

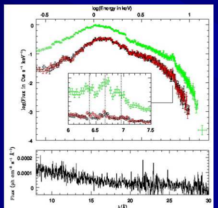

Top right: EPIC (pn in green, MOS in red/blakc) and RGS spectra of π Aqr, with a close-up showing the iron complex; Bottom left: lightcurves of π Aqr with 1ks bins; Bottom right: pn lightcurve of π Aqr with 10s bins and associated periodogram.

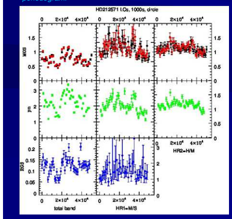

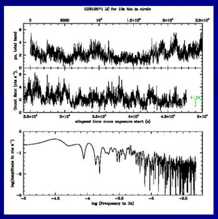

A new γ-Cas analog

(Nazé et al. 2017, A&A, letter, in press)

- The target list of our survey included a B-star with a high count rate in XMM slew survey (ROSAT count rate just below the cutoff): π Aqr, a varying Be star rotating half-critically
- It was observed in mid-November 2013
    - Data were reduced with SAS v16, filtered for flares
    - Pile-up possible : epatplot exercise negative but data extraction in both a circle and an annulus for safety
- RGS & EPIC: spectra quite featureless, except for the marginal presence of NVIIλ24.8Å and the iron complex: flurorescence line at 6.4 keV and the ionized lines at 6.7 and 7.0 keV → thermal but hot !
- Spectral fitting
    - Main temperature: 10-12keV
    - Local absorption needed
    - Iron subsolar
    - Log(L_x/L_{bol})=-5.5

    → too hot, absorbed and bright for intrinsic (wind) emission but not bright enough for HMXB

    → typically γ-Cas !
- Lightcurve
    - Short (min – flare-like) and intermediate (hour) variations, but no periodicity
    - Long (./. ROSAT, slew survey) changes too !

    → typically γ-Cas !
- Impact on our understanding of the γ-Cas phenomenon
    - π Aqr is a binary but companion ≠ compact and in close orbit ./. disk → no room for a compact accreter
      → γ-Cas phenomenon arises in Be star & its disk…

LIÈGE université

Yaël Nazé*, Constantin Cazorla, Gregor Rauw, Thierry Morel *(Univ. of Liège, Belgium)*

**FNRS*